Local Delamination Failure of Thin Material Layers

by

Bin Wang

DOCTORAL THESIS

Submitted in partial fulfilment of the requirements for the award of

Doctor of Philosophy

of Loughborough University

January 2017

The following list of papers are based on the work in this thesis

1. Post-local buckling-driven delamination in bilayer composite beams; Composite Structure 133 (2015), 1058-1066.
2. Room temperature spalling of α-alumina films grown by oxidation; Engineering Fracture Mechanics; (available online, March 14 2017).
3. Spallation of thin films driven by pocket of energy concentration; Theoretical and Applied Fracture Mechanics; (in press).

Dedicated to

my wife and my daughters

and to the memory of my parents

Abstract

Thin material layers have found various applications with various roles of functions, such as in fibre reinforced laminated composite materials, in integrated electronic circuits, in thermal barrier coating material system, and etc.. Interface delamination is a major failure mode due to either residual stress or applied load, or both. Over the past several decades, extensive research works have been done on this subject; however, there are still uncertainties and unsolved problems. This thesis presents the new developed analytical studies on local delamination failure of thin material layers.

Firstly, the analytical theories are developed for post-local buckling-driven delamination in bilayer composite beams. The total energy release rate (ERR) is obtained more accurately by including the axial strain energy contribution from the intact part of the beam and by developing a more accurate expression for the post-buckling mode shape. The total ERR is partitioned by using partition theories based on the Euler beam, Timoshenko beam and 2D-elasticity theories. By comparing with independent test results, it has been found that for macroscopic thin material layers the analytical partitions based on the Euler beam theory predicts the propagation behaviour very well and much better than the others.

Secondly, a hypothesis is made that delamination can be driven by pockets of energy concentration (PECs) in the form of pockets of tensile stress and shear stress on and around the interface between a microscopic thin film and a thick substrate. Both straight-edged and circular-edged spallation are considered. The three mechanical models are established using mixed-mode partition theories based on classical plate theory, first-order shear-deformable plate theory and full 2D elasticity theory. Experimental results show that all three of the models predict the initiation of unstable growth and the size of spallation very well; however, only the 2D elasticity-based model predicts final kinking off well. Based on PECs theory, the room temperature spallation of α-alumina oxidation film is explained very well. This solved the problem which can not be explained by conventional buckling theory.

Finally, the analytical models are also developed to predict the adhesion energy between multilayer graphene membranes and thick substrates. Experimental results show that the model based on 2D elasticity partition theory gives excellent predictions. It has been found that the sliding effect in multilayered graphene membranes leads to a decrease in adhesion toughness measurements when using the circular blister test.

Acknowledgements

I am sincerely grateful to my supervisor, Prof. Dr. Simon Wang. I thank him for his friendship, guidance, support and all the expertise he has shared with me. I also thank Dr. Andrew Watson, Dr. Chris Harvey for their supports given to me.

Also, I am very grateful to the financial support from the Department of Aeronautical and Automotive Engineering and Loughborough University for my PhD research project.

Table of Contents

List of Figures

List of Tables

List of Symbols

a	crack length
b	width of a beam
A	amplitude of buckled mode shape or upward deflection of film bubble
$E_1,\ E_2$	Young's modulus of upper and lower beams
$\overline{E}$	effective Young's modulus of film
$G,\ G_I,\ G_{II},$	total, mode I and mode II ERRs
$G_{Ic},\ G_{IIc}$	film-substrate pure mode I and II interface fracture toughness
G_c	film-substrate mode mixity dependent interface fracture toughness
$\overline{G_c}$	averaged film-substrate interface fracture toughness
G_{cf}	fracture toughness of film
$h_1,\ h_2,\ h$	thicknesses of upper, lower and intact beams
K	stress intensity factor
$K_{1,IIC}$	Mode I and II critical stress intensity factors
L	total length of beam
M_1	bending moment in upper beam
M_{1B}	delamination tip bending moment in upper beam
$M_{xB},\ N_{xBe}$	crack tip longitudinal bending moment and effective force
$M_{rB},\ N_{rBe}$	crack tip radial bending moment and effective force
$N_1,\ N_2,\ N_3$	axial forces in upper, lower and intact beams
$N_{1B},\ N_{2B},\ N_{3B}$	delamination tip axial forces on upper, lower and intact beams
α	critical buckling strain correction factor
$\theta,\ \theta'$	pure-mode-I modes
$\beta,\ \beta'$	pure-mode-II modes
γ	thickness ratio, $\gamma = h_2/h_1$
ε_c	critical local-buckling strain
ε_0	end-shortening compressive strain, $\varepsilon_0 = u_0/L$
$\varepsilon_1,\ \varepsilon_2,\ \varepsilon_3$	compressive axial strains in the upper, lower and intact beam

η	Young's modulus ratio, $\eta = E_2/E_1$
r , θ	radial and circumferential coordinates of circular film bubble
R_B	half-crack length of straight-edged delamination; radius of circular-edged delamination
u_0	end-shortening displacement
V_1	deflection of buckled upper beam
U_a	'bubble energy'; increase in combined strain energy and surface energy due to bubble separation
U_b	bending strain energy of film bubble
U_i	in-plane strain energy of film bubble
U_s	surface energy of delaminated surfaces of film bubble
U_0	strain energy of film bubble before separation
w	upward deflection of film bubble
x , y	lengthwise and widthwise coordinates of straight-edge film bubble
z	out-of-plane coordinate
β	kink-off angle
ε_x^R , σ_x^R	averaged axial relaxation strain and stress due to bending deflection
ε_r^R , σ_r^R	averaged radial relaxation strain and stress due to bending deflection
ε_0 , σ_0	uniform residual compressive strain and stress in film
ν	Poisson's ratio of film
ρ	ratio of film-substrate pure mode I and II interface fracture toughness
ψ	ratio of film-substrate pure mode II and I interface fracture toughness

List of Abbreviations

APS	Air plasma-spray
CUD	Constrained unidirectional
CZM	Cohesive zone model
DCB	Double cantilever beam
EB-PVD	Electron-beam physical vapour deposition
ENF	End-notched flexure
ERR	Energy release rate
FEA	Finite element analysis
FEM	Finite element method
FRMM	Fixed ratio mixed-mode
FSDT	First-order shear deformation theory
LEFM	Linear elastic fracture mechanics
LSB	Large scale buckling
MD	Multidirectional
MMB	Mixed-mode bending
PEC	Pocket energy concentration
PVD	Physical vapor deposition
TBC	Thermal barrier coating
TGO	Thermal growth oxidation
UD	Unidirectional
UENF	Unsymmetrical end-notched flexure
VCCT	Virtual crack closure technique
XFEM	Extended finite element method

Chapter 1 Introduction

1.1 Introduction

Thin layer/substrate material systems are commonly seen in many engineering applications, such as thermal barrier coating material system in aero engines, erosion resistance coating material system in oil transportation pipes, modern carbon /glass fibre reinforced plastic materials in aircraft, and thin film/substrate systems for electronic packages etc. The film and coating are usually very thin in comparison with the thickness of the substrate and often sustain in-plane residual stresses in service condition due to the mismatch of material properties, such as thermal expansion coefficients, or release of pre-strains in the substrate; also, the residual stress could be induced through manufacture process. In general, the residual stress has a detrimental effect on the layered material systems; it causes interface delamination and leads to partial or complete failure of the material systems.

With the increase of the residual stresses in the thin layer, the cracks could initiate and further propagate along the interface; as the crack length attains to a critical level, the interface delamination is driven by buckling and post-buckling loads. Typically, thin layer delamination is coupled with fracture and buckling mechanism.

As the crack developed in brittle, isotropic and homogeneous bodies, the crack propagation obeys the 'criterion of local symmetry', the cracks tend to kink by an angle into a direction so that the advancing crack tip is a pure mode I fracture [1,2]. The interface cracks of layered material advance either kink by an angle or along the interface depending on the competition of interface fracture toughness to that of the adjoining materials. If the fracture toughness of interface adjoining materials is strong enough, then the crack is constrained to advance along the path of the interface; the crack propagation is in the form of mixed mode, typically mixed mode I and mode II.

As mentioned above the delamination of layered materials is a process of failure under mixed mode fracture mechanics. Over the past several decades, various mixed mode partition theories have been developed by researchers. Commonly used one is the mixed mode partition theory based on stress intensity factors of 2D elasticity theory developed by Hutchinson [14]. In the work [3-11] and many others, the mixed mode partition theory is utilised based on 2D elasticity theory [14] and the assumption of rigid or brittle interface.

However, the experimental test results from very experienced researchers [15-21,30] do not agree with the predictions of the theory [14]. On the other hand, these experimental results [15-21] agree very well with the predictions from the mixed mode partition theory [22-29] that is based on Euler beam or classical plate theory for the rigid or brittle interface. The experimental results from recent studies, which were conducted by Harvey and Wang [22,23] show that the interface delamination between two layers of macroscopic thickness (such as the thickness of the layer in the order of mm) are governed by the global classical partition theory. Due to the complexity and diversity of the layered material systems and the failure modes, there are still uncertainties on this subject need to be investigated and resolved.

1.2 Project motivation

The above conclusion that the brittle interface fracture in the thin beam, plate and shell structures is governed by the Euler beam, the classical plate partition theory is for a thin layer of macroscopic thickness. The layer thickness of the interface delamination investigated by Harvey and Wang [22,23] is in the range of millimetres. However, it is not sure which theory governs the interface delamination of thin layers of microscopic thickness, namely, the thickness in the order of micrometres and nanometre thickness. Moreover, despite many research works have been carried out on the subject of thin layer delamination for several decades, there are still many unsolved problems. For example, the mechanisms of spallation of α- alumina oxidation film in the room temperature and the descrease of adhesion thoughness of multi-layered graphene membranes remain unsolved.

1.3 Project aims

The aim of the present work attempts to develop analytical mechanical models to study the mechanics of interface delamination of thin-layer-substrate material systems based on the classical, shear deformable plate and 2D elasticity theories. Whenever possible, the developed theory will be verified against experimental results in literature. Some analytical mechanical models developed in this work attempt to predict the interface crack process including crack propagation, stable, unstable delamination and spalling off of the thin

material layers. The models developed might provide an accurate analytical tool for researchers and designers to design durable, reliable thin layer material systems.

1.4 Thesis outline

The thesis contains following chapters:

Chapter 1

The motivation and objectives of the work are presented.

Chapter 2

Background knowledge of linear elastic fracture mechanics is presented and the literature review on the subject of interface delamination is conducted. Two Harvey and Wang's experimental assessment papers [22,23] serve as major references for the interface delamination between two layers of macroscopic thickness in this chapter. Detailed theories, experimental results are recorded with conclusions showing classical partition theory giving excellent predictions for delamination between two macroscopically thick layers.

Chapter 3

A study on thin layer delamination under mechanical compressive loads is presented after a brief literature review on the subject; the analytical theories are developed for post-local buckling-driven delamination in bilayer composite beams with macroscopic layer thickness. The total energy release rate (ERR) is obtained more accurately by including an axial strain energy contribution from the intact part of the beam and by developing a more accurate expression for the post-buckling mode shape. The total ERR is partitioned using partition theories based on the Euler beam, Timoshenko beam and 2D elasticity theories. Independent experimental tests by Kutlu and Chang [32] are used to verify the analytical results. The results show that, in general, the analytical partitions based on the Euler beam theory predict the propagation behaviour very well and much better than the partitions based on the Timoshenko beam and 2D elasticity theories.

Chapter 4

The work of the thin layer delamination under mechanical loads in Chapter 3 is extended to the study of the thin layer delamination under thermal loads. At first, the literature review on the subject of Thermal Barrier Coating (TBC) is given; then, a normalised analytical approach is developed to show the general trends of thermal barrier coating interface crack propagation and stability by using Euler beam, Timoshenko beam and 2D elasticity mixed mode partition theories. A case study is conducted to verify the general trends predicted by the normalised approach.

Chapter 5

A hypothesis is made that delamination can be driven by pockets of energy concentration (PECs) in the form of pockets of tensile stress and shear stress on and around the interface between a thin film and a thick substrate, where PECs can be caused by thermal, chemical or other processes. Based on this hypothesis, three analytical mechanical models are developed to predict several aspects of thin-film spallation failure including nucleation, stable and unstable growth, size of spallation and final kinking off. Both straight-edged and circular-edged spallation are considered. The three mechanical models are developed using partition theories for mixed-mode fracture based on classical plate theory, first-order shear-deformable plate theory and full 2D elasticity theory. Experimental results for room temperature spallation of α-Al_2O_3 oxide films of microscopic thickness [124] show that all three of the models predict the initiation of unstable growth and the size of spallation very well; however, only the 2D elasticity-based model predicts final kinking off well. The energy for the nucleation and stable growth of a separation bubble comes solely from the PEC energy on and around the interface, which is 'consumed' by the bubble as it nucleates and grows. Unstable growth, however, is driven both by PEC energy and by buckling of the separation bubble. Final kinking off is controlled by the fracture toughness of the interface and the film and the maximum energy stored in the separation bubble.

Chapter 6

The presence of sliding in multi-layered graphene membranes increases the fracture mode ratio G_I/G_{II}, leading to a decrease in adhesion toughness measurements when using the circular blister test. There is a large reduction of adhesion energy from monolayer to multilayer graphene membranes observed in the work [159]. In this chapter, a mechanical

model is developed with considering the fracture mode mixity and the sliding effect to give a complete calculation and correct interpretation of the adhesion energy. The study performed in this chapter shows that the delamination of thin layer of Nano thickness is controlled by 2D elasticity partition theory.

Chapter 7 Conclusions and further work are presented in this chapter.

Chapter 2 Interface delamination between two layers of macroscopic thickness

2.1 Introduction

Many modern materials are layered; laminated composite materials are one of the most representative of layered materials. One of the most common failure modes of laminated composite materials is delamination. The remote loadings applied to the composite components typically result in interlaminar tension and shear stresses that create mixed-mode I, II and III delamination. In general, the total strain energy release rate (ERR), G, contains the mode I component due to interlaminar tension, G_I, the mode II component due to interlaminar sliding shear, G_{II}, and the mode III component, G_{III}, due to interlaminar scissoring shear, as shown in Figure 2-1. In the case of one-dimensional fracture, the total ERR G contains only pure mode I, G_I and pure mode II, G_{II}.

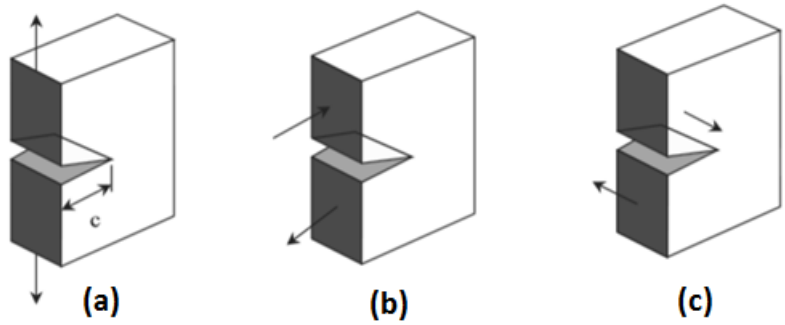

Figure 2-1: a) pure mode I, b) pure mode II, c) pure mode III.

In brittle, isotropic and homogeneous materials, it is well known that cracks propagate under pure mode I conditions [1,2] to obey the 'criterion of local symmetry'. However, the interface crack of layered materials is often constrained to propagate along the interface since the interface normally represent a plane of weakness. Typically, the interface crack propagates as a mixed mode and can even propagates under pure mode II loading.

In this chapter, the characteristic behaviours of interface delamination between two layers are presented by reviewing the relevant research works from published literatures. Two Harvey and Wang's experimental assessment papers [22,23] provide the major understanding on the subject of the interface delamination between two layers of macroscopic thickness. However, it is necessary to present some background knowledges of fracture mechanics at first.

2.2 Linear elastic fracture mechanics

Linear Elastic Fracture Mechanics (LEFM) is the fundamental theory of fracture, originally developed by Griffith (1921) [33], and completed in its essential form by Irwin (1957, 1958) [34,35], and Rice (1968) [36]. LEFM is a highly simplified but sophisticated theory that deals with cracks in elastic materials.

The theory of linear elastic fracture mechanics has been developed using a stress intensity factor (K) determined by the stress analysis, and expressed as a function of stress and crack size.

Inglis (1913) [37] reported that the local stresses around a corner or hole in a stressed plate could be many times higher than the average applied stress. Inglis demonstrated that the degree of stress magnification at the edge of the hole in a stressed plate depended on the radius of curvature of the hole. The radius of curvature at the tip of the ellipsis $\rho = \frac{b^2}{a}$.

$$k = 1 + 2\sqrt{\frac{a}{\rho}} \tag{2.1}$$

Where a is the hole radius, b is the half width of the hole and ρ here is the radius of curvature of the tip of the hole, k is the stress concentration factor.

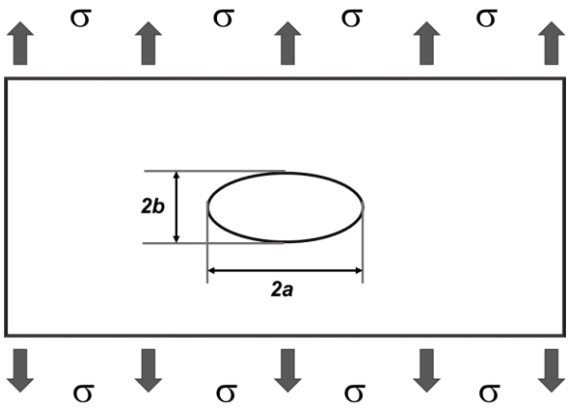

Figure 2-2: Stress concentration of an elliptical hole in a plate.

For a very narrow elliptical hole the stress concentration factor is much greater than one, see Figure 2-2. For a circular hole, the stress concentration factor is about three. The stress concentration factor does not depend on the absolute size or length of the hole but only on the ratio of the size to the radius of curvature.

Despite this progress made by Inglis, however the fundamental nature of the fracture mechanism remained unsolved until Griffith (1921). For example: why large cracks tend to propagate more easily than small cracks? This question cannot be answered by Inglis's "stress concentration" approach. In 1921, Griffith of the Royal Aircraft Establishment in England published a paper and proposed the energy-balance concept of fracture based on the principle of energy conservation laws of mechanics and thermodynamics.

Griffith proposed that the reduction in strain energy due to the formation of a crack must be equal to or greater than the increase in surface energy required by the new crack faces. According to Griffith, there are two conditions necessary for crack growth: 1) the bonds at the crack tip must be stressed to the point of failure. The stress at the crack tip is a function of the stress concentration factor, which depends on the ratio of its radius of curvature to its length; 2) for an increment of crack extension, the amount of strain energy released, must be greater than or equal to that required for the surface energy of the two new crack faces.

The first condition is based on Inglis's stress condition and the second one is the development by Griffith based on energy balance principle. The second condition can be expressed as:

$$\frac{dU_s}{da} \geq \frac{dU_\gamma}{da} \tag{2.2}$$

Where U_s is the strain energy, U_γ is the surface energy, and da is the crack length increment. Equation (2.2) expresses that for a crack to extend, the rate of strain energy release per unit of crack extension must be at least equal to the rate of surface energy requirement.

Taking the derivative, the above equation can be written as the form of energy release rate (J/m per unit width):

$$\frac{\pi\sigma_a^2 a}{E} \geq 2\gamma \tag{2.3}$$

Where γ is the fracture surface energy of the solid, σ_a is the stress applied.

Further, the critical stress σ_c for crack propagation can be determined:

$$\sigma_c = \sqrt{\frac{2E\gamma}{a\pi}} \tag{2.4}$$

The energy balance criterion indicates whether crack growth is possible, but whether it will actually occur depends on the state of stress at the crack tip. A crack will not extend until

crack tip are loaded to their tensile strength, even if there is sufficient strain energy stored to permit crack growth. Fracture only occurs when the stress at the crack tip is sufficient to break the bonds there. In practice, stress singularities due to an "infinitely sharp" crack tip are avoided by plastic deformation of the material. The concept of linear fracture mechanics is based on the small-scale yielding hypothesis in the crack tip zone. In thin film material systems, it is sometimes difficult to justify the use of the small-scale yielding hypothesis due to the small geometrical dimensions involved. In such cases, the concept of stress intensity factor becomes a more subjective matter.

Energy Release Rate

Griffith's (1921) [33], original work dealt with brittle materials—specifically glass. For ductile materials, such as steel, the surface energy predicted by Griffith's theory is usually unrealistically high. Irwin (1957) [34] realised that in a ductile material, the total energy supplied to the crack tip was not fully absorbed for creating new surfaces but instead by energy dissipation due to plastic flow in the material near the crack tip.

The strain energy available for surface energy of new crack faces cannot be simply applied to ductile solids. For example, in crystalline solids, considerable energy is consumed in the movement of dislocations in the crystal lattice and this may happen at applied stresses well below the ultimate strength of the material. Dislocation movement in a ductile material is an indication of yield or plastic deformation. Irwin modified Griffith's equation to take into account the plastic zone by simply including this term in the original Griffith equation:

$$G_c = 2\gamma \tag{2.5}$$

The modified form

$$G_c = 2\gamma + G_p \tag{2.6}$$

Then the equation (2.4) is rewritten as

$$\sigma_c = \sqrt{\frac{EG_c}{a\pi}} \tag{2.7}$$

Since the potential reduction in total potential energy in the body for a unit crack growth must exceed material fracture toughness G_c in order to grow the crack. Irwin was the first to observe that if the size of the plastic zone around a crack is small in comparison to the size of the crack, the energy required to grow the crack will not be critically dependent on the state

of stress at the crack tip. In other words, a purely elastic solution may be used to calculate the amount of energy available for fracture if the plastic zone is small.

The energy dissipated during fracture per unit of newly created fracture surface area is defined as energy release rate (ERR), and it is denoted by *G*. This quantity is central to fracture mechanics because the energy that must be supplied to a crack tip for it to grow must be balanced by the amount of energy dissipated due to the formation of new surfaces and other dissipative processes such as plasticity.

Linear elastic approach is applicable to the brittle or quasi brittle materials; it may be also used to assess fracture in non-brittle materials if the amount of plastic flow is small compared to both the crack length and the width of the sheet, *i.e.* conditions of 'small-scale yielding'.

For the purposes of calculation, the energy release rate is defined as

$$G = -\frac{\partial(U - V)}{\partial A} \tag{2.8}$$

Where U is the potential energy available for crack growth, V is the work associated with any external forces acting, and A is the crack area. The unit of *G* is J/m^2.

The failure criterion of energy release rate states that a crack will grow when the available energy release rate G is greater than or equal to a critical value G_C.

$$G \geq G_C \tag{2.9}$$

Stress intensity factor

Williams (1957) [38] established the stress intensity factors *K* to show how stresses vary near a crack tip. By using elasticity and Ary stress function approach, he showed that the stresses vary proportionally to the inverse square root of distance *r*.

Williams showed that the stress field $\sigma(r,\theta)$ in the vicinity of an infinitely sharp crack tip could be described mathematically by:

$$\sigma_{yy} = \frac{K_1}{\sqrt{2\pi * r}} \cos\frac{\theta}{2}(1 - \sin\frac{\theta}{2}\sin\frac{3\theta}{2}) \tag{2.10}$$

The first term on the right-hand side of equation (2.10) describes the magnitude of the stress whereas the terms involving θ describe its distribution. The "stress intensity factor" K_1 is defined as:

$$K_1 = \sigma_a Y\sqrt{\pi a} \tag{2.11}$$

σ_a is the externally applied stress, Y is a geometry factor, and a is the crack half-length. The stress intensity factor K_1, which includes both applied stress and crack length, is a combined "scale factor", which characterises the magnitude of the stress at some coordinates (r, θ) near the crack tip. The shape of the stress distribution around the crack tip is the same for cracks of all lengths. The stress intensity factor K_1 provides a numerical "value," which quantifies the magnitude of the effect of the stress singularity at the crack tip. There is a critical value for K_1 for different materials, which corresponds to the unstable crack propagation or residual strength of the material.

K_{1C}, the critical value of K_1

The value of K_1 at the point of crack unstable is called the critical stress intensity factor K_{1C}. K_{1C} is a material property and usually is used to characterise fracture toughness. The unit of K_{1C} is MPa*m^0.5. Low values of K_{1C} mean that, for a given stress, a material can only withstand a small length of crack before a crack unstable. Catastrophic fracture occurs when the equilibrium condition is unstable.

Equivalence of G and *K*

Energy release rate G and stress intensity factor K are related. From Equation (2.12) the strain energy release rate can be written as the function of stress and crack length; that is, for a double-ended crack within an infinite solid, the rate of release in strain energy per crack tip is:

$$G = \frac{\pi\sigma^2 a}{E} \tag{2.12}$$

$$G = \frac{K_1^2}{E} \tag{2.13}$$

When $K_1 = K_{1C}$, then G_c becomes the critical value of the energy release rate for the material which leads to crack extension and possibly fracture of the specimen. The relationship between K_1 and G is significant because it means that the K_{1C} condition is a necessary and sufficient criterion for crack growth since it contains both the stress and energy balance criteria. The value of K_{1C} describes the stresses (indirectly) at the crack tip as well as the strain energy release rate at the onset of crack extension.

2.3 Mixed mode partition

2.3.1 Mixed mode interface delamination

As known, the behaviour of interface cracking is significantly different from that of cracks in homogeneous media. The stress fields around the crack tip show an oscillatory singularity (Williams 1959) [51], as do the relative displacements between the surfaces of the crack (England 1965) [52] as well. These are associated with a physically inadmissible interpenetration of the crack surfaces near the crack tips.

Williams [51] was the first to study the problem of a crack lying on the interface between two dissimilar isotropic materials in 1959. It is well known from the analysis of Williams that at the tip of an interface crack the stress singularity is of the order r^{λ}, r is the radial distance from the crack tip, where λ is the complex eigenvalue given by

$$\lambda = -\frac{1}{2} + i\varepsilon \tag{2.14}$$

Where ε here is the bi-material constant, dependent on the properties of the materials across the interface.

$$\varepsilon = \frac{1}{2\pi}\ln[\frac{1-\beta}{1+\beta}] \tag{2.15}$$

$$\beta = \frac{\mu_1(1-2\kappa_2)-\mu_2(1-2\kappa_1)}{2[\mu_1(1-\kappa_2)+\mu_2(1-\kappa_1)]} \tag{2.16}$$

$$\kappa_j = \frac{\nu_j}{1+\nu_j} \quad \text{plane stress} \tag{2.17}$$

$$\kappa_j = \nu_j \quad \text{plane strain} \tag{2.18}$$

and μ_j = shear moduli, ν_j = Poisson's ratios and j = 1, 2 for material 1 and 2.

The presence of the term ε results in oscillatory behaviour in stresses as the crack tip is approached ($r \to 0$). The associated displacements are also oscillatory behind the crack tip as ($r \to 0$), and the crack faces interpenetrate or overlap each other. Considerable conceptual difficulties have arisen due to the presence of oscillatory singularity.

England [52] showed that this kind of oscillation is physically inadmissible but is confined to a very small region near the ends of the crack and can be ignored. To avoid the difficulties of oscillatory behaviour in stresses at the crack tip, the strain energy release rate is adopted and defined in the same way as in homogeneous materials, i.e., the rate of change of strain energy (ΔU) with virtual crack extension (Δa) as $\Delta a \to 0$. Malyshev and Salganik [53] are the first to derive the expression for total strain energy release rate G. Later several authors including Rice [54], Rice and Sib [55], Hutchinson et al. [56], Comninou [57], Sun et al. [58-60] and Raju [61] have all confirmed the unambiguity of G. Now, the attention is shifted to the evaluation of strain energy release rate components G_I and G_{II} since fracture can often be predicted by using individual mode components.

2.3.2 Mixed mode partition theories

Fracture mode partitions play a key role in the development of crack propagation criteria. Double cantilever beams (DCBs) are typical representatives of one-dimensional fracture problems and often used to determine critical energy release rates of materials. The Williams partition rules were given in his pioneering work [39]. He successfully identified one pair of pure mode conditions (mode I and II), which are valid for Euler double cantilever beams (DCBs) with bending moments alone. Unfortunately, the other set of pure mode conditions and the stealthy interactions between pure modes were missed in his work. As a result, his partition theory is only able to give the correct partition for symmetric DCBs. Another piece of pioneering work [40] was given by Schapery and Davidson who claimed that Euler beam theory does not provide quite enough information to obtain a decomposition of energy release rate into opening and shearing mode components. Hutchinson and Suo [14] presented their combined numerical and analytical rules based on stress intensity factors and claimed Williams rules [39] containing conceptual errors. Some other earlier works are given in refs. [41–43]. Several recent research works on the topic are quoted here among many others.

They are Wang and Qiao [44], Nguyen and Levy [45], Yan and Shang [46], Ouyang and Li [47], and Zou et al. [48,49]. C. M. Harvey [25] provided a detail review of mixed mode partition theories and presented the "Wang–Harvey partition theories" in his PhD thesis.

There are various partition theories. These are (i) a partition theory by Williams (1988) [39], based on Euler beam theory; (ii) a partition theory by Suo (1990) [41] and Hutchinson and Suo (1992) [14], based on 2D elasticity theory; and (iii) the Wang–Harvey partition theories based on the Euler and Timoshenko beam theories. S. Wang and C. Harvey [27-29] developed analytical partition theories based on both Euler and Timoshenko beam theories by using a completely new approach. The work reveals the in-depth mechanics of the complex problems between numerical simulations and different analytical theories. It attempts to clarify all the confusions in both numerical and analytical aspects.

The Wang–Harvey partition theories

Within the context of linear elastic fracture mechanics (LEFM) the total Energy Release Rate (ERR) *G* can be expressed as follows in a general form:

$$\begin{aligned} G = &\{M_{1B}, M_{2B}, N_{1B}, N_{2B}, P_{1B}, P_{2B}\} \times [C] \\ &\times \{M_{1B}, M_{2B}, N_{1B}, N_{2B}, P_{1B}, P_{2B}\}^T \end{aligned} \tag{2.19}$$

Where *G* is a quadratic form and non-negative definite, the general description and loading convention of DCB are presented in Figure 2-3.

According to Wang–Harvey partition theories [25-29], an analogy of *G* is the kinetic energy of a vibrating structure, which can be partitioned into individual modal energies by using natural or free vibration modes. This leads to the physical understanding: A mixed-mode fracture is formed by natural or pure fracture modes, the total ERR G can be partitioned by using these modes. This means that there exist two fundamental pure modes and all other pure modes can be determined by using them with orthogonality.

From Irwin's VCCT:

$$G_I = \frac{F_{op} * D_{op}}{2\delta A}, G_{II} = \frac{F_{sh} * D_{sh}}{2\delta A}, \tag{2.20}$$

Where F_{op} and F_{sh} are forces for opening and shear respectively; D_{op} and D_{sh} are displacement for opening and shear respectively.

For the simplicity, firstly is to consider the partition of a brittle one-dimensional beam subjected to bending moment only, $\{M_{1B}, M_{2B}, 0, 0, 0, 0\}$. The materials in consideration are assumed to be linearly elastic.

Pure mode I due to $D_{sh} = 0$: $M_{2B} = \theta_1 M_{1B}$, pure mode I due to $F_{sh} = 0$: $M_{2B} = \theta_1^{'} M_{1B}$.

Pure mode II due to $D_{op} = 0$: $M_{2B} = \beta_1^{'} M_{1B}$, pure mode II due to $F_{op} = 0$: $M_{2B} = \beta_1 M_{1B}$.

The mixed mode partition of mode I and II can be obtained in Eq. (2.21) and (2.22) respectively.

$$G_I = c_I \left(M_{1B} - \frac{M_{2B}}{\beta_1} \right) \left(M_{1B} - \frac{M_{2B}}{\boldsymbol{\beta}_1'} \right) \tag{2.21}$$

$$G_{II} = c_{II} \left(M_{1B} - \frac{M_{2B}}{\boldsymbol{\theta_1}} \right) \left(M_{1B} - \frac{M_{2B}}{\theta_1'} \right) \tag{2.22}$$

Where θ_1 and $\theta_1^{'}$ are called symmetrical pair of pure mode I; β_1 and $\beta_1^{'}$ are called symmetrical pair of pure mode II. They all depend on substrate and interface material properties, fracture locations, fracture propagation size and mechanics theories used. It is difficult to find out $\theta_1^{'}, \beta_1$ directly using $F_{sh} = 0$ and $F_{op} = 0$ as they are related to the complex interface stresses, while it is much easier to find out out θ_1 and $\beta_1^{'}$ directly using $D_{sh} = 0$ and $D_{op} = 0$. With the help of orthogonality as expressed as eq. (2.23) and (2.24), if one parameter in the equation is known, the other one can be determined using orthogonality.

$$\{1, \theta_1, 0, 0, 0, 0\}[C]\{1, \beta_1, 0, 0, 0, 0\}^T = 0 \tag{2.23}$$

$$\{1, \theta_1', 0, 0, 0, 0\}[C]\{1, \beta_1', 0, 0, 0, 0\}^T = 0 \tag{2.24}$$

Or in short, $\beta_1 = orthogonal(\theta_1)$, $\theta_1^{'} = orthogonal(\beta_1^{'})$.

Now the mixed mode partition of bending moment only can be extended to consider the general loading cases, $\{M_{1B}, M_{2B}, N_{1B}, N_{2B}, P_{1B}, P_{2B}\}$. The mixed mode partition of mode I and II can be obtained in Eq. (2.25) and (2.26) respectively.

$$G_I = c_I \left(M_{1B} - \frac{M_{2B}}{\beta_1} - \frac{N_{1B}}{\beta_2} - \frac{N_{2B}}{\beta_3} - \frac{P_{1B}}{\beta_4} - \frac{P_{2B}}{\beta_5} \right) \left(M_{1B} - \frac{M_{2B}}{\boldsymbol{\beta}_1'} - \frac{N_{1B}}{\beta_2'} - \frac{N_{2B}}{\beta_3'} - \frac{P_{1B}}{\beta_4'} - \frac{P_{2B}}{\beta_5'} \right) \tag{2.25}$$

$$G_{II} = c_{II}\left(M_{1B} - \frac{M_{2B}}{\boldsymbol{\theta_1}} - \frac{N_{1B}}{\theta_2} - \frac{N_{2B}}{\theta_3} - \frac{P_{1B}}{\theta_4} - \frac{P_{2B}}{\theta_5} \right)\left(M_{1B} - \frac{M_{2B}}{\theta_1'} - \frac{N_{1B}}{\theta_2'} - \frac{N_{2B}}{\theta_3'} - \frac{P_{1B}}{\theta_4'} - \frac{P_{2B}}{\theta_5'} \right) \quad (2.26)$$

$\theta_1, \beta_1^{'}$ is the fundamental pair of pure modes I and II; θ_i , θ_i' $(i = 1, 2, ..., 5)$ is the symmetrical pairs of pure mode I modes; β_i , β_i' $(i = 1, 2, ..., 5)$ is the symmetrical pairs of pure mode II modes. The first set of orthogonal pure modes I and II is $\theta_i = \mathbf{orthogonal}(\beta_j)\,(i,\ j = 1, 2, ..., 5)$; the second set of orthogonal pure modes I and II is $\theta_i' = \mathbf{orthogonal}(\beta_j')\,(i,\ j = 1, 2, ..., 5)$. Once $\theta_1, \beta_1^{'}$ are determined either analytically or empirically or numerically, all other pure modes are conveniently obtained by using the orthogonality operation.

The formula and methodology are universal for beams, plates and shells, classical, shear deformable and 2D elasticity mechanics for rigid (brittle) and non-rigid (ductile) interfaces.

As known, the main difference between Euler beam and Timoshenko beam theory is how to consider the through-thickness shear deformation. In the Euler beam theory the cross section is perpendicular to the bending line after shear deformation; however, the Timoshenko beam theory allows the rotation between the cross section and the bending line. When the through-thickness shear modulus at the crack tip tends to infinity, Timoshenko beam becomes to Euler beams, they become equal. This difference is analogically applicable to classic plate theory and first order shear- deformable plate theory.

Due to the difference between Euler beam and Timoshenko beam theory, in the Wang–Harvey Euler beam partition theory, the two sets of pure mode pairs are distinct and this leads to stealthy interactions. Under the Wang–Harvey Timoshenko beam partition theory, the two sets of pure mode pairs exactly coincide and there are no stealthy interactions. Consequently, the global partition and local partition of mixed mode are the same for Euler beam partition theory, but not for Timoshenko partition theory.

The other difference between Euler beam and Timoshenko beam mixed mode partition theories is that the P_{1B} and P_{2B} do not contribute to the strain energy in Euler beam theory, but contribute to the mixed-mode partition using Timoshenko beam theory. Since the through-thickness shear effect does not generate any axial displacement in Timoshenko beam theory, the two crack tip forces P_{1B} and P_{2B} produce pure mode I fracture only.

The detailed partition theories between Euler beam and Timoshenko beam theories are provided in Harvey-Wang's work [25,28,29]. The extensive numerical and experimental validations are performed [22-25]; it is concluded that the Wang–Harvey partition theories are readily applicable to a wide-range of engineering structures and they provide an excellent tool for studying interfacial fracture and delamination.

It was also found that the average of these two extreme cases (Euler beam and Timoshenko partition theories) provides a very accurate approximation to the 2D elasticity result from the Suo–Hutchinson partition theory [14,41,50]. Figure 2-3 shows the general description and loading convention of DCB used in Wang-Harvey partition theories. The number 1 and 2 refer to the upper and lower layers respectively. No subscript is used for the intact part of beam.

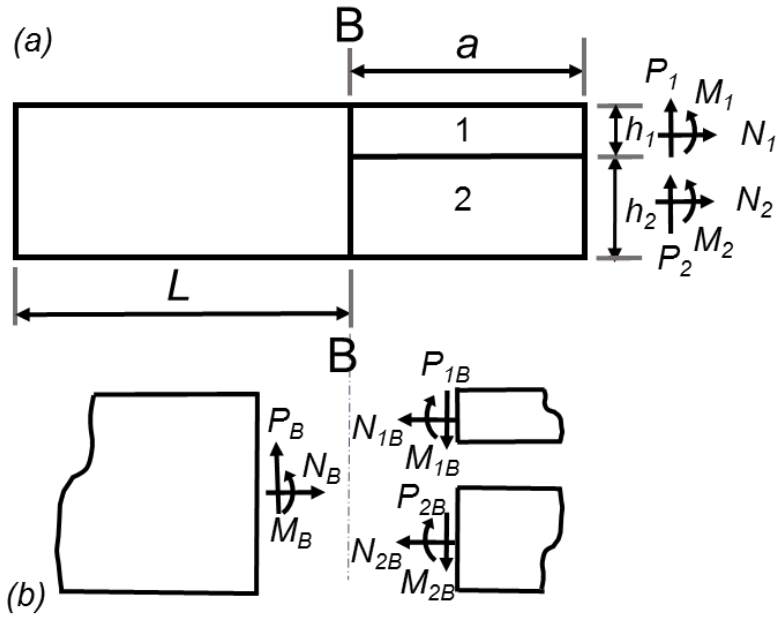

Figure 2-3: DCB (a) general description and (b) crack tip force [23]

The mode I and II components of the total energy release rate for considering bending and axial loading, denoted by G_{IE} and G_{IIE} respectively for using Euler beam partition theory, are

$$G_{IE} = c_{IE}(M_{1B} - \frac{M_{2B}}{\beta_1} - \frac{N_{1B}}{\beta_2} - \frac{N_{2B}}{\beta_3})(M_{1B} - \frac{M_{2B}}{\beta'_1} - \frac{N_{1B}}{\beta'_2} - \frac{N_{2B}}{\beta'_3}) \quad (2.27)$$

$$G_{IIE} = c_{IIE}(M_{1B} - \frac{M_{2B}}{\theta_1} - \frac{N_{1B}}{\theta_2} - \frac{N_{2B}}{\theta_3})(M_{1B} - \frac{M_{2B}}{\theta'_1} - \frac{N_{1B}}{\theta'_2} - \frac{N_{2B}}{\theta'_3}) \quad (2.28)$$

Where θ_i and β_i represent the first set of pure mode I and II relationships respectively and θ'_i and β'_i represent the second set. The detail calculation of these can be found in reference [23].

$$c_{IE} = G_{\theta 1}[(1-\frac{\theta_1}{\beta_1})(1-\frac{\theta_1}{\beta_1^{'}})]^{-1} \tag{2.29}$$

$$c_{IIE} = G_{\beta 1}[(1-\frac{\beta_1}{\theta_1})(1-\frac{\beta_1}{\theta_1^{'}})]^{-1} \tag{2.30}$$

According to the Wang–Harvey Timoshenko beam partition theory [27-29], the mode I and II components of the energy release rates for considering bending and axial loading, denoted by G_{IT} and G_{IIT} respectively are

$$G_{IT} = c_{IT}(M_{1B} - \frac{M_{2B}}{\beta_1} - \frac{N_{1B}}{\beta_2} - \frac{N_{2B}}{\beta_3})^2 \tag{2.31}$$

$$G_{IIT} = c_{IIT}(M_{1B} - \frac{M_{2B}}{\theta_1} - \frac{N_{1B}}{\theta_2} - \frac{N_{2B}}{\theta_3})^2 \tag{2.32}$$

Where

$$c_{IT} = G_{\theta 1}(1-\frac{\theta_1}{\beta_1})^{-2} \tag{2.33}$$

$$c_{IIT} = G_{\beta 1}(1-\frac{\beta_1}{\theta_1})^{-2} \tag{2.34}$$

Details of $G_{\theta 1}$ and $G_{\beta 1}$ in Eq. (2.29), (2.30), (2.33) and (2.34) are explained in reference [23].

Finally, the averaged partition theory is the average of the Wang–Harvey Euler and Timoshenko beam partitions. This partition has been found to give an excellent approximation to the partition from 2D elasticity theory [27-29]. The mode I and II components of the energy release rate for considering bending and axial loading from the averaged partition theory are denoted by G_{IA} and G_{IIA} respectively. They are

$$G_{IA} = (G_{IE} + G_{IT})/2 \tag{2.35}$$

$$G_{IIA} = (G_{IIE} + G_{IIT})/2 \tag{2.36}$$

These three partitions are reduced for isotropic materials. A thickness ratio $\gamma = h_2/h_1$ is now introduced. The present Euler beam partitions for isotropic beams reduce to

$$G_{IE} = c_{IE}(M_{1B} - \frac{M_{2B}}{\beta_1} - \frac{N_{1Be}}{\beta_2})(M_{1B} - \frac{M_{2B}}{\beta'_1}) \quad (2.37)$$

$$G_{IIE} = c_{IIE}(M_{1B} - \frac{M_{2B}}{\theta_1} - \frac{N_{1Be}}{\theta_2})(M_{1B} - \frac{M_{2B}}{\theta'_1} - \frac{N_{1Be}}{\theta'_2}) \quad (2.38)$$

Where the c_{IE} and c_{IIE} are still given by Equation (2.29), (2.30),

$$N_{1Be} = N_{1B} - N_{2B}/\gamma \quad 2.39)$$

The pure mode relationships are as below:

$$\theta_1 = -\gamma^2 \quad (2.40)$$

$$\theta_2 = -\frac{6}{h_1} \quad (2.41)$$

$$\beta_1 = -\frac{\gamma^2(3+\gamma)}{1+3\gamma} \quad (2.42)$$

$$\beta_2 = -\frac{2(3+\gamma)}{h_1(\gamma-1)} \quad \text{for } \gamma \neq 1 \quad (2.43)$$

$$\beta_2 = 0 \quad \text{for } \gamma = 1$$

$$\theta'_1 = -1 \quad (2.44)$$

$$\theta'_2 = -\frac{6(1+\gamma)}{h_1(1+\gamma^3)} \quad (2.45)$$

$$\beta'_1 = \gamma^3 \quad (2.46)$$

The isotropic $G_{\theta 1}$ and $G_{\beta 1}$ for use in equation (2.29) and (2.30) are

$$G_{\theta 1} = \frac{24\gamma}{Eb^2h_1^3(1+\gamma)} \quad (2.47)$$

$$G_{\beta 1} = \frac{72\gamma(1+\gamma)}{b^2Eh_1^3(1+3\gamma)^2} \quad (2.48)$$

The Timoshenko beam partition for isotropic beams reduced to:

$$G_{IT} = c_{IT}(M_{1B} - \frac{M_{2B}}{\beta_1} - \frac{N_{1B}}{\beta_2})^2 \quad (2.49)$$

$$G_{IIT} = c_{IIT}(M_{1B} - \frac{M_{2B}}{\theta_1} - \frac{N_{1Be}}{\theta_2})^2 \quad (2.50)$$

The Suo–Hutchinson partition theory

Suo [41], Suo and Hutchinson [14] developed a partition theory for isotropic DCBs using 2D elasticity theory and stress intensity factors, which are analytical except for one parameter determined numerically.

This partition theory assumes that a square-root singular field exists, so the partition is expressed in terms of stress intensity factors. The mode I and II stress intensity factors K_{ISH} and K_{IISH} are

$$K_{ISH} = \frac{N}{\sqrt{2h_1 U}}\cos(\omega) + \frac{M}{\sqrt{2h_1^3 V}}\sin(\omega+\varepsilon) \tag{2.51}$$

$$K_{IISH} = \frac{N}{\sqrt{2h_1 U}}\sin(\omega) + \frac{M}{\sqrt{2h_1^3 V}}\cos(\omega+\varepsilon) \tag{2.52}$$

Where the M and N are linear combination of the applied loads:

$$N = -N_1 + C_1(N_1+N_2) - C_2[M_1+M_2+\frac{h_1}{2}(N_2-\gamma * N_1)]/h_1 \tag{2.53}$$

$$M = M_1 - C_3[M_1+M_2+\frac{h_1}{2}(N_2-\gamma * N_1)] \tag{2.54}$$

$$C_1 = \frac{1}{1+\gamma}, \qquad C_2 = \frac{6\gamma}{(1+\gamma)^3}, \quad C_3 = \frac{1}{(1+\gamma)^3} \tag{2.55}$$

And the geometric factors U, V and ε are functions of γ:

$$U = \frac{\gamma^3}{3+6\gamma+4\gamma^2+\gamma^3} \quad \text{and } V = \frac{\gamma^3}{12(1+\gamma)^3} \tag{2.56}$$

$$\frac{\sin\varepsilon}{\sqrt{UV}} = \frac{6(1+\gamma)}{\gamma^3} \tag{2.57}$$

With help of numerical solution, the ω is determined

$$\omega = 52.1^\circ - 3^\circ/\gamma \tag{2.58}$$

For the spalling case, $\gamma \to 0$, $\omega = 52.1^\circ$, the mode I and II stress intensity factors become:

$$K_{ISH} = \frac{M_1}{b}\sqrt{\frac{6}{h_1^3}}\sin(52.1^\circ) - \frac{N_1}{b}\sqrt{\frac{2}{h_1}}\cos(52.1^\circ) \tag{2.59}$$

$$K_{IISH} = -\frac{M_1}{b}[\sqrt{\frac{6}{h_1^3}}\cos(52.1^\circ) - \frac{N_1}{b}\sqrt{\frac{1}{2h_1}}\sin(52.1^\circ) \tag{2.60}$$

The relationship between stress intensity factor and energy release rate for plane stress is $K^2 = EG$; for plane strain, E can be simply replaced by $E/(1-v^2)$.

Similar to the Timoshenko beam partition theory, the 2D elasticity partition theory has different global and local mixed mode partitions, the results are mesh size dependant. As mentioned, Euler beam partition theory is a global mixed mode partition, the results are insensitive to mesh size at the crack tip.

The Williams partition theory

Williams (1959) [51] was the first to study the problem of a crack lying on the interface between two dissimilar isotropic materials. He was one of the first researchers to attempt to partition a mixed mode [39]. His theory has been applied to the various test methods for laminates [15,16,39]. His pioneering work was partially successful, in that this theory correctly predicts a pair of pure modes and also gives the correct partition for a symmetric DCB, i.e. $\gamma = 1$. However, it cannot identify the other pure modes and missed the stealthy interactions between pure modes according to S. Wang and C. Harvey [26-29]. The Williams partition, denoted by G_{IW} and G_{IIW}, is now introduced here. Again, for consistency, the notation has been changed where appropriate to match the conventions in this thesis.

$$G_{IW} = \frac{6(M_{2B} - M_{1B}\gamma^3)^2}{b^2 E h_1^3 \gamma^3 (1+\gamma^3)} \tag{2.61}$$

$$G_{IIW} = \frac{18\gamma(M_{1B} + M_{2B})^2}{b^2 E h_1^3 (1+\gamma^3)(1-\gamma+\gamma^2)} + \frac{(1-\gamma)^2 (N_{2B} - \gamma N_{1B})^2}{2b^2 E h_1 \gamma^3 (1+\gamma)} \tag{2.62}$$

2.3.3 Mixed mode partition using numerical methods

Virtual crack closure technique (VCCT) and cohesive interface element model are commonly used in the finite element analysis of delamination features. The two methods employ similar principle, and they simulate the crack propagation by the energy release rate criterion. The principle of VCCT is based on classical fracture mechanics, which investigates the behaviour of crack propagation when an initial crack is designated. While cohesive element is a numerical model based on damage mechanics, in which the stiffness of the element decrease when passing a critical stress, until a complete failure is reached, and then the bonding

element is eliminated to simulate the propagation of a fracture. Therefore, the entire process of crack initiation to propagation could be analysed by cohesive models.

The crack closure method is based on Irwin's crack closure integral [35]. The method is based on the assumption that the energy released when the crack is extended by δa is identical to the energy required to re-close the crack by that same distance. This method needs two complete FEM simulations (before and after crack extension). The VCCT is based on the same assumptions as the crack closure method. However, in addition, it is assumed that a crack extension of δa does not significantly alter the state at the crack tip. As a result of this assumption, the ERR partition can be calculated with one FEM simulation only using the VCCT.

In recent years, Ronald Krueger [62-65] carried out series of the benchmark assessment of automated delamination propagation capability in finite element codes for standard software Abaqus, Ansys and MD Nastran and Marc. However, the assessments are mainly based on DCB, ENF and MMB beams, the feasibility of using these standard FEA software for specific problem, like buckling driven delamination, mixed mode partition for bi-material interface is not very clear. At least further validation works are required before using these standard FEA codes.

Rybicki and Kanninen [66] seems to be the first to evaluate of both mode I and mode II stress intensity factors from the results of a single analysis. The method does not use stresses, the conventional constant strain elements have been used, and a coarse grid near the crack tip was found to be sufficient. The axial and vertical forces at the crack tip were obtained by placing very stiff springs between adjacent points and evaluating the forces in these springs. The better results are obtained by using four-node quadrilateral, non- singular elements.

It is convenient to maintain the same size for the elements, of which nodal force and displacement are used. If this is not the case, then a modification to handle this case is needed. At first, the VCCT was used to calculate energy release rate mode I and mode II. Then mode I and mode II stress intensity factors are calculated from energy release rate.

The relationship between G and the stress intensity factor for an isotropic material in plane strain is established using Irwin's crack closure integral [35],

$$G = \frac{(1-\nu^2)}{E} K_I^2 + \frac{(1-\nu^2)}{E} K_{II}^2 \qquad (2.63)$$

The accuracy to predict strain energy release rate for bi-material interface depends on the mesh density applied to crack propagation area. From Raju's study [61], the individual energy release rate did not show convergence as the delamination tip elements were made smaller. In contrast, the total strain energy release rate, G, converged and remained unchanged as the delamination tip elements were made smaller and agreed with the total G analytical calculated.

For two different anisotropic materials, the singularity is not the classical square root singularity but is of the form $r^{-1/2+i\gamma}$, where r is the radial distance measured from the delamination tip. The γ depends on the material properties of the two materials. This imaginary power leads to the stress oscillations very close to the delamination tip. The oscillatory component of the singularity may cause the non-convergence of the individual G components. In the finite element analysis, this means that the computed mode I and mode II strain energy release rates will be dependent on the crack tip element size and do not show convergence as the crack tip elements are made smaller.

B. Dattaguru, et al. performed another convergence study for simulate mode I and mode II energy release rate for bi-material interface delamination [67]. The strain energy release rate components G_I and G_{II} in mode I and mode II at the tip of an interface crack in a bi-material plate under tension in a direction normal to the interface were evaluated using finite element analysis. The strain energy release rate components G_I and G_{II} are calculated at the crack tip. The results show that G_I and G_{II} are likely to show an oscillatory trend at infinitesimally small $\Delta a/a$. Based on the results obtained, it appears that such oscillations are likely to occur only when the virtual crack extension proposed Δa is less than the contact zone size r. Figure 2-4 shows the changes of G_I, G_{II} and total G_T with reducing the mesh size as the mesh size at crack tip becomes smaller, $\Delta a/a \to 0$, the G_{II} is close to total G_T.

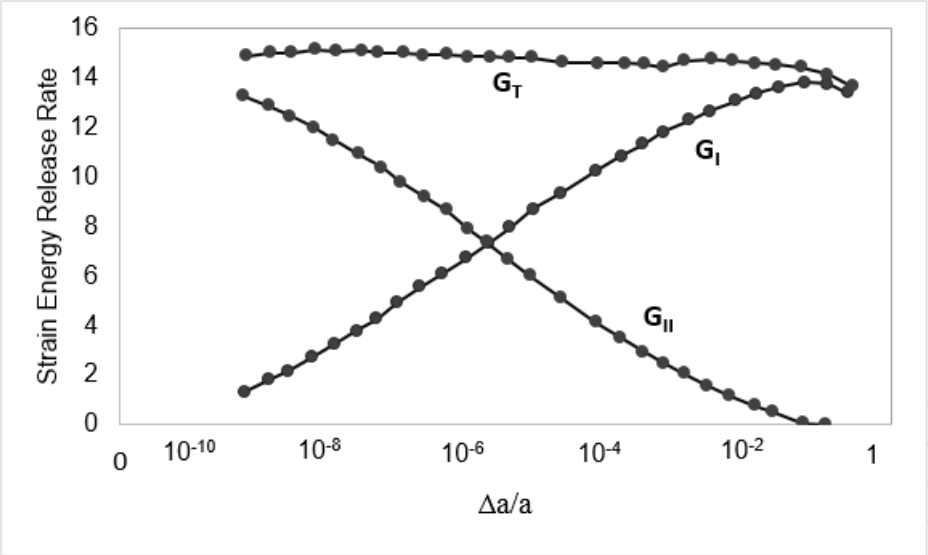

Figure 2-4: ERR convergence of an edge cracked bi-material plate subjected to tension [67].

The difficulty with the convergence of the strain energy release rate components G_I and G_{II} as $\Delta a / a \to 0$ led Raju [61] to consider a finite thickness adhesive layer at the interface with the crack at the centre of the adhesive layer. The comparison energy release rates done by Raju [61] for the 'bare' interface laminate, i.e. one without the resin layer, and for the laminate with the resin showed that the 'bare' interface models are a very good approximation for the resin case if the delamination tip elements were one-quarter to one-half of the ply thickness.

2.3.4 Mixed mode failure criteria

As a crack grows, the required energy must be balanced by the amount of energy dissipated due to the formation of new surfaces and other dissipative processes, such as plasticity. When the elastic energy released due to a potential increment of crack growth exceeds the demand for surface energy for the same crack growth, the crack propagation will start. In interface cracking, since mixed-mode cracks propagating along an interface cannot kink into a mode I fracture, therefore propagation is generally in a form of a mixed-mode.

Reeder evaluated the many different mixed-mode failure criteria for predicting delamination growth [68]. Failure criterion on stress or strain near the crack tip, crack opening displacement, stress intensity factor, or strain energy release rate are reviewed [68]. Strain energy release rate is commonly used as a good measure of a materials resistance to

delamination extension, and most of the failure criteria can be written in terms of a critical strain energy release rate or fracture toughness.

Zou Z. et al. [48] provided an evaluation of the mixed-mode failure criteria and general guideline for selecting an appropriate criterion for some materials. It is crucial to use correct mixed mode failure criterion to predict the delamination. The evaluation [48] is based on MMB test. MMB test allows almost any combination of mode I and mode II loading. The experimental tests [48] show that the failure response of different materials is so different that no single criterion based on G_{IC} and G_{IIC} can model all delamination failure. The arbitrary parameter is introduced, if the parameter can be changed so that the criterion can fit the test data. Zou Z. et al. [48] reported that the fracture surfaces of different materials change significantly with mixed-mode ratio. The similarity in the fracture surfaces of these materials may explain the similarity between the shapes of the failure responses of these two materials.

Since the mode I and mode II fracture toughness data is readily available, the mixed-mode failure criteria will be written in terms of the pure-mode toughness, G_{IC} and G_{IIC}, when possible. Once the mixed-mode response of a material has been determined, the shape of the response can be compared to the different failure criteria presented here.

The simplest criterion which allows for the effect of mixed-mode partition is the 'linear criterion', Eq. (2.64), which normalises each component of ERR against its critical pure-mode value. If the sum of these normalised components reaches one, then the crack propagates. As shown, the failure locus is a straight line connecting the pure mode I and mode II fracture toughness.

Linear mixed mode failure criterion is the one often used; if the failure locus and critical energy release rates G_{Ic} and G_{IIc} for the material are known,

$$\frac{G_I}{G_{IC}} + \frac{G_{II}}{G_{IIC}} = 1 \tag{2.64}$$

For the condition the energy release rate G_I and G_{II} meet the criteria as expressed in equation above, then the crack propagation starts.

The next failure criterion for mixed mode delamination is quadratic failure criterion.

$$\left(\frac{G_I}{G_{IC}}\right)^2 + \left(\frac{G_{II}}{G_{IIC}}\right)^2 = 1 \tag{2.65}$$

The other criteria introduced by Benzeggah and Kenane [69] using a simple mathematical relationship between G_c and G_{II}/G_I.

$$G_c = G_{IC} + (G_{IIC} - G_{IC})(\frac{G_{II}}{G_T})^{\eta} \quad (2.66)$$

This is typically called B-K criterion. The exponent η is determined by a curve fit.

The process to work out the B-K criterion is as follows:

A quasi static mixed-mode fracture criterion is determined by plotting the interlaminar fracture toughness, G_c, versus the mixed-mode ratio, G_{II}/G_T, determined from data generated using pure mode I Double Cantilever Beam (DCB) (G_{II}/G_T=0), pure mode II End Notched Flexure (ENF) (G_{II}/G_T=1), and Mixed-Mode Bending (MMB) tests of varying ratios, as shown in Figure 2-5 for material C12K/R6376. A curve fit of these data is performed to determine a mathematical relationship between G_c and G_{II}/G_T. Failure is expected when, for a given mixed-mode ratio G_{II}/G_T, the calculated total energy release rate, G_T, exceeds the interlaminar fracture toughness, G_c. G_T is the total critical strain energy release rate.

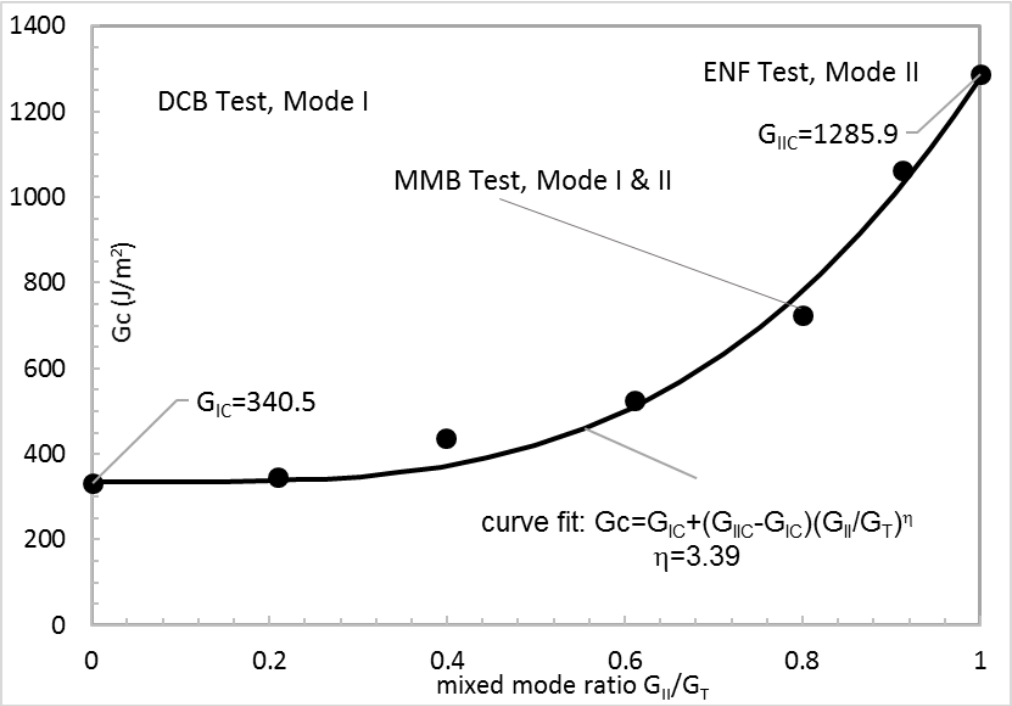

Figure 2-5: Mixed-mode fracture criterion for composite materials [63].

When choosing a failure criterion, the number of arbitrary variables should be considered, and whether criterion is in a form, which can be easily used. A simpler criterion with fewer variables is preferred. After the appropriate failure criterion for the material is chosen, a

square fit to the experimental data can be performed to optimise any arbitrary constants of the criterion.

2.3.5 Mixed mode fracture toughness test

Delamination toughness under mode I opening load and mode II shear load can be measured with the double cantilever beam (DCB) test, the end notch flexure (ENF) test, see Figure 2-6, respectively. The MMB test (Figure 2-6) allows almost any combination of mode I and mode II loading to be tested with the same test specimen configuration.

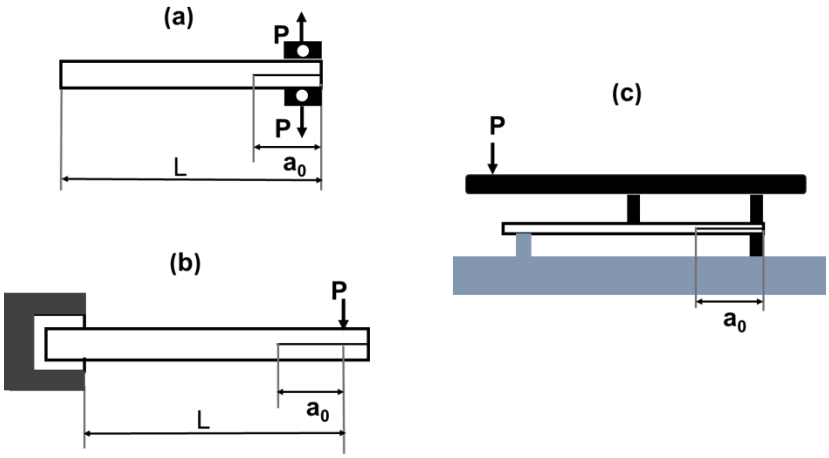

Figure 2-6: Illustration of DCB, ENF and MMB test.

MMB is a simple combination of a DCB (mode I) specimen and an ENF (mode II) specimen. Load is applied to a beam specimen with an end crack by means of a lever where the distance, L, between the load point and the fulcrum can be varied. The design of the MMB apparatus allows us to introduce mode I loading at the end of the lever and mode II loading at the fulcrum.

2.4 Experimental assessments of interface delamination between two layers of macroscopic thickness

2.4.1 Wang–Harvey's first experimental assessment

The different approaches to partitioning the mixed-mode interface fractures are introduced in section 2.3.2. These are (i) a partition theory by Williams [39] based on Euler beam theory; (ii) a partition theory by Suo [50] and Hutchinson and Suo [14] based on 2D elasticity theory;

and (iii) the Wang–Harvey partition theories [27-29] based on the Euler and Timoshenko beam theories. The performance of these mixed mode partition theories was first investigated by C. Harvey and S. Wang (2012) [22] using results from the various experimental tests presented in the literatures. Their studies showed that the Wang–Harvey Euler beam partition theory provides the best explanation for all the experimental observations for the interface delamination between two layers of macroscopic thickness; all the layer thicknesses of tested specimens are in the millimetre range. The excellent agreement has been achieved with the linear failure locus for predicting the interface fracture toughness. It is also observed that the global partition of energy release rate predicts the most accurate results in a good agreement with the experimental data from the specimens tested by Charalambids M. et al. [17] and Hashemi S. et al. [18].

In the experimental assessment conducted by C. Harvey and S. Wang [22], firstly the experimental data from asymmetric DCB test is used. As shown in Figure 2-7 (a), equal and opposite bending moments are applied to the upper and lower arms of an asymmetric beam specimen. The crack tip loads are therefore $M_{1B} = -M_{2B} = M$ and $N_{1Be} = 0$. Experimental measurements of the total critical energy release rate Gc for epoxy-matrix/carbon-fibre specimens with various values for h_1 (top layer thickness) and h_2 (bottom layer thickness) are extracted from [17] for comparison; the G_C values predicted by the various partition theories in section 2.3.2 for each specimen are compared against the experimentally measured G_C values. Generally, if the failure locus and critical energy release rates G_{IC} and G_{IIC} for the material are given, the total critical energy release rate Gc for a specimen can be calculated using Eq. (2.67). The critical mode I and mode II energy release rate G_{IC} and G_{IIC} can be determined experimentally by DCB and ENF test as mentioned in section 2.3.5. In this assessment, the values used are G_{IC} = 0.27kN/m and G_{IIC} =0.63kN/m [18]. In Table 2-1, mixed mode ratio G_I/G are predicted for an epoxy carbon-fibre asymmetric DCB by different partition theories, the Gc is calculated using Eq. (2.67) to compare with the Gc obtained from experimental tests [17].

$$G_C = \left[\frac{(G_I / G)}{G_{IC}} + \frac{1-(G_I / G)}{G_{IIC}} \right]^{-1} \tag{2.67}$$

Both the Wang–Harvey Euler beam theory and the Williams partition theory predict that the fracture is pure mode I for all values of h_1 and h_2. This is the condition of $M_{2B} = M_{1B} = \theta_1'$, pure mode I [27,28]. Therefore, $G_C = G_{Ic}$ for all the specimens. The experimental G_C values

show very small variation. The Wang–Harvey Euler beam and Williams's theories are both compatible with the experimental results. The Wang–Harvey Timoshenko beam partition theory shows significantly more variation and in the majority of cases is not close to the experimental G_C values. As expected [28], the Suo–Hutchinson and averaged partition theories are very similar.

It is therefore concluded that all theories, except of the Wang–Harvey Timoshenko beam partition theory, are compatible with these experimental results. However, only from asymmetric DCB test, it is not sufficient to draw further conclusion. As the next, the FRMM **(**fixed-ratio mixed-mode**)** test data [17] are used for the further investigation.

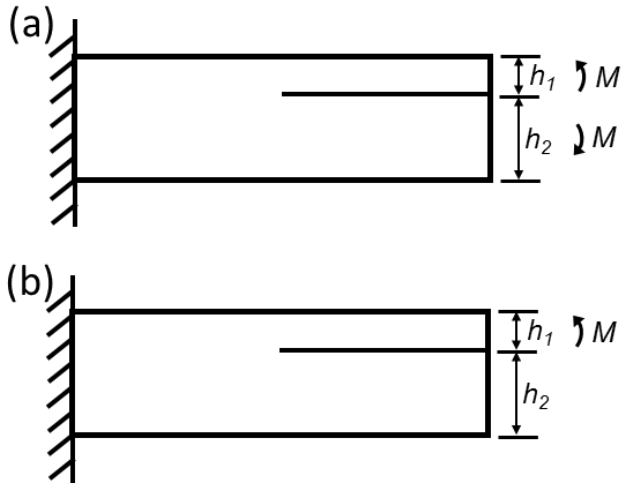

Figure 2-7: Tests with asymmetric beam (a) symmetric DCB test and (b) FRMM test [22].

Figure 2-7 (b) shows the fixed-ratio mixed-mode (FRMM) test in which a bending moment M is applied to the upper arm only of an asymmetric beam specimen. The crack tip loads are therefore $M_{1B} = M$ and $M_{2B} = N_{1Be} = 0$, which produces a mixed mode. The total critical energy release rate Gc can be measured experimentally, and Gc was partitioned into G_I and G_{II} using the Williams partition theory. These values of G_I and G_{II} are the black, filled circle markers shown in Figure 2-8.

From Figure 2-8, it is seen that the Wang–Harvey Euler beam partition theory performs much better than the other partition theories when compared with the linear failure locus. A trend line, which is represented by the black dashed line in Figure 2-8, has been plotted through the Wang–Harvey Euler beam partition theory. For comparison, a solid black trend line has also been plotted through the Williams partition.

The results from the other partition theories are shown in Figure 2-8. The mixed mode partition of experimental measured Gc using Wang–Harvey Timoshenko beam partition theory forms a separate vertical curve. The Suo–Hutchinson and the averaged partitions are very similar and form another curve half way between the curves from the Wang–Harvey Euler and the Timoshenko beam partitions. Since the linear failure locus is generally regarded to be a good approximation to the actual failure locus, it can be concluded that, at least for these specimens, the Wang–Harvey local Timoshenko beam and averaged partition theories and the Suo–Hutchinson partition theory cannot give the partition that predicts the fracture propagation. It can be observed that the Wang–Harvey Euler beam partition gives much closer agreement with the expected linear failure locus and expected G_{Ic} and G_{IIc} than the Williams partition.

Table 2-1: Measured Gc for an asymmetric DCB together with the values from the various partition theories [22].

	Measured		Suo-Hutchinson		Williams		Wang-Harvey theories				
							Euler		Timoshenko		Averaged
γ	*h* *(mm)*	Gc (kN/m)	G_I/G (%)	Gc (kN/m)	GI/G (%)	Gc (kN/m)	GI/G (%)	Gc (kN/m)	GI/G (%)	Gc (kN/m)	GI/G (%)
1.33	3.85	0.26	96.4	0.28	100.0	0.27	100.0	0.27	94.2	0.28	97.1
1.55	3.70	0.27	92.4	0.28	100.0	0.27	100.0	0.27	87.7	0.29	93.9
1.97	3.33	0.28	85.5	0.29	100.0	0.27	100.0	0.27	75.7	0.31	87.8
3.72	10.00	0.29	75.3	0.31	100.0	0.27	100.0	0.27	50.1	0.38	75.1
4.11	2.86	0.29	75.2	0.31	100.0	0.27	100.0	0.27	47.4	0.39	73.7

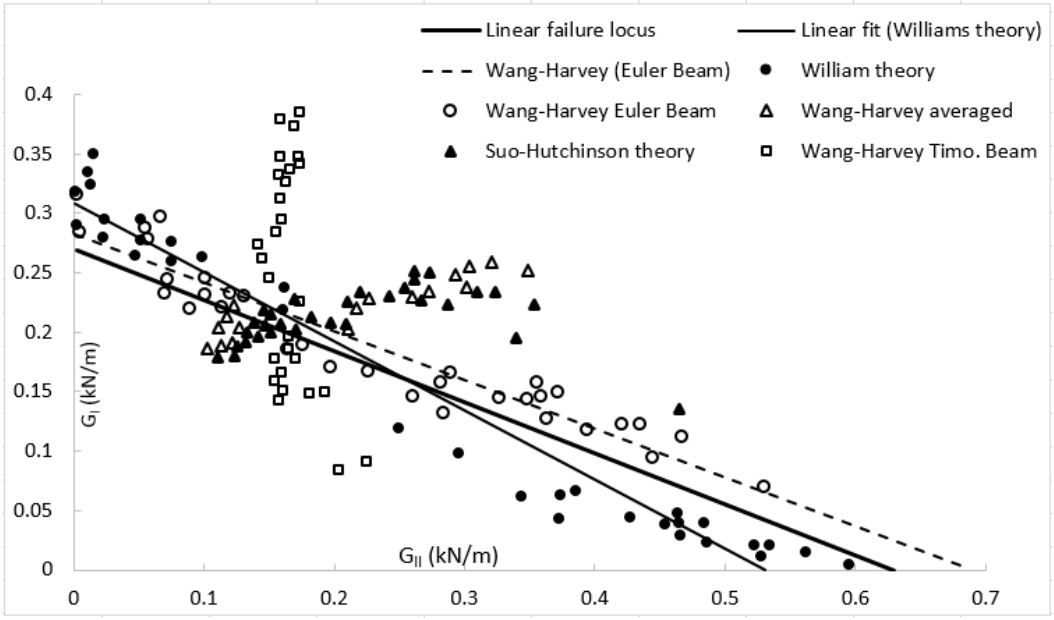

Figure 2-8: A comparison of the FRMM test partitions from various partition theories [22].

The experimental assessments from C. Harvey and S. Wang [22] are based on the assumption that the linear failure criterion, Eq. (2.64). From Eq. (2.64) it can be seen that the interface delamination failure is affected by different mixed mode partition theories except of the case if $G_{Ic} = G_{IIc}$. Linear failure criterion is regarded as to be reasonably accurate and to give a good approximation to the failure locus. Among many different mixed-mode failure criteria suggested for predicting delamination growth, Reeder [68] gave a comprehensive review of them, and suggested that the linear failure criterion is the one most often used in the literature. In addition, there is a wealth of data that either strongly supports the criterion [89], or suggests criteria that are close to it [25], [140,141,150–158]. Linear failure criterion is also the approach used by Charalambides et al. [17].

$$\frac{G_I}{G_{IC}} + \frac{G_{II}}{G_{IIC}} = 1 \tag{2.64}$$

Global and local partition

There is an important difference between a local partition and a global partition for predicting interface delamination. Local partition is based on the location to the crack tip B whilst the global partition is based the region Δa, which is the region mechanically affected by the presence of the crack. Mathematically, the global partition is calculated by including the whole crack influence region in the integration limits; the local partition only considers the

near crack tip region. The total energy release rate is not affected by the limits of the crack closure integral [36], however the partition of energy release rate is affected [28,29]. Mathematically Wang–Harvey Euler beam partition theory shows two sets of pure modes (the first θ_i, β_i set and the second $\theta_i^{'}$, $\beta_i^{'}$), which are both locally and globally pure. The local and global partitions are therefore the same when using the Wang–Harvey Euler beam partition theory. For the Wang–Harvey Timoshenko beam partition theory, there are two sets of locally pure modes, which exactly coincide on the first set θ_i, β_i from the Wang–Harvey Euler beam partition theory. There are also two sets of globally pure modes and they are the same as the pure modes from the Wang–Harvey Euler beam partition theory. Therefore, when using the Wang–Harvey Timoshenko beam partition theory, the local partition exhibits no stealthy interaction (because the two sets of local pure modes coincide) and is different to the Wang–Harvey Euler beam partition theory. However, the global partition is the same as the Wang– Harvey Euler beam partition theory. Since the averaged partition theory is the average of the Wang–Harvey Euler and Timoshenko beam partition theories, it behaves in the same way. The global partition is the same as the Wang–Harvey Euler beam partition theory but the local partition is generally different. This difference between local and global partitions is important for determining fracture propagation between interfaces and under what circumstances.

The FEM simulation was developed by Wang–Harvey based on the Euler and Timoshenko beam theories and 2D elasticity theory using normal and shear point interface springs with very high stiffness to model perfectly bonded plies [25]. The energy release rate partition is calculated using the virtual crack closure technique in conjunction with these interface springs. The numbers of spring elements are increased from one, ten, and twenty to thirty, as expected, as the numerical partition becomes a global one, the local partition theory closely approaches the Wang–Harvey Euler beam partition theory [28].

In summary, the performance of five different partition theories has been investigated by using experimental results from the literature for arrange of tests; the partition theories used are the Williams theory [39], the Suo–Hutchinson theory [14,41,50] and the Wang–Harvey partition theories [27–29], based on the Euler and Timoshenko beam theories. The thicknesses of the assessed specimens are all in macroscopic range, the results are presented in Figure 2-8. The Wang–Harvey Euler partition theory with linear failure locus offers the best and most simple explanation for all the experimental observations. This indicates clearly

that the Wang-Harvey global partition theory provides the best prediction for the interface delamination in the macroscopic layer thickness.

2.4.2 Wang–Harvey's second experimental assessment

The second assessment to investigate the capability of different approaches of mixed mode partition to predict the interfacial fracture toughness of generally composite beams was done by Wang and Harvey [23]. The Wang and Harvey's Euler beam partition theory [27-29] is compared with Davidson et al.'s non-singular-field partition theory and the singular-field partition approach [19,20] and [115] by using existing test data from literature [20,21]. The Davidson et al.'s singular-field partition approach is based on 2D elasticity theory and finite element method. The test data from [20] and [21] are used by Wang and Harvey to validate the mixed mode partition and the material fracture toughness predicted by using different mixed mode partition theories.

Davidson et al.'s partition theories include a singular-field partition theory and a non-singular-field theory. Both theories are derived by using a combined analytical and numerical approach based on 2D elasticity with stress intensity factors. Davidson et al.'s partition theory assumes a rigid crack interface. Davidson et al.'s 2D-elasticity non-singular-field partition theory [19,20] and [115] is based on 2D elasticity theory, it is given by the following formula:

$$\frac{G_{II}}{G} = \frac{[N_c\sqrt{C_1}\cos\Omega + M_c\sqrt{C_2}\sin(\Omega+\Gamma)]^2}{C_1N_c^2 + C_2M_c^2 + 2\sqrt{C_1C_2}N_cM_c\sin\Gamma} \tag{2.68}$$

Where N_c and M_c are the concentrated crack tip force and moment respectively, the parameters c_1, c_2 and Γ are introduced in reference [20]. Details of Ω, which is called the 'mode mix parameter', is given in eq. (2.69)

$$\Omega = \begin{cases} -24(\eta < -0.468) \\ 60.409\eta - 41.738\eta^3(if\ -0.468 < \eta < 0.468) \\ 24(\eta > 0.468) \end{cases} \tag{2.69}$$

Note that η in Eq. (2.61) is given by $\eta = \log_{10}(\gamma)$, where γ is the thickness ratio. The mode mix parameter Ω is determined with the aid of experimental data. Davidson et al.'s 2D-

elasticity non-singular-field partition theory was developed with the support of the experimental parameter; this is an important reason that its partition approach has a good correlation with experimental data and with Wang and Harvey's Euler beam theory.

In the second assessment conducted by Wang and Harvey [23], the experimental data from three groups of test specimens are considered, namely, unidirectional specimens (UD), constrained unidirectional specimens (CUD) and multidirectional (MD) specimens. Two sets of graphite/epoxy laminates are utilised in the experimental tests, they are C12K/R6376 of low toughness and T800H/3900-2 of high toughness.

Firstly, the UD specimens made from C12K/R6376 material with midplane and offset delamination is considered. All three partition methods give largely identical partition results for midplane delamination. By using these results from midplane delamination, a failure locus is experimentally determined in terms of the total critical ERR Gc and calculated G_{II}/G. Next, the different partition theories are assessed against this failure locus for offset delamination. The results of predicted fracture toughness by three different mixed partition methods are shown in Figure 2-9. It is seen that Wang and Harvey's Euler beam partition theory and Davidson et al.'s non-singular-field partition theory give largely identical partition results and agree very well with the failure locus; however, the singular-field partition results are generally not in good agreement with this failure locus.

The comparison was also done for the difference between the partitions G_{II}/G from both partition theories over a range of bending moment ratios, M_{2B}/M_{1B}, and thickness ratios γ (h_i/h_2). Within the range of layer thickness ratio $1/3<\gamma<3$, the excellent agreement between Wang and Harvey's Euler beam theory and Davidson et al. non-singular-field partition theory; also, both are in good agreement with experimental data [20]. However, when $\gamma<1/3$, the Wang and Harvey's Euler beam partition theory has a good agreement with the experiment data from [30], it is much better than the Davidson et al.'s non-singular partition theory.

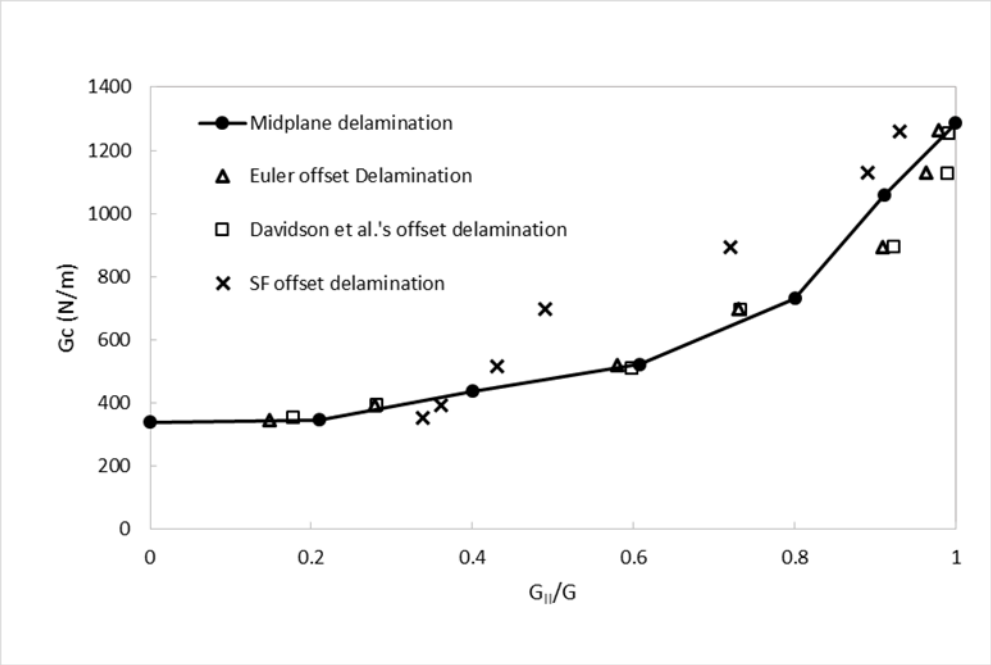

Figure 2-9: Fracture toughness of midplane and offset delamination in UD laminates [20].

Constrained unidirectional specimens, CUD specimens made from C12K/R6376 material are considered with midplane and offset delamination. The CUD specimens contain a delamination that was bounded by a single 0° ply on either side, and these plies were themselves bounded by plies at a small angle. Effectively, in these specimens, the damage zone is constrained to be within the two 0° plies. The critical fracture toughness Gc and the mixed mode partition G_{II}/G predicted by difference partition theories are shown in Figure 2-10. It is seen that the partition results from the three approaches are largely the same as their counterparts in the UD specimen. That is, the addition of the $\pm 15°$ angle plies, sandwiching the two $0°$ fracture layers in the CUD specimens, has negligible effect on the partition; however, the fracture toughness has some changes. Some are significant. For example, the toughness of UD UENF (unsymmetrical end-notched flexure) 20/12 (number of top plies/ number of bottom plies) is 1259 N/m while the toughness of CUD UENF 20/12 is 976 N/m. In general, the Wang and Harvey's Euler beam partition theory and Davidson et al.'s non-singular-field partition theory both agree well with the failure locus, except for the UENF specimen.

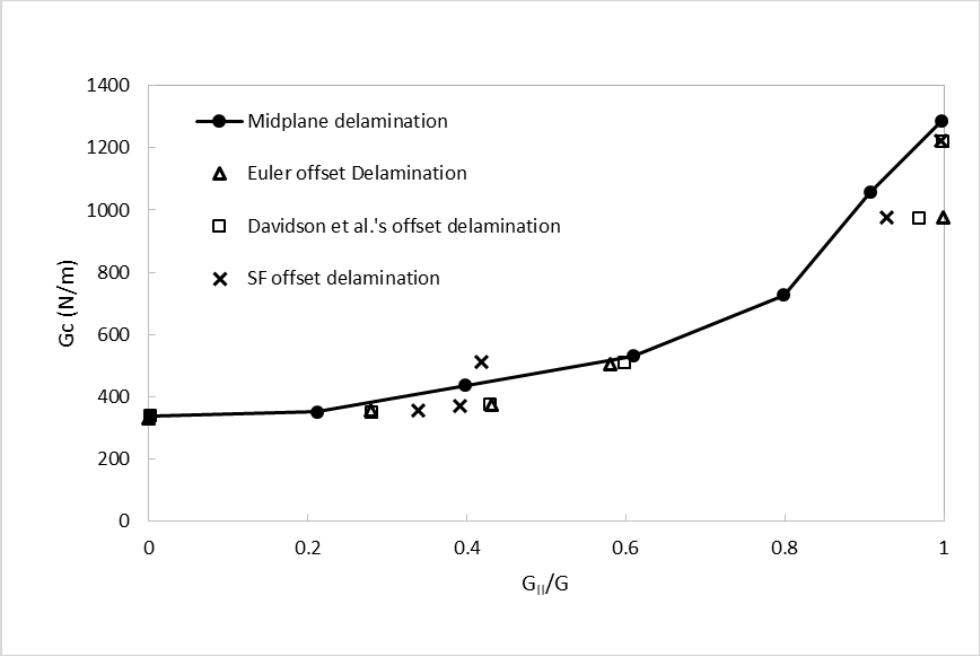

Figure 2-10: Fracture toughness of midplane and offset delamination in CUD laminates [20].

Multidirectional specimens made from C12K/R6376 material with varied layups are considered with offset delamination. The results of predicted fracture toughness by three different mixed partition methods are shown in Figure 2-11. The partition results from singular-field partition approach are still in poor agreement with the failure locus. The partition results from Wang and Harvey's Euler beam partition theory and Davidson et al.'s non-singular-field partition theory have significant differences. Although they are both still in a better agreement with the failure locus than the singular field approach, the agreement is not as good as that seen for the UD and CUD specimens. Through their study, they realised that effect of the different fracture toughness values, G_{Ic} and G_{IIc}, between two different crack interfaces, for example, 0/0 vs. 0/45 contributes to the differences. It is obvious that if the fracture toughness values G_{Ic} and G_{IIc} of the angle ply interfaces in the MD specimens are different from that of the UD specimens, even the correct partition results for MD specimens will not agree well with the failure locus determined from the midplane UD specimens.

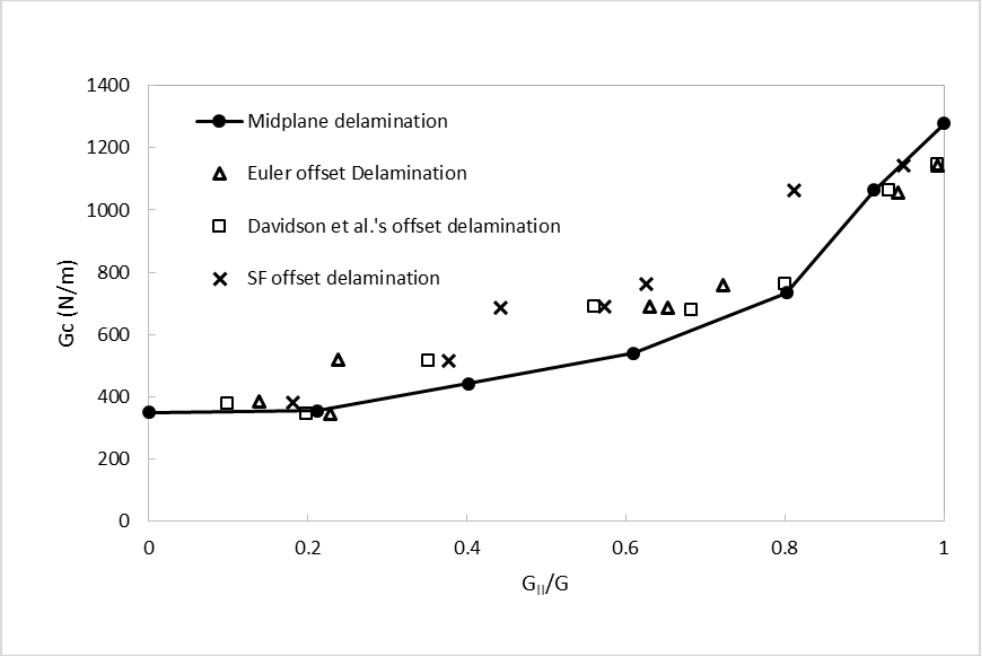

Figure 2-11: Fracture toughness of midplane and offset delamination in MD laminates [20].

In summary, the Wang and Harvey's Euler beam partition theory [27-29] has excellent agreement with experimental test results and gives very accurate predictions of interfacial fracture toughness laminated composite beams with arbitrary layups, various thickness ratios and various loading conditions. The thicknesses of all tested specimens used for validation are in millimetre range. Davidson et al.'s non-singular-field partition theory [19,20] and [115] has excellent agreement with experimental test results and with Wang and Harvey's Euler beam partition theory (inside the range $1/3<\gamma<3$) for UD laminated composite materials. Its accuracy is still very good for MD laminated composite beams; however, it has been observed and argued that overall Wang and Harvey's Euler beam partition theory [27-29] offers improved accuracy. In general, the singular-field approach based on 2D elasticity and the finite element method give poor predictions.

2.5 Conclusions

In this chapter, the concept of linear fracture mechanics, the interface delamination and the relevant mixed mode partition theories are introduced. There are five basic foundations of fracture mechanics developed over the time. They are 1) Energy release rate concept developed by Griffith in 1921; 2) Stress intensity factor at the crack tip introduced by Williams in 1957; 3) VCCT discovered by Irwin in 1958; 4) J integral presented by Rice in

1968; 5) Mixed mode partition theories proposed by different researchers in recent decades. However, there are still some uncertainties on the mixed mode partition theories due to the complexity and diversity of mixed mode fracture mechanics, it is often unclear which theory should be applied to the specific problems.

In this chapter, the assessments of different mixed mode partition theories are presented by reviewing the works conducted by S. Wang and C. Harvey [22,23]. The following mixed mode partition theories are studied: (1) a partition theory by Williams [39] based on Euler beam theory; (2) a partition theory by Suo [50] and Hutchinson and Suo [14] based on 2D elasticity theory; (3) Davidson et al.'s non-singular-field partition theory; (4) Davidson et al.'s singular-field partition approach [19,20] and (5) the Wang–Harvey partition theories [27-29] based on the Euler and Timoshenko beam theories. These mixed mode partition theories are examined by S. Wang and C. Harvey [22,23] against test data from the literatures [17,18]. From their two experimental assessment works [22,23], the following conclusions are obtained: (1) Different mixed mode partition theories may show different performace; for the interface delamination between two layers of macroscopic thickness, Wang and Harvey's Euler beam partition theory gives very accurate predictions of interfacial fracture toughness for laminated composite beams. The delamination of a thin layer of macroscopic thickness on a brittle interface cannot propagate in the manner as an infinitesimally small growth. Instead, it does propagate with a finitely small growth [32]. The Euler beam, Timoshenk beam mixed mode partition theory [24-29] and the 2D elasticity partition theory [14] assume an infinitesimally small growth; however, the Euler beam mixed mode partition theory is insensitive to the growth size. Because of this behaviour the name of 'global partition theory' is given. In contrast, the Timoshenko beam and 2D elasticity partition theories are sensitive to the growth size. Consequently, the name of 'local partition theory' is given. Now, it is seen that the Euler beam mixed mode partition theory represents the 'finitely small growth' physics very well. The above explains why it gives accurate predictions for brittle interface fracture toughness of generally laminated composites beams [22,23,30,31]. (2) The excellent agreement has been achieved with the linear failure locus for predicting the interface fracture toughness. (3) The global partition of energy release rate predicts the most accurate results in a good agreement with the experimental data from the specimens tested by Charalambids M. et al. [17] and Hashemi S. et al. [18].

To confirm the conclusions made above, a study of buckling driven delamination of laminated composite beam is conducted in the next chapter; further, in the chapter 4 to 6 the

Euler beam, Timosheno beam and 2D elasticity mixed mode partition theories are applied to develop the analytical models for solving various mixed mode delamination problems. It attempts to examine the predictions from Wang-Harvey mixed mode partition theories against the independent experimental results and also to extend the knowledge of mixed mode partition theories to solve different interfacial delamination problems.

Chapter 3 Post local buckling driven delamination under mechanical compressive loads

3.1 Introduction

Interface delamination in layered materials is often driven by buckling and post-buckling loads. Some examples include the delamination of laminated composite beams, plates and shells under in-plane compression, and the surface spalling of thermal and environmental barrier coatings. This topic has been extensively studied in the last few decades. References [3-11] are only several examples among numerous publications on the topic, which are more closely related to the present work. References [12,13] are examples of latest studies from which more recent studies can be found. Some examples include the delamination of laminated composite beams, plates and shells under in-plane compression, the surface spalling of aluminium protective coatings and thermal barrier coatings. Xu J. et al. [153] gives a recent review; among many of others, the studies are reported on buckling driven delamination with straight edge [70,84,86], circular edge [70,83], elliptical edge [70] and telephone cord shapes [85].

Analytical, numerical and experimental approaches are all used for this kind of study. Some representative analytical, numerical and experimental studies are given in the works [14,70], [71-74] and [32,75], respectively. The first pioneering and instrumental work was done by Chai (1981) [87], the full analytical developments for calculating total ERR G based on Euler beam theory in cases of thin film, thick column and general post local buckling driven delamination in laminated beam-like plates; however, no partition of the total ERR G into its individual mode I and II ERR components, G_I and G_{II}, is attempted [87]. Chai's study is based on a homogeneous, isotropic and linear elastic material; in his work, classic Euler beam theory is used to calculate the strain energy rate for thin layer buckled state:

$$G = \frac{Eh(1-\nu^2)}{2}(\varepsilon_0 - \varepsilon_{cr})(\varepsilon_0 + 3\varepsilon_{cr}) \tag{3.1}$$

Where E is the Young's modulus, ν is Poisson's ratio, h is the thin layer thickness. End shortening strain and critical buckling strain are defined as ε_0 and ε_{cr} respectively. Increasing the end shortening strain ε_0 to exceed the critical buckling strain ε_{cr}, the thin layer starts to buckle.

Essentially identical results are received in 1984 by Evans and Hutchinson [79] for thin film problem. The circular blister in biaxial compressed film was investigated and energy release rate was given. The work for the mixed mode of the interface crack tip was firstly carried out by Whitcomb [133], who showed that the crack tip becomes predominately mode II as a one-dimensional layer buckle spreads. The virtual crack closure method was used to calculate mode I and mode II strain-energy release rates, G_I and G_{II}, respectively. The forces transmitted through the node at the crack tip and the relative displacements of the two nodes on the crack boundary closest to the crack tip were used in the calculation. Whitcomb was concerned with compressive failure modes in layered composite. Later, Storakers [81] and Rothschilds et al. [82] dealed with various aspects of buckling and delamination in laminated composite materials. In the work [82], the elastic restraint model (ERM) combined with existing FSM modelling of the crack-tip region yields the expressions for the mode I and mode II components of the strain energy release rate G_I and G_{II} to predict the critical load at the onset of delamination growth. The experimental data were produced for a wide range of G_I/G_{II} ratios at the onset of crack growth; linear mixed-mode crack growth criterion is used to predict critical loads.

In Hutchinson's work (1992) [14], the analytical calculations for both the total ERR G and its components G_I and G_{II} for the thin film post local buckling driven delamination was given for straight edged and circular blister. Expression of total energy release rate is in agreement with Chai [70], Evans and Hutchinson [79]. The partition is based on a 2D elasticity partition theory [14], the elastic mismatch of film/substrate can be considered in the portion through the Dundurs' elastic mismatch parameters, α and β. A crack propagation condition was derived as well.

A study on the configuration stability of circular, buckling-driven film delamination was presented by J.W. Hutchinson et al. [83]. An initial calculation is developed for the mechanics of the growth of an axisymmetric blister under conditions of equi-biaxial compression. A second calculation produced the result that the crack front of such a blister can become unstable to small perturbations. Under the relevant conditions, the blister loses its axisymmetric and develops lobes around the perimeter with an order that depends on the magnitude of a/a_c and on the mixed mode failure criterion appropriate for the interface. A series of model experiments were performed in conjunction with the analysis. These experiments showed excellent, quantitative agreement with the trends predicted by the

theory. Furthermore, the experiments emphasised the important role that crack-front instabilities play in the development of the "worm-like" delamination.

The numerical studies are developed by using layer-wise plate/shell theory [71-74]. The layer-wise plate theory has been developed to account delamination of layered composite materials subjected to end-shortening strain and in-plane shearing. The interface in-plane and transverse springs are developed and energy release rate and its based failure criteria are used to simulate the delamination process [71,72]. The studies in Refs. [32,75,76] are based on 2D elasticity theory and the study in Ref. [76] also uses the 3D finite element method. The virtual crack closure technique is used to calculate the ERRs in Refs. [71,72,75,76]. The cohesive zone model is used in the works [73,74]. The interface element incorporating with layer wise theory is employed to simulate the delamination propagation under buckling driven delamination for composite layered materials [73].

The delamination in a laminated composite beam is analysed with cohesive zone model (CZM) and layer-wise third-order shear and normal deformation theory (TSNDT) by Batra RC et al. [74]. All geometric nonlinearities are considered including the von Karman nonlinearity. The mode I and mode II deformation is extracted. They found that the buckling load is influenced by the applied loading rate. A series of experiments was conducted by Thouless et al. [89] to study buckle driven delamination of thin films under plane strain compression to compare with analytical development of energy release rate and mixed mode phase angle. The experiments were conducted with thin film sheets bonded to a steel substrate with film/substrate material elastic mismatch. In a series of experiments, Ogawa et al. (1986) [125] demonstrated the configurational instabilities focused on beam sputtered and magnetron sputtered molybdenum films on glass substrates where the nucleation and progression of film delamination and buckling were recorded using interference contrast microscopy. The delamination and buckling of Sic coatings on Si substrates were studied experimentally by Argon et al. (1989) [137] in an investigation of the intrinsic toughness of interfaces. Hutchinson et al. (1992) [14] performed a systematic experimental study of the growth and configurational stability of initially circular delamination of films in equi-biaxial compression.

A relevant experiment work and analytical model on the topic of buckling driven delamination is done by Kutlu Z, et al. [32,75]. In their work part I [75], an analytical model was developed to investigate the compression response of laminated composite panels

containing multiple through-the- width delamination; also, a nonlinear finite element analysis was developed based on the model. The delamination growth model and the local fibre-matrix failure model were implemented into the finite element model. The model consists of three portions: stress analysis, contact analysis, and failure analysis. Linear elastic fracture mechanics and failure criteria were selected in the failure analysis for predicting delamination growth and for predicting local fibre-matrix failure within each layer respectively.

In the experiment work [32], the specimens with various ply orientations were fabricated from both flat and cylindrical composite panels containing one to two pre-implanted through-the-width delamination. Specimens were tested by uniaxial compression, and strain gauges were utilised to record the strain history as a function of the applied load from initial loading to final failure. Numerical simulations were performed according to the test conditions. Comparisons were then made between the predictions and the measured test data. Overall, the predictions agreed with the data very well. Parametric studies were also performed using the finite element analysis to demonstrate the effect of the size, location and number of the delamination on the compression response of laminated composites.

Although post-buckling driven delamination generally occurs as mixed-mode fracture with all three opening, shearing and tearing actions (i.e. mode I, II and III), post-buckling driven one-dimensional (1D) delamination has received more attention because it is simpler, still captures the essential mechanics. The term '1D delamination' means that a delamination propagates in one direction with mode I opening and mode II shearing action only. Some examples of 1D delamination include through-width delamination in beams, and blisters in laminated composite plates and shells.

The focus of the present work is 1D post-local buckling-driven delamination. A detailed definition of this will be given in next section. Key tasks in studying 1D post-local buckling-driven delamination include: (1) determining the critical buckling strain and the post-buckling deformation, (2) calculating the post-local buckling total energy release rate (ERR) G, (3) partitioning the total ERR G into its individual mode I and II ERR components, G_I and G_{II}, which govern the propagation of mixed-mode delamination, and (4) predicting the delamination propagation behaviour.

The present work aims to develop an improved analytical method to complete the four key tasks stated above. The structure of this chapter is as follows: the analytical development is

given in section 3.2, the numerical verification and experimental validation are reported in section 3.3, and finally the conclusions are given in section 3.4.

3.2. Analytical development

Figure 3-1 shows a post-locally buckled bilayer composite beam. The Young's moduli of the upper and lower layers are E_1 and E_2 respectively, and the corresponding thicknesses are h_1 and h_2 with $h_2 >> h_1$. The beam has a total length L and a width b with a central through-width interfacial delamination of length a. The delamination tips are labelled 'B'. The beam is clamped at both ends and is under uniform end-shortening compression. The local buckling, as shown, divides the beam into three parts, namely, the locally-buckled part labelled '1', the substrate part labelled '2' and the intact parts labelled '3'. The deformation of three parts of the beam are assumed as linear elastic. The following development assumes that the whole process of buckling, post-buckling and delamination propagation is localised in the upper layer, that is, the bending action in both parts 2 and 3 is negligible.

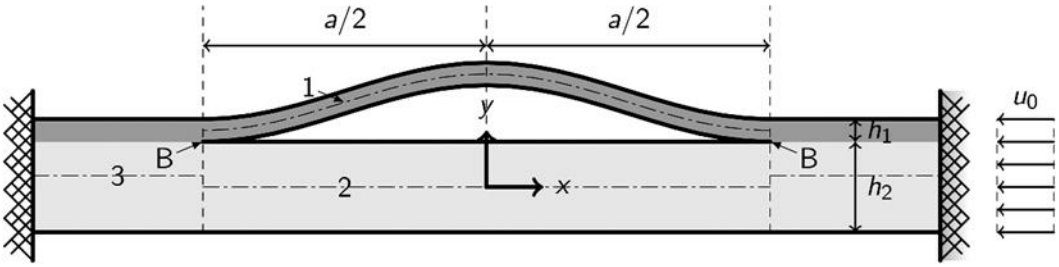

Figure 3-1: A post-locally buckled bilayer composite beam due to delamination under compression.

3.2.1. Deformation, internal forces and bending moments

The uniform end-shortening compression is represented by a strain ε_0, defined as $\varepsilon_0 = u_0 / L$ with u_0 being the end-shortening displacement. The compressive axial strains of the neutral surfaces of each the three parts of the beam are represented by ε_i (with $i = 1,2,3$). Similarly, N_i and $M_i(x_i)$ represent the axial forces and bending moments respectively in each part, where x_i is the axial axis on each neutral surface. The directions of the axes of the three parts

together are shown in Figure 3-1 where only their directions are indicated. The axial forces N_i can be expressed as

$$N_i = -E_1 A_{ie} \varepsilon_i \tag{3.2}$$

Where the effective cross-sectional areas A_{ie} are given by

$$A_{2e} = bh_1 \eta\gamma \quad A_{3e} = bh_1 (1+\eta\gamma) \tag{3.3}$$

and $\eta = E_2/E_1$ and $\gamma = h_2/h_1$, which are the modulus and thickness ratios respectively. Before the local buckling of part 1, $\varepsilon_i = \varepsilon_0$, $N_i = -E_1 A_{ie} \varepsilon_0$ and $M_i(x_i) = 0$, that is, all three parts are under constant uniform axial compressive strain ε_0 and there is no bending. After the local buckling of part 1, part 1 is under both axial compression and bending action while parts 2 and 3 are still assumed to be under axial compression only without bending action. The axial strain ε_1 is assumed to remain constant at the critical local-buckling strain ε_c throughout [14,70], that is,

$$\varepsilon_1 = \varepsilon_c \tag{3.4}$$

The axial strain ε_2 can be expressed by using the axial equilibrium condition, $N_1 + N_2 = N$ giving

$$\varepsilon_2 = \varepsilon_3 + \frac{\varepsilon_3 - \varepsilon_c}{\eta\gamma} \tag{3.5}$$

from which it is obvious that $\varepsilon_2 > \varepsilon_3$. Also, the axial strain ε_3 should be smaller than the end-shortening strain ε_0 after local buckling, that is, $\varepsilon_3 < \varepsilon_0$. From these two observations, it is reasonable to assume that the following is a good approximation:

$$\varepsilon_2 = \varepsilon_0 \tag{3.6}$$

Then Eq. (3.5) gives

$$\varepsilon_3 = \frac{\varepsilon_c + \eta\gamma\varepsilon_0}{1+\eta\gamma} \tag{3.7}$$

In order to determine the critical local buckling strain ε_c and bending moment $M_1(x_1)$ accurately, it is essential to find an accurate post-locally buckled mode shape. Here, it is assumed to be

$$V_1(x_1) = \frac{A}{2}\left[\cos\left(\frac{2\alpha\pi x_1}{a}\right) - \cos(\alpha\pi)\right] \tag{3.8}$$

where α is the correction factor for the quality of the clamped end condition at the crack tip. In Refs. [14,87], the value of α is taken as 1. The critical local-buckling strain ε_c can be determined by considering the free-body diagram of a symmetrical half of the buckled upper layer shown in Figure 3-2.

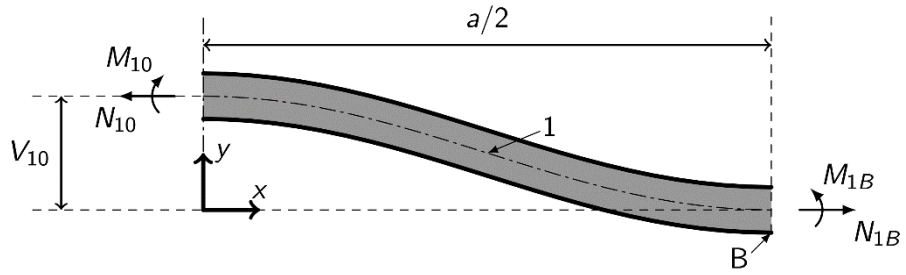

Figure 3-2: Free-body diagram of a symmetrical half of the buckled upper layer.

Horizontal equilibrium combined with Eqs. (3.2) and (3.4) gives $N_{10} = N_{1B} = -E_1 A_1 \varepsilon_c$ and bending moment equilibrium gives $M_{1B} = M_{10} - N_{10} V_{10}$, which together give $M_{10} = M_{1B} - E_1 A_1 \varepsilon_c V_{10}$. Classical beam theory and Eq. (3.8) give $M_{10} = -4E_1 I_1 V_{10}(\alpha\pi/a)^2 - 2E_1 I_1 A(\alpha\pi/a)^2 \cos(\alpha\pi)$. Therefore, the critical local-buckling strain ε_c is obtained as

$$\varepsilon_c = \frac{(\alpha\pi)^2}{3}\left(\frac{h_1}{a}\right)^2 \tag{3.9}$$

The value of the correction factor α for the problem under consideration can be determined either from numerical simulations or from experimental tests. More details about the value of α will be given in section 3.3 which deals with the experimental validation. The amplitude *A* is now determined by using the following assumption, where $(1-\varepsilon_c)a/2$ represents half-length of part 1 at the instant of local buckling, $(1-\varepsilon_0)a/2$ represents the half-length of part 2 during post-local buckling, and ds represents the differential arc length of part 1's buckled mode shape:

$$\frac{(1-\varepsilon_c)a}{2} = \int ds = \int_0^{(1-\varepsilon_0)a/2} \sqrt{1+\left(\frac{dV_1}{dx_1}\right)^2}\, dx_1 \tag{3.10}$$

Note that this assumption implies that the curved half-length of the buckled part 1 remains constant at $(1-\varepsilon_c)a/2$ during post-buckling. In order to determine the amplitude A accurately, particularly in the deep post-buckling region, a third-order series expansion based on $(dV_1/dx_1)^2$ is used to expand the integrand on the right-hand-side of Eq. (3.10), which results in the following:

$$(\varepsilon_0-\varepsilon_c)a=\int_0^{(1-\varepsilon_0)a/2}\left[\left(\frac{dV_1}{dx_1}\right)^2-\frac{1}{4}\left(\frac{dV_1}{dx_1}\right)^4+\frac{1}{8}\left(\frac{dV_1}{dx_1}\right)^6\right]dx_1 \tag{3.11}$$

Let $\varepsilon_a=\varepsilon_0-\varepsilon_c$, which represents the additional end-shortening strain beyond the critical buckling, and approximate the upper limit on the integration as $(1-\varepsilon_0)a/2\approx a/2$.

$$\varepsilon_a a\approx\int_0^{a/2}\left[\left(\frac{dV_1}{dx_1}\right)^2-\frac{1}{4}\left(\frac{dV_1}{dx_1}\right)^4+\frac{1}{8}\left(\frac{dV_1}{dx_1}\right)^6\right]dx_1 \tag{3.12}$$

Substituting Eq. (3.8) into Eq. (3.12) and evaluating the integration gives

$$C_6\overline{A}^6+C_4\overline{A}^4+C_2\overline{A}^2-\varepsilon_a=0 \tag{3.13}$$

where

$$\overline{A}=\frac{A\alpha\pi}{2a} \tag{3.14}$$

$$C_2=1-\frac{\sin(2\alpha\pi)}{2\alpha\pi} \tag{3.15}$$

$$C_4=-\frac{3}{4}+\frac{\sin(2\alpha\pi)}{2\alpha\pi}-\frac{1}{4}\frac{\sin(4\alpha\pi)}{4\alpha\pi} \tag{3.16}$$

$$C_6=\frac{5}{4}-\frac{15}{8}\frac{\sin(2\alpha\pi)}{2\alpha\pi}+\frac{3}{4}\frac{\sin(4\alpha\pi)}{4\alpha\pi}-\frac{1}{8}\frac{\sin(6\alpha\pi)}{6\alpha\pi} \tag{3.17}$$

Since α is typically close to 1, the harmonic terms can be neglected as a further approximation. The polynomial in Eq. (3.13) can then be solved, which gives the amplitude A as

$$A=\frac{2\sqrt{15}a}{15\alpha\pi}\left|\frac{\sqrt{\varepsilon^{1/3}\left(\varepsilon^{2/3}+3\varepsilon^{1/3}-51\right)}}{\varepsilon^{1/3}}\right| \tag{3.18}$$

where

$$\varepsilon = 30\sqrt{3}\sqrt{675\varepsilon_a{}^2 - 243\varepsilon_a + 71} + 1350\varepsilon_a - 243 \tag{3.19}$$

The bending moment at the delamination tip *B* is then obtained by using Eqs. (3.8), (3.9), and (3.18),

$$M_{1B} = \frac{\sqrt{3}E_1 b h_1{}^2 c_\alpha \sqrt{\varepsilon_c \varepsilon_a}}{3} \tag{3.20}$$

where

$$c_\alpha = -\frac{\sqrt{15}}{15\sqrt{\varepsilon_a}} \left| \frac{\sqrt{\varepsilon^{1/3}\left(\varepsilon^{2/3} + 3\varepsilon^{1/3} - 51\right)}}{\varepsilon^{1/3}} \right| \cos(\alpha\pi) \tag{3.21}$$

3.2.2 Strain energy and total energy release rate

By using the internal bending moment in part 1 and the internal axial forces in parts 1, 2 and 3, but neglecting the internal bending moments in parts 2 and 3, the strain energy U in one half of the symmetrical post-buckled beam is

$$\begin{aligned} U &= \frac{1}{2}\left[E_1 A_1 \varepsilon_c{}^2 \frac{a}{2} + \int_0^{a/2} E_1 I_1 \left(\frac{d^2 V_1}{dx_1^2} \right)^2 dx_1 + E_1 A_{2e} \varepsilon_0{}^2 \frac{a}{2} + E_1 A_{3e} \varepsilon_3{}^2 \frac{L-a}{2} \right] \\ &= \frac{1}{2}\left[\frac{N_1{}^2}{E_1 A_1} \frac{a}{2} + \int_0^{a/2} \frac{M_1{}^2}{E_1 I_1} dx_1 + \frac{N_2{}^2}{E_1 A_{2e}} \frac{a}{2} + \frac{N_3{}^2}{E_1 A_{3e}} \frac{L-a}{2} \right] \end{aligned} \tag{3.22}$$

The total ERR *G* is then calculated as

$$G = \frac{1}{2bE_1}\left[\frac{M_{1B}{}^2}{I_1} + \frac{N_{1B}{}^2}{A_1} + \frac{N_{2B}{}^2}{A_{2e}} - \frac{N_{3B}{}^2}{A_{3e}} \right] \tag{3.23}$$

It is worth noting that ERR represents the strain energy density difference or ‘pressure’ across the delaminated and intact parts. Since uniform axial compression results in no strain energy density difference, it does not produce any ERR. Therefore, an effective axial force N_{1Be} is defined as

$$N_{1Be} = -E_1 A_1 (\varepsilon_1 - \varepsilon_2) = E_1 b h_1 \varepsilon_a \tag{3.24}$$

The total ERR *G* in Eq. (3.23) then becomes

$$G=\frac{1}{2bE_1}\left[\frac{{M_{1B}}^2}{I_1}+\left(\frac{1}{A_1}-\frac{1}{A_{3e}}\right){N_{1Be}}^2\right]=\frac{6}{E_1b^2{h_1}^3}\left({M_{1B}}^2+\frac{\lambda{h_1}^2}{12}{N_{1Be}}^2\right) \tag{3.25}$$

where $\lambda=\eta\gamma/(1+\eta\gamma)$. Substituting M_{1B} from Eq. (3.20) and N_{1Be} from Eq. (3.24) into Eq. (3.25) gives

$$G=\frac{1}{2}E_1h_1\varepsilon_a\left(4{c_\alpha}^2\varepsilon_c+\lambda\varepsilon_a\right) \tag{3.26}$$

Note that when $\lambda=1$, $\alpha=1$ and $c_\alpha=1$ Eq. (3.20) becomes the same as that in Refs. [14,87].

3.2.3. Partitions of energy release rate

3.2.3.1. Euler beam partition

From the reference [22,26-29], the Euler beam partition of the total ERR G in Eq. (3.25) can be written as

$$G_{IE}=c_{IE}\left(M_{1B}-\frac{N_{1Be}}{\beta}\right)\left(M_{1B}-\frac{N_{1Be}}{\beta'}\right) \tag{3.27}$$

$$G_{IIE}=c_{IIE}\left(M_{1B}-\frac{N_{1Be}}{\theta}\right)\left(M_{1B}-\frac{N_{1Be}}{\theta'}\right) \tag{3.28}$$

where (θ,β) and (θ',β') are the two sets of orthogonal pure modes. The θ and β' pure modes correspond to zero relative shearing displacement and zero relative opening displacement respectively just ahead of the crack tip [22,26-29]. Using the beam mechanics in section 3.2.1 in conjunction with these conditions, and then the orthogonality condition [22,26-29] through the ERR in Eq. (3.25) to obtain the orthogonal θ' and β pure modes, gives the following:

$$(\theta,\beta)=\left(-\frac{6}{h_1},\frac{2}{\lambda h_1}\right) \tag{3.29}$$

$$(\theta',\beta')=(0,\infty) \tag{3.30}$$

Note that the zero value of θ' results from the approximate nature of the total ERR G in Eq. (3.25) and is due to neglecting the bending action in parts 2 and 3 of the bilayer beam. This

does not prevent from the mode II ERR G_{IIE} from being obtained as it is readily obtained as $G-G_{IE}$ when the mode I ERR G_{IE} is known. The coefficient c_{IE} in Eq. (3.27) is calculated by using Eqs. (3.25) and (3.27) together, and noting that $G=G_{IE}$ when $M_{1B}=1$ and $N_{1Be}=\theta$, giving

$$c_{IE}=\frac{6}{E_1b^2h_1^3}\left(1+\frac{\lambda h_1^2}{12}\theta^2\right)\Bigg/\left[\left(1-\frac{\theta}{\beta}\right)\left(1-\frac{\theta}{\beta'}\right)\right]=\frac{6}{E_1b^2h_1^3} \tag{3.31}$$

Now the ERR partitions, G_{IE} and G_{IIE}, are known in terms of the delamination tip bending moment M_{1B} in Eq. (3.20) and the effective axial force N_{1Be} in Eq. (3.24). For the sake of convenience, they are also given below in terms of the critical buckling strain ε_c and the additional end-shortening strain ε_a.

$$G_{IE}=E_1h_1c_\alpha\sqrt{\varepsilon_c}\varepsilon_a\left(2c_\alpha\sqrt{\varepsilon_c}-\sqrt{3}\lambda\sqrt{\varepsilon_a}\right) \tag{3.32}$$

$$G_{IIE}=E_1h_1\lambda\varepsilon_a^{3/2}\left(\sqrt{3}c_\alpha\sqrt{\varepsilon_c}+1/2\sqrt{\varepsilon_a}\right) \tag{3.33}$$

Note that when $N_{1Be}>\beta M_{1B}$ or $\sqrt{\varepsilon_a}>\left(2c_\alpha\sqrt{\varepsilon_c}\right)/\left(\sqrt{3}\lambda\right)$, the crack tip normal stress becomes compressive, and so G_{IE} is taken to be zero with $G_{IIE}=G$.

3.2.3.2. Timoshenko beam partition

From reference [22,26-29], the Timoshenko beam partition of the total ERR *G* in Eq. (3.25) can be written as

$$G_{IT}=c_{IT}\left(M_{1B}-\frac{N_{1Be}}{\beta}\right)^2 \tag{3.34}$$

$$G_{IIT}=c_{IIT}\left(M_{1B}-\frac{N_{1Be}}{\theta}\right)^2 \tag{3.35}$$

where

$$c_{IT}=\frac{6}{E_1b^2h_1^3}\left(1+\frac{\lambda h_1^2}{12}\theta^2\right)\left(1-\frac{\theta}{\beta}\right)^{-2}=\frac{6}{(1+3\lambda)E_1b^2h_1^3} \tag{3.36}$$

$$c_{IIT}=\frac{6}{E_1b^2h_1^3}\left(1+\frac{\lambda h_1^2}{12}\beta^2\right)\left(1-\frac{\beta}{\theta}\right)^{-2}=\frac{6}{(1+1/(3\lambda))E_1b^2h_1^3} \tag{3.37}$$

In terms of the critical buckling strain ε_c and the additional end-shortening strain ε_a, they become

$$G_{IT}=\frac{1}{2(1+3\lambda)}E_1h_1\varepsilon_a\left(2c_\alpha\sqrt{\varepsilon_c}-\sqrt{3}\lambda\sqrt{\varepsilon_a}\right)^2 \tag{3.38}$$

$$G_{IIT}=\frac{\lambda}{2(1+3\lambda)}E_1h_1\varepsilon_a\left(2\sqrt{3}c_\alpha\sqrt{\varepsilon_c}+\sqrt{\varepsilon_a}\right) \tag{3.39}$$

Again, note that when $N_{1Be}>\beta M_{1B}$ or $\sqrt{\varepsilon_a}>\left(2c_\alpha\sqrt{\varepsilon_c}\right)/\left(\sqrt{3}\lambda\right)$, the crack tip normal stress becomes compressive, and so G_{IT} is taken to be zero with $G_{IIT}=G$.

3.2.3.3. 2D elasticity partition

In general, if there is a material mismatch across the interface and Young's modulus ratio $\eta=E_2/E_1$ is not equal to 1, then the 2D-elasticity-based partition of ERR is crack extension size-dependent ERR due to the complex stress intensity factor [51]. It has been one most challenging fracture mechanics problems to obtain analytical solutions for the ERR partition and the stress intensity factors. Recently Harvey et al. [150,151] have solved this problem by using a novel and powerful methodology. It is expected, however, that the effect of material mismatch across the delamination is not significant in this study as the local deformation in the upper layer dominates the fracture. Therefore, the 2D-elasticity-based partition theory [14,78] for homogeneous beams with no material mismatch across the interface is used instead. The total ERR G in Eq. (3.25) can be partitioned as

$$G_{I2D}=c_{I2D}\left(M_{1B}-\frac{N_{1Be}}{\beta_{2D}}\right)^2 \tag{3.40}$$

$$G_{II2D}=c_{II2D}\left(M_{1B}-\frac{N_{1Be}}{\theta_{2D}}\right)^2 \tag{3.41}$$

where

$$\left(\theta_{2D}\,,\,\beta_{2D}\right)=\left(-\frac{2.697}{h_1}\,,\,\frac{4.450}{\lambda h_1}\right) \tag{3.42}$$

$$c_{I2D} = \frac{6}{E_1 b^2 h_1^3}\left(1+\frac{\lambda h_1^2}{12}\theta_{2D}^2\right)\left(1-\frac{\theta_{2D}}{\beta_{2D}}\right)^{-2} = \frac{4.450^2\left(12+2.697^2\lambda\right)}{12\left(4.450+2.697\lambda\right)^2}\frac{6}{E_1 b^2 h_1^3} \tag{3.43}$$

$$c_{II2D} = \frac{6}{E_1 b^2 h_1^3}\left(1+\frac{\lambda h_1^2}{12}\beta_{2D}^2\right)\left(1-\frac{\beta_{2D}}{\theta_{2D}}\right)^{-2} = \frac{2.697^2\left(12\lambda+4.450^2\right)\lambda}{12\left(4.450+2.697\lambda\right)^2}\frac{6}{E_1 b^2 h_1^3} \tag{3.44}$$

In terms of the critical buckling strain ε_c and the additional end-shortening strain ε_c, they become

$$G_{I2D} = \frac{12+2.697^2\lambda}{6\left(4.450+2.697\lambda\right)^2}E_1 h_1 \varepsilon_a\left(4.450 c_\alpha\sqrt{\varepsilon_c}-\sqrt{3}\lambda\sqrt{\varepsilon_a}\right)^2 \tag{3.45}$$

$$G_{II2D} = \frac{\left(12\lambda+4.450^2\right)\lambda}{6\left(4.450+2.697\lambda\right)^2}E_1 h_1 \varepsilon_a\left(2.697 c_\alpha\sqrt{\varepsilon_c}+\sqrt{3}\sqrt{\varepsilon_a}\right)^2 \tag{3.46}$$

Again note that when $N_{1Be} > \beta_{2D} M_{1B}$ or $\sqrt{\varepsilon_a} > \left(4.450 c_\alpha\sqrt{\varepsilon_c}\right)/\left(\sqrt{3}\lambda\right)$, the crack tip normal stress becomes compressive, and so the G_{I2D} is taken to be zero and $G_{II2D} = G$.

3.2.4. Crack propagation and stability

In general, the propagation criterion can be expressed in the form

$$f\left(G_I, G_{II}, G_{Ic}, G_{IIc}\right) = 0 \tag{3.47}$$

where G_{Ic} and G_{IIc} are the respective critical mode I and II ERRs. The form of Eq. (3.47) is not unique but is crack interface-dependent and is determined from experimental testing for a given interface. At the instant when Eq. (3.47) is met, two scenarios could occur. One is unstable crack propagation in which the crack continues to advance without increasing end-shortening. The other is the stable crack propagation in which the crack stops propagating unless further end-shortening is applied. Mathematically, these two scenarios can be expressed as

$$\frac{\partial f}{\partial a} = \begin{cases} \geq 0 & \text{unstable} \\ \leq 0 & \text{stable} \end{cases} \tag{3.48}$$

Alternatively, the stability of crack propagation can be checked by finding the value of *f* at the critical end-shortening strain for propagation at the initial delamination length and then at

a slightly increased delamination length. An increasing value of f indicates unstable propagation. The stable and unstable crack propagation is discussed in detail in the next section for the case studies.

3.3 Numerical verification and experimental validation

This section aims to examine the capability of the analytical development in section 3.2 for predicting the propagation behaviour of post-local bucking-driven delamination by making comparisons with independent numerical [71,72] and experimental data [32,75]. The quantities of interest are the critical propagation end-shortening strain, the ERR partitions during propagation and the propagation stability. Two composite beams [32,75] are studied, which both contain a single through-width delamination, and which are subjected to uniform end-shortening displacement at the clamped ends, as shown in Figure 3-1. The composite beams are made from T300/976 graphite/epoxy plies and have a total length L equal to 50.8 mm, and a width b equal to 5.08 mm. Table 3-1 gives more details of the two cases. The double slashes "//" denote the location of the delaminated interface. All plies have equal thickness. The ply longitudinal modulus E_1 is 139.3 GPa. The critical ERR for mode I G_{Ic} is 87.6 N/m and for mode II G_{IIc} is equal to 315.2 N/m. Experimental studies [32,75] suggest that the material has a linear failure criterion, that is, the Eq. (3.47) takes the form

$$f\left(G_I, G_{II}, G_{Ic}, G_{IIc}\right) = \frac{G_I}{G_{Ic}} + \frac{G_{II}}{G_{IIc}} - 1 = 0 \tag{3.49}$$

which will be used in the following studies. For these two cases, an empirical formula for the critical buckling strain correction factor α in Eq. (3.9) is obtained by using finite element method simulations and is given by

$$\alpha^2 = 11.738\left(\frac{h_1}{a}\right)^2 - 3.6654\left(\frac{h_1}{a}\right) + 0.9755 \tag{3.50}$$

A 2D axial symmetrical finite element model was built in Abaqus 6.13.1 with fixed top layer thickness (h_1) and varied crack length (a). The critical buckling strain was obtained from finite element model with eigenvalue solver. The FEA results are compared with analytical results, the derivations vs ratio of top layer thickness to varied crack length, (h_1/a), are calculated. The Eq. (3.50) is received from approximation of these comparisons.

Table 3-1: Configurations of two composite beams containing a central through-width delamination.

Case	Lay-up	α (mm)	h_1 (mm)	h (mm)
1	$[0_4 / 0_{12} // 0_4]$	38.1	0.518	2.59
2	$[0_4 / 0_{12} // 0_4]$	19.05	0.508	2.54

3.3.1. Comparison of total ERR G with independent numerical results

Accurate calculation of total ERR G is a crucial pre-requisite step towards the accurate prediction of propagation behaviour. The following exercise aims to examine the accuracy of the total ERR G given by Eq. (3.26) and the solutions in the works [14,87] by them against independent numerical results ref. [72]. Table 3-2 and Table 3-3 record the comparisons for Case 1 and Case 2 respectively. In general, good agreement is observed between the present solutions and the numerical results ref. [72] for both cases. The solutions from Refs. [14,87] have reasonable agreement for Case 1 and very poor agreement for Case 2.

Table 3-2: Total ERR G results for Case 1

ε_0 (10^{-3})	G (N/mm)		
	Ref. [72]	Eq. (3.26)	Refs. [14,87]
1.00	0.0424	0.0405	0.0399
1.20	0.0663	0.0628	0.0646
1.40	0.0931	0.0874	0.0921
1.60	0.1208	0.1142	0.1225
1.80	0.1499	0.1435	0.1559
2.00	0.1796	0.1750	0.1920
2.20	0.2125	0.2088	0.2311
2.40	0.2441	0.2450	0.2731

Table 3-3: Total ERR G results for Case 2.

ε_0 (10^{-3})	G (N/mm)		
	Ref. [72]	Eq. (3.26)	Refs. [14,87]
2.20	0.0324	0.0365	0.0000
2.30	0.0642	0.0658	0.0000
2.40	0.0949	0.0958	0.0202
2.50	0.1335	0.1263	0.0541
2.60	0.1716	0.1573	0.0887

3.3.2. Comparison of delamination propagation behaviour with independent experimental results

It is well known that fracture toughness depends on fracture mode partition. The validity of a particular mixed-mode partition theory can only be validated against experimental tests [32]. Thorough and comprehensive experimental test data from several independent research groups [17-21,30] shows [22,23] that Wang and Harvey's Euler beam partition theory gives the most accurate prediction of mixed-mode fracture toughness. The exercise in this section aims to establish whether this partition theory also governs the propagation of mixed-mode delamination driven by post-local buckling.

Case 1 is considered first. Table 3-4 and Figure 3-3 record the delamination propagation behaviour predicted by the three partition theories described in section 3.2. The symbol *f* in Table 3-4 represents the propagation criterion in Eq. (3.49) with $f < 0$ indicating no propagation and $f = 0$ indicating stable propagation. Both the Euler and Timoshenko beam partition theories predict an initial mixed-mode delamination followed by a pure-mode-II delamination, with delamination propagation beginning in the pure-mode-II region at an end-shortening strain $\varepsilon_0 = 2.76 \times 10^{-3}$ and reaching the clamped ends at an end-shortening strain of $\varepsilon_0 = 2.92 \times 10^{-3}$. Although the propagation is stable, it takes only 0.17×10^{-3} of extra end-shortening strain (or 0.0085 mm of end-shortening displacement) to extend the delamination by 12.7 mm. This might suggest an observation of unstable propagation in experimental tests. The 2D elasticity partition theory predicts a mixed-mode delamination which begins to propagate at an end-shortening strain of $\varepsilon_0 = 2.52 \times 10^{-3}$ and reaches the clamped ends at an end-shortening strain $\varepsilon_0 = 2.91 \times 10^{-3}$. It takes an extra end-shortening strain of 0.39×10^{-3} (or 0.0020 mm of end-shortening displacement) to extend the delamination by the same 12.7 mm, which is much larger than the 0.17×10^{-3} of extra end-shortening strain predicted by the Euler and Timoshenko partition theories. This might suggest an observation of stable propagation in experimental tests. The propagation behaviour is also shown graphically in Figure 3-3 as delamination length a versus the end-shortening strain ε_0. The two beam partition theories predict a much steeper growth rate than the 2D elasticity partition theory does. It is seen that the predictions from the two beam partition theories are considerably different from that of the 2D elasticity partition theory.

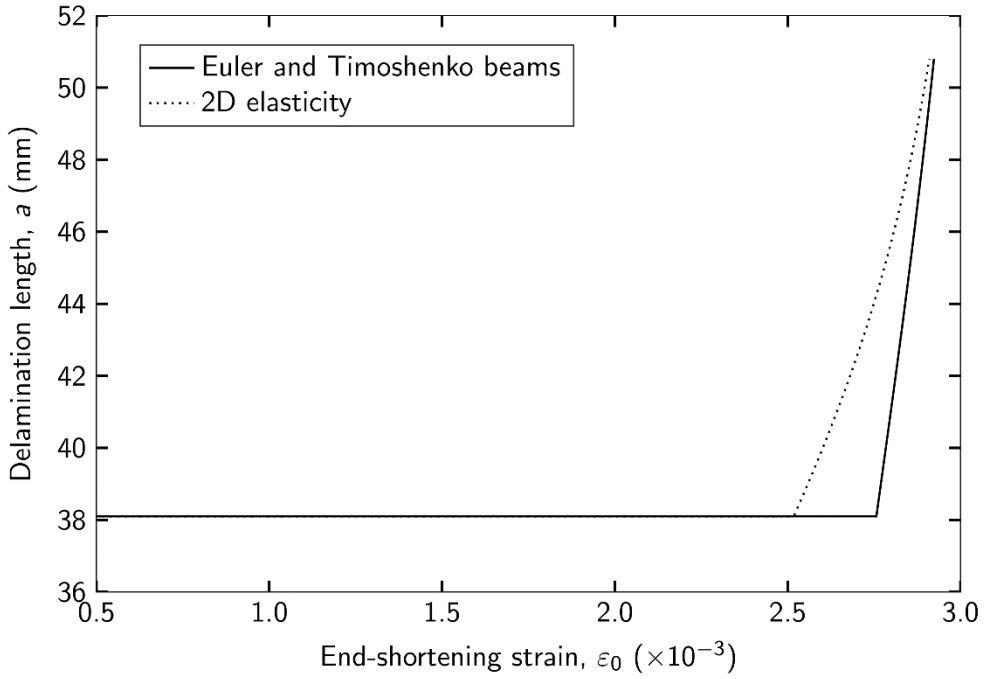

Figure 3-3: Delamination length vs. end-shortening strain for Case 1

Table 3-4: Delamination propagation behaviour of Case 1

ε_0	Euler			Timoshenko			2D Elasticity		
(10^{-3})	a (mm)	f	G_{II}/G (%)	a (mm)	f	G_{II}/G (%)	a (mm)	f	G_{II}/G (%)
0.60	38.10	<0	18.6	38.10	<0	80.3	38.10	<0	43.6
1.00	38.10	<0	66.5	38.10	<0	96.2	38.10	<0	69.4
1.40	38.10	<0	88.4	38.10	<0	99.5	38.10	<0	80.2
1.80	38.10	<0	100.0	38.10	<0	100.0	38.10	<0	86.6
2.20	38.10	<0	100.0	38.10	<0	100.0	38.10	<0	90.8
2.52	38.10	<0	100.0	38.10	<0	100.0	38.10	0	93.1
2.60	38.10	<0	100.0	38.10	<0	100.0	39.96	0	95.0
2.70	38.10	<0	100.0	38.10	<0	100.0	42.53	0	96.9
2.76	38.10	0	100.0	38.10	0	100.0	44.24	0	97.8
2.80	41.12	0	100.0	41.12	0	100.0	45.73	0	98.4
2.90	48.75	0	100.0	48.75	0	100.0	50.23	0	99.6
2.91	49.59	0	100.0	49.59	0	100.0	50.80	0	99.7
2.92	50.80	0	100.0	50.80	0	100.0	-	-	-

Experimental test data in reference [32] are used next to assess the accuracy of each partition theory. The tests record the history of the compression force per unit width F against the

upper surface mid-span axial strain ε_{sc}. The compression force per unit width is calculated analytically as

$$F = \left(N_1 + N_2\right)/b = E_1 h_1 \left(\varepsilon_c + \eta\gamma\varepsilon_0\right) \tag{3.51}$$

and the upper surface mid-span axial strain is calculated analytically as

$$\varepsilon_{sc} = -\frac{h_1}{2}\left(\frac{d^2 V_1}{dx_1^{\,2}}\right)_{x_1=0} - \varepsilon_c = \frac{h_1 A\alpha^2\pi^2}{a^2} - \varepsilon_c \tag{3.52}$$

Figure 3-4 compares the three partition theories with the test results [32]. The following points are noted: (1) the analytical critical local-buckling compression force is much smaller than the experimental one. One possible reason for this is the sticking of the specimen's sub-laminates through the Teflon film—inserted to create the initial delamination—during manufacturing, thus increasing the buckling load [32]. Note that both the analytical and experimental results display bifurcation type local-buckling, which appears as the first sharp corner in the figure. (2) By cross-comparing with the results in Table 3-4, the two beam partition theories predict pure-mode-II propagation, beginning at the second sharp corner and ending at the third one, which corresponds to the complete delamination. During the delamination propagation process, the compression force does not change very much, which equates to an almost-unstable propagation. On the other hand, the 2D elasticity partition theory predicts mixed-mode propagation, starting smoothly and ending at about the same point predicted by the two beam prediction theories. During the delamination propagation, the compression force does change significantly, which equates to a stable propagation. (3) The experimental results [32] do show an almost-unstable propagation and both the initial- and end-propagation compression forces agree very well with the predictions of the two beam partition theories. (4) The significant discrepancy between the analytical and experimental critical local-buckling compression forces results in a significant difference between the predicted and experimental loading curves. This needs to be investigated in order to examine the partition theories more thoroughly.

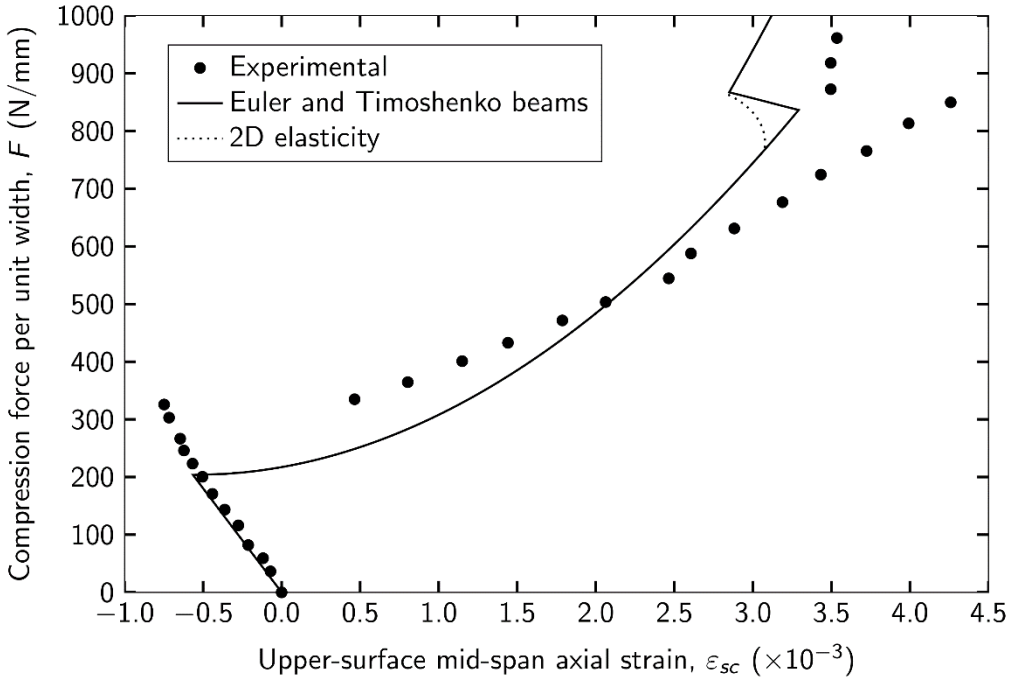

Figure 3-4: Compression force per unit width F vs. upper-surface mid-span strain ε_{sc} for Case 1 using the analytical buckling strain ε_c.

In the following, an approximate expression for the critical local-buckling end-shortening strain ε_{ce} is derived where the subscript e indicates that it is based on experimental results. Similar to in Eq. (3.9), ε_{ce} is written as

$$\varepsilon_{ce} = \frac{(\alpha_e \pi)^2}{3}\left(\frac{h_1}{a}\right)^2 = \left(\frac{\alpha_e}{\alpha}\right)^2 \varepsilon_c \tag{3.53}$$

where the correction factor α_e needs to be determined based on experimental results. It is perhaps the case that, in general, the ratio α_e/α varies with the ratio h_1/a; however, α_e/α is assumed here to be constant at its value at the initial-buckling delamination length due to lack of experimental results for other crack lengths. The accuracy of this assumption will be examined shortly. It is now only required to determine the value of α_e at the point of initial buckling. From Figure 3-4, two approximate critical local-buckling end-shortening strains ε_{ce} are found from the upper-surface mid-span axial strain and the compression force at the bifurcation point of the experimental results: (1) Since $\varepsilon_1 = \varepsilon_0$ before the local buckling of part 1, at this location $\varepsilon_{ce} = \varepsilon_{sc} = 0.748\times10^{-3}$. (2) Before the local buckling of part 1, $\varepsilon_2 = \varepsilon_0$ also, giving $F = E_1 h_1 \varepsilon_0 (1+\eta\gamma)$ or $\varepsilon_{ce} = F/[E_1 h_1 (1+\eta\gamma)] = 0.903\times10^{-3}$ at this location. By

averaging these two values, an approximate critical local-buckling end-shortening strain is obtained as $\varepsilon_{ce} = 0.825\times10^{-3}$. Therefore, the value of α_e at the critical local-buckling point is determined from Eq. (3.53) to be $\alpha_e = 1.163$ and the ratio $\alpha_e/\alpha = 1.207$. The critical local-buckling strain ε_{ce} at any delamination length is then calculated from Eq. (3.53) as $\varepsilon_{ce} = 1.207^2\varepsilon_c$.

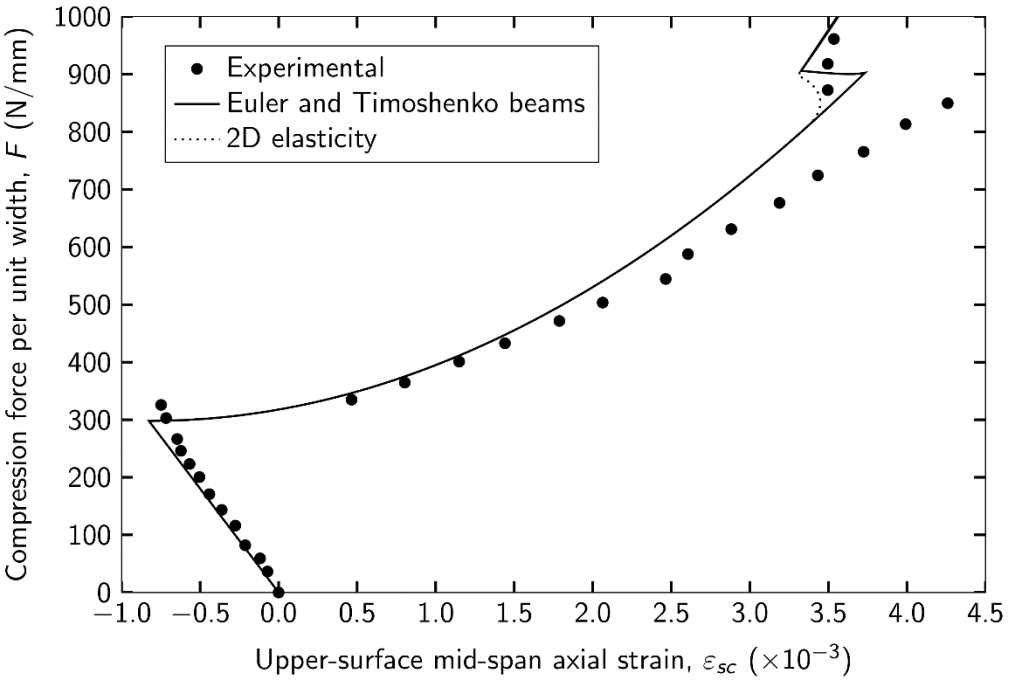

Figure 3-5: Compression force per unit width *F* vs. upper-surface mid-span strain ε_{sc} for Case 1 using the experimental buckling strain ε_{ce}.

Figure 3-5 compares the test results [32] with the three partition theories, which now use the critical local-buckling end-shortening strain ε_{ce} based on experimental results. The two beam partition theories predict the propagation behaviour very well and much better than the 2D elasticity partition theory does. The delamination propagation is indeed the pure-mode-II propagation predicted by the two beam partition theories. It is now clear that the 2D elasticity partition theory does not provide the right partition for predicting the propagation behaviour of buckling-driven delamination for Case 1. The question of which beam partition theory provides the right partitions when the propagation is not pure mode II, however, still needs to be answered. Case 2 is considered next to answer this question.

Case 2 is now considered in the same manner. Table 3-5 and Figure 3-6 record the delamination propagation behaviour predicted by the three partition theories. All three

partition theories predict an initial mixed-mode delamination after the local buckling of the upper layer at $\varepsilon_c = 2.073\times10^{-3}$, followed by unstable mixed-mode delamination propagation and then stable propagation. The Euler beam partition theory predicts mode-I-dominated unstable propagation occurring at an end-shortening strain of $\varepsilon_0 = 2.46\times10^{-3}$, during which the delamination extends to a total length of 28.99 mm. Then the delamination propagates stably as mode-II-dominated to a total length of 29.67 mm corresponding to end-shortening strain $\varepsilon_0 = 2.69\times10^{-3}$ after which the delamination propagates stably as pure-mode-II to the clamped ends at an end-shortening strain $\varepsilon_0 = 2.97\times10^{-3}$. The Timoshenko beam partition theory predicts mode-II-dominated unstable propagation occurring at an end-shortening strain of $\varepsilon_0 = 2.92\times10^{-3}$, during which the delamination extends to a total length of 46.68 mm. Then the delamination propagates as pure-mode-II to the clamped ends at an end-shortening strain of $\varepsilon_0 = 2.97\times10^{-3}$. The 2D elasticity partition theory predicts a fairly mixed-mode unstable propagation occurring at an end-shortening strain of $\varepsilon_0 = 2.56\times10^{-3}$, during which the delamination extends to a total crack length of 37.45 mm. Then the delamination propagates as mode-II-dominated to the clamped ends at an end-shortening strain of $\varepsilon_0 = 2.96\times10^{-3}$. In a sense, the 2D elasticity partition theory is an 'average' of the two beam partition theories. The propagation behaviour is also shown graphically in Figure 3-6 as delamination length a versus the end-shortening strain ε_0. It is seen that the predictions from the three partition theories are considerably different from each other. In contrast with the prediction for Case 1, for Case 2 the Timoshenko beam partition theory gives very different predictions to those from the Euler beam partition theory.

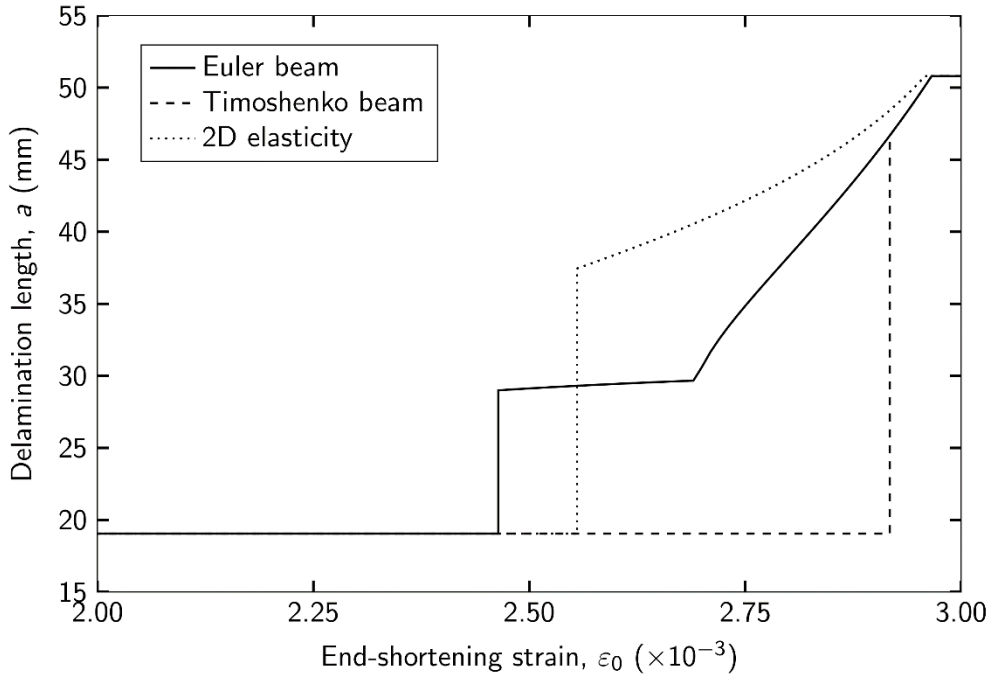

Figure 3-6: Delamination length vs. end-shortening strain for Case 2.

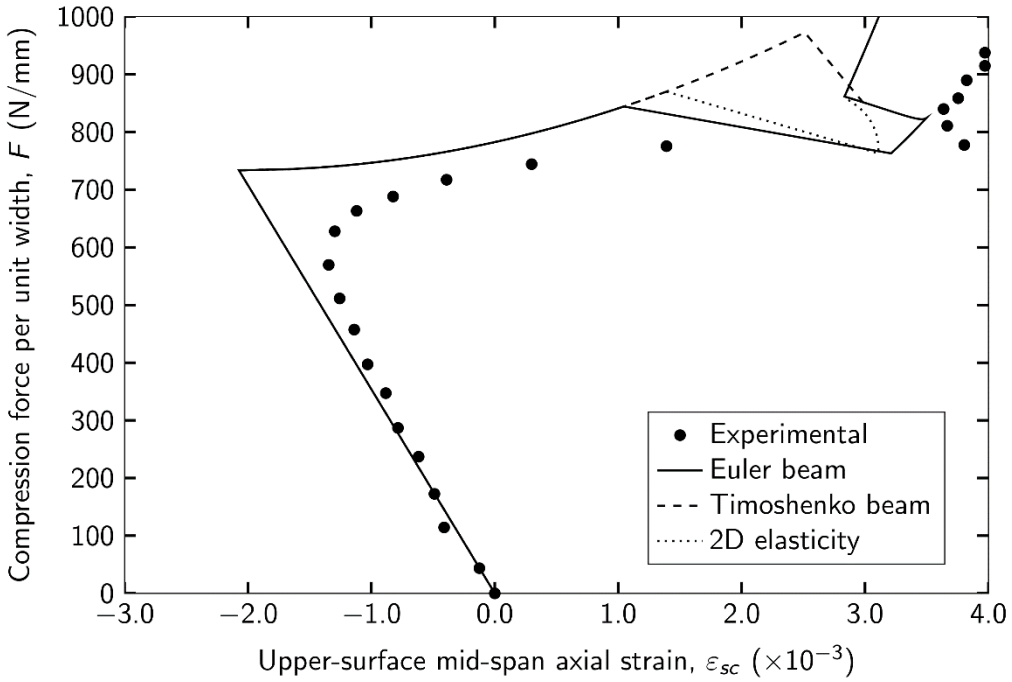

Figure 3-7: Compression force per unit width F vs. upper-surface mid-span strain ε_{sc} for Case 2 using the analytical buckling strain ε_c.

Table 3-5: Delamination propagation behaviour of Case 2

ε_0	Euler			Timoshenko			2D Elasticity		
(10^{-3})	a (mm)	f	G_{II}/G (%)	a (mm)	f	G_{II}/G (%)	a (mm)	f	G_{II}/G (%)
2.30	19.05	<0	25.0	19.05	<0	83.1	19.05	<0	47.2
2.34	19.05	<0	27.2	19.05	<0	84.0	19.05	<0	48.5
2.38	19.05	<0	29.3	19.05	<0	84.8	19.05	<0	49.6
2.42	19.05	<0	31.2	19.05	<0	85.6	19.05	<0	50.7
2.46	19.05	≥ 0	33.2	19.05	<0	86.4	19.05	<0	51.8
2.46	28.99	0	92.7	19.05	<0	86.4	19.05	<0	51.8
2.50	29.13	0	94.0	19.05	<0	86.9	19.05	<0	52.6
2.54	29.26	0	95.4	19.05	<0	87.6	19.05	<0	53.5
2.56	29.31	0	95.9	19.05	<0	87.8	19.05	≥ 0	53.9
2.56	29.31	0	95.9	19.05	<0	87.8	37.45	0	93.4
2.60	29.44	0	97.3	19.05	<0	88.4	38.41	0	94.4
2.64	29.55	0	98.5	19.05	<0	88.9	39.33	0	95.2
2.68	29.64	0	99.6	19.05	<0	89.4	40.29	0	96.0
2.72	32.56	0	100.0	19.05	<0	89.8	41.33	0	96.7
2.76	35.55	0	100.0	19.05	<0	90.3	42.45	0	97.4
2.80	38.27	0	100.0	19.05	<0	90.7	43.69	0	98.0
2.84	40.98	0	100.0	19.05	<0	91.1	45.08	0	98.6
2.88	43.82	0	100.0	19.05	<0	91.5	46.67	0	99.1
2.92	46.68	0	100.0	19.05	≥ 0	91.8	48.43	0	99.5
2.92	46.68	0	100.0	46.68	0	100.0	48.43	0	99.5
2.94	48.53	0	100.0	48.53	0	100.0	49.67	0	99.7
2.96	50.11	0	100.0	48.53	0	100.0	50.80	0	99.8
2.97	50.80	0	100.0	50.80	0	100.0	-	-	-

Similar to the study for Case 1, experimental test data in reference. [32] are used to assess the accuracy of each partition theory. Figure 3-7 shows the histories of the compression force per unit width F against the upper surface mid-span axial strain ε_{sc} as measured in testing and as predicted by the three partition theories. In general, it is seen that the predictions from the Euler beam partition theory agree quite well with the test results, that the predictions from the Timoshenko beam partition theory are poor, and that the predictions from the 2D-elasticity partition theory are somewhere in the middle.

As was seen for Case 1, the critical local-buckling compression force predicted analytically may not agree very well with the experimentally observed value. In order to examine the partition theories more thoroughly, it is necessary to correct for any discrepancy between the analytical and experimental critical local-buckling compression forces. Figure 3-7, however, shows that an imperfection-type initial buckling is observed in experiments (whereas a bifurcation-type initial buckling is predicted by the analytical theories). To account for this, the intersection point of the linear regions of the pre-buckling and post-buckling responses in the experimental data in Figure 3-7 (data markers 1 to 6, and 15 to 17 respectively) is used to approximate the experimental values of the upper-surface mid-span axial strain ε_{sc} and the compression force F at the point of bifurcation-type local buckling, which are found to be $\varepsilon_{sc} = -1.834\times10^{-3}$ and $F = 672\,\mathrm{N}$. As before for Case 1, these values give two approximate critical local-buckling end-shortening strains ε_{ce}. When averaged, $\varepsilon_{ce} = 1.867\times10^{-3}$ is obtained with $\alpha_e = 0.893$ and $\alpha_e/\alpha = 0.949$. The critical local-buckling strain ε_{ce} at any delamination length is then calculated from Eq. (3.53) as $\varepsilon_{ce} = 0.949^2\,\varepsilon_c$.

Figure 3-8 shows the comparisons between the three partition theories and the test results [32]. In general, it is seen that the predictions from the Euler beam partition theory agree well with the test results, that the predictions from the Timoshenko beam partition theory are poor, and that the predictions from the 2D-elasticity partition theory are, again, somewhere in the middle.

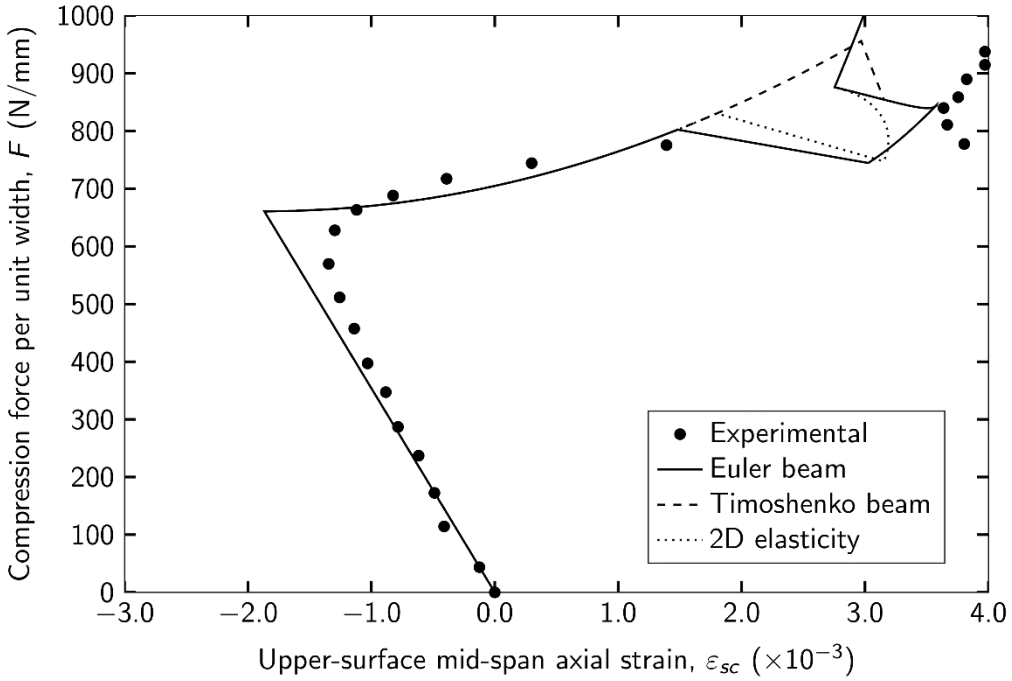

Figure 3-8: Compression force per unit width F vs. upper-surface mid-span strain ε_{sc} for Case 2 using the experimental buckling strain ε_{ce}.

3.4 Conclusions

Based on the Euler beam, Timoshenko beam and 2D-elasticity mixed-mode fracture partition theories [14,22,24-29], analytical theories have been developed for predicting the propagation behaviour of post-local buckling-driven delamination in bilayer composite beams. The conclusions are as follows: (1) Accurate calculation of the total ERR G is essential in order to obtain accurate predictions. This work has presented a more accurate analytical formula for total ERR G than that in Refs. [14,87] by developing a more accurate expression for the post-buckling mode shape and also by including the axial strain energy contribution from the intact part of beam. Very good agreement is observed between the present analytical results and the numerical results [72]. (2) The accuracy of critical local-buckling strain is also a key factor in making accurate predictions. Empirical values, obtained either numerically or experimentally for particular cases, give more accurate predictions. (3) The method used to partition the total ERR G into G_I and G_{II} is another key factor for making accurate predictions. This work presents three partition theories, namely, the Euler beam, Timoshenko beam and 2D elasticity partition theories. Independent experimental tests by Kutlu and Chang

[32] show that, in general, the analytical theory based on the Euler beam partition theory predicts the propagation behaviour very well and much better than the theories based on the Timoshenko beam and 2D elasticity partition theories, when using the critical local-buckling strain derived with the aid of experimental results. (4) Buckling-driven delamination is a major form of failure in engineering structures made of composite layered materials. One important example is the thermal buckling-driven cracking of thermal barrier coatings used in aero-engines. The present Euler beam analytical theory provides a valuable tool for the engineering design of such material structures.

Chapter 4 Post local buckling driven delamination under thermal loads

4.1 Introduction

This chapter and chapter 5 will study some failure behaviours of Thermal Barrier Coating (TBC) material systems. A detailed introduction is given in this chapter.

Thermal barrier coating systems are multilayer material systems to provide thermal insulation to the metallic/super-alloy engine parts from high temperature environment. Typical application of TBC is as gas turbine engine for aircraft propulsion, power generation and marine propulsion. The TBC is commonly manufactured by air plasma-spray (APS) or electron-beam physical vapour deposition (EB-PVD). The former is used for aircraft engine and latter is for gas turbine.

Air plasma spray (APS) is a type of thermal spray process to produce thin film on the substrate. In the thermal spray process, a thermal plasma arc or a combustion flame is used to melt and also to accelerate particles of metals, ceramics, polymers, or their composites to high velocities in a directed stream towards the substrate. The sudden deceleration of the particle upon the substrate surface leads to lateral spreading and rapid solidification of the particle, it forms a 'splat' in a very short time. Successive impingement of the droplets leads to the formation of a lamellar structure in the deposit [131].

Electron beam physical vapour deposition (EB-PVD) is a form of physical vapour deposition in which a target anode is bombarded on the substrate surface with an electron beam under high vacuum environment. It is a physical process facilitating the transform of atoms from a solid or molten source onto a substrate. In this process, thermal energy is supplied to a source from which atoms are evaporated. The evaporated atoms travel through reduced background pressure in the evaporation chamber and condense on the growth surface [131].

The EB-PVD coating produces a feathery microstructure with a columnar grain structure that offers excellent compliance to thermal cycling. EB-PVD coatings exhibit enhanced durability under aero-engine thermal loading environments. On the other hand, a typical APS coating displays a layered architecture, this brick wall like layered structure with interpenetrating porosity and interfaces offers compliance, but lesser extent than the columnar grain structure. The APS TBCs are suitable for the environment with lower operating temperatures, reduced

temperature gradients, and fewer thermal cycles. Typically, the low-cost APS method is used to deposit TBCs on stationary engine parts (combustor, shroud, vanes), whereas EB-PVD TBCs are more durable used primarily on the most demanding hot-section parts in jet engines such as blades.

The TBC system commonly consists of four layers: superalloy substrate, bond coat, TGO and top layer, see Figure 4-1. Typically, the top layer is a ceramic layer, which has lower thermal conductivity to provide thermal isolation [132], the thickness of the top layer is normally 100 to 300 um with a columnar grain structure that provides strain tolerance. The strain tolerance is designed to avoid instantaneous delamination due to thermal mismatch. The bond coat is an oxidation-resistant metallic layer, normally 30 to 100 um in thickness; it essentially dictates the spallation failure of the TBC. Its primary function is to provide a reservoir from which Al can diffuse to form a protective α -Al_2O_3 TGO while maintaining cohesion with the TBC without reacting with it; bond coat also compensates the thermal mismatch of different layers. The third layer is a thermal growth oxide (TGO) layer that is formed at the peak operating conditions between the bond coat and the ceramic top layer. The TGO thickness is typically 0.1 to 10 um. The substrate is a thick layer of nickel or cobalt based metallic alloy, it is the structural component, which needs to be protected from high temperature operation conditions.

The ceramic top layer is typically made of Y_2O_3 stabilised ZrO_2 (YSZ). YSZ has a high thermal expansion coefficient and low thermal conductivity [132]. The in-plane stiffness of top layer is relative small, for example, the elastic modulus of the top layer is about 50GPa. The top layer can be further grouped to one dense layer at the bottom with thickness several micrometres and the other more compliant layer at the top.

The TGO layer is formed between the top layer and bond coat in operation condition, for instance, the bond-coat temperature in gas-turbine engines typically exceeds 700°C, resulting in bond-coat oxidation and the formation of the thermally grown oxide. The thickness of TGO layer increases during the operation condition. It is better that the TGO forms as α -Al_2O_3 and that its growth is slow, uniform, and defect free. The formation of the TGO layer initially provides a diffusion barrier, retarding further bond-coat oxidation, but the growth of the TGO thickness leads to the degradation of TBC interface toughness and the interface delamination.

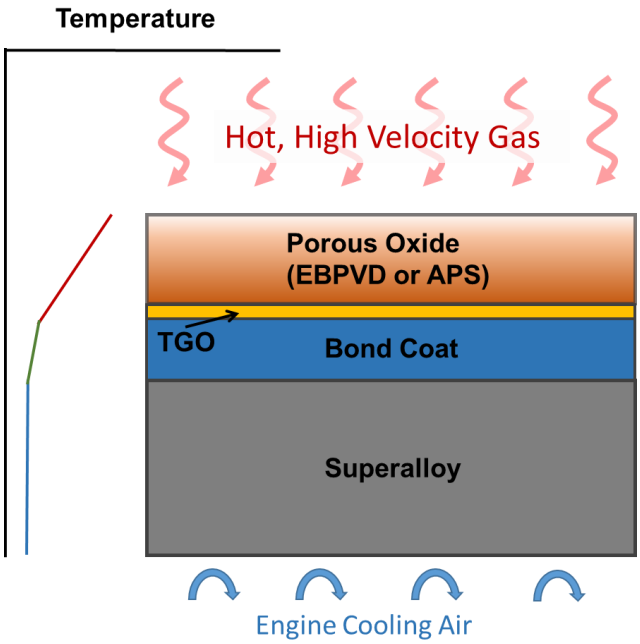

Figure 4-1: Schematic illustration multilayer TBC system (not to scale) [133]

Originally, the TBCs were introduced to extend the life of stationary engine parts such as the combustor, but in the late 1980s, TBCs were first used on rotating blades. Over several decades, the driving force for development of the TBC systems is to increase the durability and reliability of the components under high thermal loading operation conditions. From the 70s to 90s, the TBCs were not "prime reliant"; the ceramic coating was not considered in the design of the temperature capability of the underlying metal parts. Later, the TBC system is gradually considered as "prime reliant" [133]: TBCs are required to maintain thermal protection for prolonged service times and thermal cycles without failure. Typically, these service times are 1000s of hours for jet engines being cycled between a maximum temperature of ~ 1300°C and room temperature (take-off/landing and on-ground), and 10,000s of hours for power-generation engines with fewer thermal cycles (maintenance shut-downs) [133].

These industrial demands are the driving force for the development of TBC material systems. Over several decades, a large number of research works have been conducted on the subject of TBC material systems, the experimental, analytical and numerical methods are used to investigate the TBC failure modes, to develop the TBC lifetime prediction model and to improve the durability and performance of TBC material systems. An overview of the research works on the subject of TBC material systems is conducted from section 4.1.2 to 4.1.5 to show the typical studies with the focus on the interface delamination under mixed

mode delamination. The purpose of this review is attempt to summarise the main characteristics of TBC research works and to serve as basis for the development of TBC life prediction model.

4.1.1 Thermal barrier coating failure

N. P. Padture et al. (2002) [132] addressed that TBC is the material system where a complex interplay occurs with all of the following phenomena: diffusion, oxidation, phase transformation, elastic deformation, plastic deformation, creep deformation, thermal expansion, thermal conduction, radiation, fracture, fatigue, and sintering. The TBC failures are similar, the coating spalls off, the engine parts are exposed to the hot gases, and this leads to the underlying metal rapidly oxidation or melting; however, there are several mechanisms contributing to the observed failures [132]:

A. the thermal expansion mismatch stresses
B. TGO growth
C. the oxidation of the metal
D. the continuously changing compositions, microstructures, interfacial morphologies, and properties of the TBC system.

A detailed summary of damage accumulation, the failure and life prediction of TBC is presented by Nitin P. Padture et al. [132]. They described that the progressive roughening (ratcheting) of the bond-coat/TGO/topcoat interfaces occurs during the thermal cycling, the roughening manifests in the form of TGO penetration into the bond-coat and results in out-of-plane stresses normal to the metal/ceramic interface. They addressed that these stresses, in combination with the interfacial imperfections, are primarily responsible for TBC failure.

The mechanisms of TBC interface delamination caused by TGO displacement into bond coat with each thermal cycle were further investigated by D.R. Mumm (2001) [91] experimentally in detail. Their study revealed a localised, cyclic instability in the TGO that results in lateral cracking of the TBC above the ratcheting sites. These cracks grow and coalesce, resulting in a delamination large enough to cause large scale buckling and spalling.

As a response of TBC thermo-mechanical process, an out of plane displacement instability occurs in the TGO, with ensuing crack evolution in the TBC over-layer. The prior literature

indicates the possibility of two such morphological instabilities. One is the formation of regular, relatively long wavelength undulations, referred to as “rumpling” [94,97–99]. The second comprises of a localised penetration of the TGO into the bond coat. It has been referred to as “ratcheting” [100]. Both “rumpling” and “ratcheting” relate to an interface morphology, they describe the shape of the interface displacement. In a desired status, the TGO should remain elastic to the highest temperatures and not creep to prevent “rumpling” [133]; otherwise, it may lead to the development of local separations at the TBC interface.

The “ratcheting” was studied by He, M. Y. et al. in 2000 experimentally [100]. A deep insight is provided by their study to understand the evolution of TGO growth and the interface delamination. The TGO systematically thickens at the peak temperature with parabolic growth kinetics. The instabilities are manifest as displacements of the TGO into the underlying bond coat that grow systematically as cycling increases. As the instabilities grow larger, cracks develop in the overlying TBC layer. These cracks extend laterally as the instabilities penetrate further into the bond coat, and eventually coalesce into a separation zone large enough to cause large-scale buckling and failure [9].

Similar study of the progressively roughen (“rumple") on the initial flat platinum-modified nickel aluminide bond coat surface with thermal cycling was performed by Tolpygo, V. K. et al. [94]. They discussed mechanisms of the observed rumpling and the implications of the bond coat surface evolution leading to the failure of thermal barrier coatings.

Another study on rumpling was done by D.S. Balint et al. [106]. Their study explored the main factors causing the rumpling. At 600 °C, bond coat creep, thermal expansion mismatch occurs between substrate and oxide layer or bond coat; also the bond coat expansion is caused due to phase transformation. These mismatch cause undulation growths. Undulation growth is driven by the lateral growth strain in the TGO and occurs at a rate governed by many factors, including power law creep of bond coat and plastic yielding of the TGO. They concluded that increasing the bond coat creep strength reduces undulation growth.

The TBC failure typically occur as a sequence of crack nucleation, propagation and coalescence events [9,92,101]; it can be summarised as follows: (a) The stress due to thermal mismatch and its induced strain energy release rate concentrate in the vicinity of the TGO imperfections, causing small cracks and separations to nucleate [95]. (b) Once nucleated, the cracks extend at a rate governed by the magnitude of the stresses around the imperfections

and the associated energy release [96]. (c) Failure occurs when cracks from neighbouring imperfections coalesce and detach the layer over a sufficient area to cause large-scale buckling (LSB) or edge delamination [9,93].

The TBC failure is driven primarily by the high compressive stresses in the TGO [104], the extremely large compression residual stress (3-6GPa) could be developed in the TGO layer due to thermal mismatch as the system cools to ambient temperature; also a relative smaller stress, less than 1GPa is induced through TGO growth [102],[138]. In summary, the TGO growth is a key factor to TBC failure [102], delamination at the interface between the TGO and the bond coat, with subsequent spalling, is the chief failure mechanisms for electron beam deposited TBCs [94], [146].

4.1.2 Early research works (80s and 90s)

Thermal barrier coating (TBCs) were first successfully tested in the turbine section of a research gas turbine engine in the mid-1970s and entered in the service in early 1980s. Firstly the plasma- sprayed coatings were brought into application; in 1990s, the physical vapour deposition (PVD) was successfully brought into commercial service and this made a significant progress to the TBC development.

The early research works in 80s mainly focused on the TBC materials and process optimisation, the failure mechanisms understanding, the lifetime prediction and modelling. One of the most important researcher is R. A. Miller and his research group from NASA-Lewis Research Centre. Begin 80s, thermal barrier coating is just used in the combustor section of some advanced gas turbine engines but not have been introduced into the turbine section of any commercial engine. The goal of his research is to provide the technology base and incorporation TBC into the engine bill-of-materials. In his published paper in 1980 [134], the spalling failure in the TBC system was mentioned and an overview of TBC system was introduced. It shows that the major efforts at that time were to investigate process parameters to achieve better TBC performance. In 1982, he investigated the TBC failures using burner or furnace tests, the surface crack and spalling failure were found in the test specimen [135]. The tests showed that this type of failure could be reproduced only if the atmosphere was oxidizing. He pointed out that the cooling stresses arising from thermal expansion mismatch between the ceramic layer and the bond coat, and the oxidation of the bond coat at the

irregular bond coat/ceramic interface are the main driven factors for the crack and spalling. His study confirmed that the coating life is both time and cycle dependent.

The works done by R. A. Miller leads to further development of life prediction model for TBC systems. Typically, the life prediction contains two steps work, the first is to investigate the coating degradation and to test the delamination toughness; the second step is to develop a life prediction model. In 1984, R. A. Miller presented a lifetime prediction model [136]. The model is to calculate cycles-to-failure as a function of heating cycle duration. It was based on the assumption that oxidation is the single important time-dependent factor which limits the life of these coatings, and that oxidation-induced strains combine with cyclic strains to promote slow crack growth in the ceramic layer.

The other important life prediction model is presented from NASA annual research report in 1986 [145]. That was the most systematic work carried out to investigate the TBC failures by the tests. The experiments were conducted to determine relevant failure modes of the thermal barrier coating systems. Analytical studies coupled with appropriate TBC physical and mechanical properties were employed to derive a life prediction model relative to the predominant failure mode(s). The spalling was confirmed as the predominant mode of TBC failure by experiments and also by flight service components. It had been realised that the bond coat oxidation damage at the metal-ceramic interface contributes significantly to cracking in the ceramic layer.

The next relevant life prediction model was presented in 1988 by T. A. Cruse et al.[146], it addressed that the cyclic thermal loading and thermal exposure play relevant roles in controlling the spallation life of the coating. A life prediction model has been developed based on a damage accumulation algorithm that includes both cyclic and time-dependent damage. The cyclic damage is related to the cyclic inelastic strain range in the ceramic coating; the time-dependent damage is related to the oxidation kinetics at the bond-ceramic interface. The model accounts for cyclic mechanical damage through time independent hysteresis (plasticity) and time-dependent hysteresis (creep).

The other relevant life prediction model was presented in 1988 [147]. It addressed that the cyclic thermal loading and thermal exposure play relevant roles in controlling the spallation life of the coating. A life prediction model has been developed based on a damage accumulation algorithm that includes both cyclic and time-dependent damage. The cyclic damage is related to the cyclic inelastic strain range in the ceramic coating; the time-

dependent damage is related to the oxidation kinetics at the bond-ceramic interface. The model accounts for cyclic mechanical damage through time independent hysteresis (plasticity) and time-dependent hysteresis (creep).

Until that time, the works presented are based on the first-generation plasma deposited zirconia TBC; the life prediction model correlates spallation life with exposure time, temperature and number of thermal cycles [145].

The next representative NASA TBC life prediction model was introduced in 1992 [148]. TGO growth and induced TGO strain levels are correlated with ceramic spallation life measured in an instrumented burner rig. Burner rig test parameters were varied to generate design data over a wide range of simulated mission cycles. These tests were grouped in three generic cycle types: the "strain emphasis" cycle, where many rapid thermal cycles were imposed, the "oxide emphasis" cycle, where significant hold time was imposed at the cycle maximum temperature, and the "mixed mode" cycle, which combined elements of the strain and oxide cycles.

As an example of the life prediction model, the power law life model was developed [148]:

$$N = A\Delta\varepsilon^{b} \tag{4.1}$$

Where N is the cyclic life, A is an empirical normalising constant depending on the amount of oxide growth, b is the empirical power law coefficient. The strain range $\Delta\varepsilon$ is assumed as the maximum TGO tensile mechanical strain. The TGO elastic strains were used instead of EB-PVD ceramic strains, the TGO mechanical strain was due to the thermal growth mismatch between the TGO and the substrate.

To use mixed mode fracture mechanics to study the TBC failure was found in two papers from NASA conference publication. The work done by Klod Kokini et al. (1995) [88] studied edge crack, interface crack using tests to simulate the thermal loading condition, the study addressed that the both cracks subjected to the (opening and shearing) mixed mode. Stress intensity factors K_I and K_{II} are used to characterise the mixed mode fracture [88].

Another example of analytical model for TBC spalling life perdition for EV-PVD and plasma spray TBC is introduced by David M. Nissley [149] in 1995. Empirical TBC spalling life models are developed based on a combination of failure mode observation, TBC spalling life data and stress analysis. TBC failure was assumed to occur when the imposed stress at the

interface exceed the material strength at or near the interface. The top ceramic layer buckling is realised as the failure mode spalling.

The next work to mention is a study conducted by Maurice Gella et al. [90] in 1999, an investigation of the spalling depending on strength and stress with thermal cycling is performed. Five thermal barrier coating test specimens were thermally cycled between room temperature and 1121°C to determine relative spallation life. Bond strength and bond stress measurements were carried out on two EB-PVD coatings as a function of thermal cycling. Bond strength measurements were made using a modified direct pull-test. Bond stress measurements were made in the thermally grown oxide using a laser photoluminescence technique, the change of the strength and stress is dominated by thermal cycling and these are related to oxidation and micro-debonding effects.

In summary, in the early time of the TBC research, the development of life prediction methodologies consists of identification of critical failure mechanisms, stress/strain modelling, and the development of mathematical expressions that define life in terms of stress state and relevant failure criteria. The analytical life prediction models were strong relied on the tests; the mixed mode fracture mechanics and buckling driven delamination were not systematically considered. This situation has been changed in the 21st century.

4.1.3 Review of TBC analytical model

In the 21st century, more TBC material systems are developed; the performance, durability and reliability of TBC system are improved. The research works on thermal barrier coating have been continued and further developed. The deeper understanding of the TBC failure modes has been gained and better life prediction model of spalling are developed; however, due to the complexity and diversity of TBC structures and the severity of operating conditions, TBC research remain a challenge tasks for the researchers.

To develop a mechanical analytical model is a crucial step towards the thermal barrier coating life prediction. The studies are conducted from different aspects by researchers to gain the understandings of the thermal barrier coatings. In 1999, Sung Ryul Choi et al., [9] studied the edge delamination and buckling delamination, which occur at the interface between the bond coat and the TGO. They found that the low in-plane elastic moduli of the porous zirconia layer benefit the buckling delamination but suppress the edge delamination;

small scale delamination arise when the TBC topcoat has a very low modulus; the larger scale delamination occur when the topcoat is stiff. In addition, they proposed a quantitative model for the two competing delamination mechanisms and presented a "failure map" to illustrate the dependences on the topcoat in-plane stiffness. They reported there is a range of in-plane moduli where both mechanisms can be suppressed.

In their work, the failure mechanisms of edge-delamination and buckling delamination are studied. They reported that the edge-delamination is developed when the in-plane moduli of the thick topcoat are moderately high, caused by the large elastic strain energy which develops during cooling. The edge crack is described as the pure mode II delamination. The energy release rate is derived as follows:

$$G_0 = \frac{1-\nu^2}{2E}\sigma_0^2 h_1 \tag{4.2}$$

Where h_1 is the thickness of the topcoat.

If initial interface edge flaws approach several film thicknesses and G_0 reaches steady state, then edge-delamination is expected whenever the G_0 exceeds the mode II interface toughness. It can be seen that in steady state the edge crack condition is dependent on the residual stress, film thickness but not dependent on the crack length.

The energy release rate for buckling delamination of a straight-sided blister is expressed as

$$G_{side} = G_0(1-\frac{\sigma_c}{\sigma_0})(1+3\frac{\sigma_c}{\sigma_0}) \tag{4.3}$$

This is based on critical buckling condition of a debonded film, width 2a and thickness h_1; clamped edge condition. The critical buckling stress σ_c is expressed as Eq. (4.4) for both end pivoted condition.

$$\sigma_c = \frac{\pi^2}{12}\frac{E}{(1-\upsilon^2)}\left(\frac{h_1}{a}\right)^2 \tag{4.4}$$

The energy release rate averaged over the crack front can be obtained by an integration of Eq. (4.3) with respect to crack width because this gives the energy released per unit of front in steady state [14]:

$$G_{front} = G_{side}(1-\frac{\sigma_c}{\sigma_0})(1+3\frac{\sigma_c}{\sigma_0})^{-1} \quad (4.5)$$

It can be observed that the energy release rate at the curved front is always less than that along the sides. Figure 4-2 shows the edge delamination and buckling delamination. For the buckling delamination, the energy release rate can be determined in the front or at the side of the crack.

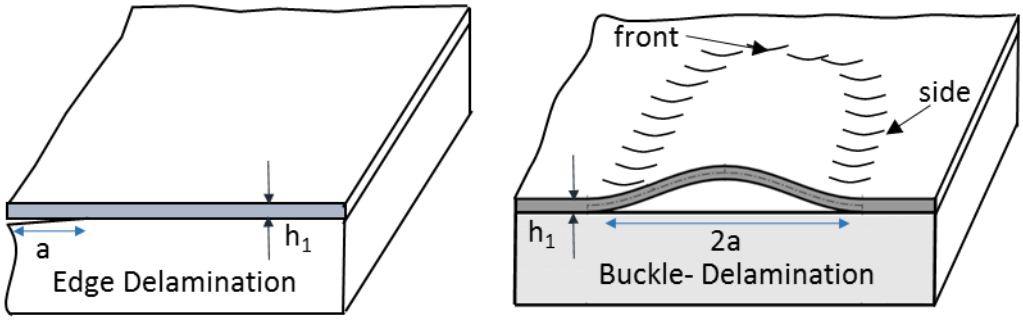

Figure 4-2: Edge delamination and buckling delamination (straight- sided blister)

In their studies, they developed an analytical approach to calculate the energy release rate for edge delamination and buckling delamination considering TBC as single layer and also as multilayer; they investigated the effects of topcoat in-plane stiffness to the edge and buckling delamination. In their study, the results for delamination of the single layer film are generalized for the film with multiple layers. They pointed out that the buckling delamination is in the form of mixed mode I and II; however, no mixed mode partition is considered to describe the delamination in their work.

The edge effect and the edge delamination of thin film were studied by H. H. YU et al. in 2001 [5]. In their study, the interface edge effect on the film delamination was classified as two types: (a) a film whose edge lies in the interior of the substrate Figure 4-3 (a); (b) a film whose edge is aligned with the edge of the substrate, Figure 4-3 (b). An analytical method is introduced to analyse the residual stress distribution in a film near its edge, the energy release rate and the mode mix for an interface delamination. The authors addressed the significant differences between the two cases. First, the elastic mismatch between the film and the substrate is more pronounced in case (b), but not in case (a); second, it is much quicker for a) to reach the energy release rate steady state than for (b). For (a), the energy release rate approaches the steady state, when the crack has extended less than one film thickness. By contrast, in case (b) the energy release rate reaches the steady-state rate until the crack extends to ten or more film thicknesses from the edge. In case (b), the edge effect provides a

significant protection against edge delamination, whereas in case (a) it does not. This edge effect is clearly illustrated in Figure 4-4.

The steady state energy release rate is expressed as follows. This is the same expression as the ERR used for edge delamination from reference [9].

$$G_{ss} = \frac{1-\nu^2}{2E}\sigma_0^2 h_1 \tag{4.6}$$

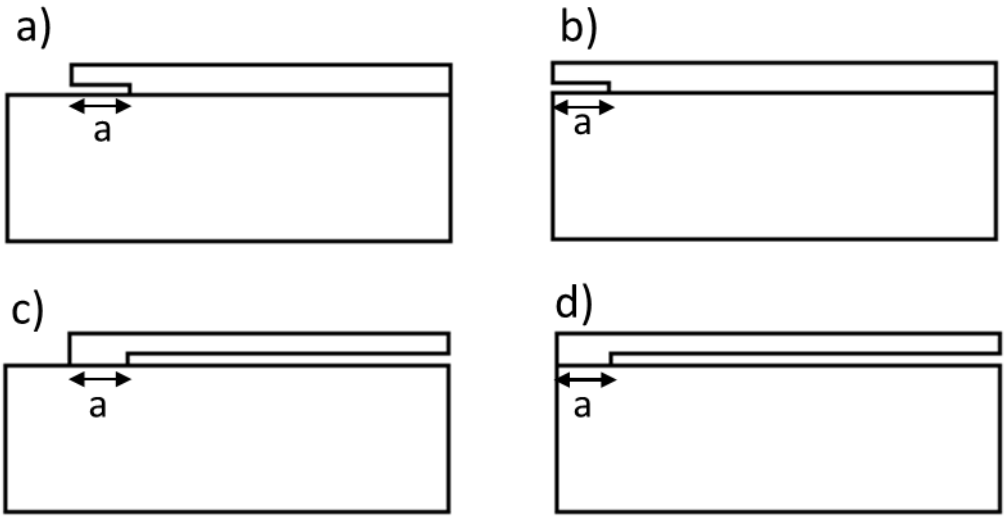

Figure 4-3: (a) interior edge, (b) edge at a corner, (c) crack approaches from interior to interior edge and (d) to corner edge [5].

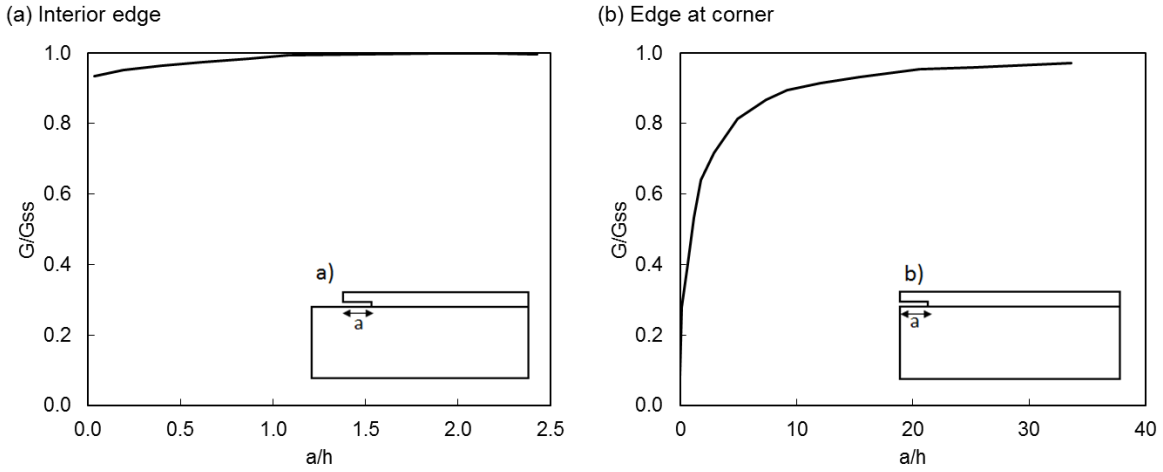

Figure 4-4: Normalised ERR as a function of crack length *a* to film thickness *h* ratio [5].

The second type of the edge effect is investigated wherein the interface crack approaches the edge of the film from the interior. The film displays a different type of behaviour when the

crack approaches one film edge from interior, see Figure 4-3 (c) and (d). The crack tip and the edge "sense" each other from a large distance whether the edge is at a corner or in the interior of the substrate. As they become close, the remaining residual stress in the film decreases and the energy release rate drops. The crack propagation will stop when the energy release rate drops to the level of the interface toughness. Zhuk et al. [142] realised this edge effect in the experimental measurement of the interface toughness of a Ni-polymer bilayer bonded to a silicon substrate. He, Evans and Hutchinson [143] termed such behaviour as "convergent debonding". In their work the energy release rate and mode mixity are calculated analytically for the edge crack like c) and d) in Figure 4-3.

Next relevant study to explore the mechanisms of controlling the thermal barrier coating durability is conducted by A.G. Evens et al. in 2001 [101]. They reported that the TGO layer develops the large compressive residual stress due to thermal mismatch to the substrate upon cooling; also the stresses arise during TGO growth. They addressed that the high concentration of compressive residual stress causes the high-energy density and benefits the crack nucleation and propagation in the interface. A detailed explanation of the stress development, redistribution and relaxation with focus on the sign and magnitude in the vicinity of imperfections and on the consequences of thermal cycling are provided in their work. The analytical approaches are developed for the stress due to thermal mismatch and growth of oxide layer, TGO thickness growth and stress intensity factor in the crack tip. In addition, they presented a buckling map to show the different stages of buckling and buckling propagation with consideration of mode mixity.

A.G. Evens et al.'s work [101] explored the mechanisms behind the TBC failure and developed the analytical approaches to describe the relevant contributors to the failures. The buckling driven and mixed mode delamination is addressed in their study; this is one of the most comprehensive studies contributed to TBC research.

Another interesting study was presented by P.Y. Thery et al. [105] to use an energy balance method to predict the TBC life. An energetic model of spallation is developed based on a two-layer analytical model to represent the TBC material system. The analytical model only considers the strain energy contribution from TGO layer and YSZ top layer. Due to the observation from their tests, they concluded that the strain energy from bond coat and substrate plays an insignificant role to the TBC failure. This energy balance analytical model is based on the principle that the strain energy stored in the YSZ and TGO layers must be

balanced by the surface energy, which is required to form new surface due to interface crack propagation. This condition is only true if the plastic deformation at the crack tip is sufficient small.

The TBC interface investigated by P.Y. Thery et al [105] is a brittle material. According to their energy balance model, the TBC failure is induced by the accumulation of strain energy in the ceramic layers and resisted by the interfacial fracture toughness. The available energy release rate at each stage of the evolution of the TBC is compared to the critical crack propagation energy Gc needed for spontaneous spallation using failure criterion $W_{available} \geq Gc$. The material fracture toughness Gc can be determined from the modified 4-point bending adhesion measurements.

The available energy is so considered that the scale-curved energy must be removed from stored energy.

$$W_{available} = W_{stored} - W_{scale\_curved} \tag{4.7}$$

Where $W_{curved\_scale} = W_{curved}(YSZ) + W_{curved}(TGO)$

The stored energy consists of the strain energy from YSZ layer and TGO layer:

$$W_{stored} = W_{stored}(YSZ) + W_{stored}(TGO) \tag{4.8}$$

For each component (i=YSZ or TGO)

$$W_{stored}(i) = \frac{(1-\nu_i^2)}{2E_i}\sigma_i^2 h_i \tag{4.9}$$

Where h is the thickness of the layer, E and ν are, respectively, its in-plane Young's modulus and its Poisson's ratio.

In the study carried out by P.Y Thery et al. [105], the energy-based spallation model compares the decreasing of TBC adhesion energy and the increasing elastic stored energy due to the growth of thermal oxide and possible sintering phenomena. This lifetime predictions are validated by the experimental lifetimes and a good correlation is achieved. It indicates the feasibility of using energy balance method to predict TBC spalling failures based on two layers assumption for the brittle materials.

In contrast to the works done by P.Y Thery et al. [105] only considering the strain energy contribution from TGO layer and YSZ top layer, the TBC interface delamination influenced by substrate compliance is investigated by Hong-Hui Yu et al. [107-109]. The work of Cotterell and Chen [109], who were the first to call attention to the importance of substrate deformation [109]. If the substrate is compliant, the critical buckling load and the energy release rate of the interface crack can be significantly affected [109]. Yu and Hutchinson analysed the effects of compliance of substrate by introducing compliance coefficients [107]; their study [107] confirms the findings of Cotterell and Chen [109] and extends their results to arbitrary combinations of mismatch and blister size. The critical buckling condition, the energy release rate and the mode mix of the interface delamination crack are calculated as a function of the elastic mismatch between the film and substrate. Substrate deformation has a significant effect on thin film buckling delamination when the ratio of the film modulus to substrate modulus exceeds about three. The results show that the more compliant the substrate is, the easier for the film to buckle and easier for the interface crack to propagate after buckling. This conclusion was confirmed by other researchers as well [108].

Until now, it can be seen that many efforts have been given to the development of analytical mechanical model to predict the TBC life over several decades; the good correlations between experimental tests and analytical model have been achieved; the mechanism of mixed mode fracture mechanics and the buckling driven delamination have been considered. However, there is still some uncertainties in the current analytical mechanical models presented above. For instance, there is no consistent model to predict the TBC failure from crack nucleation, propagation, stable and unstable growth and final spallation; it is unsure which mixed mode partition theory governs the prediction of TBC failure and the life model.

4.1.4 Finite Element Modelling

In 80s, in the early time of TBC research work, the finite element analysis has been found with experimental results to develop life prediction models for the plasma-sprayed TBC. As an example, a two-dimensional, axisymmetric finite element analysis with cyclic loading and material nonlinearities has been developed at company GE [117]. This finite element analysis was carried out to examine the stresses that occur during the operation cycle showing that a considerable residual stress exists in the specimen. The plastic deformation of substrate, bond coat and the top coating creep are considered in the FE analysis. At that time, this FE Model

is limited to a maximum of three materials, it was not possible to directly model the substrate, bond coat, oxide scale, and topcoat with separate materials; the substrate properties were substituted for the bond coat.

The next FE model to be mentioned is that one developed by J. Cheng et al. [118] in 1998 with elastic and plastic material properties to determine the thermal/residual stress in the bond coat of an EB deposited TBC. Based on the test data from the cyclic furnace testing performed on TBC specimens and the observation of progressive failure [103], they found that purely elastic analysis failed to show some important tensile regions associated with the observed failure. The stresses computed in the elastic analysis were higher than those from the elastic/plastic calculations. The elastic calculations fail to show tensile stresses that occur on reheating; the stresses upon reheating that are missed in elastic analysis were responsible for some of the observed cracking. In addition, J. Cheng et al [118] realised that the failure is associated with interface irregularities that are not always sinusoidal, therefore, the finite element models were built with actual interface geometries from the image processing of metallographic sections, which were found in the experiments by them. Generally the actual interface geometries have higher local curvature in place of the more commonly used sinusoidal geometries, to use of actual interface geometries results in the calculation of higher local stresses. All the analyses were carried out using the finite element code Abaqus version 5.6.

In the same year, a FE model was used by A.M. Freborg et al. [119] to simulate the oxidation induced stresses in thermal barrier coatings. The finite element model was developed to evaluate stresses induced by thermal cycling of a typical plasma sprayed TBC system. The failure mechanisms of thermal barrier coatings have been examined through a finite element model of residual stress generation due to oxidation, topcoat creep and bond coat creep. The results indicate that topcoat and bond coat creep generate tensile stresses at bond coat peak and off-peak locations, while generating compressive stresses in the valley regions. In this FE model, the element “birth” and “death” techniques are utilised to replace the bond coat element with the same size of oxide bond coat elements at defined time intervals. The first oxide birth was in the elements located at the ceramic metal interface. Subsequent growth occurred through oxide elements birthed at the scale/metal interface at the start of the high temperature of the cycle. The oxide elements were allowed to ‘‘grow’’ during steady state to the full volume. In this way, the stress due to oxide growth, relaxation of growth stresses and

thermal cycling was incorporated in the model. Since the oxide elements were birthed at the oxide/bond coat interface, the model simulates the inward growth of an oxide scale.

The next is to introduce a 2D axisymmetric FE Model, which was built using ABAQUS to simulate an oxidation process in 2001 [120]**.** In this FE model, an oxidation process wherein the new TGO forms at the interface, an anisotropic growth law is used. The growth of the TGO is simulated by imposing stress-free strains in accordance with a user subroutine. It consists of two components, ε_g and ε_t. The magnitude of the strain per cycle normal to the interface, ε_t (which governs the thickening), is taken to be much larger than the strain per cycle, ε_g parallel to the interface (which causes lengthening of the TGO and induces the growth stress). Thickening of the TGO is modelled by adding a strain, ε_t in the row of TGO elements next to the bond coat. Moreover, in order to limit the growth stress to levels found experimentally, the TGO is allowed to undergo high temperature stress relaxation.

The next important contribution to the FE simulation of TBC is the work done by U. Hermosilla et al. in 2009 [121], a coupled FE model integrating the mechanical response and microstructure evolution with considering the TGO growth, volume changes and the impact to TBC damage. A coupled microstructural–mechanical analysis was used to study the high temperature behaviour of coatings and the accumulation and concentration of stresses that may responsible for spallation upon cooling. A microstructure evolution model, a 1D diffusion model is developed to simulate phase changes under different temperature conditions using thermodynamic phase equilibrium calculation.

One of the major purposes of the work [121] is to understand the development of stresses due to the growth of the oxide layer. Initial models assumed a simple parabolic growth law for the oxide layer; the models were then developed to consider the evolving properties of the substrate and bond coat, and a more rigorous model of the oxidation process was implemented. The formation of the thermally grown oxide (TGO) is modelled by considering the volume change due to oxidation. In turn, the model predicts the evolution of stresses at the positions within the TGO layer. The TGO growth was modelled by applying swelling strain rates to the material that composes the initial oxide layer.

Similar FE model is built by U. Hermosilla et al. in 2013 [122] to simulate microstructure phase transformation and material degradation of TBC material system. A one-dimensional finite element diffusion model is developed to simulate diffusion of elements between the

substrate material and the bond coat in TBC. The TGO growth is simulated within the model and coupled with diffusion of the oxide-forming element. Microstructure changes and material degradation under different temperatures with varied bond coat compositions are simulated using this FE model. The results show that the accumulation of high out-of-plane tensile stress within the alumina layer as an additional phenomenon that could drive high temperature crack nucleation.

Based on the studies presented above, it is seen that the finite element method is capable to predict some aspects of TBC failures. It is the work in the future to extend the analytical model developed in this chapter to a complete TBC life prediction model with the supporting of numerical and experimental method.

4.1.5 TBC delamination fracture toughness test

Thermal Barrier Coating interface fracture toughness test plays an important role to develop the life prediction model; however, there are challenges and difficulties linked with the test. Robert Vaßen described these challenges in 2012 [111]. For example, the TBC properties change during operation, typically leading to degradation of fracture toughness; the TBC service conditions are often extremely harsh, combining high temperatures, steep temperature gradients, fast temperature transients, high pressures, and additional mechanical loading, also oxidative and corrosive environments. It is difficult to reproduce the operation conditions in the laboratory. The coating system also changes with time and temperature as inter-diffusion occurs, microstructures evolve, and the properties of the constituent multilayer materials change. The mechanical properties are not stable because they vary and change with the loading conditions, etc.

Robert G Hutchinson provided a review of tests for measuring mixed mode delamination toughness in 2011 [112]. He reviewed and commented the relevant mixed mode delamination toughness test methods. He stated that the modified four-point bend test is an effective means of measuring delamination toughness under conditions with a nearly equal mix of mode I and II components, see Figure 4-5. It is also possible to measure toughness over the full range of mode mix relevant to coating delamination. The four-point bending test was at first introduced by Charalambides et al. [144] to measure the critical energy release rate at the metal-ceramic interface, then Hofinger et al. [113] proposed a modification of the four-point

bending test wherein stiffeners are bonded to the surface of the coating with a gap cut at the centre to allow delamination to occur. It prevents the large plastic deformation in the substrate, which is caused by required large bending during the test.

There are also other advantages to the modified four-point bending test method. If the stiffener balances the substrate, the coating interface will lie near the neutral bending axis; therefore, the bending load does not change the stress at the coating interface away from the crack tip. The energy for delamination is primarily provided by the elastic energy stored in the stiffener. In addition, if the coating is thin compared with the stiffener, most of the residual stress in the coating will not be released in the test because the coating remains bonded to the stiffener.

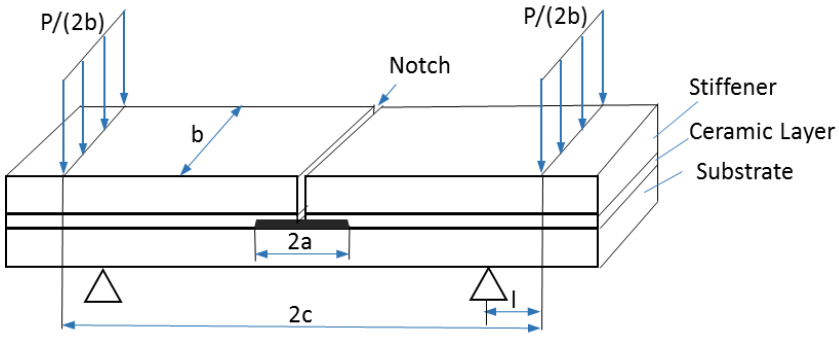

Figure 4-5: Modified notched four- point bending test

The next possibility to determine the delamination toughness is to use the indent test, see Figure 4-6, the advantages of indent test is that it requires only minimum sample preparation along with small quantities of material and is easy to perform. The basic principle is that the indenter penetrates the coating and generates plastic and elastic deformations in the system, driving cracks in the interface between the coating and substrate. However, a major shortage is the difficulty of interpreting the test results; also, it requires the finite element modelling to quantify displacements of the bond coat and superalloy substrate. These disadvantages lead to the limitation of using indent test to measure TBC interface fracture toughness.

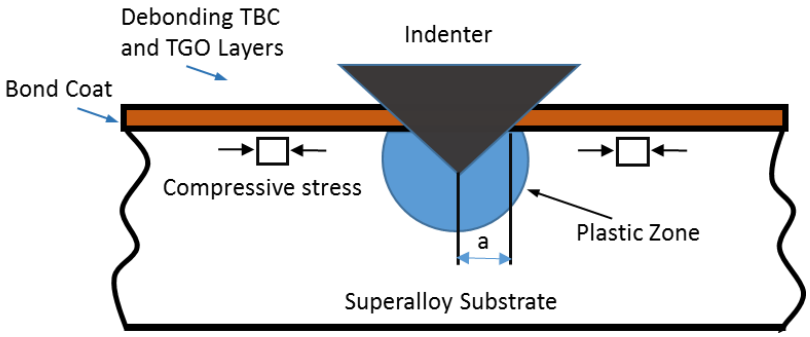

Figure 4-6: Illustration of indent test to determine the interface fracture toughness [114].

The next two important test methods are “barb test” and “push-out test” which were developed by Kagawa and his colleagues [116], [139]. They are similar and both are used to determine the mode II delamination toughness. The coating is subject to additional compression by forcing it against a hard block. The force at which the coating delaminates is used to determine the critical energy release rate and the associated toughness. The disadvantage of these tests is to add compression to any residual compression in the coating, and they impose a delamination displacement and shearing stress on the interface. The barb and pushout tests require highly refined specimen preparation and sophisticated testing which are likely to limit their use for routine toughness testing.

Kagawa and his colleagues have collected an extensive data showing how the toughness degrades with thermal exposure and with thermal cycling using pushout and barb test. Two relevant tests carried out to determine the mode II fracture toughness of TBC are to study the life time dependence on the thermal cycle and time exposure [110], [139].

A pushout is used to test TBC shear delamination toughness by Kagawa et al. [139]. The measured delamination toughness varied from 9 to 95 J/m^2. Thermal cycling tests of an EB-PVD TBC were conducted under four maximum hot temperatures of 1000, 1025, 1050, and 1100 °C. A pushout test method was used to quantify effect of thermal cycling temperatures on the delamination toughness of the EB-PVD TBC system. The delamination toughness depends strongly on hot time temperature. At the hot temperature 1000 °C, the delamination toughness achieved a maximum value up to 95 J/m^2. Thereafter, the toughness decreases with the increase of hot temperatures and was about 9 J/m^2 for the hot temperature 1100 °C. Influence of the hot temperature on the microstructure change is also revealed and related to the interface delamination toughness. During the thermal cycling tests, the TGO was formed

between the TBC and the bond coat. The delamination toughness is affected by various parameters such as the average TGO layer thickness, total hot time, and hot time temperature.

The other test was done by Kagawa is to study the change of interface fracture toughness of EB-PVD TBC system with thermal exposure using push-out test [110]. The measured delamination toughness varied from 10 to 115 J/m^2. The test results show a significant decrease of TBC delamination toughness with time exposure in the high temperature conditions.

In this chapter, buckling driven delamination of TBC layer due to thermal load is considered by extending the theory in chapter 3.

4.2 Development of normalised mixed mode partition

4.2.1 Introduction

As discussed in the section 4.1, the "Thermal Barrier Coating" (TBC) is a multilayer composite material system to provide thermal insulation to the engine parts from high temperature environment. Due to the mismatch of thermal expansion coefficient between the TBC layers the residual stress is often induced either during the temperature cycles or the time exposure in high temperatures, or both. In addition, the residual stress can be caused by manufacture process of TBC material system. As a detrimental effect of the accumulation of the residual stress in the TBC layers, the cracks could nucleate, propagate and coalesce in the interface, finally the thermal barrier coating layer delaminates and spalls off from substrate material.

The delamination of the TBC interface is often characterised as mixed mode crack propagation, which is driven by buckling loads. In the case where the interface fracture toughness is weaker than those of adjoining materials, the path of the crack propagation is constrained along the interface, the TBC layer delamination is in the form of mixed mode fracture. As the length of the interface crack and the compressive stress attain a critical level, the TBC layer buckles away from substrate, then the further crack propagation is driven by buckling and postbuckling mechanism.

The mixed mode partition theory plays a crucial role to predict the TBC failure. In this section, the Wang–Harvey Euler beam partition theory, Timoshenko beam partition theory

and 2D elasticity partition theories [27-29] are utilised to develop a normalised analytical approach to predict the trends of TBC failures. Under the thermal loading the deformation of TBC layers and substrate is assumed in linear elastic range. The studies in this section contain the mixed mode partition, the mixed mode crack propagation and the crack propagation stability. It attempts to show the general trends of TBC life prediction with minimum presence of detailed thermal barrier coating material data. It forms a relevant part of TBC life prediction models, which will be developed in the future with the support of experimental and numerical works. The experimental and numerical works are planned in the future to validate the normalised analytical approaches.

4.2.2 Normalised mixed mode partition

The TBC delamination can be simplified as the thin layer delamination caused by compressive residual stress induced by thermal loading. The TBC material system is simplified as bilayer material system with straight edge: one thin layer and one substrate. The substrate is assumed as the rigid body with infinite stiffness. The energy release rate is calculated from top layer. The total energy release rate and mixed mode partition using Wang–Harvey's Euler beam, Timoshenko beam and 2D elasticity partition theories can be written as Eq. (4.10) to (4.16) respectively by setting $c_\alpha = 1$ for the simplicity from the equation (3.26), (3.32) to (3.33), (3.38) to (3.39) and (3.45) to (3.46) in section 3.2.3. Where c_α is a correction factor to correct bending moment calculation, Eq. (3.21).

Total Energy Release Rate:

$$G = \frac{1}{2} E_1 h_1 \varepsilon_a \left(4\varepsilon_c + \varepsilon_a\right) \tag{4.10}$$

Euler Beam Partition:

$$G_{IE} = E_1 h_1 \sqrt{\varepsilon_c}\, \varepsilon_a \left(2\sqrt{\varepsilon_c} - \sqrt{3}\sqrt{\varepsilon_a}\right) \tag{4.11}$$

$$G_{IIE} = E_1 h_1 \varepsilon_a^{3/2} \left(\sqrt{3}\sqrt{\varepsilon_c} + 1/2\sqrt{\varepsilon_a}\right) \tag{4.12}$$

Timoshenko Beam Partition:

$$G_{IT} = \frac{1}{8} E_1 h_1 \varepsilon_a \left(2\sqrt{\varepsilon_c} - \sqrt{3}\sqrt{\varepsilon_a}\right) \tag{4.13}$$

$$G_{IIT} = \frac{1}{8} E_1 h_1 \varepsilon_a \left(2\sqrt{3}\sqrt{\varepsilon_c} + \sqrt{\varepsilon_a}\right) \tag{4.14}$$

2D Elasticity Partition:

$$G_{I2D} = 0.062888 E_1 h_1 \varepsilon_a \left(4.450\sqrt{\varepsilon_c} - \sqrt{3}\sqrt{\varepsilon_a}\right)^2 \tag{4.15}$$

$$G_{II2D} = 0.103768 * E_1 h_1 \varepsilon_a \left(2.697\sqrt{\varepsilon_c} + \sqrt{3}\sqrt{\varepsilon_a}\right)^2 \tag{4.16}$$

Based on the Eq. (4.10) to (4.16) the normalised expressions are derived using $\overline{G}$, $\overline{G}_I$ and $\overline{G}_{II}$ to represent a normalised G, G_I and G_{II} for total energy release rate, mode I and mode II ERR, respectively. They are written as Eq. (4.17) to (4.23).

$$\overline{G} = \frac{G}{E_1 h_1 \varepsilon_c^2} = \frac{1}{2}\frac{\varepsilon_a}{\varepsilon_c}\left(4 + \frac{\varepsilon_a}{\varepsilon_c}\right) \tag{4.17}$$

Euler Beam Partition:

$$\overline{G}_{IE} = \frac{G_{IE}}{E_1 h_1 \varepsilon_c^2} = \frac{\varepsilon_a}{\varepsilon_c}\left(2 - \sqrt{3}\left(\frac{\varepsilon_a}{\varepsilon_c}\right)^{\frac{1}{2}}\right) \tag{4.18}$$

$$\overline{G}_{IIE} = \frac{G_{IIE}}{E_1 h_1 \varepsilon_c^2} = \left(\frac{\varepsilon_a}{\varepsilon_c}\right)^2\left(\sqrt{3}\left(\frac{\varepsilon_a}{\varepsilon_c}\right)^{-\frac{1}{2}} + \frac{1}{2}\right) \tag{4.19}$$

Timoshenko Beam Partition:

$$\overline{G}_{IT} = \frac{G_{IT}}{E_1 h_1 \varepsilon_c^2} = \frac{1}{8}\left(\frac{\varepsilon_a}{\varepsilon_c}\right)\left(2 - \sqrt{3}\left(\frac{\varepsilon_a}{\varepsilon_c}\right)^{\frac{1}{2}}\right)^2 \tag{4.20}$$

$$\overline{G}_{IIT} = \frac{G_{IIT}}{E_1 h_1 \varepsilon_c^2} = \frac{1}{8}\left(\frac{\varepsilon_a}{\varepsilon_c}\right)\left(2\sqrt{3} + \left(\frac{\varepsilon_a}{\varepsilon_c}\right)^{\frac{1}{2}}\right)^2 \tag{4.21}$$

2D Elasticity Partition:

$$\overline{G}_{I2D} = \frac{G_{I2D}}{E_1 h_1 \varepsilon_c^2} = 0.062888\left(\frac{\varepsilon_a}{\varepsilon_c}\right)\left(4.450 - \sqrt{3}\left(\frac{\varepsilon_a}{\varepsilon_c}\right)^{\frac{1}{2}}\right)^2 \tag{4.22}$$

$$\overline{G}_{II2D} = \frac{G_{II2D}}{E_1 h_1 \varepsilon_c^2} = 0.103768\left(\frac{\varepsilon_a}{\varepsilon_c}\right)\left(2.697 + \sqrt{3}\left(\frac{\varepsilon_a}{\varepsilon_c}\right)^{\frac{1}{2}}\right)^2 \tag{4.23}$$

The crack running in contact condition can be expressed as Eq. (4.24) and (4.25) for using Euler beam, Timoshenko beam and 2D elasticity partition theories respectively based on reference [27-29]:

$$\frac{\varepsilon_a}{\varepsilon_c} > \frac{4}{3} \tag{4.24}$$

$$\frac{\varepsilon_a}{\varepsilon_c} > \frac{4.45^2}{3} \tag{4.25}$$

As known, to use simplified one-dimensional approach, the strain produced by thermal loading can be written as $\varepsilon = \Delta\alpha * \Delta T$; where $\Delta\alpha$ is the difference of material thermal expansion coefficient between TBC thin layer and substrate; ΔT is the temperature difference referenced to a temperature point, where no thermal stress is induced. Typically, the reference temperature of TBC material system exceeds 1000 °C.

The following expression is used to convert the strain into the temperature loading:

$$\frac{\varepsilon_a}{\varepsilon_c} = \frac{\varepsilon_0 - \varepsilon_c}{\varepsilon_c} = \frac{\varepsilon_0}{\varepsilon_c} - 1 = \frac{\Delta T}{\Delta T_c} - 1 \tag{4.26}$$

Where ε_c and ΔT_c are the critical buckling strain and the critical temperature drop at buckling respectively.

With the equations (4.17) to (4.26), the mixed mode partition can be calculated using Euler beam, Timoshenko beam and 2D elasticity partition theories according to the increased thermal loading $\Delta T / \Delta T_c$ ratio.

At the point where the $\Delta T / \Delta T_c$ equals to 1, the top TBC layer just buckles; to increase ΔT and to assume a fixed ΔT_c, the top layer buckles further and the energy release rate at the crack tip increases as well. From Figure 4-7, it can be seen that the mode II is significantly larger than mode I, this trend is predicted by all three partition theories with exception that Euler beam partition theory predicts higher proportion of mode I than mode II at the $\Delta T / \Delta T_c$ ratio from 1 to approximately 1.25. This trend can be more clearly observed from Figure 4-8: the Euler beam partition theory shows the ratio of $\overline{G}_I$ to $\overline{G}$ is higher than 50% in the range of $\Delta T / \Delta T_c$ increasing from 1.0 to about 1.25.

Figure 4-8 illustrates the mode mixity ratio of $\overline{G}_I$ to $\overline{G}$ over thermal loading ratio $\Delta T / \Delta T_c$, where $\overline{G}$ represents normalised total ERR from Eq. (4.8). From Figure 4-8 it can be seen that the Euler beam partition theory shows the highest ratio of mode I until $\Delta T / \Delta T_c$ increases to 1.7; after this point, 2D elasticity partition theory predicts the highest ratio of mode I. In contrast, Timoshenko beam partition theory predicts the lowest ratio of $\overline{G}_I$ to $\overline{G}$ over

$\Delta T / \Delta T_c$. The higher ratio of the mode I to total ERR normally indicates an earlier and faster delamination since the interface mode I fracture toughness often is significantly lower than that of mode II.

The crack running in contact conditions are presented in Figure 4-8 as well. As the thermal loading ratio $\Delta T / \Delta T_c$ equals to 2.41, Euler and Timoshenko beam partition theories show the same condition of crack running in contact; the 2D elasticity partition theory presents a higher loading point for crack running in contact, where $\Delta T / \Delta T_c$ ratio equals to 7.76. Once the crack running in contact, the crack propagates in the form of pure mode II, the G_{II} is identical as the total G.

The evolution of normalised mode I ERR, $\overline{G}_I$ is presented in Figure 4-9. It can be seen that the mode I ERR increases at first, then decreases and finally turns into pure mode II. This trend is predicted by all three partition theories; however, it occurs at different loading ratio of $\Delta T / \Delta T_c$ according to different partition theories. The speed of TBC delamination is influenced by the mode mixity ratio of mode I to total G and the evolution of mode I during the loading cycle.

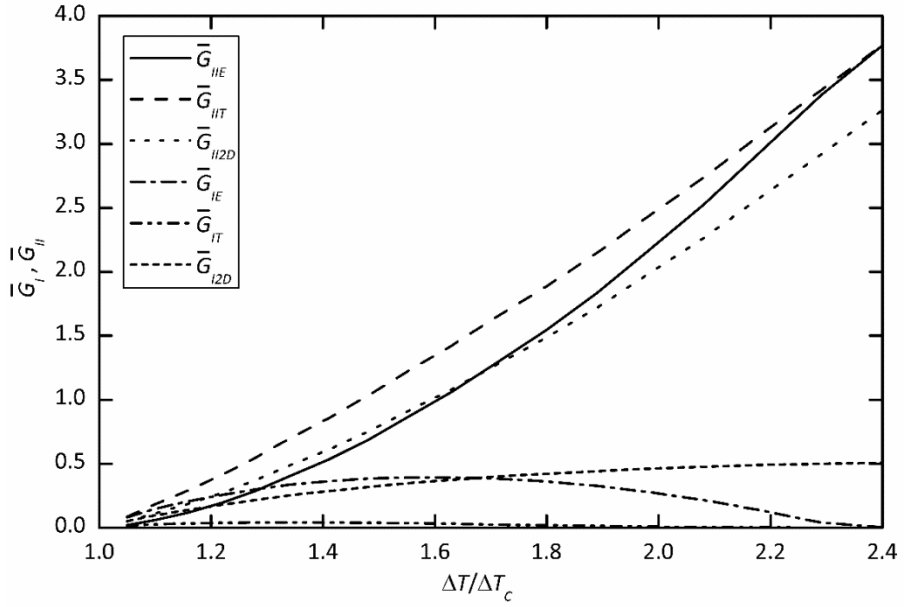

Figure 4-7: Mixed mode partition between Euler beam, Timoshenko beam and 2D elasticity partition theories

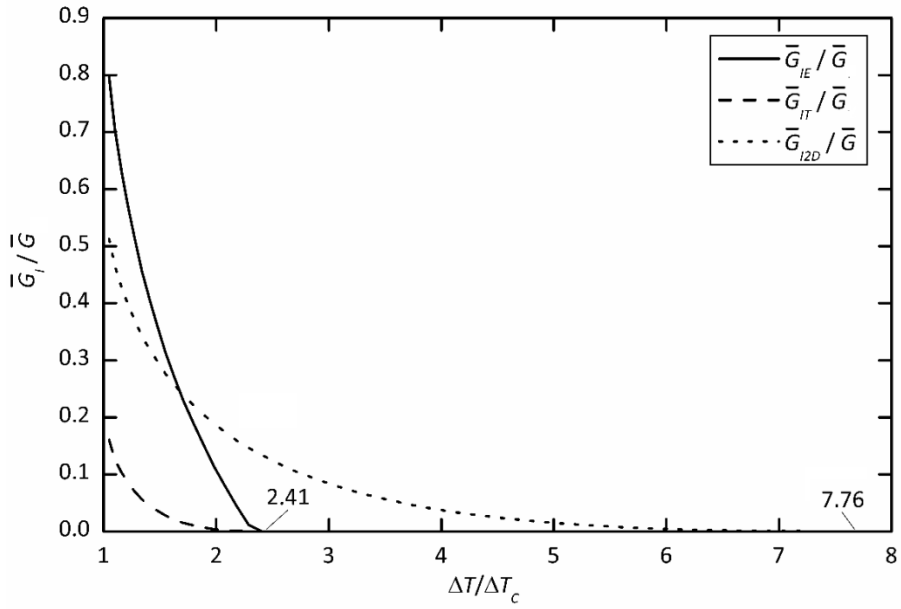

Figure 4-8: Comparison of $\overline{G}_I / \overline{G}$ between Euler beam, Timoshenko beam and 2D elasticity partition theories.

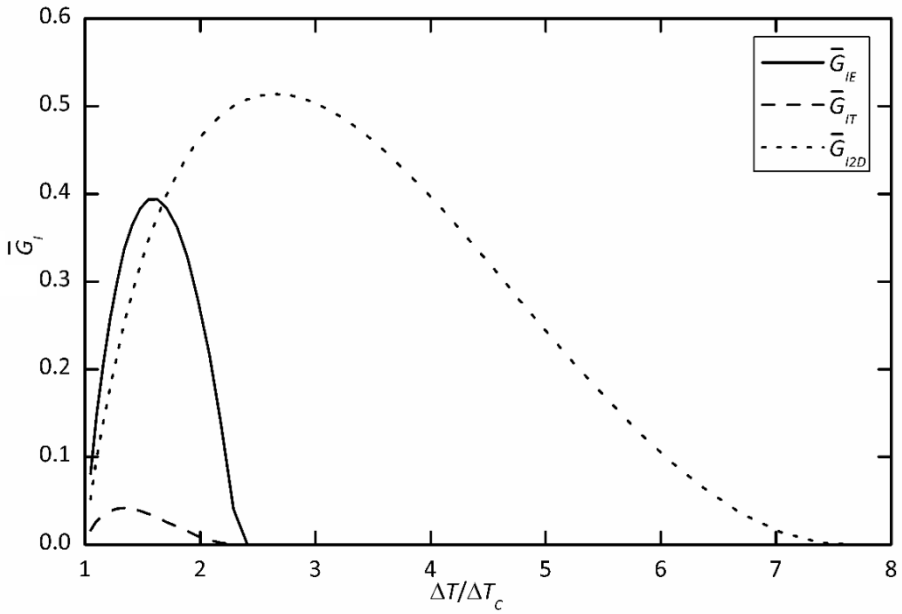

Figure 4-9: Comparison of $\overline{G}_I$ evolution between Euler beam, Timoshenko beam and 2D elasticity partition theories

4.2.3 Normalised mixed mode crack propagation

Mixed mode interface crack propagation can be expressed mathematically as Eq. (4.27).

$$f(G_I, G_{II}, G_{IC}, G_{ICI}) = 0 \tag{4.27}$$

Where G_I, G_{II} are the energy release rate of the mode I and mode II, respectively; G_{IC} and G_{IIC} are the interface fracture toughness of mode I and mode II, respectively.

Equation (4.28) and (4.29) are the linear and quadratic failure criterion, respectively.

$$f(G_I, G_{II}, G_{Ic}, G_{IIc}) = \frac{G_I}{G_{Ic}} + \frac{G_{II}}{G_{IIc}} - 1 = 0 \tag{4.28}$$

$$f(G_I, G_{II}, G_{Ic}, G_{IIc}) = (\frac{G_I}{G_{Ic}})^2 + (\frac{G_{II}}{G_{IIc}})^2 - 1 = 0 \tag{4.29}$$

Interface mixed mode crack propagation or delamination can be predicted using failure criterion equations. The fracture toughness G_{IC} and G_{IIC} can be written as normalised form as Eq. (4.30) and (4.31).

$$\overline{G}_{IC} = \frac{G_{IC}}{E_1 h_1 \varepsilon_c^2} \tag{4.30}$$

$$\overline{G}_{IIC} = \frac{G_{IIC}}{E_1 h_1 \varepsilon_c^2} \tag{4.31}$$

Also, the ratio ψ is introduced to express the relation of fracture toughness mode I and mode II as $G_{IIC} = \psi G_{IC}$. The linear and quadratic failure criterion can be written as normalised form:

$$(\overline{G}_I + \overline{G}_{II} \frac{1}{\psi}) = \overline{G}_{IC} \tag{4.32}$$

$$((\overline{G}_I)^2 + (\overline{G}_{II})^2 \frac{1}{\psi^2}) = (\overline{G}_{IC})^2 \tag{4.33}$$

From the expression (4.30) to (4.33), it is seen that to predict the crack propagation requires the material fracture toughness data G_{IC} and G_{IIC}. Once the G_{IC} and G_{IIC} from experimental data are applied to Eq. (4.30) and (4.31), the prediction of interface delamination can be made from the Eq. (4.32) and (4.33). A "delamination index" is introduced as the right term of Eq. (4.32) and (4.33) for using linear and quadratic failure criterion respectively.

Figure 4-10 presents the "delamination index" according to the increased $\Delta T / \Delta T_c$ ratio using linear failure criterion and Eq. (4.32) by Euler beam, Timoshenko beam and 2D partition theories respectively. Figure 4-11 shows the similar results but using quadratic failure

criterion. In these figures, the values of "delamination index" are calculated assuming TBC interface fracture toughness G_{IC}=10N/m, G_{IIC}=50N/m, top layer thickness h_1=0.02mm, E=50GPa and the initial crack length a_0=0.5mm.

The sequence of crack propagation predicted by different partition theories is shown in Figure 4-10 and Figure 4-11 for using linear and quadratic failure criterion respectively. The horizontal line is the "threshold of delamination index", which is calculated by Eq. (4.30) or right term of Eq. (4.32) using linear failure criterion as follows.

$$\varepsilon_c = \frac{\pi^2}{3}(\frac{h_1}{a_0})^2 = \frac{\pi^2}{3}(\frac{0.02mm}{0.5mm})^2 = 0.005264 \tag{4.34}$$

$$\overline{G}_{IC} = \frac{G_{IC}}{E_1 h_1 \varepsilon_c^2} = \frac{20N/mm}{50000MPa \times 0.02mm \times 0.005264} = 0.36 \tag{4.35}$$

The left term of Eq. (4.32) is the value calculated from normalised mode I and mode II ERRs and named as "Delamination index". As the "Delamination index" increases and reaches the "threshold of delamination index", for example 0.36 for using linear failure criterion, the crack propagation starts. In the Figure 4-10, the Euler beam partition theory predicts the earliest crack propagation; the Timoshenko beam partition theory shows the latest crack propagation and the 2D elasticity partition theory is in the middle. The results are consistent with the prediction from the ratio of mode I to total ERR (G_I/G) in Figure 4-8 in section 4.2.2, the higher ratio of mode I ERR normally indicates an earlier delamination.

Similarly, the "threshold of delamination index" of using quadratic failure criterion is calculated as 0.13 by using (4.34) and (4.33) based on interface fracture toughness G_{IC}=10N/m, G_{IIC}=50N/m. It is presented as the lower horizontal line in Figure 4-11. Compared with delamination predicted by using linear failure criterion in Figure 4-10, a slightly later delamination was predicted by using quadratic failure criterion in Figure 4-11. To predict later interface delamination means a less conservative approach for the practice application.

The sequence of crack propagation predicted by different mixed mode partition theories is dependent on the interface fracture toughness. In Figure 4-10 and Figure 4-11 it can be observed that the delamination index curve of 2D elasticity overtakes the Euler delamination index curve at the thermal loads ratio of $\Delta T / \Delta T_c$ about 1.7, this means that the 2D elasticity partition theory predicts earlier delamination than Euler beam partition theory does. This case

is illustrated by the upper horizontal lines in Figure 4-10 and Figure 4-11 for using linear and quadratic failure criteria respectively. The values of "threshold of delamination index" are calculated using arbitrarily 1.95 times of G_{IC}=10N/m and G_{IIC}=50N/m, namely G_{IC}=19.5N/m and G_{IIC}=97.5N/m. It is seen that the 2D elasticity partition theory predicts the earliest delamination for both of using linear and quadratic failure criterion; Euler partition theory predicts the second earliest delamination for using linear failure criterion but last for using quadratic failure criterion.

The trends of crack propagation sequence can be also observed from the mode I ERR mixity curve in Figure 4-8 and Figure 4-9. The higher ratio of mode I ERR normally indicates an earlier delamination since the mode I fracture toughness is often smaller than mode II fracture toughness in the interface.

It is worth noting that the "threshold of delamination index" presented in Figure 4-10 and Figure 4-11 is only to calculate the starting point of the interface crack propagation or delamination. From Eq. (4.34), it can be seen that the critical buckling strain ε_{cr} is depedent on the crack length. As the interface crack advances from initial crack length a_0 to the next crack length a_1, the critical buckling strain corresponding to the a_1 decreases; subsequently, the "threshold of delamination index" increases. In other words, after the crack propagation started, the "threshold of delamination index" is not a constant value, it varies with the crack length but it still can be calculated using Eq. (4.34), (4.30) and (4.31).

The other observation from the "delamination index" presented in Figure 4-10 and Figure 4-11 is that the Euler beam partition theory exhibits the high nonlinearity with increased thermsl loading compared with those calculated by Timoshenko beam and 2D elasticity partition theories. The high nonlinearity of "delamination index" can be traced back to the mixed mode partition theories. The mode I and mode II ERR calculated by Euler beam partition theory also show high nonlinearity in Figure 4-7.

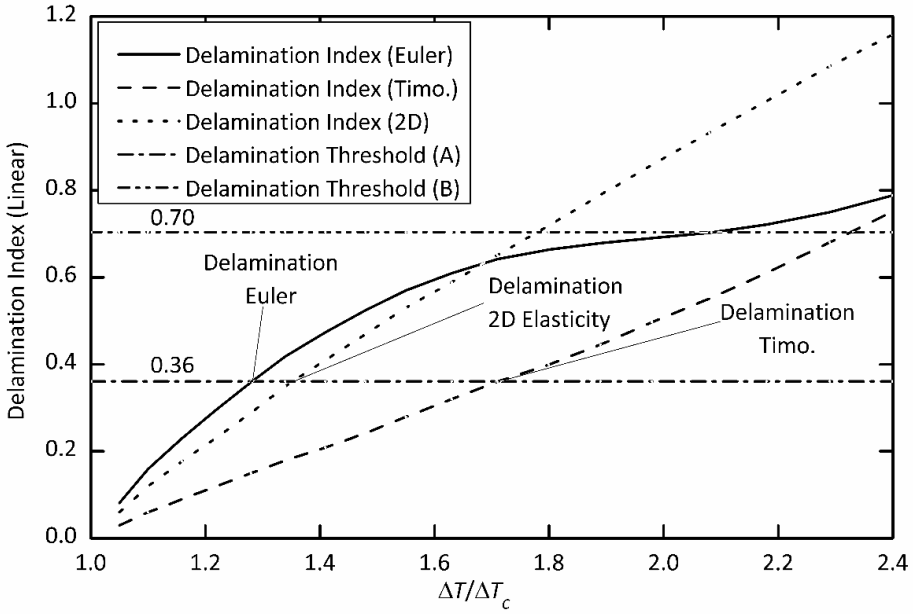

Figure 4-10: Crack propagation condition by various partition theories using linear criterion

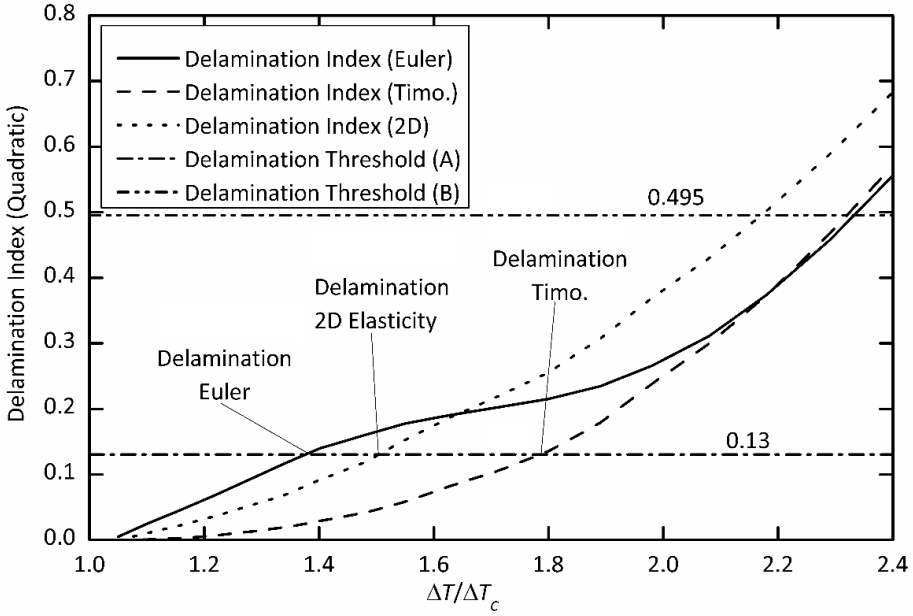

Figure 4-11: Crack propagation condition by various partition theories using quadratic criterion

4.2.4 Crack propagation stability

Eq. (4.28) and (4.29) are the linear and quadratic failure criterion respectively to calculate the interface delamination condition. At the instant where the condition of Eq. (4.28) or (4.29) is met, two scenarios of crack propagation occur: stable or unstable crack propagation. For the

stable crack propagation, the advance of the crack requires further loads input, either mechanical or thermal loading; for the unstable crack propagation, the crack propagation does not require further mechanical or thermal loads. Stable crack propagation can be controlled; however, the unstable crack propagation normally links with total failure of the structure if it is controlled.

Mathematically, these two scenarios can be expressed with Eq. (4.36).

$$\frac{\partial f}{\partial a} = \begin{cases} \geq 0 & \text{unstable} \\ \leq 0 & \text{stable} \end{cases} \tag{4.36}$$

The interface crack and stability of crack propagation are dependent on the mixed mode partition. In this section, the crack propagation stability is studied based on the mixed mode partition theory by Euler beam, Eq. (4.18) and (4.19), Timoshenko beam Eq. (4.20) and (4.21), and 2D elasticity Eq. (4.22) and (4.23); G_{IIC} is expressed as ψG_{IC}, the linear failure criterion, Eq. (4.28) is used and it is written as:

$$\psi G_I + G_{II} - \psi G_{IC} = 0 \tag{4.37}$$

Substituting G_I and G_{II} in Eq. (4.37) with these from Eq. (4.18) to (4.23), the interface crack and the stability equations are obtained as follows:

Using Euler Beam Partition:

$$G_{IE} = E_1 h_1 \sqrt{\varepsilon_c}\,\varepsilon_a \left(2\sqrt{\varepsilon_c} - \sqrt{3}\sqrt{\varepsilon_a}\right) \tag{4.2}$$

$$G_{IIE} = E_1 h_1 \varepsilon_a^{3/2} \left(\sqrt{3}\sqrt{\varepsilon_c} + 1/2\sqrt{\varepsilon_a}\right) \tag{4.3}$$

$$f(\varepsilon_c) = \psi E_1 h_1 \sqrt{\varepsilon_c}\,\varepsilon_a \left(2\sqrt{\varepsilon_c} - \sqrt{3}\sqrt{\varepsilon_a}\right) + E_1 h_1 \varepsilon_a^{3/2} \left(\sqrt{3}\sqrt{\varepsilon_c} + 1/2\sqrt{\varepsilon_a}\right) - \psi G_{IC} = 0 \tag{4.38}$$

Where $\varepsilon_a = (\varepsilon_0 - \varepsilon_c)$

$$\begin{aligned} f(\varepsilon_c) = {} & \psi E_1 h_1 \left(2\varepsilon_c(\varepsilon_0 - \varepsilon_c) - \sqrt{3}(\varepsilon_0 - \varepsilon_c)^{\frac{3}{2}} \sqrt{\varepsilon_c} \right) \\ & + E_1 h_1 \left(\sqrt{3}(\varepsilon_0 - \varepsilon_c)^{\frac{3}{2}} \sqrt{\varepsilon_c} + \frac{1}{2}(\varepsilon_0 - \varepsilon_c)^2 \right) - \psi G_{IC} = 0 \end{aligned} \tag{4.39}$$

It can be expressed as the function of crack length *a*

$$f(a)=\psi E_1 h_1\left(2\varepsilon_c(\varepsilon_0-\varepsilon_c)-\sqrt{3}(\varepsilon_0-\varepsilon_c)^{\frac{3}{2}}\sqrt{\varepsilon_c}\right)$$
$$+E_1 h_1\left(\sqrt{3}(\varepsilon_0-\varepsilon_c)^{\frac{3}{2}}\sqrt{\varepsilon_c}+\frac{1}{2}(\varepsilon_0-\varepsilon_c)^2\right)-\psi G_{IC}=0 \quad (4.40)$$

Where $\varepsilon_{cr}=\frac{\pi^2}{3}(\frac{h_1}{a})^2$ from Eq. (4.34).

Using Timoshenko Beam Partition:

$$f(\varepsilon_c)=\psi\frac{1}{8}E_1 h_1\varepsilon_a\left(2\sqrt{\varepsilon_c}-\sqrt{3}\sqrt{\varepsilon_a}\right)^2$$
$$+\frac{1}{8}E_1 h_1\varepsilon_a\left(2\sqrt{3}\sqrt{\varepsilon_c}+\sqrt{\varepsilon_a}\right)^2-\psi G_{IC} \quad (4.41)$$

$$f(a)=\psi\frac{1}{8}E_1 h_1\left(2\sqrt{(\varepsilon_0-\varepsilon_c)}\sqrt{\varepsilon_c}-\sqrt{3}(\varepsilon_0-\varepsilon_c)\right)^2$$
$$+\frac{1}{8}E_1 h_1\left(2\sqrt{3}\sqrt{(\varepsilon_0-\varepsilon_c)}\sqrt{\varepsilon_c}+(\varepsilon_0-\varepsilon_c)\right)^2-\psi G_{IC}=0 \quad (4.42)$$

Using 2D Elasticity Partition:

$$f(\varepsilon_c)=\psi 0.062888E_1 h_1\varepsilon_a\left(4.450\sqrt{\varepsilon_c}-\sqrt{3}\sqrt{\varepsilon_a}\right)^2$$
$$+0.103768^* E_1 h_1\varepsilon_a\left(2.697\sqrt{\varepsilon_c}+\sqrt{3}\sqrt{\varepsilon_a}\right)^2-\psi G_{IC}=0 \quad (4.43)$$

$$f(a)=\psi 0.062888E_1 h_1\left(4.450\sqrt{(\varepsilon_0-\varepsilon_c)}\sqrt{\varepsilon_c}-\sqrt{3}(\varepsilon_0-\varepsilon_c)\right)^2$$
$$+0.103768^* E_1 h_1\left(2.697\sqrt{(\varepsilon_0-\varepsilon_c)}\sqrt{\varepsilon_c}+\sqrt{3}^*(\varepsilon_0-\varepsilon_c)\right)^2-\psi G_{IC}=0 \quad (4.44)$$

Crack running in contact:

$$f(\varepsilon_c)=\frac{1}{2}E_1 h_1\varepsilon_a(4\varepsilon_c+\varepsilon_a)-\psi G_{IC}=0 \quad (4.45)$$

$$f(a)=\frac{1}{2}E_1 h_1(\varepsilon_0-\varepsilon_c)(3\varepsilon_c+\varepsilon_0)-\psi G_{IC}=0 \quad (4.46)$$

Equation (4.40), (4.42), (4.44) and (4.46) define the condition where the crack propagation starts; the first order derivative of the equation (4.40), (4.42), (4.44) and (4.46) defines the stability condition of interface delamination; however, the analytical solution of the first order derivatives of these equations are ineffective expressions for practice usage. Alternatively, numerical expression can be employed to show the stability condition of

interface delamination. It can be observed from the loading curve, if further mechanical or thermal loading is required to promote the incremental crack propagation Δa, the crack propagation is in a stable manner; if no further loading is required but the crack continue to advance with Δa, the crack propagation is unstable.

For the crack running in contact condition, mode II dominates the interface crack and it is replaced by total energy release rate. Therefore, Eq. (4.46) is applicable for all three partition theories for the crack running in contact.

To investigate the crack propagation stability, it requires the detail material data. An example of case study is provided in the next section with illustrations of stable and unstable crack propagation.

4.2.5 Case study

A case study is performed with the thermal barrier coating parameters as presented in Table 4-1. The TBC is simplified as a bilayer straight edge plate with top layer $20\,um$ and an infinite stiff substrate. The top layer $20\,um$ is so considered that the topcoat consists of effective $10\,um$ thickness from "strain tolerance" top layer and $10\,um$ dense layer. The TGO layer, bond coat and substrate are simplified as one rigid substrate. The width of TBC is assumed as 1.0 mm, the thermal expansion coefficient $\alpha_1 = 8.0^{-6}/°\text{C}$ and $\alpha_2 = 1.6^{-5}/°\text{C}$ are applied to the top layer and the substrate respectively. The mode I and II fracture toughness are assumed as 10N/m and 50N/m respectviely. The reference temperature is defined as 1300°C.

To assume the TBC material system as a bilayer system is a simplification as an initial step towards the development of mechanical model for predicting TBC life. It attempts to gain the basic trends to guide the experimental and numerical work in the future for TBC life model development.

Table 4-1: TBC configuration and material properties for case study

E_1 [MPa]	a_0 [mm]	h_1 [mm]	α_1 [1/°C]	α_2 [1/°C]	G_{IC} [N/m]	G_{IIC} [N/m]
50,000	0.5	0.02	8.0e-6	1.6e-5	10	50

The critical buckling strain ε_{cr} is calculated from the crack length a and the top layer thickness h_1 using equation (4.34) based on plane stress and both end clamped condition.

$$\varepsilon_{cr} = \frac{\pi^2}{3}(\frac{h_1}{a})^2 \tag{4.34}$$

The corresponding critical buckling temperature T_c can be calculated using ε_{cr} from (4.34) with Δα (difference of material thermal expansion coefficient between top layer α_1 and substrate α_2).

$$T_c = 1300°C - \Delta T_c = 1300°C - \frac{\varepsilon_{cr}}{\Delta T} \tag{4.46}$$

Where ΔT_c represents the temperature difference from reference temperature 1300°C to the critical buckling temperature T_c.

It is assumed that the strain energy of top layer is produced once the top layer starts to buckle. In other words, when the temperature decreases from stress free reference temperature 1300°C to the critical buckling temperature T_c, the top layer starts to buckle. The strain energy release rate accumulates with further reduced temperature until the crack propagation criterion is satisfied by mode I and mode II energy release rate. At this point, the crack starts to propagate.

In the case study, the thermal loading $\Delta T/ \Delta T_c$ ratio at the point where the propagation starts is shown in Figure 4-12: 1.28, 1,72 and 1.35 is predicted by Euler beam partition, Timoshenko beam partition and 2D elasticity partition theory respectively. The results are identical as those were calculated using normalised approach and linear failure criterion in Figure 4-10.

Figure 4-13 shows the energy release rate according to $\Delta T/ \Delta T_c$ ratio by using Euler beam, Timoshenko beam and 2D elasticity partition theories. The same results for the ratio of G_I to total G and the crack running in contact condition can be observed as those using normalised approach.

Figure 4-14 shows the temperature profiles, which are required to advance the crack versus the crack propagation length. The phase of stable and unstable crack propagation can be seen obviously. In the Figure 4-14 the solid line is the temperature profile predicted by Euler beam partition theory for the crack from initial length 0.5mm to 1.5mm. The crack propagation starts from point A, where the temperature is about 460°C, to A', this is a phase of unstable crack propagation, since the crack advances from 0.5mm to 0.57mm (A') has no further

temperature loading required. Temperature increase means the decrease of the thermal loading.

Similar unstable phases can be observed in Figure 4-14: from point B (T=167°C) to B' (crack length about 1.0mm) is predicted by Timoshenko partition theory; from point C (T=410°C) to C' (crack length about 0.7mm) is predicted by 2D elasticity partition theory.

Table 4-2 records the delamination propagation behaviour of case study presented in Figure 4-12 to Figure 4-14. The symbol f in Table 4-2 represents the propagation criterion in Eq. (3.49) introduced in chapter 3 with $f < 0$ indicating no propagation, $f = 0$ indicating stable propagation and $f > 0$ indicating unstable crack. The temperatures marked with bold text indicate the unstable crack propagation.

Table 4-2: Delamination propagation behaviour of case study

$\Delta T / \Delta T_c$	Euler				Timoshenko				2D Elasticity			
	T(°C)	a (mm)	f	G_{II}/G (%)	T(°C)	a (mm)	f	G_{II}/G (%)	T(°C)	a (mm)	f	G_{II}/G (%)
1.00	642	0.50	<0	-	642	0.50	<0	-	642	0.50	<0	-
1.05	612	0.50	<0	0.77	600	0.50	<0	0.15	606	0.50	<0	0.51
1.11	572	0.50	<0	0.70	570	0.50	<0	0.12	570	0.50	<0	0.46
1.26	472	0.50	<0	0.53	470	0.50	<0	0.07	474	0.50	<0	0.38
1.28	459	0.50	<0	0.51	445	0.50	<0	0.06	458	0.50	<0	0.37
1.35	**481**	0.52	>0	0.45	410	0.50	<0	0.05	410	0.50	<0	0.34
1.37	**485**	0.53	>0	0.44	400	0.50	<0	0.05	**415**	0.51	>0	0.33
1.44	**488**	0.54	>0	0.39	354	0.50	<0	0.04	**439**	0.53	>0	0.31
1.49	**490**	0.55	>0	0.35	322	0.50	<0	0.03	**450**	0.54	>0	0.29
1.68	**462**	0.57	>0	0.24	196	0.50	<0	0.02	**464**	0.58	>0	0.25
1.72	444	0.58	0	0.21	167	0.50	<0	0.01	**462**	0.58	>0	0.24
1.87	212	0.59	0	0.16	**182**	0.53	>0	0.01	**458**	0.61	>0	0.20
2.21	210	0.60	0	0.05	**201**	0.58	>0	0.01	**430**	0.64	>0	0.16
2.39	208	0.61	0	0	**208**	0.61	>0	0	400	0.67	0	0.15
3.23	**217**	0.70	>0	0	**217**	0.70	>0	0	340	0.75	0	0.09
4.26	205	0.80	0	0	**205**	0.80	>0	0	282	0.82	0	0.08
5.47	189	0.90	0	0	**189**	0.90	>0	0	212	0.91	0	0.01
6.84	174	0.99	0	0	**174**	0.99	>0	0	174	0.99	0	0
6.86	172	1.00	0	0	**172**	1.00	>0	0	172	1.00	0	0
8.41	157	1.10	0	0	157	1.10	0	0	157	1.10	0	0

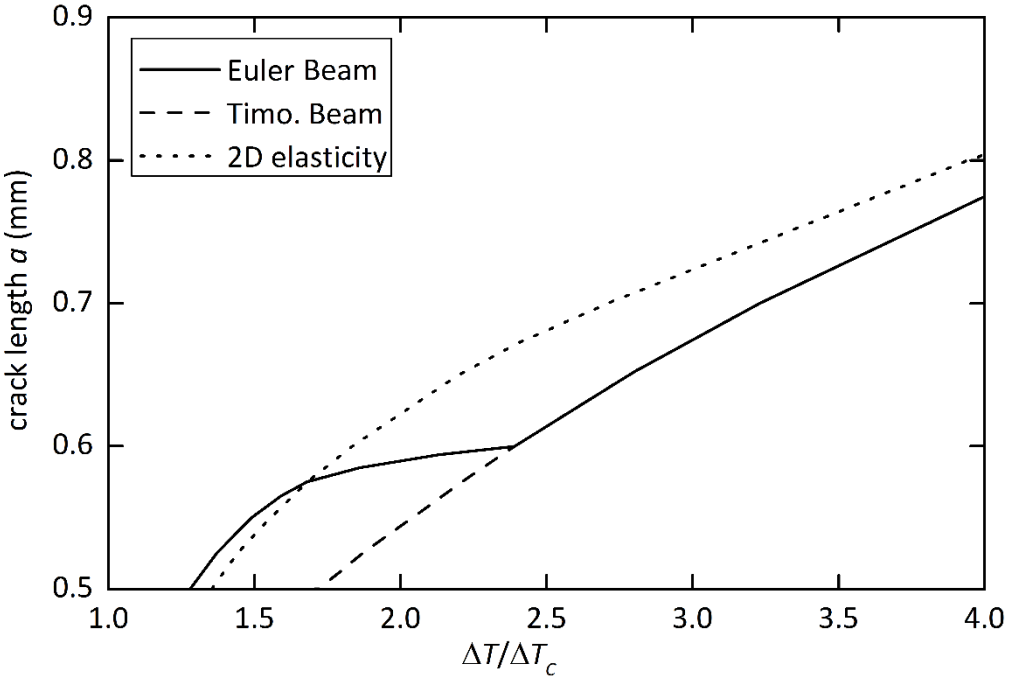

Figure 4-12: Delamination length vs. $\Delta T/ \Delta T_c$ thermal loading for case study

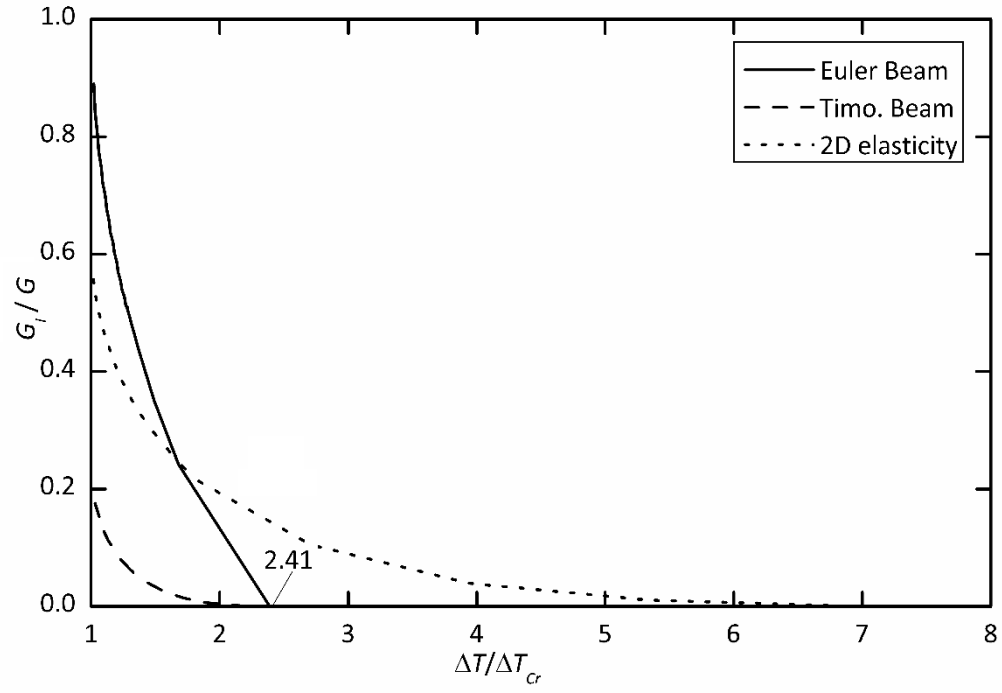

Figure 4-13: Mode I ERR mixity vs thermal loading $\Delta T/ \Delta T_c$ for case study

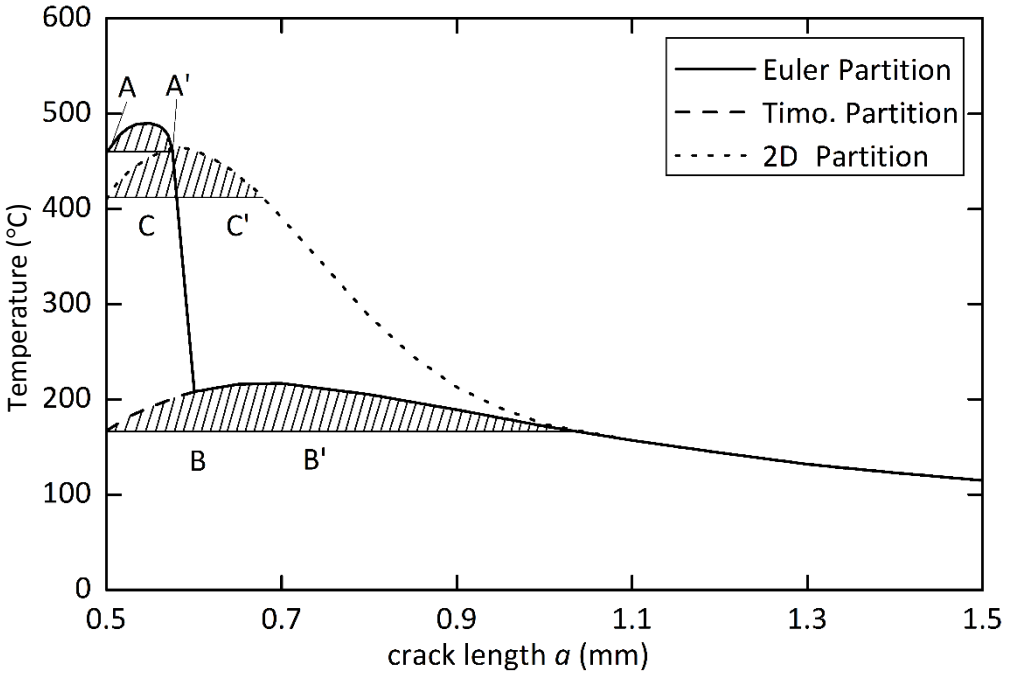

Figure 4-14: Temperature loading vs. stable and unstable delamination for case study

In summary, the results from the case study show the same trends as those predicted by analytical mechanical models for the top layer buckling and the TBC interface crack propagation; the stability trend of crack propagation is demonstrated in the case study by using Euler beam, Timoshenko beam and 2D elasticity partition theories. It can be concluded that the normalised analytical approach can be used for the further development of the TBC life model.

4.3 Conclusions

In this chapter, the buckling-driven delamination of thermal barrier coatings used in aero-engines is studied. The normalised analytical approaches are developed based on the Euler beam, Timoshenko beam and 2D elasticity partition theories to predict the trends of TBC interface crack delamination with minimum presence of detail TBC material data. Based on the normalised mixed mode partition and the linear or quadratic failure criterion, “delamination index” is developed using mode I and mode II interface fracture toughness to predict the interface crack propagation. Following conculsions can be obtained from the

study in this chapter: (1) The sequence of crack propagation is not only dependent on the mixed mode partition theories but also relates to the interface fracture toughness G_I and G_{II}. (2) An earlier crack propagation is predicted by using linear failure criterion rather than using quadratic failure criterion. (3) The crack propagation stability can be well illustrated by using the "T-a" curve (temperature loading "T" vs. crack propagation length "a" curve), to use numerical incremental crack length $a+\Delta a$ combining with graphic illustration is convinent to show crack propagation stability.

In the end of this chapter, the normalised approaches are verified by a case study with detailed material data; the results show a excellent correlation between case study and developed normalised approaches. The work in this chapter provides some clear trends with minimum presence of real material data and it is particularly useful to develop the life prediction model for TBC material system with numerical method and experimental tests, which are planned in the future.

Chapter 5 Local delamination driven by pockets of energy concentration

5.1 Introduction

As presented in chapter 4, the TGO layer of thermal barrier coating contains the main relevant mechanisms controlling the TBC failure. To study the failure of TGO layer is a key step towards the development of TBC life model. In chapter 4, a normalised approach is introduced to simplify the TBC as a bilayer material system; the general trends are obtained by using various mixed mode partition theories. In this chapter the spallation failure of α-Al_2O_3 oxide film is studied based on new developed Pockets of Energy Concentration (PEC) hypothesis, it attempts to explore the mechanisms of TBC spallation, which is controlled by TGO layer.

A commercial heat-resistant Kanthal alloy forms a protective film of α-Al_2O_3 oxide which may spall from the alloy surface under certain conditions. The thin film separation or spallation was observed after cooling in the room temperature, but not during the time of heating and cooling [123]. The observations of a thin film delamination and spalling at room temperature are presented by V. K. Tolpygo and D. R. Clarke [123]. During the cooling process, residual compressive stress in α-Al_2O_3 oxide films on the surface of Fe-Cr-Al Kanthal A-1 heat-resisting alloy gradually increases due to material thermal expansion mismatch. It is expected that the buckling and spalling of the oxide layer occur when the compressive stress reaches to a critical level. However, the observations contradict this understanding: the failure occurs by spontaneous buckling and spalling at room temperature under a constant residual stress in the film. The extent of buckling and spalling does not decrease by reducing the residual stress in the film. In addition, the experiment shows that spalling (and buckling) occurs only at the intermediate cooling rates (5–200°C min^{-1}). The oxide exhibits failure after cooling at intermediate rates but remains intact after cooling at either higher or lower rates [123]. In addition, the extent of buckling and spalling depends on the thickness of the substrate.

This unique failure of thin film is described as spontaneous spalling, it is well investigated by V.K. Tolpygo, D.R. Clarke [123,124]. The works [123,124] contain the investigation of failure mechanisms and development of analytical model to describe it. The measurements of the residual stress in the alumina films for different cooling rates and metal thickness are

carried out, the aim of their tests is to establish the driving force for spallation and also to characterise the extent of any stress relaxation that occurs during the cooling.

A commercial heat-resistant alloy annealed in vacuum at 1100°C for 25h was used in the test. The specimen was cut into rectangular plates (12×12 mm^2) of different thickness. Four groups of specimens with the same oxidation thickness h_{ox} = 4.9±0.1 um but different substrate thickness 0.53, 1.05, 2.00, and 2.65 mm were tested. After isothermal oxidation, each specimen was cooled to room temperature at a constant rate, while several cooling rates in the range 2 – 1000°C min^{-1} were used. The residual stress in alumina scales was evaluated based on the stress-induced frequency shift of the Cr^{3+} photoluminescence [170,171]. Residual stress was measured in the adequate selected location in order to attain biaxial stress state, σ_{xx} and σ_{yy} .

Two major conclusions were received from the phenomenon observed from the tests:

- The general trend for each group of specimens is a significant decrease of the residual stress with decreasing the cooling rate.
- At any given rate, the stress is smaller on thinner specimens.

In their experimental studies, it is realised that the stress relaxation during the cooling rate reduces the residual stress. Stress relaxation can be caused by metal creep, oxide creep or both, it occurs both in the metal and oxide. The extent of stress relaxation strongly depends on the cooling rate. This is an important observation to understand the problem.

Since fast cooling is assumed to have only little relaxation, the residual stresses attained after cooling at the highest rate (500 or 1000°C min^{-1}) are equal to the maximum stress σ_{ox}^{*}, corresponds to a purely thermo-elastic behaviour of the metal and oxide. The maximum stress σ_{ox}^{*} represents a sum of the stress existing in the scale during oxidation (the growth stress, $(\sigma_{ox})_G$, and the thermal-mismatch stress induced by cooling, $(\sigma_{ox})_T$. However, as for the lower cooling rate and thinner substrate, the residual stress is smaller than σ_{ox}^{*}, and the difference $\Delta\sigma = \sigma_{ox}^{*} - \sigma_{ox}$, indicates the extent of stress in the oxide relieved during cooling due to relaxation. The symbol σ_{ox} indicates the residual stress corresponding to the certain cooling rate.

The existing models of spalling of compressive stressed films is based on classic buckling principle that spalling takes place when the compressive stress in the thin film exceeds the critical level. However, the results presented in the literature [123,124] show a much complex effect. It is also found that the amount of spalled oxide has a clear correlation with the metal thickness: it is larger on thinner specimens and smaller on thicker ones which is contrary to expectation.

Various hypotheses were thoroughly and insightfully examined in the work [123,124]. The first category of them is the flaw or imperfection hypothesis [127,128] aiming to explain the nucleation and growth of the separations. The flaw includes pre-existing separations, cavities and other defects, pre-existing inclusions such as Z_r - containing oxide, impurity segregations at the oxide-metal interface due to slow cooling rates. However, optical microscopy studies showed that no any interfacial separations or spallation exist in all the specimens when examined immediately after cooling to the room temperature. When examining the exposed metal surface after spallation there is no any interfacial cavities or voids except for areas near sharp edges at the periphery of the specimens. The size of Z_r –rich oxide particles contained in the films is largely in the same range of the film thickness which is unable to provide interface flaws capable of resulting in film buckling. In fact, these Z_r –rich oxide particles often resist the propagation of separations resulting in a great majority of stable separations. It is usually expected that some impurities, such as sulphur, carbon, phosphorous for instance, may segregate at the interface due to the gradual decrease of solubility of the metal during non-fast cooling. However, an investigation of the interface segregation show little difference between slow and fast cooling. Therefore, the first category of hypotheses is invalidated.

The second category is the stress corrosion hypothesis due to moisture [129] aiming to explain the time dependent growth behaviour of these separations. To have a convincing invalidation of this hypothesis, some specimens after slow cooling were placed in a sealed container in a purified nitrogen atmosphere with zero humidity. The spallation was still as prevalent as during the regular exposure in the ambient atmosphere [123].

Since the cooling rates govern the separation and spallation behaviour, a third category of hypothesis is that the metal plastic strain during cooling is the key factor governing the spallation as it is directly related to the cooling rates. However, carefully designed experiments showed that the metal plastic strain during cooling is not sufficient to cause spallation of the film [123].

In addition, several other hypotheses were also considered, such as condensation of equilibrium thermal vacancies at the interface during cooling, diffusion of hydrogen or carbon monoxide from the metal to the film causing disruption to the film at room temperature, metal embrittlement or hardening near the interface. However, the work [123], states that none of these hypotheses is consistent with all the experimental results.

A more recent study [130] on the same topic presents some contradictory observations. The major one is that the impurity segregation at the film metal interface is a key factor on the separation and spallation of the film.

In order to attain a satisfactory explanation for these observations, several possible reasons are discussed by V.K. Tolpygo, D.R. Clarke [123,124], such as slow cooling, impurity segregation, moisture induced, and so on. However, none of these hypotheses is consistent with all the experimental results. Although the correlation is not yet clear, the present work insists that the amount of spalled oxide is mainly associated with the extent of stress relation during cooling, and influenced by some other factors, which remain to be established.

Similar study on alumina scale thin film spontaneous spalling as that conducted by V. K. Tolpygo and D. R. Clarke [123] was carried out by Xiao Ping and his research group [130]. In their study the experiment works were performed on the substrate thickness range from 0.477 to 7.608 mm and cooling rate from 1°C min^{-1} to 100°C min^{-1}. They confirmed that the spalling occurs at intermediate cooling rate and no spalling takes place at high cooling rate. Meanwhile, the grain size of Fecralloy decreases with increase in cooling rate. However, contrary to what found by V. K. Tolpygo and D. R. Clarke, the amount of spallation on the alumina scale increases with the substrate thicknesses. They think the different results may be caused from the use of different alloys.

In their experimental research, it is found that the interface toughness falls within a small range for the samples with the same cooling rate and different substrate thicknesses. This indicates that the bonding between alumina scale and Fecralloy substrate is affected by the cooling rate but not by the thickness of substrate. This is also proved by their estimated calculations.

Further, the chromium carbide layer thickness increased with decrease of cooling rate and the extent of segregation is of the same level for the samples with different thicknesses. Therefore, it is inferred by the authors that the interfacial chromium carbide segregation effect may weaken the bonding and is crucial for alumina scale adherence.

Through this research, they finally draw a conclusion that the combination of residual stresses, grain size change and the Cr-carbide segregation together controls the spallation.

In Tolpygo and Clarke's second work [124], the experimental tests are performed with varied oxide film thicknesses and residual stresses in the oxide film. The residual stress in the alumina scale, after oxidation at 1200°C, is systematically varied between −2.8 and −5.5 GPa, by appropriate choice of the oxidation time, metal–oxide thickness ratio and cooling rate. They attempt to study the development of interface separation and establish a relation between residual stress and spalling behaviour.

By the experiment, it was observed that the separation growth will lead to spallation. The residual stress is lower in the separated region, and its minimum typically corresponds to the centre of separation. However, the stable separation does not produce spalls because the propagation of interface cracks was arrested for some reasons and the separation size was still smaller than the calculated critical size d_b for buckling diameter. Buckling of the oxide layer occurs if initial separations of diameter larger than d_b exist at the oxide–metal interface. However, according to what they observed from the test results, the actual buckling diameter is smaller than using d_b predicted. They explained this as not all the separations eventually spall and some of them remain stable indefinitely at a size smaller than the calculated critical buckling diameter.

In the work done by the Tolpygo and Clarke's [124], an analytical approach to determine the spall diameter, d_s and the height H of the spherical arc of film buckling deflection are developed. However, despite of many efforts have been given by Tolpygo and Clarke and the good results have been obtained; the phenomenon of α-Al_2O_3 oxide spontaneous spalling hasn't been fully explained; in addition, the current finite element method is not able to solve this kind of problems due to lack of the knowledge on the failure mechanism and the driving force for the spallation; therefore, the further studies and new analytical approaches on this subject are necessary.

5.2 Hypotheses of pockets of energy concentration (PEC)

A hypotheses is made in this section that pockets of energy concentration (PEC) can be formed by pockets of tensile stress and shear stress, with the former being dominant [123,124], around the interface between a thin film and a thick substrate because of thermal effects, chemical effects and etc. Based on the PEC hypothesis, three mechanical models are developed analytically to predict some aspects of the process of thin film spallation failure including nucleation, stable and unstable growth, the size of spallation and final kinking off. Spallation with both straight edge and circular edge are considered. The classical plate model is established based on classical plate mixed mode partition theory while the shear deformable plate and 2D elasticity models are established based on the first order shear deformable plate and 2D elasticity mixed mode partition theories.

Experimental results in the next section show that all three of the models predict the initiation of unstable growth and the size of spallation very well; however, only the 2D elasticity-based model predicts final kinking off well. The energy for the nucleation and stable growth of a separation bubble comes solely from the PEC energy on and around the interface, which is 'consumed' by the bubble as it nucleates and grows. Unstable growth, however, is driven both by PEC energy and by buckling of the separation bubble. Final kinking off is controlled by the fracture toughness of the interface at the film and the maximum energy stored in the separation bubble. This work will be particularly useful for the study of spallation failure in thermal barrier coating material systems planned in the future.

In the studies on buckling driven delamination, it is conventional to assume either an existing interface crack larger than the critical buckling characteristic dimension or an existing imperfection [127,128]. However, some cases of thin film delamination [123,124] show no any evidence of existing interface cracks or imperfection, but still with buckling behaviour. The work conducted by V. K. Tolpygo, D. R. Clarke in 1999 and 2000 presented a series of experimental studies on room temperature circular spallation of α - alumina films grown by oxidation on Fe-Cr-Al alloy with very impressive observations which contradicts the classic buckling and interface crack mechanisms.

In the work [123,124], the Al_2O_3 oxide films of different thicknesses were firstly formed on the surface of Fe-Cr-Al heat-resisting alloy substrates of different thickness at 1200°C with different heating hours. Then, the film substrate material systems were cooled down to room

temperature with different cooling rates. Interestingly, no spallation failure was observed during cooling at any cooling rates when the compressive residual stress gradually increases due to thermal expansion mismatch. Surprisingly, however, for slow cooling rates (5-200°C min^{-1}), it was observed that circular separations of films nucleate, grow in height and propagate in radius at room temperature with constant compressive residual stress, this compressive residual stress is far below the critical buckling stress. After a period of slow and stable growth, some separations grow abruptly and spall off. Most intriguingly, for extremely slow cooling rates ($\leq 2° \min^{-1}$) and very fast cooling rates ($\geq 500° \min^{-1}$), no separation and spallation were observed.

In the case of fast cooling, nearly no plastic or creep relaxation occurs in both oxide and metal due to cooling and the mechanical process is purely thermo-elastic [123]. It might be reasonable to expect that this process result in uniform biaxial in plane compressive stress in the film and no interfacial stress apart from the areas near the edges of the specimens. Therefore, there are no PECs formed in the film metal material system even though the film has the largest residual stress.

In contrast, nearly complete plastic or creep relaxation occurs in both the film and the metal during extremely slow cooling. The 'complete' here means that a fully plastic relaxation is achieved at any temperature during cooling. That is, any slower cooling rates will produce the same plastic relaxation history with respect to cooling temperature. Thus, it might be also reasonable to expect that the slow cooling rate result in uniform biaxial in plane compressive stress in the film and no interfacial stress apart from the areas near the edges of the specimens. Therefore, there are no PECs formed in the film metal material system with the film having the smallest residual stress.

Now, it becomes clear that the intermediate cooling rates are unable to produce converged plastic relaxation. The present study makes the hypothesis that the non-converged plastic relaxation results in pockets of tensile stress and shear stress at the interface and its neighbour materials while still producing uniform in-plane residual stress in the film. The pockets of tensile stress and shear stress results in PECs. These PECs cause interface separation nucleation, growth and spallation of the film. When this process is regarded as the continuation of the non-converged plastic relaxation, the time dependence of the process is apparent. However, it is not considered in this work. The present work focuses on the development of an analytical mechanical model based on the PECs hypothesis to predict the

separation behaviour including nucleation, stable and unstable growth, and final spallation and kinking off.

It is necessary to have a brief introduction to the experimental procedure recorded from the work [123,124]. A commercial heat-resistant alloy Kanthal A-l with nominal composition Fe -21.2%C_r5.6%Al (wt. %) was used in the experimental tests. The alloy was annealed in vacuum at 1100^{o}C for 25 hours and cut into rectangular plates (12 x 12 mm^2) of different thickness (0.53, 1.05, 2.00 and 2.65 mm thick). After polishing to 3 um finish and cleaning in acetone, all the specimens were oxidized at 1200^{o}C in ambient air for times ranging from 0.5 to 100 hours to give different oxide thickness ranging from 0.5 to 8.0 um. After the isotheral oxidation, each specimen was cooled to room temperature at a constant rate. Several cooling rates in the range 2-1000^{o}C/min were used. The nucleation, growth and spallation of the α- alumina film separations from the Fe-Cr-Al alloy substrate at constant room temperature and constant residual stress were monitored using different experimental techniques. Figure 5-1 shows a general view of a specimen after α- alumina spallation at room temperature, the spalled regions of the alumina scale, exposing bare metal surface, appear bright against the darker intact oxide. The randomly distributed white spots are the spallation sites. It can be observed that they all are nearly circular and have nearly the same size. The thicknesses of alumina and the alloy of the specimen shown in Figure 5-1 are 4.9 mm and 1.05 mm, respectively. The oxidation time of this specimen is 25 hour at 1200^{o}C in ambient air. Six cooling rates are shown. When cooling rate is below 2^{o}C min^{-1} there is no any spallation observed as converged plastic relaxation is achieved at any temperature during cooling resulting in no PECs. When cooling rate is above 500^{o}C/min there is no any spallation observed either as the cooling process is purely thermo-elastic resulting in no PECs.

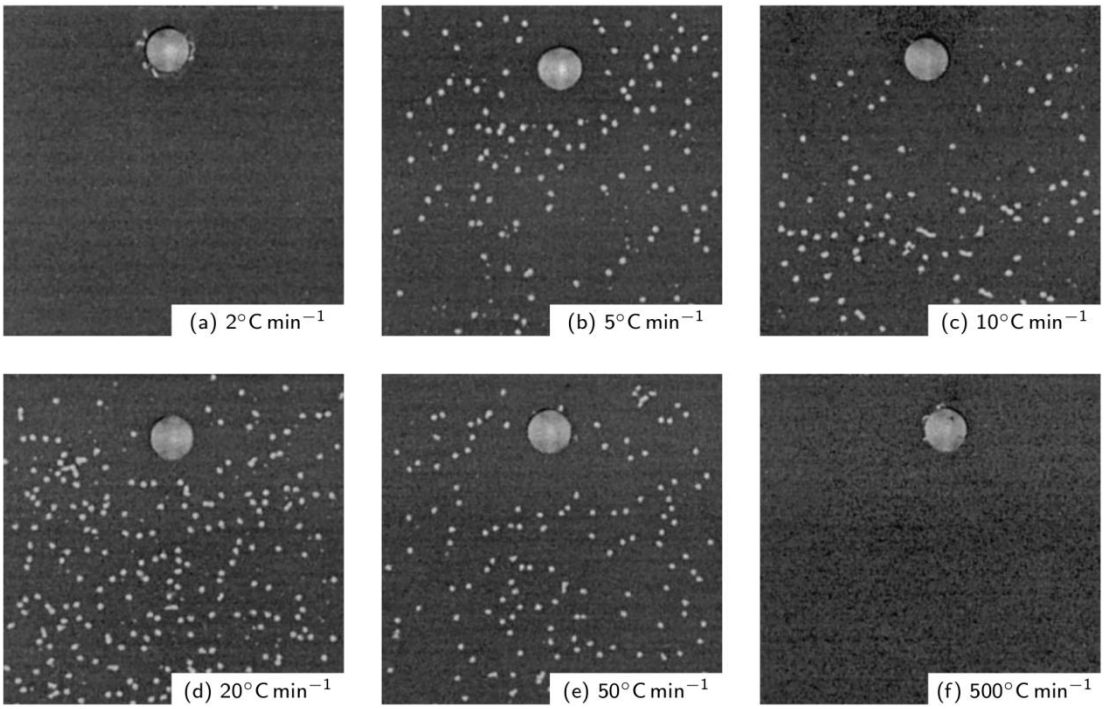

Figure 5-1: View of a group of 1.05-mm thick Kanthal samples after 25-h oxidation at 1200°C cooled to room temperature [123].

Figure 5-2 shows the sequence of optical images illustrating the nucleation, growth and spallation of one typical separation from another specimen where the thickness of the oxide scale is about $4.9\,um$ and the residual stress is 4.3 GPa. Figure 5-2 (a)-(e) show the nucleation, stable growth stages which took 22 minutes. The time values were counted from when the specimen was just reached room temperature from cooling. In Figure 5-2 (a)-(d) the radius of the nearly circular separation are far below the critical value for buckling. In the work [124], it is called incipient buckle. Here, it is conveniently called separation bubble as its radius is far too small to cause buckling, particular in Figure 5-2 (a)-(c). The abrupt growth starts at Figure 5-2 (e) and spallation failure occurs at Figure 5-2 (f) only taking just 1 minute. The following work aims to develop a mechanical model analytically to explain some aspects of the above observations.

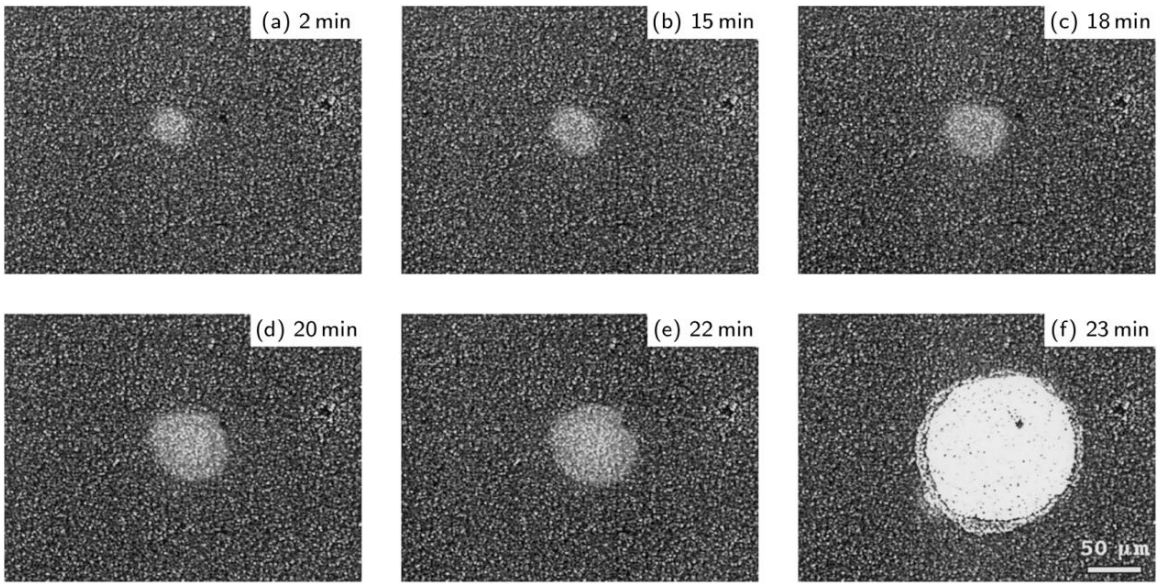

Figure 5-2: The sequence of the nucleation and growth of a bubble with time at room temperature [124].

5.3 Analytical model for delamination with straight edges

In this section, a mechanical model is developed analytically with straight edges based on the PECs hypothesis to explain several aspects of thin-film spalling including the nucleation, stable and unstable growth, size of spallation and final kinking off. Figure 5-3 shows a rectangular thin film substrate composite material system with a through the width *b* interface delamination of length $2R_B$. The delamination tip or the edge of the bubble are donated by the label "B". The thickness of the film *h* is assumed so small that only the in-plane residual stresses are induced before delamination. The thickness of the substrate is so large that it has little global deformation such as bending, extension and twisting due to the residual stresses in the film. Both film and substrate materials are assumed to be homogeneous and isotropic. The film material has Young's modulus *E* and Poisson's ratio ν. In general, a uniaxial uniform residual stress $\sigma_x = \sigma_0, \sigma_y = 0, \tau_{xy} = 0$ will be achieved when the width of the film is less than two times the thickness for a long film strip. Therefore, a plane stress model is suitable for this case. On the other hand, a biaxial uniform residual stress $\sigma_x = \sigma_0, \sigma_y = \sigma_0, \tau_{xy} = 0$ is achieved when both the width and length of the film are larger than twenty times the thickness [5,7], and a plane strain model is suitable for this case. Since the development for both models are essentially the same with the Young's modulus *E* in

plane stress model changing to be $\bar{E} = E/(1-\nu^2)$ in plane strain model. In the following development, a uniaxial uniform residual stress $\sigma_x = \sigma_0, \sigma_y = 0, \tau_{xy} = 0$ state is used.

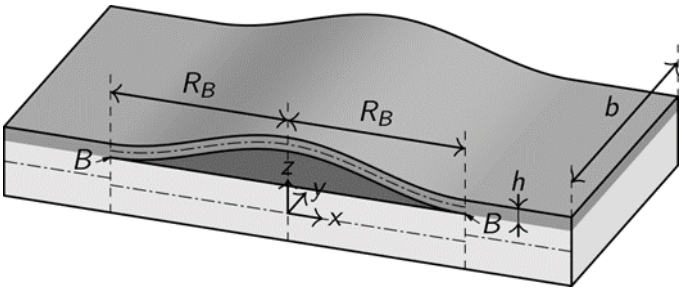

Figure 5-3: A delamination bubble with straight edges

5.3.1 Nucleation of a delamination bubble, PEC and ERR

According to the PECs hypothesis, the nucleation of PEC-driven delamination is caused by pockets of tensile stress and shear stress, with the former being dominant [123,124], on and around the interface. The details are unclear and not considered in present work. Once a delamination is nucleated, the strain energy of the tensile stress is liberated and becomes the bottom surface energy of the delamination, the surface energy of the alloy substrate underneath the bubble, and part of the strain energy in the delaminated bubble. Note that "delamination bubble" is used here to differentiate it from "delamination buckle" as the length of the bubble $2R_B$ at this stage is far shorter than the critical buckling length. In order to calculate the strain energy in the bubble, its shape is approximated to be sinusoidal and represented by Eq. (5.1).

$$w(x) = \frac{A}{2}\left[1 + \cos\left(\frac{\pi x}{R_B}\right)\right] \tag{5.1}$$

With w representing the upward deflection and A being the amplitude. Clamped edge condition at $x = \pm R_B$ is assumed as the thickness ratio between the film and the substrate is very small in the present study. The elastic bending strain energy can be readily calculated using classical beam theory as Eq. (5.2).

$$U_b = \frac{1}{2} b \int_{-R_B}^{R_B} \frac{\bar{E} h^3}{12} \left(\frac{d^2 V}{dx^2}\right)^2 dx = \frac{\pi^2}{6} \bar{E} R_B h b \left(\frac{h}{R_B}\right)^2 \left(\frac{\pi}{4}\frac{A}{R_B}\right)^2 \tag{5.2}$$

Where $\overline{E} = E$ for plane stress condition and $\overline{E} = E/(1-\nu^2)$ for plane strain condition. The elastic in-plane strain energy is calculated using Hooke's law as

$$U_i = 2R_B bh\left[u_0 - \sigma_0 \varepsilon_x^R + \frac{\overline{E}}{2}\left(\varepsilon_x^R\right)^2\right] \tag{5.3}$$

and where u_0 in Eq. (5.3) is the residual strain energy density in the film given by

$$u_0 = \begin{cases} \dfrac{1}{2E}\sigma_0^2 & \text{for uniaxial - residual - stress} \\ \dfrac{1-\nu}{E}\sigma_0^2 & \text{for biaxial - residual - stress} \end{cases} \tag{5.4}$$

As mentioned earlier, plane stress and plane strain models are suitable for uniaxial and biaxial stress cases respectively. The averaged axial relaxation strain in the bubble is calculated by using the conventional von Kármán geometric nonlinearity assumption.

$$\varepsilon_x^R = \frac{1}{2R_B}\int_0^{R_B}\left(\frac{dV}{dx}\right)^2 dx = \left(\frac{\pi}{4}\frac{A}{R_B}\right)^2 \tag{5.5}$$

The averaged axial relaxation stress is then given by

$$\sigma_x^R = \overline{E}\,\varepsilon_x^R = \overline{E}\left(\frac{\pi}{4}\frac{A}{R_B}\right)^2 \tag{5.6}$$

For brittle materials, the the surface energy is

$$U_s = b\int_{-R_B}^{R_B} G_c(x)dx = 2R_B b\overline{G_c} \tag{5.7}$$

Where $G_c(x)$ is the interface fracture toughness which is position dependent as crack tip loading conditions vary with propagation. The $\overline{G_c}$ is the averaged fracture toughness over the delaminated surface. Note that when $A/h \ll 1$, $G_c(x)$ is constant as shown later. This is the case considered in the present study. Collecting U_b , U_i , U_s together gives

$$U = U_0 + U_a \tag{5.8}$$

where $U_0 = 2R_B bhu_0$ is the strain energy only before any separation, and U_a is

$$U_a = 2R_B bh\sigma_0\left\{\frac{1}{2\bar{\varepsilon}_0}\left(\varepsilon_r^R\right)^2 + \left[\frac{\pi^2}{12\bar{\varepsilon}_0}\left(\frac{h}{R_B}\right)^2 - 1\right]\varepsilon_r^R + \frac{1}{\overline{\varphi}_0}\right\} \tag{5.9}$$

U_0 is the mechanical energy containing strain energy only before separation and U_a is the additional increase in mechanical energy after separation with $\bar{\varepsilon}_0 = \sigma_0 / \bar{E}$ and $\bar{\varphi}_0 = h\sigma_0 / \bar{G}$. It can be shown that U_a is always positive and monotonically increase with respect to the relaxation strain ε_r^R or the bubble amplitude A when $(R_B / h)^2 < \pi^2 / (12\bar{\varepsilon}_0)$. It is seen, therefore, that a separation bubble represents another type of PEC. Its energy comes from the PEC energy 'consumed' by the bubble as it nucleates and grows. Although there is a close relationship between U_a and the PEC energy, there are some differences between them. Here, U_a is called 'bubble energy'. When the PEC energy is able to provide the bubble energy U_a for nucleation, nucleation of a separation bubble will occur. It is expected that the bubble energy U_a governs the growth behavior of a bubble. According to this understanding, the described bubble separation behavior is an effect of positive bubble energy; therefore, this work only considers $U_a \geq 0$. Obviously, when the bubble energy disappears, then $U_a = 0$, a bubble will stop growing. Details about U_a are given during the following development, for bubble nucleation, stable growth, unstable growth, spallation and kinking off.

After nucleation, the delamination bubble bends away from the substrate. That is, it grows in height and produces the driving force for axial growth, i.e. the energy release rate (ERR) at the bubble edge. When ERR exceeds the interface fracture toughness the bubble length grows. From the work [14,152], the total ERR G is given as

$$G = \frac{6}{\bar{E}h^3}\left(M_{xB}^2 + \frac{h^2}{12} N_{xBe}^2 \right) \tag{5.10}$$

Where M_{xB} and N_{xBe} are crack tip longitudinal bending moment and effective axial force per unit width respectively. They can be readily calculated in terms of ε_x^R by using classical beam theory as

$$M_{xB} = \frac{\bar{E}h^3}{12}\left(\frac{d^2 w}{dx^2} \right)_{x=R_B} = \frac{2\bar{E}h^3}{3A}\left(\frac{\pi}{4}\frac{A}{R_B} \right)^2 = \frac{2\bar{E}h^3}{3A}\varepsilon_x^R \tag{5.11}$$

$$N_{rBe} = \left[\sigma_0 - \left(\sigma_0 - \sigma_x^R \right) \right] h = \bar{E}h\left(\frac{\pi}{4}\frac{A}{R_B} \right)^2 = \bar{E}h\varepsilon_x^R \tag{5.12}$$

Substituting M_{xB} from Eq. (5.11) and N_{xBe} from Eq. (5.12) into Eq. (5.10) gives

$$G = \frac{6M_{xB}^2}{\bar{E}h^3}\left(1+\frac{3}{16}\left(\frac{A}{h}\right)^2\right) \tag{5.13}$$

It is well known that the mixed-mode interface fracture toughness is mode mixity dependent which varies with different partition theories [14]. Extensive experimental tests [15-17,20-23,30,152] have shown that the partition theory based on Euler beam or classical plate theory [28-29] gives very accurate predictions of interface fracture toughness for macroscopic mixed-mode fracture while the partition theories based on Timoshenko beam theory [28-29] or the first order shear deformable plate theory and 2D elasticity [14] give poor predictions. However, for the delamination behavior of micro-scale and nano-scale thin films it is still uncertain which partiton theory gives accurate predictions. This work therefore aims to develop three analytical models to predict the PEC-driven spallation behavior of thin films and to examine their respective performances. The three mechanical models are established based on these three partition theories: Euler beam or classical plate partition theory, Timoshenko beam or first-order shear-deformable plate partition theory, and 2D elasticity partition theory.

After the total ERR G in Eq. (5.13) is partitioned into mode I ERR G_I and Mode ERR II G_{II}, a failure criterion is used to check if the delamination grows or not. In general a growth criterion can be expressed in the form

$$f\left(G_I, G_{II}, G_{Ic}, G_{IIc}\right) = 0 \tag{5.14}$$

Where G_{Ic} and G_{IIc} are the respective critical mode I and II ERRs. The form of Eq. (5.14) is not unique but is crack interface-dependent and is determined from experimental testing for a given interface. Many previous studies such as the work [22,23,152] have shown that the following linear propagation criterion [68] agrees with experimental results very well for brittle interfaces:

$$\frac{G_I}{G_{Ic}} + \frac{G_{II}}{G_{IIc}} = \frac{1}{G_{Ic}}\left(G_I + \frac{G_{II}}{\psi}\right) = 1 \tag{5.15}$$

Where $G_{IIc} = \psi G_{Ic}$ is assumed with a factor ψ. For the sake of comparison all the three partition theories mentioned above will be used in the following developments.

5.3.2 Mechanical model based on Euler beam

5.3.2.1 Stable growth of the delamination bubble driven by PEC energy

Based on Euler beam theory or classical plate theory [28,29] the mode I and II ERRs for brittle interfacial fracture are given as

$$G_{IE} = \frac{6M_{xB}^2}{\bar{E}h^3}\left(1-\frac{3}{4}\frac{A}{h}\right), G_{IIE} = G - G_{IE} \tag{5.16}$$

where the subscript E denotes Euler beam or classical plate partition theory. By substituting the ERRs from Eq. (5.16) into Eq. (5.15), the propagation criterion becomes

$$\left(\frac{A}{h}\right)^2\left[1-\left(1-\frac{1}{\psi}\right)\frac{3}{4}\frac{A}{h}+\frac{3}{16\psi}\left(\frac{A}{h}\right)^2\right] = \frac{96\bar{\varepsilon}_0}{\pi^4\varphi_{0E}}\left(\frac{R_B}{h}\right)^4 \tag{5.17}$$

Where $\varphi_{0E} = h\sigma_0/G_{cE}$. Note that, consistent with the notation described above, G_{cE} is the film-substrate mode-dependent interface fracture toughness G_c based on Euler beam partition theory. It is seen from Eqs. (5.13) and (5.16) that when $A/h << 1$ then $G_I/G \approx 1$, that is, the delamination is pure mode I. Therefore, $G_{cE} = G_{Ic}$ and $\varphi_{0E} = h\sigma_0/G_{Ic}$. The amplitude for crack growth is therefore obtained from Eq. (5.17) as

$$\left(\frac{A}{h}\right)_{GRE}^2 = \frac{96\bar{\varepsilon}_0}{\pi^4\varphi_{0E}}\left(\frac{R_B}{h}\right)^4 \tag{5.18}$$

With the subscript GR denoting growth. Substituting Eq. (5.18) into Eqs. (5.5,5.6) gives the relaxation strain and stress

$$\left(\varepsilon_x^R\right)_{GRE} = \frac{6\bar{\varepsilon}_0}{\pi^2\varphi_{0E}}\left(\frac{R_B}{h}\right)^2 \tag{5.19}$$

$$\left(\sigma_x^R\right)_{GRE} = \frac{6G_{cE}}{\pi^2 h}\left(\frac{R_B}{h}\right)^2 \tag{5.20}$$

Note that these three quantities, i.e. $(A/h)_{GRE}, (\varepsilon_x^R)_{GRE}, (\sigma_x^R)_{GRE}$ are independent of the residual stress σ_0. The bubble energy U_a at growth can be obtained by substituting Eq. (5.19) into Eq. (5.9)

$$\left(U_a\right)_{GRE} = 2R_B b G_{cE}\left\{\frac{3}{2}+\frac{6\bar{\varepsilon}_0}{\pi^2}\left(\frac{R_B}{h}\right)^2\left[\frac{3}{\pi^2\varphi_{0E}}\left(\frac{R_B}{h}\right)^2-1\right]\right\} \tag{5.21}$$

The first term in Eq. (5.21) is the sum of the bending strain energy and surface energy while the rest is the relaxed in-plane strain energy negligible if small R_B due to the high powers of R_B in these terms. Therefore, the first term is then regarded as the nucleation energy or the PEC energy required for nucleation. That is, $(U_a)_{NUE} = 3R_B b G_{cE}$ where R_B is very small. It is seen that a third of the nucleation PEC energy is used to bend the delamination outwards after nucleating the interface delamination using two thirds of its energy. When the PEC energy is able to provide the energy $(U_a)_{GRE}$ the delamination bubble nucleates and grows. Two scenarios could occur. One is a slow and stable growth when R_B is smaller than the critical buckling characteristic length. The other is unstable growth when R_B approaches to the critical buckling characteristic length. The stable bubble becomes an unstable buckle. The initiation of unstable growth is considered next.

5.3.2.2 Initiation of unstable growth by buckling

With the slow and stable growth, the in-plane compressive stress $\sigma_0 - \sigma_x^R$ reduces in the bubble with increase in its length R_B. At a certain point the following buckling condition is met.

$$\sigma_0 - \sigma_r^R = \bar{\bar{E}} \frac{(\alpha\pi)^2}{12} \left(\frac{h}{R_B} \right)^2 \tag{5.22}$$

Where α is a correction factor as the buckling occurs at the existence of the amplitude A which can be treated as an initial imperfection. Alternatively, it is treated as an effect of boundary conditions in the present work. That is, the range of values is $0.5 \le \alpha \le 1.0$ with the two limits corresponding to simply supported and clamped edge conditions, respectively. A good approximation can be the average of the extreme values, i.e. $\alpha = 0.75$ which is used in the present study. By using Eq. (5.20) and (5.22), the initiation of unstable growth is found at

$$\left(\frac{R_B}{h} \right)^2_{UGE} = \frac{\pi^2 \varphi_{0E}}{12} \left[1 - \left(1 - \frac{\alpha^2}{\Omega_E} \right)^{1/2} \right] \tag{5.23}$$

with the subscript UG denoting the initiation of unstable growth and

$$\Omega_E = \frac{1}{2}\bar{\varepsilon}_0\varphi_{0E} = \frac{h\sigma_0^2}{2\bar{E}G_{cE}} \tag{5.24}$$

Also, note that there is no unstable growth when $\Omega_E < \alpha^2$. Binomial expansion of the expression in the square bracket in Eq. (5.23) if $\Omega_E >> \alpha^2$, Eq. (5.23) becomes

$$\left(\frac{R_B}{h}\right)^2_{UGE} = \frac{(\alpha\pi)^2}{12\bar{\varepsilon}_0} \tag{5.25}$$

Substituting Eq. (5.25) into Eqs. (5.18), (5.19) and (5.20), and use of Eq. (5.24) where appropriate, results in Eqs. (5.26), (5.27) and (5.28), respectively.

$$\left(\frac{A}{h}\right)^2_{UGE} = \frac{\alpha^4}{3\Omega_E} \tag{5.26}$$

$$\left(\varepsilon_x^R\right)_{UGE} = \frac{\alpha^2}{2\varphi_{E0}} \tag{5.27}$$

$$\left(\sigma_x^R\right)_{UGE} = \frac{\alpha^2\bar{E}}{2\varphi_{0E}} = \frac{\alpha^2 G_{cE}\bar{E}}{2h\sigma_0} = \frac{\alpha^2\sigma_0}{4\Omega_E} \tag{5.28}$$

The bubble energy at the initiation of unstable growth is obtained by substituting Eq. (5.25) into Eq. (5.21) and using Eq. (5.24).

$$(U_a)_{UGE} = 2R_B bG_{cE}\left(\frac{3-\alpha^2}{2} + \frac{\alpha^4}{16\Omega_E}\right) \approx \left(3-\alpha^2\right)R_B bG_{cE} = \frac{(3-\alpha^2)\alpha\pi bhG_{cE}}{2\sqrt{3\bar{\varepsilon}_0}} \tag{5.29}$$

5.3.2.3. Unstable growth and spallation driven by buckling and bubble energy

The developments in the section are generally approximate due to neglect of the dynamic effect from the abrupt unstable growth and the effect of large amplitude *A*. Some more detailed discussions on this will be given later in this section and in the section of experimental verification. Since the bubble U_a plays a key role in the growth of the separation, the variation of the bubble energy at growth $(U_a)_{GR}$ in Eq. (5.25) is considered first. By differentiating $(U_a)_{GR}$ in Eq. (5.21) with respect to (R_B/h), its maximum occurs at

$$\left(\frac{R_B}{h}\right)^2_{MUE} = \frac{\pi^2\varphi_{0E}}{10}\left[1-\left(1-\frac{5}{6\Omega_E}\right)^{1/2}\right] \tag{5.30}$$

with the subscript *MU* denoting the maximum $(U_a)_{GRE}$. Note that when $\Omega_E < 5/6$ there is no solution. Binomial expansion of the expression in the square bracket in Eq. (5.30) for $\Omega_E >> 5/6$ leads to

$$\left(\frac{R_B}{h}\right)^2_{MUE} = \frac{\pi^2}{12\bar{\varepsilon}_0} \tag{5.31}$$

Substituting Eq. (5.31) into Eqs. (5.18), (5.19) and (5.20), and use of Eq. (5.24) where appropriate, results in Eqs. (5.32), (5.33) and (5.34), respectively.

$$\left(\frac{A}{h}\right)^2_{MUE} = \frac{1}{3\Omega_E} \tag{5.32}$$

$$\left(\varepsilon_x^R\right)_{MUE} = \frac{1}{2\varphi_{0E}} \tag{5.33}$$

$$\left(\sigma_x^R\right)_{UME} = \frac{\bar{E}}{2\varphi_{0E}} = \frac{G_{cE}\bar{E}}{2h\sigma_0} = \frac{\sigma_0}{4\Omega_E} \tag{5.34}$$

Note that $(R_B/h)_{MUE}$ in Eq. (5.31) is equal to $(R_B/h)_{UGE}$ in Eq. (5.25) with $\alpha = 1.0$ for a clamped edge condition. Substituting Eq. (5.31) into Eq. (5.21) gives the bubble energy as

$$(U_a)_{MUE} = 2R_B bG_{cE}\left(1 + \frac{1}{16\Omega_E}\right) \approx 2R_B bG_{cE} = \frac{\pi bhG_{cE}}{\sqrt{3\bar{\varepsilon}_0}} \tag{5.35}$$

More importantly, the $(U_a)_{GRE}$ becomes to be zero at

$$\left(\frac{R_B}{h}\right)^2_{SPE} = \frac{\pi^2\varphi_{0E}}{6}\left\{1 - \left[1 - \frac{3}{2\Omega_E}\right]^{1/2}\right\} \tag{5.36}$$

Note that when $\Omega_E < 3/2$ there is no solution. Binomial expansion of the expression in the square bracket in Eq. (5.40) for $\Omega_E < 3/2$ leads to

$$\left(\frac{R_B}{h}\right)^2_{SPE} = \frac{\pi^2}{4\bar{\varepsilon}_0} \tag{5.37}$$

Substituting Eq. (5.37) into Eqs. (5.18), (5.19) and (5.20), and use of Eq. (5.24) where appropriate, results in Eqs. (5.38), (5.39) and (5.40), respectively.

$$\left(\frac{A}{h}\right)^2_{SPE} = \frac{3}{\Omega_E} \tag{5.38}$$

$$\left(\varepsilon_x^R\right)_{SPE} = \frac{3}{2\varphi_{0E}} \tag{5.39}$$

$$\left(\sigma_x^R\right)_{SPE} = \frac{3\overline{E}}{2\varphi_{0E}} = \frac{3G_{cE}\overline{E}}{2h\sigma_0} = \frac{3\sigma_0}{4\Omega_E} \tag{5.40}$$

At this moment it is reasonable to expect that the unstable growth stops as there is no driving energy. However, if the kinetic energy in the buckle is large enough to break the film at its edge, the buckle spalls. The subscript SP in above equations denotes spallation.

A sketch of the variation of $\left(U_a\right)_{GRE}$ in Eq. (5.21) is now given in Figure 5-4. Note that the sketch of the variation of $\left(U_a\right)_{GRE}$ for a delamination with a circular edge is based on Eq. (5.75) and the analysis in section 5.3.3. The bubble energy $\left(U_a\right)_{GRE}$, given by Eq. (5.21), increases with growth up to $\left(R_B\right)_{MUE}$, given by Eq. (5.30) and approximately by Eq. (5.31). This increase comes from the PEC. Because of the increasing nature of the bubble energy $\left(U_a\right)_{GRE}$ in this region, the growth is expected to be generally slow and steady, even in the first range of unstable growth, that is, in the range $\left(R_B\right)_{UGE} \le R_B \le \left(R_B\right)_{MUE}$. Unstable growth starts at $\left(R_B\right)_{UGE}$, given by Eq. (5.23) and approximately by Eq. (5.25). In the first region of unstable growth, the bubble length grows by a factor of about $1/\alpha = 1.333$, and the amplitude by a factor of about $1/\alpha^2 = 1.778$. When the PEC is too weak to provide the bubble energy, the bubble will stop growing, even in the first unstable growth range.

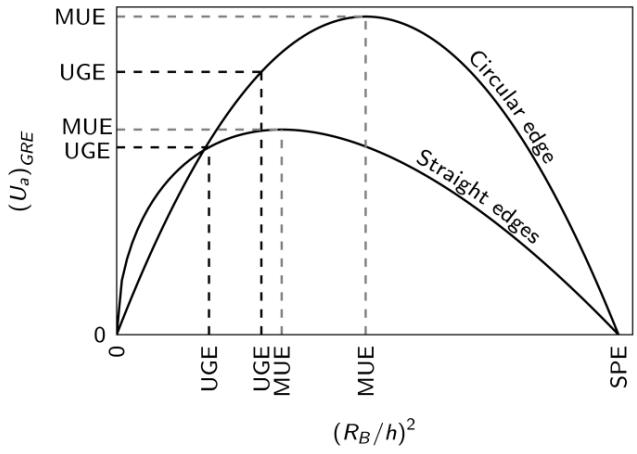

Figure 5-4: Sketch of the variation of $\left(U_a\right)_{GRE}$ with respect to $\left(R_B/h\right)^2$ for a delamination with straight edges and a circular edge.

The bubble energy $(U_a)_{GRE}$ decreases with growth after $(R_B)_{MUE}$ and reduces to zero at $(R_B)_{SPE}$, given by Eq. (5.36) and approximately by Eq. (5.37). This decreasing nature has two meanings. The first is that the bubble is no longer able to store any further bubble energy from the PEC. The second is that the bubble energy $(U_a)_{GRE}$, cumulated in the range $0 \le R_B \le (R_B)_{MUE}$, is being transformed into kinetic energy. This is consistent with the fact that the bifurcation-type buckling occurs at around $(R_B)_{MUE}$, resulting in more 'violent' growth after $(R_B)_{MUE}$. In this second region of unstable growth, that is, in the range $(R_B)_{MUE} \le R_B \le (R_B)_{SPE}$, the bubble length grows by a factor of about 1.732, and the amplitude by a factor of about 3. Obviously, the bubble will stop growth at $(R_B)_{SPE}$ as the bubble energy becomes zero. The minimum kinetic energy can be estimated as $(U_a)_{MUE}$ in Eq. (5.35) by assuming that the PEC boundary ends at $(R_B)_{MUE}$ resulting in no contribution to the kinetic energy. When $(U_a)_{GRE}$ is large enough to break the film, then spallation occurs, that is, the interface crack kinks into the film. The kink-off angle β is measured from the interface as shown in Figure 5-5.

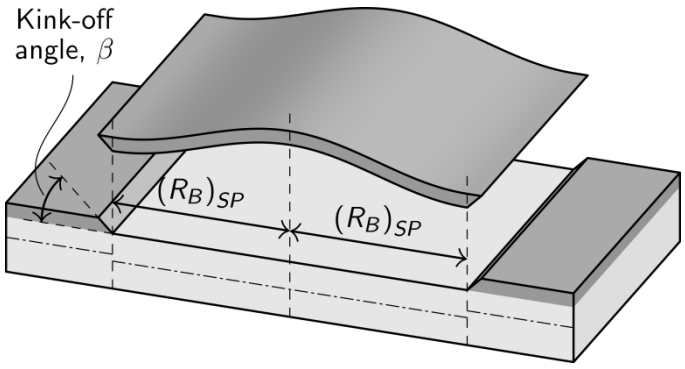

Figure 5-5: The kink-off angle of a straight-edged film spallation.

The kink-off angle can be determined using

$$(U_a)_{MUE} = 2(R_B)_{MUE} b G_{cE} = \frac{2bh}{\sin(\beta)} G_{cf} \tag{5.41}$$

where G_{cf} is the fracture toughness of the film material, which is generally different to the fracture toughness of the film-substrate interface G_{cE}. Note that the left-hand side of Eq. (5.41) comes from Eq. (5.35) and the right-hand side is the breaking surface energy of the

oxide film as shown in Figure 5-5. The kink-off angle is then obtained from Eq. (5.41) as follows, after substituting $(R_B)_{MUE}$ and $(R_B)_{SPE}$ from Eqs. (5.31) and (5.37) respectively:

$$\beta_E = \arcsin\left(\frac{2\sqrt{3\bar{\varepsilon}_0}}{\pi}\frac{G_{cf}}{G_{cE}}\right) \tag{5.41b}$$

5.3.3 Mechanical model based on Timoshenko beam

Since the development in this section follows closely with that in section 5.3.2 only several key equations are recorded here. Based on Timoshenko beam theory or first order shear deformable plate theory [28,29] the mode I ERR is given as

$$G_{IT} = \frac{6M_{xB}^2}{4\bar{E}h^3}\left(1-\frac{3}{4}\frac{A}{h}\right)^2,\ G_{IIT} = G - G_{IT} \tag{5.42}$$

where the subscript T denotes Timoshenko beam or shear deformable plate partition theory. It is seen from Eq. (5.13) and (5.42) that when $A/h \ll 1$, G_I/G approaches to 0.25, a mode II dominated mixed mode. Therefore, the total critical ERR G_{cT} is found by using Eqs. (5.13), (5.15) and (5.42).

$$G_{cT} = \frac{4\psi}{3+\psi}G_{Ic} = \lambda_T G_{Ic} = \lambda_T G_{cE} \tag{5.43}$$

$$\lambda_T = \frac{4\psi}{3+\psi} \tag{5.44}$$

Thus, this gives

$$\varphi_{0T} = \frac{h\sigma_0}{G_{cT}} = \frac{\varphi_{0E}}{\lambda_T},\ \Omega_T = \frac{1}{2}\bar{\varepsilon}_0\varphi_{0T} = \frac{\Omega_E}{\lambda_T} \tag{5.45}$$

The mechanical model can be readily obtained by replacing G_{cE}, φ_{0E} and Ω_E in the mechanical model based on Euler beam or classical plate partition theories using G_{cT}, φ_{0T} and Ω_T, respectively. Since the critical ERR ratio ψ is usually larger than one, G_{cT} is then larger than G_{cE} while φ_{0T} and Ω_T are smaller than φ_{0E} and Ω_E, respectively. These differences result in larger values for A/h, ε_x^R and σ_x^R. However, it is interesting to note that when Ω_T is still large enough, the values of R_B/h at the initiation of unstable growth, the maximum of PEC power and final spallation are the same as those in the mechanical model based on Euler beam or classical plate partition theory.

5.3.4 Mechanical model based on 2D elastic partition theory

Similarly, based on 2D elasticity partition theory [14,78,126,150] the mode I ERR is given as

$$G_{I2D} = 0.6227\frac{6M_{xB}^2}{\bar{E}h^3}\left(1-\frac{30}{89}\frac{A}{h}\right)^2,\ G_{II2D} = G - G_{I2D} \tag{5.46}$$

where the subscript 2D denotes 2D elasticity partition theory. It is seen from Eq. (5.13) and (5.46) that when $A/h \ll 1$, G_I/G approaches to 0.6227, a mixed mode. Therefore, the total critical ERR G_{2Dc} is found by using Eqs. (5.13), (5.15) and (5.46).

$$G_{c2D} = \frac{\psi}{0.3773+0.6227\psi}G_{Ic} = \lambda_{2D}G_{Ic} = \lambda_{2D}G_{cE} \tag{5.47}$$

$$\lambda_{2D} = \frac{\psi}{0.3773+0.6227\psi} \tag{5.48}$$

Thus, this gives

$$\varphi_{02D} = \frac{h\sigma_0}{G_{c2D}} = \frac{\varphi_{0E}}{\lambda_{2D}},\ \Omega_{2D} = \frac{1}{2}\bar{\varepsilon}_0\varphi_{02D} = \frac{\Omega_E}{\lambda_{2D}} \tag{5.49}$$

The mechanical model can be readily obtained by replacing G_{cE}, φ_{0E} and Ω_E in the mechanical model based on Euler beam or classical plate partition theories using G_{c2D}, φ_{02D} and Ω_{2D}, respectively.

Again, G_{c2D} is then larger than G_{cE} while φ_{02D} and Ω_{2D} are smaller than φ_{0E} and Ω_E, respectively resulting in larger values for A/h, ε_x^R and σ_x^R. Similarly, if Ω_{2D} is still large enough, the values of R_B/h at the initiation of unstable growth, the maximum of PEC power and final spallation are the same as those in the mechanical model based on Euler beam or classical plate partition theory.

5.4 Analytical mechanical model for delamination with circular edges

The mechanical development in this section closely follows that in section 5.3 for delamination with straight edges. Only the key development are recorded here. Figure 5-6 shows circular separation bubble of radius R_B. The delamination tips or the edge of the bubble are denoted by the label 'B'. The model is developed in a polar coordinate system.

Biaxial compressive residual stress is assumed (i.e. $\sigma_r = \sigma_\theta = \sigma_0$) so the model is effectively plane strain with $\overline{E} = E/\left(1-\nu^2\right)$.

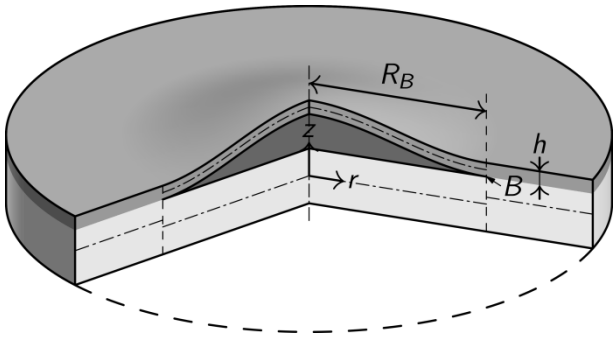

Figure 5-6: A delamination bubble with circular edge.

5.4.1. Nucleation of a delamination bubble, PEC and ERR

In order to calculate the strain energy in the bubble, its shape is approximated to be axisymmetric and represented by

$$w(r) = \frac{A}{2}\left[1+\cos\left(\frac{\pi r}{R_B}\right)\right] \tag{5.50}$$

with w representing the upward deflection and A being the amplitude. Clamped edge condition at $r = R_B$ is assumed as the thickness ratio between the oxide film and the alloy substrate is very small. Using linear elastic plate theory, the bending moments in the bubble are calculated as [25]

$$M_r = \frac{Eh^3}{12(1-\nu^2)}\left(\frac{d^2w}{dr^2}+\frac{\nu}{r}\frac{dw}{dr}\right) \tag{5.51}$$

$$M_\theta = \frac{Eh^3}{12(1-\nu^2)}\left(\frac{1}{r}\frac{dw}{dr}+\nu\frac{d^2w}{dr^2}\right) \tag{5.52}$$

The subscripts r, θ represent the polar coordinates in the radius and circumference direction, respectively. E, ν are Young's modulus and Poisson's ratio of the oxide film, respectively. The bending strain energy is calculated as

$$U_b = \frac{12\pi}{Eh^3}\int_0^{R_B}\left(M_r^2 - 2\nu M_r M_\theta + M_\theta^2\right) r\,dr \tag{5.53}$$

with subscript b representing bending. The four equations above gives

$$U_b = \frac{\pi^3}{12}\bar{E}h^3\left(\frac{\pi}{4}\frac{A}{R_B}\right)^2 = \frac{\pi^3}{12}\bar{E}h^3\varepsilon_r^R \tag{5.54}$$

and

$$\varepsilon_r^R = \left(\frac{\pi}{4}\frac{A}{R_B}\right)^2 \tag{5.55}$$

Where $\bar{E} = E/(1-\nu^2)$ and ε_r^R is the elastic radius relaxation strain due to the upward deflection by using the conventional Von-Karman geometrical nonlinearity assumption. That is,

$$\varepsilon_x^R = \frac{1}{2R_B}\int_0^{R_B}\left(\frac{dw}{dr}\right)^2 dr = \left(\frac{\pi}{4}\frac{A}{R_B}\right)^2,\ \varepsilon_\theta^R = 0 \tag{5.56}$$

The superscript R represents relaxation. The relaxation stresses in the oxide film are then easily obtained as

$$\sigma_r^R = \bar{E}\varepsilon_r^R,\ \sigma_\theta^R = \upsilon\bar{E}\varepsilon_r^R \tag{5.57}$$

The in-plane strain energy in the film is now calculated.

$$\begin{aligned} U_i &= \frac{\pi R_B^2 h}{2}\left[\left(\sigma_0 - \sigma_r^R\right)\left(\varepsilon_0 - \varepsilon_r^R\right) + \left(\sigma_0 - \sigma_\theta^R\right)\left(\varepsilon_0 - \varepsilon_\theta^R\right)\right] \\ &= \pi R_B^2 h\left[\frac{1-\nu}{E}\sigma_0^2 - \sigma_0\varepsilon_r^R + \frac{\bar{E}}{2}\left(\varepsilon_r^R\right)^2\right] \end{aligned} \tag{5.58}$$

where σ_0, ε_0 are the biaxial compressive residual stress and strain in the original non-detached film, respectively. The sum of the bottom surface energy of the bubble and the surface energy of the alloy substrate underneath the bubble is calculated as

$$U_s = 2\pi\int_0^{R_B} G_c(r)rdr = \pi R_B^2\overline{G_c} \tag{5.59}$$

Where $G_c(r)$ is the interface fracture toughness which is position dependent as fracture mode mixity at crack tip may vary due to varying loading conditions at crack tip with propagation. The $\overline{G_c}$ is the averaged fracture toughness over the separated surface. Note that when $A/h \ll 1$, $G_c(x)$ is constant. Collecting U_b, U_i, U_s together gives

$$U = U_0 + U_a \tag{5.60}$$

with

$$U_0 = \pi R_B^2 h \frac{1-\upsilon}{E} \sigma_0^2 \tag{5.61}$$

$$U_a = \pi R_B^2 h \sigma_0 \left\{ \frac{1}{2\bar{\varepsilon}_0} \left(\varepsilon_r^R\right)^2 + \left[\frac{\pi^2}{12\bar{\varepsilon}_0} \left(\frac{h}{R_B} \right)^2 - 1 \right] \varepsilon_r^R + \frac{1}{\bar{\varphi}_0} \right\} \tag{5.62}$$

U_0 is the mechanical energy containing strain energy only before separation and U_a is the additional increase in mechanical energy after separation with the $\bar{\varepsilon}_0 = \sigma_0 / \bar{E}$ and $\bar{\varphi}_0 = h\sigma_0 / \bar{G}_c$. It can be shown that U_a is always positive and monotonically increase with respect to the relaxation strain ε_r^R or the bubble amplitude A when $\left(R_B / h\right)^2 < \pi^2 / 12\bar{\varepsilon}_0$. Therefore, it is seen that the separation bubble represents a PEC arising from the tensile stress at the interface and its neighbouring area. Hence, U_a is termed as the PEC energy and $U_a / (\pi R_B^2)$, i.e. the PEC energy per unit interface area, is termed as PEC intensity. When the PEC energy is big enough, nucleation of a separation bubble will occur.

Note the similarity between the bubble energy in Eq. (5.9) for a straight-edged bubble and in Eq. (5.62) for a circular-edged bubble. The equations for total ERR are identical to those in Eqs. (5.10) to (5.13), except with the x-coordinate swapped for the r-coordinate. The linear failure criterion in Eq. (5.15) is used again. The following development is based on 2D elasticity partition theory [14,78,126]. The mechanical models based on classic plate theory and the first-order shear-deformable plate and the 2D elasticity partition theories can be readily obtained by using the same parameter replacements as for the straight-edged case, as described in sections 5.3.

5.4.2. Stable growth of a separation bubble driven by PEC energy

The separation bubble bends away from the alloy substrate after nucleation. That is, it grows in height and produces the driving force for radius growth, i.e. the energy release rate (ERR) at the bubble edge. When ERR exceeds the interface fracture toughness the radius grows. From the work [14,152], the total ERR G is given as

$$G = \frac{6}{\bar{E}h^3} \left(M_{rB}^2 + \frac{h^2}{12} N_{rBe}^2 \right) \tag{5.63}$$

Where M_{rB} and N_{rBe} are the crack tip radial bending moment and effective radial force, respectively. They can be readily calculated as

$$M_{rB} = \frac{\bar{E}h^3}{12}\left(\frac{d^2w}{dr^2}\right)_{r=R_B} = \frac{2\bar{E}h^3}{3A}\left(\frac{\pi}{4}\frac{A}{R_B}\right)^2 = \frac{2\bar{E}h^3}{3A}\varepsilon_r^R \tag{5.64}$$

$$N_{rBe} = \left[\sigma_0 - \left(\sigma_0 - \sigma_r^R\right)\right]_{r=R_B} h = 0 \tag{5.65}$$

Substituting M_{rB} from Eq. (5.64) and N_{rBe} from Eq. (5.65) into Eq. (5.63) gives

$$G = \frac{6M_{rB}^2}{\bar{E}h^3}\left(1+\frac{3}{16}\left(\frac{A}{h}\right)^2\right) \tag{5.66}$$

Eq. (5.65) results from the fact mentioned earlier that measurements of residual stress in the work [124] show approximately zero relaxation stress at the crack tip. It is well known that interface fracture toughness is mode mixity-dependent and varies with different partition theories. For delamination with circular edges the development of mechanical model based on 2D elasticity mixed mode partition theory is explained in detail, the mechanical models based on classic plate theory and first-order shear-deformable plate partition theory can be readily obtained.

The ERR partitions based on 2D elasticity theory are therefore given by

$$G_I = 0.6227\frac{6M_{rB}^2}{\bar{E}h^3} \tag{5.67}$$

$$G_{II} = 0.3773\frac{6M_{rB}^2}{\bar{E}h^3} \tag{5.68}$$

Many previous studies have shown that the following linear propagation criterion generally agrees very well with experimental results for brittle interfaces

$$\frac{G_I}{G_{Ic}} + \frac{G_{II}}{G_{IIc}} = \frac{1}{G_{Ic}}\left(G_I + \frac{G_{II}}{\psi}\right) = 1 \tag{5.69}$$

where $G_{IIc} = \psi G_{Ic}$, and G_{Ic} and G_{IIc} are the pure mode I and II critical ERRs. Substituting the partitions in Eqs. (5.67) and (5.68) into Eq. (5.69) gives the following fracture toughness.

$$G_c = \frac{\psi}{0.3773 + 0.6227\psi}G_{Ic} = \lambda G_{Ic} \tag{5.70}$$

where

$$\lambda = \frac{\psi}{0.3773 + 0.6227\psi} \tag{5.71}$$

Obviously, the fracture toughness is constant due to the constant mode mixity. Eqs. (5.64) and (5.67)–(5.70) together give the amplitude for crack growth as

$$\left(\frac{A}{h}\right)^2_{GR} = \frac{96\bar{\varepsilon}_0}{\pi^4\varphi_0}\left(\frac{R_B}{h}\right)^4 \tag{5.72}$$

where $\varphi_0 = h\sigma_0/G_c$ and the subscript GR denotes crack growth. Substituting Eq. (5.72) into Eqs. (5.56) and (5.57) gives the average relaxation strain and stress as

$$\left(\varepsilon_r^R\right)_{GR} = \frac{6\bar{\varepsilon}_0}{\pi^2\varphi_0}\left(\frac{R_B}{h}\right)^2 \tag{5.73}$$

$$\left(\sigma_r^R\right)_{GR} = \frac{6G_c}{\pi^2 h}\left(\frac{R_B}{h}\right)^2 \tag{5.74}$$

Note that these three quantities, $\left(A/h\right)_{GR}$, $\left(\varepsilon_r^R\right)_{GR}$ and $\left(\sigma_r^R\right)_{GR}$, are independent of the biaxial residual stress σ_0. The bubble energy U_a at crack growth can be obtained by substituting Eq. (5.73) into Eq. (5.62).

$$\left(U_a\right)_{GR} = \pi R_B^2 G_c\left\{\frac{3}{2} + \frac{6\bar{\varepsilon}_0}{\pi^2}\left(\frac{R_B}{h}\right)^2\left[\frac{3}{\pi^2\varphi_0}\left(\frac{R_B}{h}\right)^2 - 1\right]\right\} \tag{5.75}$$

The first term in Eq. (5.75) is the sum of the bending strain energy and surface energy while the rest is the relaxed in-plane strain energy, which is negligible if R_B is small. The first term is therefore regarded as the nucleation energy, that is, $\left(U_a\right)_{NU} = 1.5\pi R_B^2 G_c$ where R_B is very small. It is seen that one third of the nucleation energy is used to bend the separation outwards after nucleating the interface separation using two thirds of its energy.

5.4.3 Initiation of unstable growth by buckling

During slow and stable growth, the in-plane compressive stress in the bubble $\sigma_0 - \sigma_r^R$ reduces as its radius R_B increases. At a certain point the following buckling condition is met.

$$\sigma_0 - \sigma_r^R = \bar{E}\frac{(\alpha\pi)^2}{12}\left(\frac{h}{R_B}\right)^2 \tag{5.76}$$

where α is a correction factor and it can be considered an effect of boundary conditions. The range of α is $0.652 \le \alpha \le 1.220$ with the two limits corresponding to simply-supported and clamped edge conditions respectively. A good approximation may be the average of the extreme values, that is, $\alpha = 0.936$. This value is used in the present study. By using Eqs. (5.74) and (5.76), the initiation of unstable growth is found at

$$\left(\frac{R_B}{h}\right)_{UG}^2 = \frac{\pi^2\varphi_0}{12}\left[1-\left(1-\frac{\alpha^2}{\Omega}\right)^{1/2}\right] \tag{5.77}$$

with the subscript *UG* denoting the initiation of unstable growth and where

$$\Omega = \frac{1}{2}\bar{\varepsilon}_0\varphi_0 = \frac{h\sigma_0^{\,2}}{2\bar{E}G_c} \tag{5.78}$$

There is no unstable growth when $\Omega < \alpha^2$. When $\Omega >> \alpha^2$, Eq. (5.77) becomes

$$\left(\frac{R_B}{h}\right)_{UG}^2 = \frac{(\alpha\pi)^2}{12\bar{\varepsilon}_0} \tag{5.79}$$

and

$$\left(\frac{A}{h}\right)_{UG}^2 = \frac{\alpha^4}{3\Omega} \tag{5.80}$$

$$\left(\varepsilon_r^R\right)_{UG} = \frac{\alpha^2}{2\varphi_0} \tag{5.81}$$

$$\left(\sigma_r^R\right)_{UG} = \frac{\alpha^2\bar{E}}{2\varphi_0} = \frac{\alpha^2 G_c\bar{E}}{2h\sigma_0} = \frac{\alpha^2\sigma_0}{4\Omega} \tag{5.82}$$

The bubble energy at the onset of unstable growth is obtained by substituting Eq. (5.79) into Eq. (5.75).

$$\left(U_a\right)_{UG} = \pi R_B^2 G_c\left(\frac{3-\alpha^2}{2}+\frac{\alpha^4}{16\Omega}\right) \approx \frac{3-\alpha^2}{2}\pi R_B^2 G_c \approx \frac{\left(3-\alpha^2\right)\alpha^2\pi^3 h^2 G_c}{24\bar{\varepsilon}_0} \tag{5.83}$$

5.4.4 Unstable growth and spallation driven by buckling and PEC energy

Since the bubble energy U_a governs the growth behaviour of the separation, the variation of bubble energy at growth $(U_a)_{GR}$ in Eq. (5.75) is considered. Its maximum occurs at

$$\left(\frac{R_B}{h}\right)^2_{MU} = \frac{\pi^2\varphi_0}{9}\left[1-\left(1-\frac{9}{8\Omega}\right)^{1/2}\right] \tag{5.84}$$

with the subscript MU denoting the maximum $(U_a)_{GR}$. When $\Omega < 9/8$ there is no solution. When $\Omega >> 9/8$, Eq. (5.84) becomes

$$\left(\frac{R_B}{h}\right)^2_{MU} = \frac{\pi^2}{8\bar{\varepsilon}_0} \tag{5.85}$$

and

$$\left(\frac{A}{h}\right)^2_{MU} = \frac{3}{4\Omega} \tag{5.86}$$

$$\left(\varepsilon_r^R\right)_{MU} = \frac{3}{4\bar{\varphi}_0} \tag{5.87}$$

$$\left(\sigma_r^R\right)_{MU} = \frac{3\bar{E}}{4\varphi_0} = \frac{3G_c\bar{E}}{4h\sigma_0} = \frac{3\sigma_0}{8\Omega} \tag{5.88}$$

Note that $(R_B)_{MU}$ in Eq. (5.85) is equal to $(R_B)_{UG}$ in Eq. (5.79) with $\alpha = 1.220$ for a circular buckle with a clamped edge condition. Substituting Eq. (5.85) into Eq. (5.75) gives the bubble energy as

$$(U_a)_{MU} = \pi R_B^2 G_c\left(\frac{3}{4}+\frac{9}{64\Omega}\right) \approx \frac{3}{4}\pi R_B^2 G_c = \frac{3\pi^3 h^2 G_c}{32\bar{\varepsilon}_0} \tag{5.89}$$

More importantly, $(U_a)_{GR}$ becomes zero at

$$\left(\frac{R_B}{h}\right)^2_{SP} = \frac{\pi^2\varphi_0}{6}\left\{1-\left[1-\frac{3}{2\Omega}\right]^{1/2}\right\} \tag{5.90}$$

When $\Omega < 3/2$ there is no solution. When $\Omega >> 3/2$, Eq. (5.90) becomes

$$\left(\frac{R_B}{h}\right)_{SP}^2 = \frac{\pi^2}{4\bar{\varepsilon}_0} \tag{5.91}$$

and

$$\left(\frac{A}{h}\right)_{SP}^2 = \frac{3}{\Omega} \tag{5.92}$$

$$\left(\varepsilon_r^R\right)_{SP} = \frac{3}{2\bar{\varphi}_0} \tag{5.93}$$

$$\left(\sigma_r^R\right)_{SP} = \frac{3\bar{E}}{2\varphi_0} = \frac{3G_c\bar{E}}{2h\sigma_0} = \frac{3\sigma_0}{4\Omega} \tag{5.94}$$

At this moment, the unstable growth stops as there is no driving energy; however, if the kinetic energy due to fast unstable growth of the buckle is large enough to break the film at its edge, the buckle spalls. The subscript SP in the equations above denotes spallation.

A sketch of the variation of $(U_a)_{GR}$ for a delamination with a circular edge is shwon in Figure 5-4. The $(U_a)_{GRE}$ in Figure 5-4 is equivalent to the bubble energy $(U_a)_{GR}$ presented here. The $(U_a)_{GR}$ given by Eq. (5.75), increases with radial growth up to $(R_B)_{UG}$, given by Eq. (5.84) and approximately by Eq. (5.85). This increase comes from the PEC. Because of the increasing nature of the bubble energy $(U_a)_{GR}$ in this region, the growth is expected to be generally slow and steady, even in the first range of unstable growth, that is, in the range $(R_B)_{UG} \le R_B \le (R_B)_{MU}$. Unstable growth starts at $(R_B)_{UG}$, given by Eq. (5.77) and approximately by Eq. (5.79). In the first region of unstable growth, the radius grows by a factor of about $1.5^{0.5}/\alpha \approx 1.308$, and the amplitude by a factor of about $3/(2\alpha^2) \approx 1.712$. When the PEC is too weak to provide the bubble energy, the bubble will stop growing, even in the first unstable growth range.

The bubble energy $(U_a)_{GR}$ decreases with radial growth after $(R_B)_{MU}$ and reduces to zero at $(R_B)_{SP}$, given by Eq. (5.90) and approximately by Eq. (5.91). This decreasing nature has two meanings. The first is that the bubble is no longer able to store any further bubble energy from the PEC. The second is that the bubble energy $(U_a)_{MU}$, cumulated in the range $0 \le R_B \le (R_B)_{MU}$, is being transformed into kinetic energy. This is consistent with the fact that the bifurcation-type buckling occurs at around $(R_B)_{MU}$, resulting in more 'violent' growth

after $(R_B)_{MU}$. In this second region of unstable growth, that is, in the range $(R_B)_{MU} \le R_B \le (R_B)_{SP}$, the radius grows by a factor of about 1.414, and the amplitude by a factor of about 2. It is seen that the cracked area at $(R_B)_{SP}$ is twice that at $(R_B)_{MU}$. Obviously, the bubble will stop growth at $(R_B)_{SP}$ as the bubble energy becomes zero. The minimum kinetic energy can be estimated as $(U_a)_{MU}$ in Eq. (5.89) by assuming that the PEC boundary ends at $(R_B)_{MU}$ resulting in no contribution to the kinetic energy. When $(U_a)_{MU}$ is large enough to break the oxide film, then spallation occurs, that is, the interface crack kinks into the oxide film. The kink-off angle β is measured from the interface as shown in Figure 5-7.

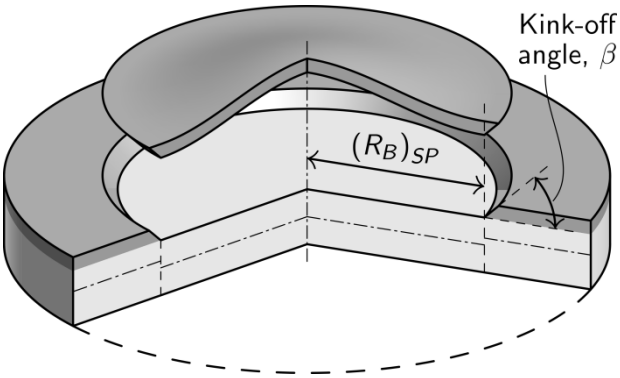

Figure 5-7: The kink-off angle of a spalled oxide film.

The kink-off angle can be determined using

$$(U_a)_{MU} = \frac{3}{4}\pi (R_B)_{MU}^2 G_c = \frac{2\pi (R_B)_{SP} h}{\sin(\beta)} G_{cf} \tag{5.95}$$

where G_{cf} is the fracture toughness of the oxide film. The kink-off angle is then given by

$$\beta = \arcsin\left(\frac{32}{3\pi} \frac{G_{cf}}{G_c} (\bar{\varepsilon}_0)^{1/2} \right) \tag{5.96}$$

The mechanical models based on classic plate theory and first-order shear-deformable plate partition theory can be readily obtained by replacing G_c, φ_0 and Ω in the mechanical model based on classical plate partition theory with and and G_{cE}, φ_{0E} and Ω_{2E} and G_{cT}, φ_{0T} and Ω_T, respectively.

Some salient points are now summarized. When using classical plate partition theory and assuming $A/h << 1$, the whole delamination process (i.e. the nucleation, stable and unstable

growth, and final spallation) for both straight-edged and circular-edged delaminations is a pure mode I fracture. Note that the bubble energy intensity decreases during delamination growth as expected; however, it is interesting to note that at the start of unstable growth and at the maximum bubble energy radius, the bubble energy intensities for straight-edged delamination are larger than those for a circular-edged delamination. This suggests that circular spallation occurs more easily than straight-edged spallation, as usually expected. When first-order shear-deformable plate or 2D elasticity partition theory is used, the whole delamination process is a mixed-mode fracture.

In the next section, predictions from the developed model are compared against experimental observations from the work [123] and [124].

5.5 Experimental verifications

In this section the mechanical models developed in section 5.3 and 5.4 are verified against the experimental results from the study [123,124] on the spalling failure of α - alumina films grown by oxidation in the room temperature. The verification of the mechanical models will be performed based on classical plate mixed fracture mode partition theory or Euler beam partition theory, the first order shear deformable plate or Timoshenko beam partition theory and 2D elasticity mixed fracture mode partition theory.

It is necessary to introduce the experimental works done in [123,124]. In the work [123,124], α -Al_2O_3 oxide films of different thicknesses were firstly formed on the surface of Fe-Cr-Al heat-resisting alloy substrates of different thickness at $1200°C$ with different heating hours. Then, the film substrate material systems were cooled down to room temperature with different cooling rates. There is no spallation failure was observed during cooling at any cooling rates when the compressive residual stress gradually increases due to thermal expansion mismatch. For some cooling rates, it was observed that circular separations of films nucleate, grow in height and propagate in radius at room temperature, and the compressive residual stress is far below the critical buckling stress, and after a period of slow and stable growth, some separations grow abruptly and spall off.

Figure 5-8 shows the sequence of optical images illustrating the nucleation, growth and spallation of one typical separation from a specimen where the thickness of the oxide scale is about $8um$ and the residual stress is 4.3 GPa. Figure 5-8 (a)-(e) show the nucleation, stable

growth stages which took 120 minutes. In Figure 5-8 (a)-(d) the radius of the nearly circular separation is far below the critical value for buckling. Here, it is conveniently called separation bubble as its radius is far too small to cause buckling, particular in Figure 5-8 (a)-(c). The abrupt growth starts at Figure 5-8 (e) and spallation failure occurs at Figure 5-8 (f) only taking just 3 minutes. The following verifications aim to verify the mechanical models developed in section 5.3 and 5.4 to explain some aspects of the above observations.

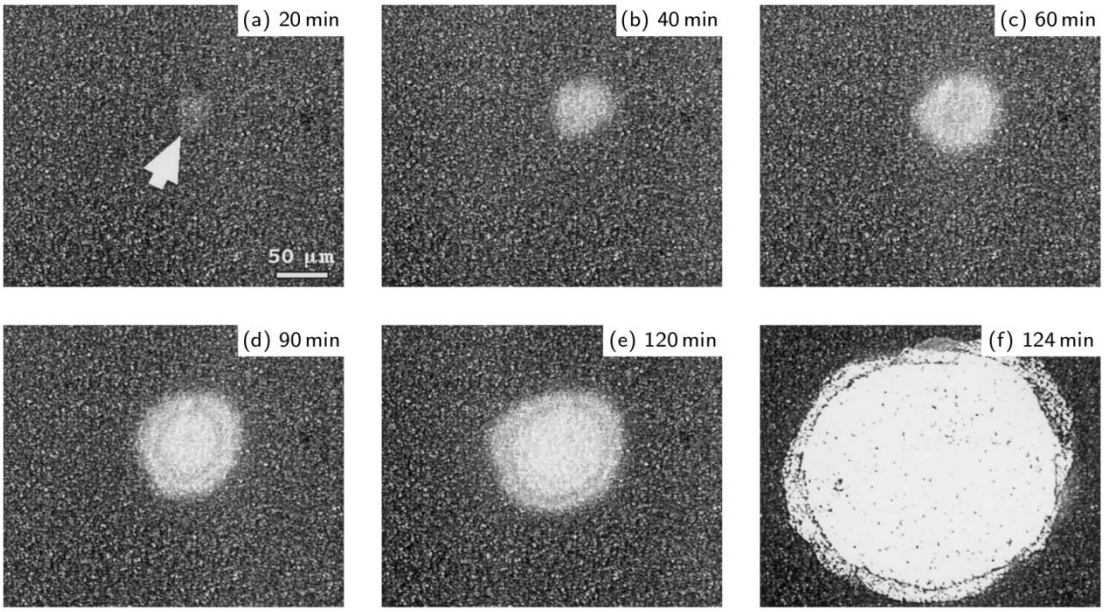

Figure 5-8: Sequence of slow growth of a separation bubble and spalling of $8um$ oxide [124].

5.5.1 Validation of specimen with similar residual stress and varied layer thickness

5.5.1.1 Unstable growth and spalling

In the following verifications, the material properties of the oxide film are Young's modulus E = 400 GPa and the Poisson's ratio $\upsilon = 0.25$ [123,124]. The interface mode I critical ERR is $G_{Ic} = 8.6\ N/m$, $G_{IIc} = \psi G_{Ic}$ with $\psi = 5$ and the critical mode I ERR of the oxide film $G_f = 20\ N/m$ [123,124].

The experimental verification starts to use Eq. (5.79) to predict the initiation of unstable growth, and to use (5.91) to predict the size of spallation. The tests done by Tolpygo and Clarke [124] contains specimens with the oxide under a similar residual stress ($\sigma_0 = 4.3 - 4.5GPa$) but with a different oxide thickness. In Figure 5-9, three sets of

validation results are presented: (a) Data from four different bubbles, successively measured on the same specimen ($h = 4.9\,\mu\text{m}$); (b) Data from two bubbles on another specimen ($h = 6.2\,\mu\text{m}$); (c) Data from a single bubble of a thick oxide ($h = 8.0\,\mu\text{m}$). The solid dots in Figure 5-9 (a), (b) and (c) represent series of measurements of the size of individual separations as a function of time at room temperature. Time equal to zero corresponds to the moment when the specimen was placed under the microscope and its temperature was close to ambient. Figure 5-9 (a) shows four different separations successively monitored using optical microscopy on a single specimen after isothermal oxidation for 25 h at 1200°C and cooling at 20°C/min. All of them were growing at a constant compressive stress, $\sigma_0 = 4.46 \pm 0.4\,\text{GPa}$ (measured in the adherent oxide far away from separations). The whole process contains nucleation, stable and unstable growth, and final spallation. Although the nucleation stage was not recorded due to the limitation of monitoring technique, e.g. the difficulty to spot a bubble on time at nucleation, the stable growth with a radius far smaller than the critical buckling value is observed. At a certain critical radius, again far smaller than the critical buckling value, the unstable growth abruptly occurs and final spallation takes place. It is very impressive to observe that all the four separations start unstable growth with very similar radius, and spall off with very similar radius as well. The two thicker oxides were produced by 50-h and 100-h oxidation and are shown in Figure 5-9 (b) and (c), respectively. The growth behaviours of two separation bubbles are shown Figure 5-9 (b). Again, the two separations start unstable growth with very similar radius, and spall off with very similar radius as well. Figure 5-9 (c) shows the growth behaviour of one separation bubble. The two horizontal lines (one dashed line and one solid line) in Figure 5-9 (a) (b) and (c) represent the predictions from Eq. (5.79) and (5.91), respectively. It is very impressive to see that the predictions from Eq. (5.79) and (5.91) have excellent agreements with the test results.

The values of Ω are 9.2728, 11.6808 and 14.1388 for Figure 5-9 (a) (b) and (c), respectively. They are much larger than $\alpha^2 = 0.936^2 = 0.8761$ in Eq. (5.77). Thus, Eq. (5.77) and Eq. (5.79) predict very close results for the initiation of unstable growth. Also, the Ω values are much larger than 1.5 as required by in Eq. (5.91). Eq. (5.90) and Eq. (5.91) predict very close results for the size of spallation.

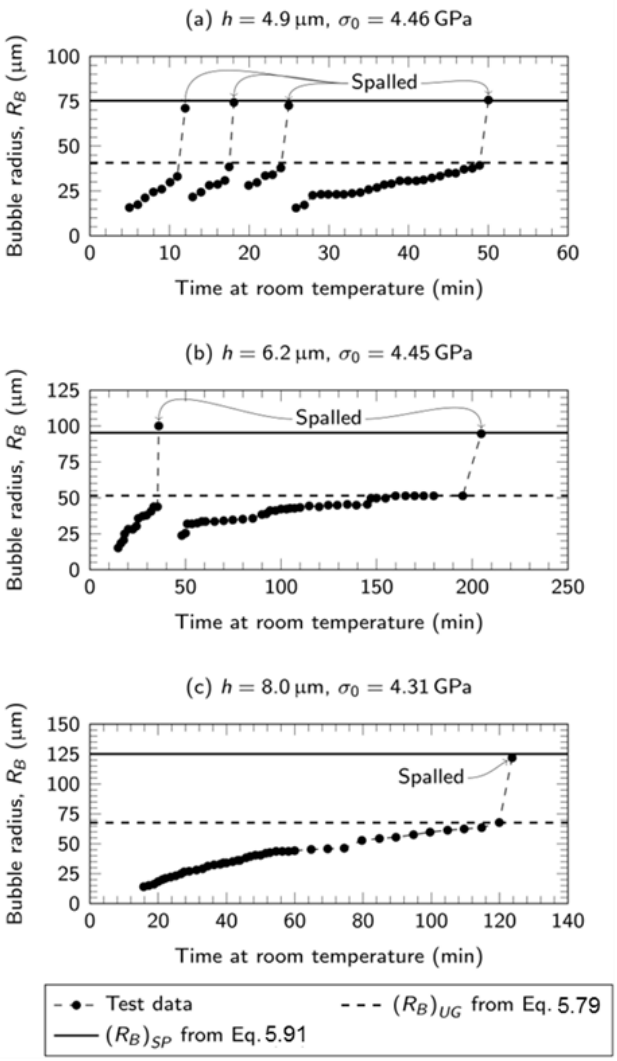

Figure 5-9: Separation bubble radius versus time at room temperature for three different samples.

5.5.1.2 Prediction using different mixed mode partition

It is worth to note that both Eq. (5.79) and (5.91) are common for the three mechanical models based on classical plate, the first order shear deformable plate and 2D elasticity mixed fracture mode partition theories when the values of parameter Ω meet certain requirements of Eq. (5.79) and (5.91). To examine the accuracy of Eq. (5.79) and (5.91), Table 5-1 shows the prediction results from Eq. (5.77) and Eq. (5.90) in comparison with those from Eq. (5.79) and (5.91). It is seen that they agree with each other very well. The SP, 2D and CP represent shear deformable plate, 2D elasticity and classical mechanical model, respectively. The ratio $\psi = G_{IIc} / G_{Ic} = 5$ is used in the calculation of SP, 2D and CP predictions. To examine the accuracy of Eq. (5.79) and (5.91) further, an extended study on Figure 5-9 (a),

(b) and (c) is also carried out by varying the critical mode I ERR G_{IC} of the oxide film while keeping all other parameters unchanged. Figure 5-10 (a)-(c) show the variation of $(R_B)_{UG}$ with respect to interface critical mode I ERR G_{Ic} for the specimens in Figure 5-9 (a), (b) and (c), respectively, using all the three mechanical models. The values of $(R_B)_{UG}$ in all the three models converge to the value in Eq. (5.79) with decreases of the mode I ERR G_{Ic}. At the value $G_{Ic} = 8.6\ N/m$ in the work [123,124], the predictions of Eq. (5.79) and Eq. (5.77) are very close to each other also as shown in Table 5-1.

Figure 5-11 shows a similar study on the variation of $(R_B)_{SP}$ with respect to the interface critical mode I ERR G_{Ic}. Again, the values of $(R_B)_{SP}$ in all the three models converge to the value in Eq. (5.91) with decreases of the mode I ERR G_{Ic}. At the value $G_{Ic} = 8.6\ N/m$ in the work [123,124], the predictions of Eq. (5.91) and Eq. (5.90) are very close to each other also as shown in Table 5-1. Again, the ratio $\psi = G_{IIc}/G_{Ic} = 5$ is used in the calculation of SP and 2D predictions in Figure 5-10 to Figure 5-11.

It is desirable to give some explanations why the three mechanical models give nearly the same predictions on the initiation of unstable growth and the size of spallation. The three mechanical models are all developed based on the assumption of small amplitude to thickness ratio, i.e. $A/h << 1$. One direct consequence of the assumption is that the crack tip radial force N_{rBe} in Eq. (5.12) has no contribution to the total ERR in Eq. (5.13). The total ERR is solely from the crack tip bending moment M_{rB} in Eq. (5.11). This results in a constant fracture mode mixity in the whole process of spallation. The first order shear deformable plate model predicts a mixed mode fracture, i.e. $G_I/G = 0.25$. The 2D elasticity model also predicts a mixed mode fracture, i.e. $G_I/G = 0.6227$. The classical plate model predicts a pure mode I fracture, i.e. $G_I/G = 1.0$. The mode mixty has no much effect on the predictions on the initiation and the size of spallation when G_{Ic} is small. That is, all three models give nearly the same prediction as shown in Figure 5-10 to Figure 5-11 and Table 5-1.

The mode mixity does, however, affect the amplitude in Eq. (5.72), of a delamination bubble, the relaxation strain in Eq. (5.73) and relaxation stress in Eq. (5.74). These three models therefore give different predictions of these quantities. Due to lack of accurate measurements of these quantities, no comparisons could be made in the present work. Comparison can,

however, be made between measurements of the kink-off angle and predictions from Eq. (5.96). Values of $h/\tan(\beta)$ are also recorded in Table 5-1. The critical mode I ERR of the oxide film is $G_{cf} = 20\ \mathrm{N/m}$. For Figure 5-9 (a), $h/\tan(\beta) = 9.10\,\mu\mathrm{m}$ was measured approximately from Tolpygo and Clarke's work [124] Fig. 3, which is a similar case. No test value for the Figure 5-9 (b) case is found in the work [123,124]. For Figure 5-9 (c), $h/\tan(\beta) = 13.46\,\mu\mathrm{m}$ was measured approximately from Figure 5-2 (f) in this work (reprinted from Tolpygo and Clarke, 2000 [124]), which is a similar case. The averages of the measurements of the four diameters at 0°, 90° and ±45° were used to obtain the test values. It is seen that the 2D elasticity model gives good predictions but the other two models do not.

It can be concluded at this point that the 2D elasticity model predicts the whole delamination process very well, including the initiation of unstable growth, size of spallation and kink-off angle. The other two models, however, only give good predictions of the initiation of unstable growth and the size of spallation.

As mentioned earlier, extensive fracture testing (Hashemi et al. [15]; Kinloch et al. [16]; Charalambides et al. [17]; Davidson et al. [19], [20]; Harvey and Wang [22], [23]); Conroy et al. [30] has shown that the partition theory based on Euler beam or classical plate theory [26-29] gives very accurate predictions of interface fracture toughness for macroscopic mixed-mode fracture while the partition theories based on Timoshenko beam theory or the first-order shear-deformable plate theory [26-29] and 2D elasticity, Hutchinson and Suo [14] give poor predictions. The very latest studies (Wang et al. [31],[126]), however, show that the 2D elasticity partition theory gives accurate predictions for the delamination behavior of micro-scale and nano-scale thin films. This may be expected since the partition theory based on Euler beam or classical plate theory is a 'global' partition theory (that is, cracks develop over finite-size length scales) which governs macroscopic fracture whereas the 2D elasticity partition theory is a 'local' partition theory (that is, infinitesimal crack growth is assumed) which governs micro- or nano-scale fracture.

However, it is worth to note the following comments. All the three mechanical models are developed based on the assumption of small amplitude to thickness ratio, i.e. $A/h \ll 1$. For Figure 5-9 (a), (b) and (c), the respective ratios at the initiation of unstable growth are $(A/h)_{UGT} = 0.3470, 0.3093, 0.2810,$ $(A/h)_{UG2D} = 0.1988, 0.1772, 0.1610$ and $(A/h)_{UGE} = 0.1388, 0.1237, 0.1124$ respectively in the three mechanical models by using Eq.

(5.26). They are very small indeed in the classical plate model, but are not small in the shear deformable plate and 2D elasticity models. The respective ratios at spallation are $(A/h)_{SPT} = 1.188, 1.059, 0.9623,$ $(A/h)_{SP2D} = 0.6808, 0.6066, 0.5513$ and $(A/h)_{SPE} = 0.4753, 0.4235, 0.3849,$ respectively. Obviously, they are not small for all the three models. Since the model predicts the spallation behaviour very well it must capture some key physics in the mechanical process. As mentioned earlier, one direct consequence of the assumption, i.e. $A/h \ll 1$, is that the crack tip radial force N_{rBe} in Eq. (5.12) has no contribution to the total ERR in Eq. (5.13). The measurements of residual stress in some stationary buckles (see Figs. 8 and 9 in the work [124]) do show $N_{rBe} = 0$ at crack tip for large values of A/h. The total ERR is solely from the crack tip bending moment M_{rB} in Eq. (5.11). Therefore, the assumption i.e. $A/h \ll 1$ is no longer required. The only restriction is that $A/h \sim 1$, i.e. the usual condition of the Von-Karman geometrical nonlinearity assumption used in Eq. (5.56). The above values of A/h are obviously within the limitation.

Table 5-1: Comparison of the present mechanical model with test data [124] for the initiation of unstable growth, the size of spallation and kinking off.

	$(R_B)_{\mathrm{UG}}$ (μm)					$(R_B)_{\mathrm{SP}}$ (μm)					$h/\tan(\beta)$(μm)			
	Eq. (5.77)			Eq.	Test	Eq. (5.90)			Eq.	Test	Eq. (5.96)			Test
Fig.5-10	SP	2D	CP	(5.79)	data	TB	2D	CP	(5.91)	data	SP	2D	CP	data
(a)	41.6	41.2	41.0	40.7	40.0	78.3	76.9	76.4	75.3	75.0	15.0	7.5	3.8	9.1
(b)	52.4	52.0	51.9	51.5	47.5	98.3	97.0	96.5	95.4	97.5	18.2	9.1	4.5	-
(c)	68.5	68.1	67.9	67.6	67.5	128.2	126.8	126.2	125.0	122.5	23.9	12.0	6.1	13.5

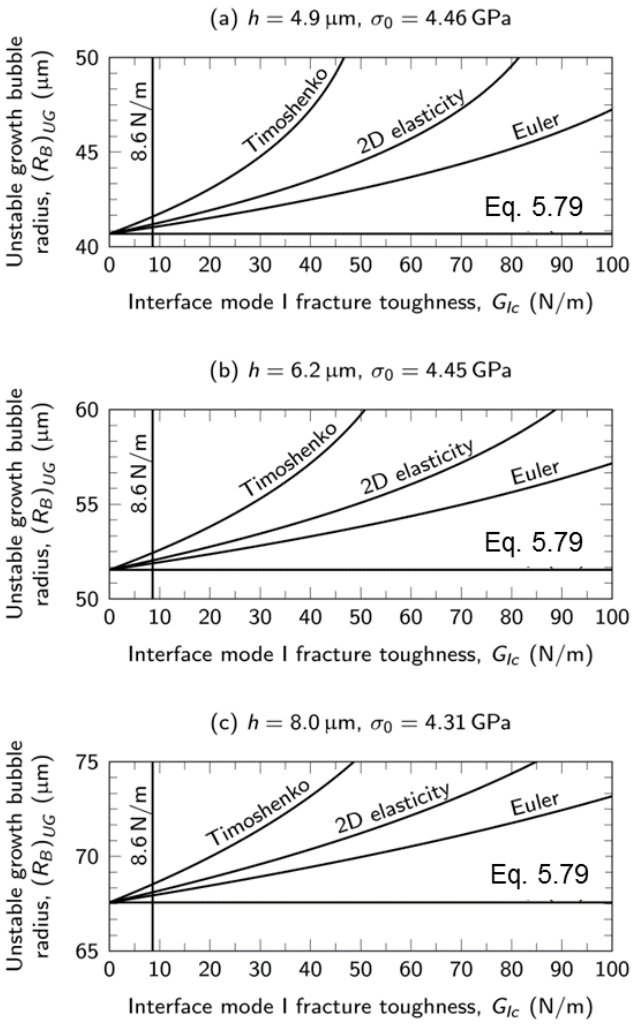

Figure 5-10: Variation of the unstable growth bubble radius $(R_B)_{UG}$ with respect to G_{Ic} according to various partition theories.

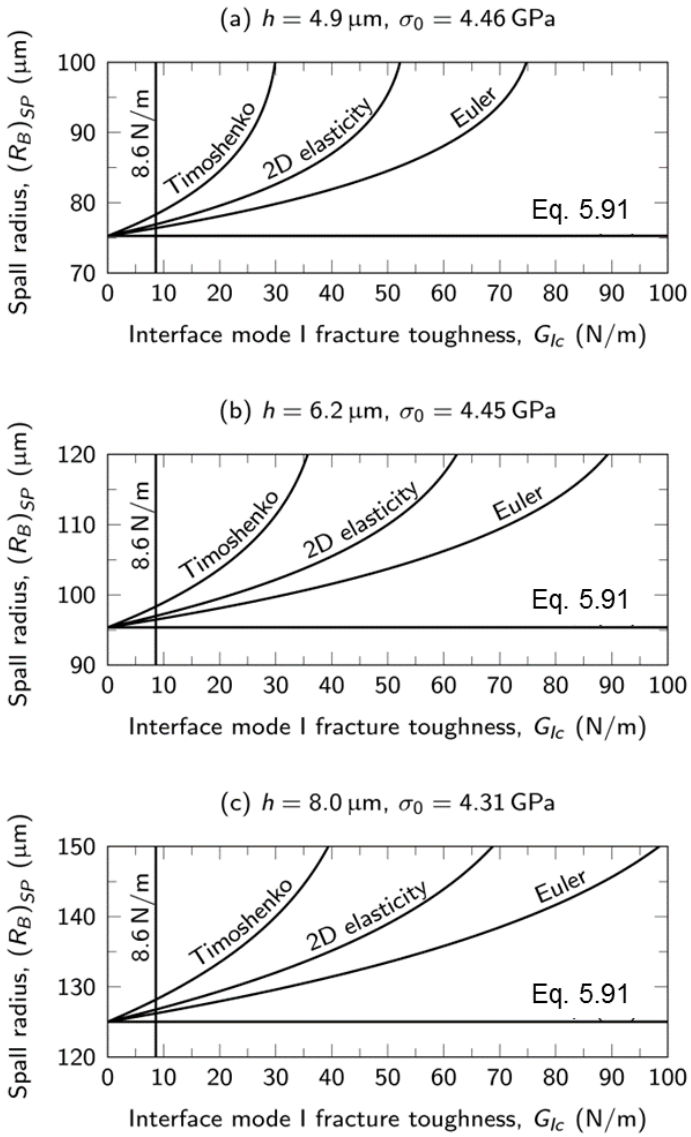

Figure 5-11: Variation of the spall radius $(R_B)_{SP}$ with respect to G_{Ic} according to various partition theories.

5.5.2 Validation of specimen with varied layer thickness and residual stress

More verifications are now performed on samples having oxide films of various thicknesses and residual stresses. The results are shown in Figure 5-12. Again, all the dots represent the measurements on the oxides with h=0.8–8.0 μm (after oxidation for 0.5–100 h) and with residual compression in the range 4–5 GPa. The solid line is from Eq. (5.91). Again, the present mechanical models predict the experimental results very well. (Since lack of experimental results, no verification is carried out on spallation with straight edges.)

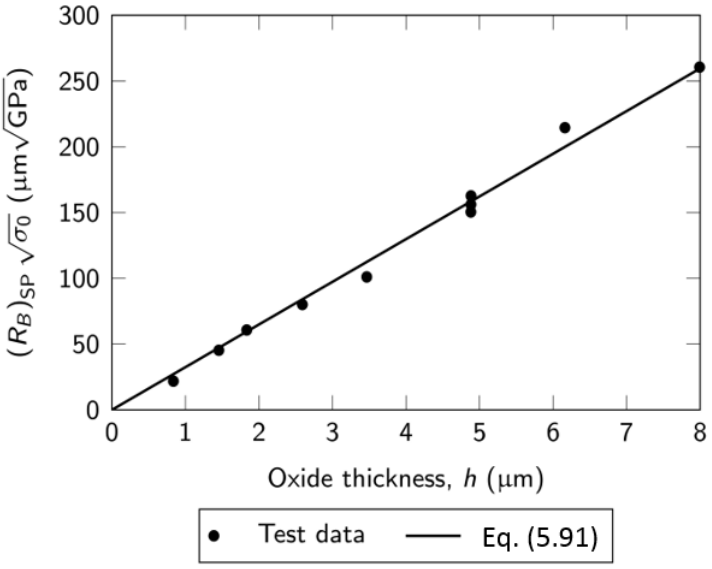

Figure 5-12: The spallation parameter $(R_B)\sigma_0^{1/2}$ as a function of the oxide thickness with test data [124]

5.5.3 Validation of specimen with similar layer thickness and varied residual stress

To further test the capability of Eq. (5.91) for prediction of spallation size, the extensive test data in the work [124] is used here as the second group of experimental verification. All measurements of the spall size after 25-h oxidation at 1200°C (h=4.9 mm) are gathered in Figure 5-13. A total of 23 specimens of different substrate thicknesses were oxidized in identical conditions and then cooled at different rates (5–200°C/ min). The spall size, R_B, was measured on 50–60 circular spalls on each specimen, and the residual stress was probed in the adherent oxide remote from the spalls. The spall radius plotted as a function of residual stress in the oxide can indeed be described very well by Eq. (5.91) shown by the top solid line. The middle solid line is from Eq. (5.85) for the position of maximum PEC energy. The bottom solid line is from Eq. (5.79) for the initiation of unstable growth. The minimum size at which bubbles were first discerned is indicated by the bottom of the shaded bulk arrow. This region can be regarded as the nucleation stage with the PEC energy $1.5\pi R_B^2 G_{Ic}$ in Eq. (5.79). It is seen that a third of the nucleation PEC energy is used to bend the separation outwards after nucleating the interface separation using two thirds of its energy. Stable growth occurs below this line and is solely driven by PEC energy in Eq. (5.79). If the PEC energy is not big enough as required by Eq. (5.79), the bubble will stop growth resulting in a stationary bubble. The region between the bottom and middle lines is regarded as the first

stage unstable growth driven by both PEC energy and buckling effect. Although the growth rate is much faster than that of stable growth it is still too slow to build up any kinetic energy. However, the bubble now changes to be a buckle due to the buckling effect. If the PEC energy is not big enough as required by Eq. (5.83), the buckle will stop growth resulting in a stationary buckle. The dash line in this region shows the largest stationary buckles observed. The region between the middle solid and top solid lines is regarded as the second stage unstable growth. The PEC energy reaches its maximum value in Eq. (5.89) at the middle solid line and contains solely static mechanical energy including strain energy and surface energy. Above this line, the tensile stress at the crack tip and its neighbouring area is solely produced by the crack and no tensile stress residual stress produced by the non-converged plastic relaxation effect. Therefore, the total energy in the buckle will remains constant afterwards including the PEC energy in Eq. (5.79) and kinetic energy due to the much more violent growth. At the size of spallation in Eq. (5.90) or (5.91), the PEC energy in Eq. (5.79) becomes zero and the crack propagation along the interface is not possible. If the kinetic energy of the same amount of that in Eq. (5.89) in the spall is not big enough to break the oxide film, a stationary spall is produced. If it is big enough to break the oxide film, that is, the Eq. (5.95) is satisfied, spallation or kinking off takes place.

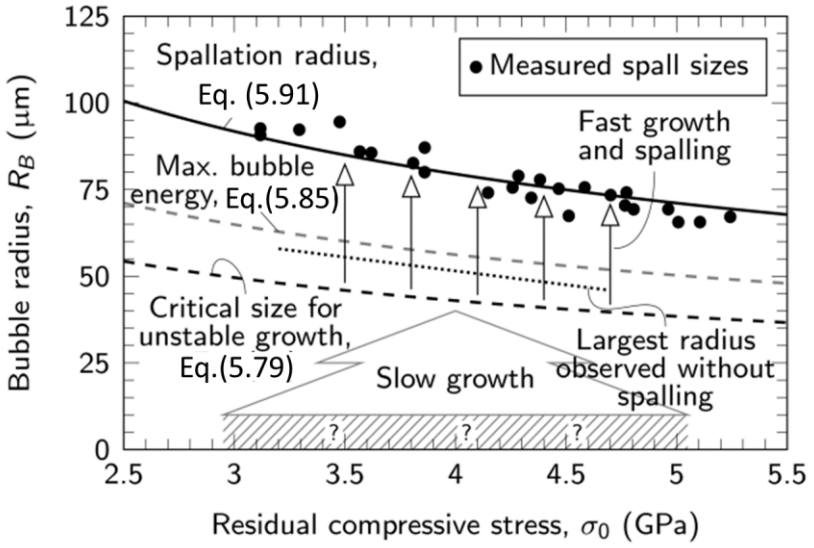

Figure 5-13: Bubble growth behaviour and spallation radius as a function of residual stress in the oxide for the same oxide thickness ($h = 4.9\,\mu m$).

5.6 Conclusions

PECs can be formed by pockets of tensile stress and shear stress on and around the interface between a thin film and a thick substrate, which can be caused by a number of different processes, including thermal effects and chemical effects. PECs can cause the interface spallation failure of thin films. Three mechanical models have been developed to predict several aspects of the spallation failure of elastic brittle thin films by using partition theories for mixed-mode fracture based on classical plate theory, first-order shear-deformable plate theory and full 2D elasticity. Based on experimental results from Tolpygo and Clarke [123,124] for circular-edged delaminations, the three models all give accurate predictions of the initiation of unstable growth of separation bubbles and the size of spallation. The 2D elasticity model also gives accurate predictions of the final kink-off angle but the classical plate and first-order shear-deformable plate models are unable to. The nucleation and stable growth of a separation bubble are solely driven by the bubble energy but unstable growth is driven by both bubble energy and buckling. Final kinking off is controlled by the toughness of the interface and the film and the maximum bubble energy.

The present mechanical models reveal a new failure mechanism of thin films under compressive residual stress and will be particularly useful to study the spallation failure of thermal barrier coating material systems.

Chapter 6 Adhesion energy of multilayer graphene membranes

6.1 Introduction

The buckling driven delamination of bilayer laminated composite beam with macroscopic layer thickness was studied in chapter 3 by using the experimental data from ref. [32], the results shows that the Euler beam mixed mode partition theory gives more accurate predictions than the 2D elasticity mixed mode partition theory does. In chapter 5, the spallation failure of α-alumina films with microscopic layer thickness was investigated by using classical plate, the first order shear deformable plate and 2D elasticity partition theories. All three partition theories predict the interface crack nucleation, stable and unstable growth very well; however, only the 2D elasticity model predicts final kinking off accurately. It is understand that the classical plate mixed mode partition theory is insensitive to the crack growth size since it is a 'global partition theory'; in contrast, the 2D elasticity partition theory is sensitive to the crack growth size and suitable for microscopic thickness layer. To confirm this, the adhesion energy of multilayer graphene membranes with thickness in nanoscale is discussed in this chapter.

The graphene membranes are often made of multilayered graphenes with intrinsically high Young's modulus and strength. To determine the adhesion energy is an essential task to define the interface mechanical properties between multilayer graphene membranes and substrates. The adhesion energy of mono- and multi-layered graphene membranes on a silicon oxide substrate was measured by Koenig et al. [159] using a pressurised blister test experimentally. It was observed there is a large decrease of adhesion energy from mono-layered blisters to multi-layered. The average adhesion energy of a monolayer graphene blister is reported as $G = 0.45 J/m^2$ whereas the multi-layered specimens have an average adhesion energy of $G = 0.31 J/m^2$. The other experimental work on the measurement of adhesion energy of multi-layered graphene membranes was done by Zong et al. [160] using point loading. The adhesion energy of the point loaded graphene blister of five layers was reported as being $G = 0.151 J/m^2$. However, fracture mode mixity and the sliding effect are not considered in the current mechanical models [159-165] in the determination of the

adhesion energy for multi-layered graphene membranes using the blister test. This has caused confusion in interpreting the adhesion energy.

In this chapter, the analytical models are developed to calculate the adhesion toughness by using the classical plate, shear deformable plate partition and 2D elasticity partition theories. The developed theories are applied to blister tests of pressure loading and point loading. The results show that the determination of adhesion toughness of multi-layered graphene membranes is governed by 2D elasticity partition theory with considering sliding effect and the analytical model gives excellent predictions for adhesion energy between multilayer graphene membranes and substrates.

6.2 Mixed mode partition theories for delamination of thin-layer materials

Figure 6-1 (a) shows a simplified thin-layer-substrate composite material system with an interface crack. The crack is assumed to be one-dimensional with either a straight edge or a circular edge, the crack propagates perpendicularly to the edge and driven by mode I and II ERRs. Figure 6-1 (b) shows the crack tip forces in the thin layer including bending moment $M_B\ (Nm/m)$, in-plane force $N_B\ (N/m)$ and shear force $P_B\ (N/m)$. The material properties of the film are the Young's modulus E and Poisson ratio υ.

The recent significant progress on mixed fracture mode partitions by the C. Harvey and S. Wang reveals that mode I and II ERRs at brittle interface can be written systematically in the following form

$$G_I = c_I\left(M_B - \frac{N_B}{\beta_2} - \frac{P_B}{\beta_4}\right)\left(M_B - \frac{N_B}{\beta_2'} - \frac{P_B}{\beta_4'}\right) \tag{6.1}$$

$$G_{II} = c_{II}\left(M_B - \frac{N_B}{\theta_2} - \frac{P_B}{\theta_4}\right)\left(M_B - \frac{N_B}{\theta_2'} - \frac{P_B}{\theta_4'}\right) \tag{6.2}$$

Where c_I and c_{II} are two constants, and (θ_i, β_i) and (θ_i', β_i') (with $i = 2,4$) represent the two sets of orthogonal pure modes which vary from different partition theories. Note that these two set of pure modes coincide each other for non-rigid interface fracture [77]. In the present study, the interface is assumed brittle and rigid, the substrate is assumed infinite stiff and top layer produces the energy release rate. Therefore, the *h* instead of h_1 is used to represent the top layer thickness in the work.

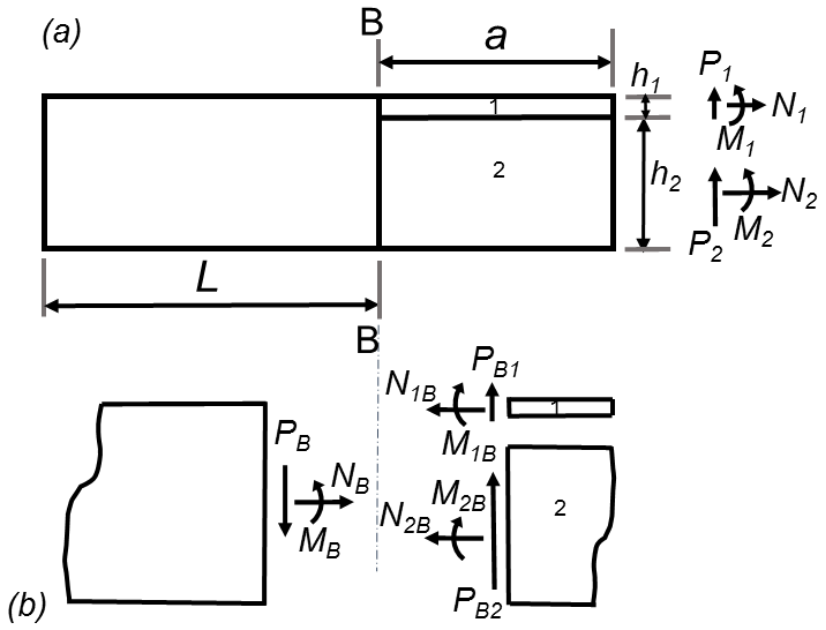

Figure 6-1: A simplified thin layered material system and its loading conditions. (a) General description. (b) Details of the crack influence region Δa

6.2.1 Euler beam partition/classical plate partition theory

When Euler beam/classical plate partition theory is used, two sets of orthogonal pure modes (θ_i, β_i) and (θ_i', β_i') (with $i = 2,4$) exist. According to [152] the Eqs. (6.1) and (6.2) become:

$$G_{IE} = \frac{6}{\bar{E}h^3}\left(M_B - \frac{N_B h}{2}\right)M_B \tag{6.3}$$

$$G_{IIE} = \frac{6}{\bar{E}h^3}\left(M_B + \frac{N_B h}{6}\right)\frac{N_B h}{2} \tag{6.4}$$

Where the subscript E represents Euler beam partition theory. $\bar{E} = E$ for plane stress with a straight edge crack and $\bar{E} = E/(1-\nu^2)$ for plane strain with a straight edge crack or for crack with a circular edge, h is the thin layer thickness. The effective crack tip through thickness shear force P_B has no effect as expected.

6.2.2 Timoshenko beam/the first order shear deformable plate partition theory

When Timoshenko beam/the first order shear deformable plate partition theory is used, two sets of orthogonal pure modes (θ_i, β_i) and (θ_i', β_i') (with $i = 2,4$) coincide with each other. According to [152] the Eqs. (6.1) and (6.2) become:

$$G_{IT} = \frac{6}{\bar{E}h^3}\left(M_B - \frac{N_B h}{2} - \frac{P_B}{\beta_{4-T}}\right)^2 0.25 \tag{6.5}$$

$$G_{IIT} = \frac{6}{\bar{E}h^3}\left(M_B + \frac{N_B h}{6}\right)^2 0.75 \tag{6.6}$$

with

$$\beta_{4-T} = -\left(3\kappa\mu / \bar{E}\right)^{1/2} / h \tag{6.7}$$

The subscript T represents Timoshenko beam/the first order shear deformable plate partition theory, and the shear correction factor is $\kappa = 5/6$ and through thickness shear modulus is $\mu = E/[2(1+\nu)]$. Note that the effective crack tip through thickness shear force P_B only produces mode I ERR.

6.2.3 2D elasticity partition theory

Within the context of 2D elasticity, two sets of orthogonal pure modes (θ_i, β_i) and (θ_i', β_i') (with $i = 2,4$) exist at rigid bilayer interface, which are also crack extension size dependent [150,151]. When the material elastic mismatch is neglected, the two sets of pure mode coincide with each other. This is the case studied in the present work. Mode I and II ERRs take the following form [152].

$$G_{I2D} = \frac{6}{\bar{E}h^3}\left(M_B - \frac{N_B h}{4.450} - \frac{P_B}{\beta_{4-2D}}\right)^2 0.6227 \tag{6.8}$$

$$G_{II2D} = \frac{6}{\bar{E}h^3}\left(M_B + \frac{N_B h}{2.697} - \frac{P_B}{\theta_{4-2D}}\right)^2 0.3773 \tag{6.9}$$

where the subscript 2D represents 2D elasticity partition theory. β_{4-2D} and θ_{4-2D} are determined in what follows. From the reference [78], β_{4-2D} is generally expressed as

$$\beta_{4\text{-}2\mathrm{D}} = \frac{\left(1/\beta_{P\text{-}2\mathrm{D}} + 1\right)}{\left(\theta_{1\text{-}2\mathrm{D}}/\beta_{1\text{-}2\mathrm{D}} - 1\right)\left(G_{\theta_{P\text{-}2\mathrm{D}}}/G_{\theta_{1\text{-}2\mathrm{D}}}\right)^{1/2}} \tag{6.10}$$

The detailed expressions and meanings of the involved quantities are given in the work [78]. The present study assumes an infinitely thick substrate and very thin film. In this case, $1/\beta_{P-2D} = 0$ and $\theta_{1-2D}/\beta_{1-2D} = -75/121 = -0.6198$ from the work [166] which is very close to $\theta_{1-2D}/\beta_{1-2D} = -0.6059$ from the work [14]. In this study $\theta_{1-2D}/\beta_{1-2D} = -0.6059$ is used. $G_{\theta_{P-2D}}$ and $G_{\theta_{1-2D}}$ reduce to be

$$G_{\theta_{P\text{-}2\mathrm{D}}} = \frac{1}{2\bar{E}h}\frac{1}{0.135535} \tag{6.11}$$

and

$$G_{\theta_{1\text{-}2\mathrm{D}}} = \frac{6}{\bar{E}h^3}\left(1 - \frac{\theta_{1-2D}}{\beta_{1-2D}}\right)^2 0.6227 \tag{6.12}$$

Therefore, Eqs (6.10-6.12) give

$$\beta_{4\text{-}2\mathrm{D}} = -\frac{1.0063}{h} \tag{6.13}$$

From the reference [73], θ_{4-2D} is generally expressed as

$$\theta_{4\text{-}2\mathrm{D}} = \frac{\left(1/\beta_{P\text{-}2\mathrm{D}} + 1\right)}{\left(\beta_{1\text{-}2\mathrm{D}}/\theta_{1\text{-}2\mathrm{D}} - 1\right)\left[G_{\beta_{P\text{-}2\mathrm{D}}}/\left(\beta_{P-2D}^2 G_{\beta_{1\text{-}2\mathrm{D}}}\right)\right]^{1/2}} \tag{6.14}$$

Where

$$G_{\beta_{1\text{-}2\mathrm{D}}} = \frac{6}{\bar{E}h^3}\left(1 - \frac{\beta_{1-2D}}{\theta_{1-2D}}\right)^2 0.3773 \tag{6.15}$$

is of finite non-zero value while $G_{\beta_{P\text{-}2\mathrm{D}}} = 0$. Therefore,

$$\theta_{4-2D} = -\infty \tag{6.16}$$

Again, note that the effective crack tip through thickness shear force P_B only produces mode I ERR.

Now, complete analytical formulas are obtained for mode I and II ERRs of thin layer delamination under general loading conditions based on Euler beam/classical plate theory, Timoshenko beam/first order shear deformable plate theory and 2D elasticity theory. In the following sections, some practical cases are considered from some available experimental assessments.

6.3 Mixed mode partition for circular blister delamination under pressure loading at the membrane limit

Circular blister delamination test under pressure loading is often used to determine the interface toughness between a thin layer material and a substrate. Total interface ERR and its partitions are considered in this section and the delamination is assumed to be on the interface.

Figure 6-2 shows a delamination test of a circular blister of radius R_B under pressure load p. Also from the work [166,167], at the membrane limit, the effective crack tip moment and force as follows.

$$M_B = \frac{h}{4}\frac{\left(Ehp^2R_B^2\right)^{1/3}}{\left[3(1-\upsilon^2)\varphi_p(\upsilon)\right]^{1/2}} \tag{6.17}$$

$$N_B = \left(Ehp^2R_B^2\right)^{1/3}\varphi_p(\upsilon) \tag{6.18}$$

$$P_B = \frac{1}{2}pR_B \tag{6.19}$$

The parameter $\varphi_p(\upsilon)$ is given as

$$\varphi_p(\upsilon) = \frac{\left(1.078+0.636\upsilon\right)^{2/3}}{2\left[6(1-\upsilon^2)\right]^{1/3}} \tag{6.20}$$

Which comes from the relationship

$$\chi_p(\upsilon) = \frac{N_B h}{M_B} = 4\left[3\left(1-\upsilon^2\right)\varphi_p(\upsilon)\right]^{1/2} = 1.078+0.636\upsilon \tag{6.21}$$

The deflection δ at the centre of the blister is

$$\delta = f_p(\upsilon)\left(\frac{pR_B^4}{Eh}\right)^{1/3} \tag{6.22}$$

with

$$f_p(\upsilon) = 0.9635\left(\frac{3(1-\upsilon)}{7-\upsilon}\right)^{1/3} \tag{6.23}$$

The factor 0.9635 in Eq. (6.23) is introduced in the present work to achieve the bench mark value of $f(1/3) = 0.645$ in the work [167] as $f_p(\nu) = \left(\frac{3(1-\nu)}{7-\nu}\right)^{1/3}$ from the work [169] is approximate.

When P_B is neglected, the total ERR is

$$G_J = \phi_p(\nu)\left(\frac{p^4 R_B^4}{Eh}\right)^{1/3} = \phi_p(\nu)\frac{Eh}{f_p^4(\nu)}\left(\frac{\delta}{R_B}\right)^4 = \phi_p(\nu)\frac{p\delta}{f_p(\nu)} \tag{6.24}$$

Where J indicates Jensen's work, [166,167]. The parameter ϕ is

$$\phi_p(\nu) = \left(\frac{1}{8\varphi_p} + \frac{(1-\nu^2)\varphi_p{}^2}{2}\right) \tag{6.25}$$

Partitions of the total ERR are considered next.

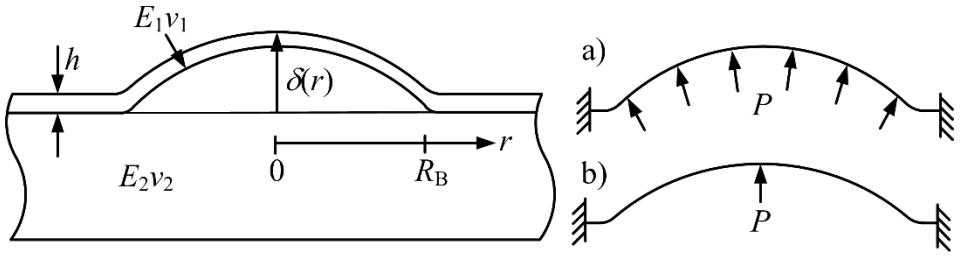

Figure 6-2: Sketch of circular blister test for interface fracture toughness determination [166].

6.3.1 Using Euler beam/classical plate partition theory

The partitions are obtained by using Eqs. (6.3), (6.4), (6.17) and (6.18).

$$G_{IE} = \frac{6M_B^2}{\bar{E}h^3}\left[1 - \frac{\chi_p(\upsilon)}{2}\right] = \frac{6M_B^2}{\bar{E}h^3}(0.461 - 0.318\upsilon) \tag{6.26}$$

$$\begin{aligned} G_{IIE} &= \frac{6M_B^2}{\bar{E}h^3}\left[1 + \frac{\chi_p(\upsilon)}{6}\right]\frac{\chi_p(\upsilon)}{2} \\ &= \frac{3M_B^2}{\bar{E}h^3}(1.180 + 0.106\upsilon)(1.078 + 0.636\upsilon) \end{aligned} \tag{6.27}$$

The mode mixity ratio G_{IE}/G_{IIE} is then

$$\rho_E = G_{IE}/G_{IIE} = \frac{0.922 - 0.636\upsilon}{1.272 + 0.865\upsilon + 0.0674\upsilon^2} \tag{6.28}$$

It is independent of the blister radius R_B. Consequently, the interface fracture toughness is also independent of the blister radius R_B, which can be determined from Eq. (6.24) by using measured critical values of applied pressure p or the centre deflection δ in experiments. The

mode mixity G_{IE}/G_{IIE} varies from 0.725 at $\upsilon=0$ to 0.351 $\upsilon=0.5$. It is a mode II dominated fracture. The total ERR G_E is the same as G_J in Eq. (6.24).

6.3.2 Using Timoshenko beam/shear deformable plate partition theory

The partitions are obtained using Eqs. (6.5), (6.6), (6.17), (6.18) and (6.20).

$$\begin{aligned} G_{IT} &= \frac{6M_B^2}{\bar{E}h^3}\left(1-\frac{\chi_p(\upsilon)}{2}+\bar{\lambda}_T\right)^2 0.25 \\ &= \frac{6M_B^2}{\bar{E}h^3}\left(0.461-0.318\upsilon+\bar{\lambda}_T\right)^2 0.25 \end{aligned} \tag{6.29}$$

$$\begin{aligned} G_{IIT} &= \frac{6M_B^2}{\bar{E}h^3}\left(1+\frac{\chi_p(\upsilon)}{6}\right)^2 0.75 \\ &= \frac{6M_B^2}{\bar{E}h^3}\left(1.180+0.106\upsilon\right)^2 0.75 \end{aligned} \tag{6.30}$$

The mode mixity ratio G_{IT}/G_{IIT} is given as

$$\rho_T = G_{IT}/G_{IIT} = \frac{1}{3}\left(\frac{0.461-0.318\upsilon+\bar{\lambda}_T}{1.180+0.106\upsilon}\right)^2 \tag{6.31}$$

and the ratio of ERR contribution from the through thickness shearing effect G_{TS} to G_J, i.e. G_{TS}/G_J

$$\eta_T = G_{TS}/G_J = 0.25\bar{\lambda}_T\left[\bar{\lambda}_T+2\left(1-\frac{\chi_p(\upsilon)}{2}\right)\right]\left\{0.25\left(1-\frac{\chi_p(\upsilon)}{2}\right)^2+0.75\left(1+\frac{\chi_p(\upsilon)}{6}\right)^2\right\}^{-1} \tag{6.32}$$

with

$$\begin{aligned} \bar{\lambda}_T &= \frac{P_B}{\beta_{4-T}M_B} = 2\left(\frac{2(1+\upsilon)\varphi_p}{\kappa}\right)^{1/2}\left(\frac{pR_B}{Eh}\right)^{1/3} \\ &= 2\left(\frac{2(1+\upsilon)\varphi_p}{\kappa}\right)^{1/2}\frac{1}{f_p(\upsilon)}\frac{\delta}{R_B} \end{aligned} \tag{6.33}$$

The parameter $\bar{\lambda}$ in Eq. (6.33) can have the following alternative expressions by using Eq. (6.22).

$$\bar{\lambda}_T = \bar{\phi}_T(\nu)\left(\frac{pR_B}{nEt}\right)^{1/3} = \bar{\phi}_T(\nu)\frac{1}{f(\nu)}\frac{\delta}{R_B} = \bar{\phi}_T(\nu)\left(\frac{p\delta}{f(\nu)nEt}\right)^{1/4} \tag{6.34}$$

Where

$$\bar{\phi}_T(\nu) = 2\sqrt{\frac{2}{\kappa}}\left((1+\nu)\varphi\right)^{1/2} \tag{6.35}$$

In Eq. (6.35) shear correction factor is $\kappa = 5/6$.

The mode mixity decreases with the increases in the blister radius R_B and approaches to zero when $R_B \to \infty$. Consequently, the interface fracture toughness also decreases with the increases in the blister radius R_B. When R_B approaches to zero, the mode mixity G_{IT}/G_{IIT} varies between 0.0509 at $\upsilon = 0$ and 0.0200 at $\upsilon = 0.5$. It is mode II dominated fracture. Moreover, the total ERR G_T is larger in general than G_J in Eq. (6.24). It is mode II dominated fracture. Moreover, the total ERR G_T is larger in general than G_J in Eq. (6.24) due to the through thickness shear force contribution. However, the numerical simulation in the latest work [168] for a single layered thin layer material in the membrane limit agree well the G_J in Eq. (6.24). This suggests that the through thickness shear force contribution disappears for a single layered thin layer materials at the membrane limit. Therefore, in the case of monolayer graphene membranes, there is no ERR contribution from the shear force. However, in the case of multi-layer graphene membranes, the interlayer sliding effect will activate the through thickness force leading to ERR contributions. To account for this effect, $\bar{\lambda}_T$ in Eqs. (6.29)-(6.32) is replaced by λ_T defined as

$$\lambda_T(n) = \left(1 - e^{1-n}\right)\bar{\lambda}_T = S(n)\bar{\lambda}_T \tag{6.36}$$

Where the assumed $S(n)$ is termed as sliding factor with *n* representing the number of graphene layers. Obviously, $S(n)$ satisfies that $S(1) = 0$ and $S(\infty) = 1$. That is, $\lambda_T(1) = 0$ for monolayer graphene membranes with zero shear force effect and $\lambda_T(\infty) = \bar{\lambda}_T$ for membranes of large number of graphene layers with full shear force effect. The total ERR can then be written in terms of the sliding component G_{ST} and G_J, the contribution from the crack tip bending moment M_B in Eq. (6.17) and in-plane force N_B in Eq. (6.18) as

$$G_T = G_J + G_{ST} = G_J\left(1 + \eta_T\right) \tag{6.37}$$

6.3.3 Using 2D elasticity partition theory

For the membrane limit, the ERR partitions are obtained by using Eqs. (6.8), (6.9), (6.17), (6.18) and (6.19).

$$\begin{aligned} G_{I2D} &= \frac{6M_B^2}{\bar{E}h^3}\left(1-\frac{\chi_p(\upsilon)}{4.450}+\bar{\lambda}_{2D}\right)^2 0.6227 \\ &= \frac{6M_B^2}{\bar{E}h^3}\left(0.758-0.143\upsilon+\bar{\lambda}_{2D}\right)^2 0.6227 \end{aligned} \tag{6.38}$$

$$\begin{aligned} G_{II2D} &= \frac{6M_B^2}{\bar{E}h^3}\left(1+\frac{\chi_p(\upsilon)}{2.697}\right)^2 0.3773 \\ &= \frac{6M_B^2}{\bar{E}h^3}\left(1.400+0.236\upsilon\right)^2 0.3773 \end{aligned} \tag{6.39}$$

The mode mixity ratio G_{I2D}/G_{II2D} is given as

$$\rho_{2D} = G_{I2D}/G_{II2D} = \frac{1}{0.6059}\left(\frac{0.758-0.143\upsilon+\bar{\lambda}_{2D}}{1.400+0.236\upsilon}\right)^2 \tag{6.40}$$

and the ratio of ERR contribution from the through thickness shear effect G_{2DS} to G_J, i.e. G_{2DS}/G_J

$$\eta_{2D} = G_{2DS}/G_J = 0.6227\bar{\lambda}_{2D}\left[\bar{\lambda}_{2D}+2\left(1-\frac{\chi_p(\upsilon)}{4.450}\right)\right]\left\{0.6227\left(1-\frac{\chi_p(\upsilon)}{4.450}\right)^2+0.3773\left(1+\frac{\chi_p(\upsilon)}{0.3773}\right)^2\right\}^{-1} \tag{6.41}$$

with

$$\begin{aligned} \bar{\lambda}_{2D} &= \frac{P_B}{\beta_{4-2D}M_B} = 3.442\left((1-\upsilon^2)\varphi_p\right)^{1/2}\left(\frac{pR_B}{Eh}\right)^{1/3} \\ &= 3.442\left((1-\upsilon^2)\varphi_p\right)^{1/2}\frac{1}{f_p(\upsilon)}\frac{\delta}{R_B} \end{aligned} \tag{6.42}$$

The parameter $\bar{\lambda}$ in Eq. (6.40) can have the following alternative expressions by using Eq. (6.22).

$$\bar{\lambda}_{2D} = \bar{\phi}(\nu)\left(\frac{pR_B}{nEt}\right)^{1/3} = \bar{\phi}(\nu)\frac{1}{f(\nu)}\frac{\delta}{R_B} = \bar{\phi}(\nu)\left(\frac{p\delta}{f(\nu)nEt}\right)^{1/4} \tag{6.43}$$

where

$$\bar{\phi}_{2D}(\nu) = 3.442\left((1-\nu^2)\varphi\right)^{1/2} \tag{6.44}$$

Again, the mode mixity decreases with the increases in the blister radius R_B and approaches to zero when $R_B \to \infty$. Consequently, the interface fracture toughness also decreases with the increases in the blister radius R_B. When R_B approaches to zero, the mode mixity G_{I2D}/G_{II2D} varies between 0.528 at $\upsilon = 0$ and 0.084 at $\upsilon = 0.5$. It is mode II dominated fracture. Again, the total ERR G_{2D} is larger in general than G_J in Eq. (6.24) due to the through thickness shear force contribution. However, the numerical simulation in the work [168] agree well the G_J in Eq. (6.24) for a single layered thin layer material in the membrane limit. This suggests that the through thickness shear force contribution disappears at the membrane limit for monolayer graphene membranes; however, it should be taken into account for multi-layered graphene membranes. To account for the sliding factor $S(n)$, $\bar{\lambda}_{2D}$ in Eqs. (6.38)-(6.41) is replaced by λ_{2D} similar as defined (6.36).

6.4 Adhesion energy of multilayer graphene membranes using circular blister test under pressure loading

Figure 6-2 (a) schematically shows a circular blister test to determine the adhesion toughness of mono- and multi-layered graphene membranes under pressure loading [159]. The thickness of mono- and multi-layered graphene membranes is in the nanometre range. It is expected that the 2D elasticity partition theory is to provide more accurate results in the prediction of interface toughness. The 2D elasticity partition theory is considered at first, then the studies of using Euler beam/the classic plate partition theory and Timoshenko beam/the first order shear deformable plate partition theory are presented in the next for comparison. The results are compared with test data from ref. [159].

From previous section, at the membrane limit, the effective bending moment and crack tip forces are

$$M_B = \frac{nt}{4}\frac{\left(nEtp^2R_B^2\right)^{1/3}}{\left[3(1-\nu^2)\varphi_p(\nu)\right]^{1/2}} \tag{6.45}$$

$$N_B = \left(nEtp^2R_B^2\right)^{1/3}\varphi_p(\nu) \tag{6.46}$$

Where the *h* in (6.17) and (6.18) is expressed as *nt* in (6.45) and (6.46).

The ratio $\eta_{2D} = G_{2DS}/G_J$ is

$$\eta_{2D} = \frac{2.491\lambda(\lambda + 1.516 - 0.286\nu)}{4.390 + 0.457\nu + 0.135\nu^2} \tag{6.47}$$

The work [159] finds the value of $Et = 347 N/m$ with $E \approx 1TPa$. Taking Poisson ratio ν to be 0.16 as in the work [159], $\varphi(0.16) = 0.3099$, $f(0.16) = 0.6907$, $\phi(0.16) = 0.4502$ and $\bar{\phi}(0.16) = 1.891$. Then, some essential equations above become

$$G_J = 0.4502\left(\frac{p^4 R_B^4}{nEt}\right)^{1/3} = 1.978 nEt\left(\frac{\delta_m}{R_B}\right)^4 = 0.652 p\delta_m \tag{6.48}$$

$$G_{2DS} = \eta_{2D} G_J = 0.5577\lambda(1.470 + \lambda) G_J \tag{6.49}$$

Using 2D elasticity partition theory:

$$G_{II\,2D} = 0.6988 G_J \tag{6.50}$$

$$\rho_{2d} = \frac{G_{I\,2D}}{G_{II\,2D}} = 0.7984(0.7351 + \lambda)^2 \tag{6.51}$$

$$\bar{\lambda}_{2d} = 1.891\left(\frac{pR_B}{nEt}\right)^{1/3} = 2.738\frac{\delta}{R_B} = 2.074\left(\frac{p\delta}{nEt}\right)^{1/4} \tag{6.52}$$

Using Euler beam partition theory:

$$\rho_E = \frac{G_{IE}}{G_{IIE}} = \frac{0.922 - 0.636\upsilon}{1.272 + 0.865\upsilon + 0.0674\upsilon^2} \tag{6.53}$$

Using Timoshenko beam partition theory:

$$\rho_T = \frac{G_{IT}}{G_{IIT}} = \frac{1}{3}\left(\frac{1.180 + 0.106\upsilon}{0.461 - 0.318\upsilon + \lambda_T}\right)^{-2} \tag{6.54}$$

$$\begin{aligned} \bar{\lambda}_T = \frac{P_B}{\beta_{4-T} M_B} &= 2\left(\frac{2(1+\upsilon)\varphi_p}{\kappa}\right)^{1/2}\left(\frac{pR_B}{Eh}\right)^{1/3} \\ &= 2\left(\frac{2(1+\upsilon)\varphi_p}{\kappa}\right)^{1/2}\frac{1}{f_p(\upsilon)}\frac{\delta}{R_B} \end{aligned} \tag{6.55}$$

Note that in the work [159] $G_J = 0.655 p\delta$, which is very close to Eq. (6.48) calculated above. In the following, the pressure p, the centre deflection δ and the radius R_B of the multilayer graphene membrane blisters in work [159] are measured from the Figure S4, S2 and S3 in work [159], respectively. The results are recorded in Table 6-1 to Table 6-5 for the mono-, two-, three-, four- and five-layer graphene membrane blisters respectively. To keep

consistency with the work [159], results are calculated using the pressure p and centre deflection δ meaning that $G_J = 0.652 p\delta$ and $\bar{\lambda}_{2D} = 2.074\left(\frac{p\delta}{nEt}\right)^{1/4}$ are used.

The average adhesion energies (G) using 2D elasticity partition are 0,424, 0.362, 0.389, 0.348 and 0.359 J/m^2 for the mono-, two-, three-, four- and five-layer graphene membrane blisters, respectively, which correspond to the following mode mixities $\rho_{2D} = G_{I2D}/G_{II2D} = 0.431, 0.714, 0.794, 0.792 \text{and } 0.786$. The large increase of the mode mixity occurs between monolayer and two-layer graphene membrane blisters, which results in a big drop in adhesion energies. The adhesion energies have no significant changes afterwards as there are no significant mode mixity changes. An overall average adhesion energy of multilayer graphene membrane blisters using 2D elasticity partition is $G = 0.364\, J/m^2$ with $\rho_{2D} = G_{I2D}/G_{II2D} = 0.764$. These results are shown in the Table 6-1 to Table 6-6 below.

For single layer graphene membranes there is no difference between using 2D elasticity, Euler beam and Timoshenko beam partition theories to calculate the interface adhesion energy except of mode I to mode II ratio. Euler partition theory predicts the constant ratio 0.581 of mode I to mode II for single and multi-layered graphene membrane without taking the sliding effect into account. Timoshenko partition theory predicts same ratio of mode I to mode II for single layered graphene membrane but different ratio for multi-layered graphene membrane with accounting the sliding effect. However, Timoshenko partition theory shows a mode II dominant mixed mode partition which has no good correlation with test data. These results are presented in Table 6-7 to Table 6-18.

The average adhesion energy of a monolayer graphene blister from the pressure loading blister test data [159] is reported as $G = 0.45 J/m^2$ whereas the multi-layered specimens have an average adhesion energy of $G = 0.31 J/m^2$. An overall average adhesion energy of multilayer graphene membrane blisters using 2D elasticity partition is $G = 0.364\, J/m^2$. It can be concluded that the 2D elasticity partition theory shows the best agreement with the data from the experimental results.

Finally, the mode I and mode II critical ERRs can be estimated using the linear failure criterion and the results in Table 6-6 based on 2D elasticity partition method. From the studies conducted in chapter 2 section 2.4 and chapter 3 it is evident that the linear failure

criterion provides the accurate results for the thin layer brittle interface delamination. The critical mode I and mode II ERRs are obtained as follows.

$$G_{IIc} = (\rho_1 - \rho_m)\left(\frac{\rho_1}{G_{II\,m}} - \frac{\rho_m}{G_{II1}}\right)^{-1} = 0.683\,J/m^2 \tag{6.56}$$

and

$$G_{Ic} = \rho_1 G_{IIc}\left(\frac{G_{IIc}}{G_{II1}} - 1\right)^{-1} = 0.226\,J/m^2 \tag{6.57}$$

In the next section, the circular blister delamination under point loading is studied to show the validity of using 2D elasticity partition theory und linear failure criterion to predict the adhesion energy of layered graphene membranes.

6.5 Adhesion energy of multilayer graphene membranes using circular blister test under point loading

Figure 6-2 (b) shows a sketch of delamination test of a circular blister of radius R_B under point load P. At small deflection, within the linear range, from the work [166,167], at the membrane limit, the effective bending moment and crack tip forces are

$$M_B = \frac{h}{4}\frac{\left[EhP^2/(\pi^2 R_B^2)\right]^{1/3}}{\left[3(1-\upsilon^2)\varphi_P(\upsilon)\right]^{1/2}} \tag{6.58}$$

$$N_B = \left[EhP^2/(\pi^2 R_B^2)\right]^{1/3}\varphi_P(\upsilon) \tag{6.59}$$

$$P_B = \frac{P}{2\pi R_B} \tag{6.60}$$

The analytical model for a point loaded [166,167], blister is very much the same as the model for the pressure load developed above. Some essential formulas are presented here. The Poisson's ratio dependent parameter $\varphi(\nu)$ can be obtained by fitting a curve to the data in Fig.15 from the work [166] as

$$\varphi(\upsilon) = 0.418\nu^3 - 0.006\nu^2 + 0.25\nu + 0.422 \tag{6.61}$$

The deflection δ at the centre of the blister is

$$\delta = f_P(\upsilon)\left(\frac{PR_B^2}{\pi Eh}\right)^{1/3} \tag{6.62}$$

and $f(\nu)$ now becomes

$$f(\upsilon) = \frac{1}{2\varphi(\upsilon)} + 2\varphi^2(\upsilon)\left(1-\upsilon^2\right) \tag{6.63}$$

The parameter $\bar{\lambda}_T$ for Timoshenko mixed mode partition theory becomes

$$\begin{aligned}\bar{\lambda}_T &= \frac{P_B}{\beta_{4-T}M_B} = 2\left(\frac{2(1+\upsilon)\varphi_P}{\kappa}\right)^{1/2}\left(\frac{P}{\pi R_B Eh}\right)^{1/3} \\ &= 2\left(\frac{2(1+\upsilon)\varphi_P}{\kappa}\right)^{1/2}\frac{1}{f_P(\upsilon)}\frac{\delta}{R_B}\end{aligned} \tag{6.64}$$

The parameter $\bar{\lambda}_{2D}$ for 2D elasticity mixed mode partition theory becomes

$$\begin{aligned}\bar{\lambda}_{2D} &= \frac{P_B}{\beta_{4-2D}M_B} = 3.442\left((1-\upsilon^2)\varphi_P\right)^{1/2}\left(\frac{P}{\pi R_B Eh}\right)^{1/3} \\ &= 3.442\left((1-\upsilon^2)\varphi_P\right)^{1/2}\frac{1}{f_P(\upsilon)}\frac{\delta}{R_B}\end{aligned} \tag{6.65}$$

Then by replacing the pressure load p with $\frac{P}{\pi R_B^2}$ in Eqs. (6.24) where P represents the point load. The energy release rate G_J from point loading can be calculated as follows:

$$G_J = \phi(\upsilon)\left(\frac{P^4}{\pi^4 R_B^4 nEt}\right)^{1/3} = \phi(\upsilon)\frac{nEt}{f^4(\upsilon)}\left(\frac{\delta}{R_B}\right)^4 = \phi(\upsilon)\frac{P\delta}{\pi R_B^2 f(\upsilon)} \tag{6.66}$$

When taking Poisson's ratio to be 0.16 [159], $\varphi(0.16) = 0.4636$, $f(0.16) = 1.4974$, $\phi(0.16) = 0.3743$, $\bar{\phi}(0.16) = 2.3134$ and $\chi(0.16) = 2.1588$. Therefore, Eqs. (6.66 and (6.65) become

$$G_J = 0.3743\left(\frac{P^4}{\pi^4 R_B^4 nEt}\right)^{1/3} = 0.07445nEt\left(\frac{\delta}{R_B}\right)^4 = 0.2500\frac{P\delta}{\pi R_B^2} \tag{6.67}$$

Using 2D elasticity partition theory:

$$\bar{\lambda}_{2D} = 2.3134\left(\frac{P}{\pi R_B nEt}\right)^{1/3} = 1.5449\frac{\delta}{R_B} = 2.0913\left(\frac{P\delta}{\pi R_B^2 nEt}\right)^{1/4} \tag{6.68}$$

$$G_{S2D} = \eta_{2D}G_J = 0.4486\lambda_{2D}\left(1.0298+\lambda_{2D}\right)G_J \tag{6.69}$$

$$G_{II\,2D} = 0.8811G_J \tag{6.70}$$

$$\rho = \frac{G_{I2D}}{G_{II2D}} = 0.5091\left(0.5149 + \lambda_{2D}\right)^2 \tag{6.71}$$

From Eq. (6.71) it can be seen that $\rho = 0.135$ for monolayer graphene in the point loading condition ($\lambda = 0$), which is much smaller than that calculated for the pressure loading condition $\rho = 0.431$. The adhesion energy for the monolayer graphene in the point loading can be calculated to be $G = 0.550\,J/m^2$ using $G_{Ic} = 0.226\,J/m^2, G_{IIc} = 0.683\,J/m^2$ (determined from pressure loading in section 6.4) and a linear failure criterion. Obviously, the adhesion energy for the monolayer graphene in the point loading is larger than $G = 0.424\,J/m^2$ predicted in the pressure loading case.

The adhesion energy for multilayer graphene under point loading can be estimated in a similar way with experimental results in work [160]. The work [160] reports the measurement of adhesion energy of five-layer graphene membrane blisters, that is $G = 0.151\,J/m^2$. Unlike the work [159] where the blister is under a pressure load, the work [160] uses nanoparticles acting as a point load. An average blister possesses a radius R_B in the range $250-300nm$ and height δ in the range $50-70nm$. The work [160] used the formula $G = 0.0625nEt\left(\delta/R_B\right)^4$ with $E = 0.5\,TPa$ and $nt = 1.7\,nm$. It is seen that the value of E is half of that in the work [160] and $n \approx 5$. The adhesion energy is reported to be $G = 0.151\,J/m^2$ meaning that $\delta/R_B = 0.2309$. Eq. (6.67) gives $G_J = 0.180\,J/m^2$. The numerical results in recent work [168] show that Eq. (6.67) gives accurate calculations. When using $E = 1.0\,TPa$ as in the work [159] $G_J = 0.360\,J/m^2$, which is much larger than $G_J = 0.288\,J/m^2$ for the pressure load.

To explain the reason, again consider the mode mixity. Using Eqs (6.67) and (6.68) for the point loaded blister with $\delta/R_B = 0.2309$, $E = 1.0\,TPa$, $nt = 1.7\,nm$ and $n = 5$, the total ERR G can be obtained as $G = 0.438\,J/m^2$, which is very close to $G = 0.424\,J/m^2$ for the monolayer graphene membrane blister under a pressure load from Table 6-6. Eq. (6.71) gives the mode mixity to be $\rho = 0.381$ which is very close to $\rho = 0.431$ for the monolayer graphene membrane blister under a pressure load from Table 6-6.

The total ERR for point loading blister test (using $E = 1.0\,TPa$) is calculated as $G = 0.438\,J/m^2$ with 2D elasticity partition theory considering sliding effect. The total ERR

G is calculated as $0.438\,J/m^2$ as well by using $G_{Ic}=0.226\ J/m^2$, $G_{IIc}=0.683\,J/m^2$, $\rho=0.381$ and a linear failure criterion. The interface fracture toughness $G_{Ic}=0.226\,J/m^2$ and $G_{IIc}=0.683\,J/m^2$ are material properties, which are determined from the pressure loading case. The mode mixity $\rho=0.381$ is calculated from five-layer graphene under point loading using 2D elasticity partition theory. The result obtained from point loading using 2D elasticity partition theory has the excellent correlation with that calculated using material mode I and mode II fracture toughness and linear failure criterion.

Except of the differences in prediction for ERR mode I and mode II mixed mode ratio ρ, the same adhesion energy $G=0.360J/m^2$, (G is identical as for G_J) are obtained for monolayer graphene membrane by using 2D elasticity, Euler beam and Timoshenko beam partition theories respectively; the mixed mode I and mode II ratio ρ is 0.135, 0.581 and 0.039 respectively. It can be seen that the Euler beam partition theory predicts the highest mode I to mode II ratio, the Timoshenko beam theory gives the lowest ratio of mode I to mode II ratio and 2D elasticity theory is in the middle. The same trends can be observed from five layer-graphene membranes for mode I to mode II ratio, they are 0.381, 0.581 and 0.132 respectively. The adhesion energy $G=0.438J/m^2,0.360J/m^2,0.485J/m^2$ are calculated by using 2D elasticity, Euler beam and Timoshenko beam partition theories respectively. The results of adhesion toughness under point load for five-layer graphene membranes by using 2D elasticity, Euler beam and Timoshenko beam partition theories are represented in Table 6-19. It can be seen that 2D elasticity partition theory predicts the adhesion energy $0.438J/m^2$, which has an excellent agreement with the results calculated from $G_{Ic}=0.226\ J/m^2$, $G_{IIc}=0.683\,J/m^2$, $\rho=0.381$ and the linear failure criterion.

6.6 Conclusions

The presence of sliding in multilayered graphene membranes increases the fracture mode ratio G_I/G_{II}, leading to a decrease in adhesion toughness measurements when using the circular blister test. In the case of a silicon oxide substrate and pressure loading [159], the mode mixity jumps up from 43% in the monolayer graphene membranes to above 71% in the two-layer graphene membranes. This increase in the mode mixity has the effect of lowering

the adhesion toughness G_c from $0.424\,J/m^2$ to $0.362\,J/m^2$. As the number of graphene layers is increased further, the mode mixity increases slightly and the average adhesion toughness of the multi-layered membranes is $G = 0.364\,J/m^2$. The critical mode I and mode II adhesion toughness are found to be $G_{Ic} = 0.226\,J/m^2$ and $G_{IIc} = 0.683\,J/m^2$, respectively using linear failure criterion.

In the case of a silicon oxide substrate and point loading [160], the mode mixity jumps from 14% in the monolayer graphene membranes to above 38% in the multilayer graphene membranes, while the adhesion toughness G_c falls down from $0.550\,J/m^2$ to $0.438\,J/m^2$. The adhesion toughness G_c in general loading conditions can be determined accurately using the critical mode I and mode II adhesion toughness $G_{Ic} = 0.226\,J/m^2$, $G_{IIc} = 0.683\,J/m^2$ and a linear failure criterion.

The studies presented in this chapter show that adhesion energy of mono-multilayered graphene membranes can be determined by mechanical models using linear failure criterion and 2D elasticity partition theory considering sliding effect. It is evident that the prediction of interface delamination of microscopic thin layers is governed by 2D elasticity partition theory.

Table 6-1: Adhesion toughness of monolayer graphene membranes (2D.)

$p\ (MPa)$	$\delta\ (\mu m)$	$R_B\ (\mu m)$	$\lambda\ (p\delta)$	$G_J\ (J/m^2)\ (p\delta)$	$G\ (J/m^2)$	$\rho = G_{I2D}/G_{II2D}$
			$p_0 \approx 3.18(MPa)$			
1.709	0.363	2.492	0	0.405	0.405	0.431
1.514	0.396	2.710	0	0.391	0.391	0.431
1.267	0.463	2.934	0	0.382	0.382	0.431
1.096	0.496	3.171	0	0.354	0.354	0.431
			Group Average	0.383	0.383	0.431
			$p_0 \approx 3.55(MPa)$			
1.648	0.405	2.756	0	0.435	0.435	0.431
1.429	0.456	2.947	0	0.425	0.425	0.431
1.242	0.493	3.168	0	0.400	0.400	0.431
			Group Average	0.420	0.420	0.431
			$p_0 \approx 3.95(MPa)$			
1.632	0.437	2.964	0	0.465	0.465	0.431
1.547	0.466	3.021	0	0.470	0.470	0.431
1.320	0.509	3.252	0	0.438	0.438	0.431
			Group Average	0.458	0.458	0.431
			$p_0 \approx 4.10(MPa)$			
1.494	0.475	3.208	0	0.463	0.463	0.431
1.429	0.502	3.376	0	0.468	0.468	0.431
1.255	0.514	3.513	0	0.421	0.421	0.431
			Group Average	0.450	0.450	0.431
			Total Average	0.424	0.424	0.431
			The Work, ref [159]	0.450	0.450	0.431

Table 6-2: Adhesion toughness of two-layer graphene membranes (2D.)

$p\,(MPa)$	$\delta\,(\mu m)$	$R_B\,(\mu m)$	λ $(p\delta)$	$G_J\,(J/m^2)$ $(p\delta)$	$G\,(J/m^2)$	$\rho = G_{I2D}/G_{II2D}$
			$p_0 \approx 3.25(MPa)$			
1.684	0.288	2.401	0.213	0.316	0.380	0.718
1.471	0.319	2.573	0.211	0.306	0.367	0.715
1.284	0.345	2.738	0.208	0.289	0.345	0.711
			Group Average	0.304	0.364	0.715
			$p_0 \approx 3.67(MPa)$			
1.380	0.341	2.830	0.212	0.307	0.367	0.715
1.189	0.376	2.978	0.209	0.291	0.348	0.711
1.085	0.407	3.146	0.208	0.288	0.344	0.711
			Group Average	0.295	0.353	0.712
			$p_0 \approx 4.35(MPa)$			
1.076	0.456	3.322	0.214	0.320	0.384	0.719
0.901	0.542	3.467	0.214	0.318	0.382	0.718
0.756	0.583	3.679	0.208	0.287	0.343	0.710
			Group Average	0.308	0.370	0.716
			Total Average	0.303	0.362	0.714
			The Work, ref [159]			0.431

Table 6-3: Adhesion toughness of three-layer graphene membranes (2D.)

$p\,(MPa)$	$\delta\,(\mu m)$	$R_B\,(\mu m)$	λ $(p\delta)$	$G_J\,(J/m^2)$ $(p\delta)$	$G\,(J/m^2)$	$\rho = G_{I2D}/G_{II2D}$
			$p_0 \approx 3.25(MPa)$			
1.623	0.280	2.467	0.259	0.296	0.370	0.789
1.376	0.339	2.615	0.261	0.304	0.380	0.792
			Group Average	0.300	0.375	0.791
			$p_0 \approx 3.67(MPa)$			
1.425	0.334	2.862	0.262	0.310	0.388	0.794
			Group Average	0.310	0.388	0.794
			$p_0 \approx 4.35(MPa)$			
1.210	0.411	3.286	0.265	0.325	0.408	0.799
1.020	0.478	3.405	0.264	0.318	0.399	0.797
			Group Average	0.321	0.404	0.798
			Total Average	0.311	0.389	0.794
			The Work, ref [159]			0.431

Table 6-4: Adhesion toughness of four-layer graphene membranes (2D.)

$p\,(MPa)$	$\delta\,(\mu m)$	$R_B\,(\mu m)$	$\lambda\ (p\delta)$	$G_J\ (J/m^2)\ (p\delta)$	$G\,(J/m^2)$	$\rho = G_{I2D}/G_{II2D}$
			$p_0 \approx 3.25(MPa)$			
1.535	0.265	2.664	0.258	0.265	0.331	0.787
1.420	0.271	2.845	0.254	0.251	0.313	0.782
			Group Average	0.258	0.322	0.785
			$p_0 \approx 3.67(MPa)$			
1.407	0.319	2.998	0.264	0.293	0.368	0.797
			Group Average	0.293	0.368	0.797
			$p_0 \approx 4.35(MPa)$			
1.118	0.414	3.513	0.266	0.302	0.380	0.801
			Group Average	0.302	0.380	0.801
			Total Average	0.278	0.348	0.792
			The Work, ref [159]			0.431

Table 6-5: Adhesion toughness of five-layer graphene membranes (2D.)

$p\,(MPa)$	$\delta\,(\mu m)$	$R_B\,(\mu m)$	$\lambda\ (p\delta)$	$G_J\ (J/m^2)\ (p\delta)$	$G\,(J/m^2)$	$\rho = G_{I2D}/G_{II2D}$
			$p_0 \approx 3.25(MPa)$			
1.700	0.244	2.459	0.253	0.271	0.337	0.780
1.621	0.252	2.587	0.252	0.267	0.332	0.778
1.417	0.305	2.686	0.256	0.282	0.351	0.784
			Group Average	0.273	0.340	0.781
			$p_0 \approx 3.67(MPa)$			
1.596	0.276	2.861	0.257	0.287	0.358	0.786
1.517	0.289	2.961	0.257	0.286	0.356	0.785
1.430	0.306	3.017	0.257	0.285	0.356	0.785
			Group Average	0.286	0.356	0.785
			$p_0 \approx 4.35(MPa)$			
1.297	0.376	3.276	0.264	0.318	0.399	0.796
1.181	0.384	3.372	0.259	0.296	0.369	0.789
1.056	0.436	3.483	0.260	0.300	0.375	0.790
			Group Average	0.305	0.381	0.792
			Total Average	0.288	0.359	0.786
			The Work, ref [159]			0.431

Table 6-6: Average adhesion toughness of multilayer graphene membranes (2D.)

Graphene Membranes	$G_J\left(J/m^2\right)$		$G\left(J/m^2\right)$		$\rho = G_{I2D}/G_{II2D}$	
	Present	Work, ref [159]	Present	Work, ref [159]	Present	Work, ref [159]
Monolayer	0.424	0.450	0.424	0.450	0.431	0.431
Multilayer	0.295	0.310	0.364	0.310	0.764	0.431

Table 6-7: Adhesion toughness of monolayer graphene membranes (Euler)

$p\,(MPa)$	$\delta\,(\mu m)$	$R_B\,(\mu m)$	λ $(p\delta)$	$G_J\,(J/m^2)$ $(p\delta)$	$G\,(J/m^2)$	$\rho_E = G_{IE}/G_{IIE}$
			$p_0 \approx 3.18(MPa)$			
1.709	0.363	2.492	0	0.405	0.405	0.581
1.514	0.396	2.710	0	0.391	0.391	0.581
1.267	0.463	2.934	0	0.382	0.382	0.581
1.096	0.496	3.171	0	0.354	0.354	0.581
			Group Average	0.383	0.383	0.581
			$p_0 \approx 3.55(MPa)$			
1.648	0.405	2.756	0	0.435	0.435	0.581
1.429	0.456	2.947	0	0.425	0.425	0.581
1.242	0.493	3.168	0	0.400	0.400	0.581
			Group Average	0.420	0.420	0.581
			$p_0 \approx 3.95(MPa)$			
1.632	0.437	2.964	0	0.465	0.465	0.581
1.547	0.466	3.021	0	0.470	0.470	0.581
1.320	0.509	3.252	0	0.438	0.438	0.581
			Group Average	0.458	0.458	0.581
			$p_0 \approx 4.10(MPa)$			
1.494	0.475	3.208	0	0.463	0.463	0.581
1.429	0.502	3.376	0	0.468	0.468	0.581
1.255	0.514	3.513	0	0.421	0.421	0.581
			Group Average	0.450	0.450	0.581
			Total Average	0.424	0.424	0.581
			The Work, ref [159]	0.45	0.45	0.431

Table 6-8: Adhesion toughness of two-layer graphene membranes (Euler)

$p\,(MPa)$	$\delta\,(\mu m)$	$R_B\,(\mu m)$	$\lambda\ (p\delta)$	$G_J\ (J/m^2)\ (p\delta)$	$G\,(J/m^2)$	$\rho_E = G_{IE}/G_{IIE}$
			$p_0 \approx 3.25(MPa)$			
1.684	0.288	2.401	0.213	0.316	0.316	0.581
1.471	0.319	2.573	0.211	0.306	0.306	0.581
1.284	0.345	2.738	0.208	0.289	0.289	0.581
			Group Average	0.304	0.304	0.581
			$p_0 \approx 3.67(MPa)$			
1.380	0.341	2.830	0.212	0.307	0.307	0.581
1.189	0.376	2.978	0.209	0.291	0.291	0.581
1.085	0.407	3.146	0.208	0.288	0.288	0.581
			Group Average	0.295	0.295	0.581
			$p_0 \approx 4.35(MPa)$			
1.076	0.456	3.322	0.214	0.320	0.320	0.581
0.901	0.542	3.467	0.214	0.318	0.318	0.581
0.756	0.583	3.679	0.208	0.287	0.287	0.581
			Group Average	0.308	0.308	0.581
			Total Average	0.303	0.303	0.581
			The Work, ref [159]			0.431

Table 6-9: Adhesion toughness of three-layer graphene membranes (Euler)

$p\,(MPa)$	$\delta\,(\mu m)$	$R_B\,(\mu m)$	$\lambda\ (p\delta)$	$G_J\ (J/m^2)\ (p\delta)$	$G\,(J/m^2)$	$\rho_E = G_{IE}/G_{IIE}$
			$p_0 \approx 3.25(MPa)$			
1.623	0.280	2.467	0.259	0.296	0.296	0.581
1.376	0.339	2.615	0.261	0.304	0.304	0.581
			Group Average	0.300	0.300	0.581
			$p_0 \approx 3.67(MPa)$			
1.425	0.334	2.862	0.262	0.310	0.310	0.581
			Group Average	0.310	0.310	0.581
			$p_0 \approx 4.35(MPa)$			
1.210	0.411	3.286	0.265	0.325	0.325	0.581
1.020	0.478	3.405	0.264	0.318	0.318	0.581
			Group Average	0.321	0.321	0.581
			Total Average	0.311	0.311	0.581
			The Work, ref [159]			0.431

Table 6-10: Adhesion toughness of four-layer graphene membranes (Euler)

$p\,(MPa)$	$\delta\,(\mu m)$	$R_B\,(\mu m)$	$\lambda\ (p\delta)$	$G_J\ (J/m^2)\ (p\delta)$	$G\,(J/m^2)$	$\rho_E = G_{IE}/G_{IIE}$
			$p_0 \approx 3.25(MPa)$			
1.535	0.265	2.664	0.258	0.265	0.265	0.581
1.420	0.271	2.845	0.254	0.251	0.251	0.581
			Group Average	0.258	0.258	0.581
			$p_0 \approx 3.67(MPa)$			
1.407	0.319	2.998	0.264	0.293	0.293	0.581
			Group Average	0.293	0.293	0.581
			$p_0 \approx 4.35(MPa)$			
1.118	0.414	3.513	0.266	0.302	0.302	0.581
			Group Average	0.302	0.302	0.581
			Total Average	0.278	0.278	0.581
			The Work, ref [159]			0.431

Table 6-11: Adhesion toughness of five-layer graphene membranes (Euler)

$p\,(MPa)$	$\delta\,(\mu m)$	$R_B\,(\mu m)$	$\lambda\ (p\delta)$	$G_J\ (J/m^2)\ (p\delta)$	$G\,(J/m^2)$	$\rho_E = G_{IE}/G_{IIE}$
			$p_0 \approx 3.25(MPa)$			
1.700	0.244	2.459	0.253	0.271	0.271	0.581
1.621	0.252	2.587	0.252	0.267	0.267	0.581
1.417	0.305	2.686	0.256	0.282	0.282	0.581
			Group Average	0.273	0.273	0.581
			$p_0 \approx 3.67(MPa)$			
1.596	0.276	2.861	0.257	0.287	0.287	0.581
1.517	0.289	2.961	0.257	0.286	0.286	0.581
1.430	0.306	3.017	0.257	0.285	0.285	0.581
			Group Average	0.286	0.286	0.581
			$p_0 \approx 4.35(MPa)$			
1.297	0.376	3.276	0.264	0.318	0.318	0.581
1.181	0.384	3.372	0.259	0.296	0.296	0.581
1.056	0.436	3.483	0.260	0.300	0.300	0.581
			Group Average	0.305	0.305	0.581
			Total Average	0.288	0.288	0.581
			The Work, ref [159]			0.431

Table 6-12: Average adhesion toughness of multilayer graphene membranes (Euler)

Graphene Membranes	$G_J\left(J/m^2\right)$		$G_J\left(J/m^2\right)$		$\rho_E = G_{IE}/G_{IIE}$	
	Present	Work, ref [159]	Present	Work, ref [159]	Present	Work, ref [159]
Monolayer	0.424	0.45	0.424	0.45	0.581	0.431
Multilayer	0.295	0.31	0.295	0.31	0.581	0.431

Table 6-13: Adhesion toughness of monolayer graphene membranes (Timo.)

$p\,(MPa)$	$\delta\,(\mu m)$	$R_B\,(\mu m)$	λ $(p\delta)$	$G_J\,(J/m^2)$ $(p\delta)$	$G\,(J/m^2)$	$\rho_T = G_{IT}/G_{IIT}$
			$p_0 \approx 3.18(MPa)$			
1.709	0.363	2.492	0	0.405	0.405	0.039
1.514	0.396	2.710	0	0.391	0.391	0.039
1.267	0.463	2.934	0	0.382	0.382	0.039
1.096	0.496	3.171	0	0.354	0.354	0.039
			Group Average	0.383	0.383	0.039
			$p_0 \approx 3.55(MPa)$			
1.648	0.405	2.756	0	0.435	0.435	0.039
1.429	0.456	2.947	0	0.425	0.425	0.039
1.242	0.493	3.168	0	0.400	0.400	0.039
			Group Average	0.420	0.420	0.039
			$p_0 \approx 3.95(MPa)$			
1.632	0.437	2.964	0	0.465	0.465	0.039
1.547	0.466	3.021	0	0.470	0.470	0.039
1.320	0.509	3.252	0	0.438	0.438	0.039
			Group Average	0.458	0.458	0.039
			$p_0 \approx 4.10(MPa)$			
1.494	0.475	3.208	0	0.463	0.463	0.039
1.429	0.502	3.376	0	0.468	0.468	0.039
1.255	0.514	3.513	0	0.421	0.421	0.039
			Group Average	0.450	0.450	0.039
			Total Average	0.424	0.424	0.039
			The Work, ref [159]	0.45	0.45	0.431

Table 6-14: Adhesion toughness of two-layer graphene membranes (Timo.)

$p\,(MPa)$	$\delta\,(\mu m)$	$R_B\,(\mu m)$	$\lambda\ (p\delta)$	$G_J\ (J/m^2)\ (p\delta)$	$G\,(J/m^2)$	$\rho_T = G_{IT}/G_{IIT}$
			$p_0 \approx 3.25(MPa)$			
1.684	0.288	2.401	0.323	0.316	0.376	0.088
1.471	0.319	2.573	0.333	0.306	0.366	0.090
1.284	0.345	2.738	0.339	0.289	0.347	0.091
			Group Average	0.304	0.363	0.090
			$p_0 \approx 3.67(MPa)$			
1.380	0.341	2.830	0.324	0.307	0.366	0.088
1.189	0.376	2.978	0.340	0.291	0.350	0.091
1.085	0.407	3.146	0.348	0.288	0.348	0.092
			Group Average	0.295	0.355	0.090
			$p_0 \approx 4.35(MPa)$			
1.076	0.456	3.322	0.369	0.320	0.391	0.096
0.901	0.542	3.467	0.420	0.318	0.400	0.106
0.756	0.583	3.679	0.426	0.287	0.362	0.107
			Group Average	0.308	0.384	0.103
			Total Average	0.303	0.367	0.094
			The Work, ref [159]			0.431

Table 6-15: Adhesion toughness of three-layer graphene membranes (Timo.)

$p\,(MPa)$	$\delta\,(\mu m)$	$R_B\,(\mu m)$	$\lambda\ (p\delta)$	$G_J\ (J/m^2)\ (p\delta)$	$G\,(J/m^2)$	$\rho_T = G_{IT}/G_{IIT}$
			$p_0 \approx 3.25(MPa)$			
1.623	0.280	2.467	0.305	0.296	0.349	0.085
1.376	0.339	2.615	0.349	0.304	0.367	0.092
			Group Average	0.300	0.358	0.089
			$p_0 \approx 3.67(MPa)$			
1.425	0.334	2.862	0.314	0.310	0.368	0.086
			Group Average	0.310	0.368	0.089
			$p_0 \approx 4.35(MPa)$			
1.210	0.411	3.286	0.336	0.325	0.389	0.090
1.020	0.478	3.405	0.378	0.318	0.390	0.098
			Group Average	0.321	0.390	0.094
			Total Average	0.311	0.372	0.091
			The Work, ref [159]			0.431

Table 6-16: Adhesion toughness of four-layer graphene membranes (Timo.)

$p\,(MPa)$	$\delta\,(\mu m)$	$R_B\,(\mu m)$	$\lambda\ (p\delta)$	$G_J\ (J/m^2)\ (p\delta)$	$G\,(J/m^2)$	$\rho_T = G_{IT}/G_{IIT}$
			$p_0 \approx 3.25(MPa)$			
1.535	0.265	2.664	0.268	0.265	0.306	0.078
1.420	0.271	2.845	0.256	0.251	0.288	0.076
			Group Average	0.258	0.297	0.077
			$p_0 \approx 3.67(MPa)$			
1.407	0.319	2.998	0.286	0.293	0.341	0.081
			Group Average	0.293	0.341	0.081
			$p_0 \approx 4.35(MPa)$			
1.118	0.414	3.513	0.317	0.302	0.358	0.087
			Group Average	0.302	0.358	0.087
			Total Average	0.284	0.332	0.082
			The Work, ref [159]			0.431

Table 6-17: Adhesion toughness of five-layer graphene membranes (Timo.)

$p\,(MPa)$	$\delta\,(\mu m)$	$R_B\,(\mu m)$	$\lambda\ (p\delta)$	$G_J\ (J/m^2)\ (p\delta)$	$G\,(J/m^2)$	$\rho_T = G_{IT}/G_{IIT}$
			$p_0 \approx 3.25(MPa)$			
1.700	0.244	2.459	0.267	0.271	0.312	0.078
1.621	0.252	2.587	0.262	0.267	0.307	0.077
1.417	0.305	2.686	0.305	0.282	0.332	0.085
			Group Average	0.273	0.317	0.080
			$p_0 \approx 3.67(MPa)$			
1.596	0.276	2.861	0.259	0.287	0.330	0.077
1.517	0.289	2.961	0.262	0.286	0.329	0.077
1.430	0.306	3.017	0.273	0.285	0.330	0.079
			Group Average	0.286	0.330	0.078
			$p_0 \approx 4.35(MPa)$			
1.297	0.376	3.276	0.309	0.318	0.376	0.085
1.181	0.384	3.372	0.306	0.296	0.349	0.085
1.056	0.436	3.483	0.337	0.300	0.360	0.090
			Group Average	0.305	0.362	0.087
			Total Average	0.288	0.336	0.082
			The Work, ref [159]			0.431

Table 6-18: Average adhesion toughness of multilayer graphene membranes (Timo.)

Graphene Membranes	$G_J\left(J/m^2\right)$		$G(J/m^2)$		$\rho_T = G_{IT}/G_{IIT}$	
	Present	Work, ref [159]	Present	Work, ref [159]	Present	Work, ref [159]
Monolayer	0.424	0.45	0.424	0.45	0.039	0.431
Multilayer	0.297	0.31	0.352	0.31	0.087	0.431

Table 6-19: Adhesion toughness of graphene membranes under point loading

Mixed Mode Partition Theory	$G_J\left(J/m^2\right)$	λ	$G_S\ (J/m^2)$	$G(J/m^2)$	$\rho = G_I/G_{II}$
$n=1, \delta/R_B = 0.2309, E = 1.0\ TPa,\ nt = 1.7\ nm$					
2D Elasticity Theory	0.360	0	0	0.360	0.135
Euler Beam Theory	0.360	0	0	0.360	0.581
Timoshenko Beam Theory	0.360	0	0	0.360	0.039
$n=5, \delta/R_B = 0.2309, E = 1.0\ TPa,\ nt = 1.7\ nm$					
2D Elasticity Theory	0.360	0.350	0.078	0.438	0.381
Euler Beam Theory	0.360	0	0	0.360	0.581
Timoshenko Beam Theory	0.360	0.360	0.125	0.485	0.132

Chapter 7 Conclusion and future work

7.1 Conclusions

Firstly, the performance of different mixed mode partition theories are reviewed via the assessments which were conducted by Wang-Harvey [22,23], it has been found that Euler beam partition theory with global partition provides the most accurate prediction for delamination toughness between two macroscopic layers. In the next, the analytical theories have been developed for predicting the crack propagation behaviour of post-local buckling-driven delamination in bilayer composite beams. The work has presented a more accurate analytical formula for total ERR G than that in Refs. [14,87] by developing a more accurate expression for the post-buckling mode shape and also by including the axial strain energy contribution from the intact part of beam; the accuracy of critical local-buckling strain is also a key factor in making accurate predictions. Three partition theories, namely, the Euler beam, Timoshenko beam and 2D elasticity partition theories are employed in the study for comparison of accuracy. Independent experimental tests by Kutlu and Chang [32] show that, in general, the analytical theory based on the Euler beam partition theory predicts the propagation behaviour very well and much better than the theories based on the Timoshenko beam and 2D elasticity partition theories. The thickness of the bilayer composite beam is in the range of millimetres.

The next important example is the thermally buckling-driven delamination of thermal barrier coatings used in aero-engines. The normalised approaches are developed based on the Euler beam, Timoshenko beam and 2D elasticity partition theories to predict the TBC interface crack delamination with minimum requiring the detail TBC material data. The TBC material system is simplified as two layer systems. The trends of crack development, propagation are clearly illustrated by using different partition methods. For specific G_{IC}=10N/m and G_{IIC}=50N/m used, the Euler beam theory predicts the earlier delamination and Timoshenko beam theory predicts the later crack propagation, the prediction of 2D elasticity partition is in the middle. The work provides some clear trends with minimum presence of real material data and it is particularly useful to develop the life prediction model for TBC material system with numerical method and experimental tests, which are planned in the future.

As another example of thin film delamination, the spontaneous spalling of α-alumina films grown by oxidation under room temperature is investigated. A hypothesis is made that

pockets of energy concentration (PECs) can be formed by pockets of stresses around the interface between a thin film and a thick substrate because of thermal effects, chemical effects and etc... Based on the PECs hypothesis, three mechanical models are developed analytically to predict some aspects of the process of thin film spallation failure including nucleation, stable and unstable growth, the size of spallation and final kinking off. The present mechanical model reveals a new failure mechanism of thin films under compressive residual stress and predict very well several aspects of the room temperature failure of α-alumina films grown by oxidation, including the initiation of unstable growth, and the size of spallation or kinking off. Spallation with both straight edge and circular edge are considered. The experimental results show that the three models predict the initiation of unstable growth and the size of spallation very well. However, only the 2D elasticity model predicts final kinking off well. The nucleation and stable growth of a separation bubble are solely driven by the PEC energy while the unstable growth is driven by both PEC energy and buckling. The final kinking off is controlled by the toughness of the interface and the film and the maximum PEC energy. The thickness of aluminum scales on the substrate is in the micrometre range.
The last example studied in this thesis is the prediction of interface adhesion energy, or interface fracture toughness. A mechanical model is developed to give a complete calculation and correct interpretation of the adhesion energy with consideration of the fracture mode mixity and the sliding effect in the determination of the adhesion energy for multi-layered graphene membranes using the blister test. The study demonstrates the accuracy of using 2D elasticity partition method for prediction the adhesion energy in nano-metre thickness range.

In conclusion, the brittle interface fracture of macroscopically thin beam, plate and shell layers is governed by the Euler beam, classical plate and shell partition theory instead of the 2D elasticity partition theory. A fracture or delamination on a brittle interface with layers of macroscopic thickness cannot propagate in the manner as an infinitesimally small growth. Instead, it does propagate with a finitely small growth [32]. Both the classical partition theory [24-29] and the 2D elasticity partition theory [14] assume an infinitesimally small growth. However, the classical partition theory is insensitive to the growth size, or in other words, the energy release rate (ERR) partitions converge at relatively large finite element mesh size [28]. In contrast, the 2D elasticity partition theory is very sensitive to the growth size, or in other words, ERR partitions converge at very small finite element mesh size [28] as assumed in the theory [14]. Consequently, it is given the name of ‘local partition theory’. It is important to note that ERR partitions based on 2D elasticity approach to the classical ones

when growth size increases [26]. It is seen that the classical partition theory represents the 'finitely small growth' physics very well.

The mechanical models developed in this thesis provide the analytical solutions to study the mechanics of interface delamination of thin-layer substrate material systems; it benefits the further experimental and numerical works to investigate the thin film delamination. The analytical models developed in this thesis provide convenient methods for researchers, designer to design a reliable thin film material systems.

7.2 Future work

Experimental and analytical works are required to develop thermal barrier coating life prediction model. Current normalised analytical model presented in chapter 4 shows only the trends of the TBC interface crack delamination with minimum presence of real material data, also the current analytical model is based on two-layer approach, the detailed experimental and analytical work on the TBC spallation is required to overcome the limitation of the current approach in chapter 4.

In chapter 5, a hypothesis is made that delamination can be driven by pockets of energy concentration (PECs) in the form of pockets of tensile stress and shear stress on and around the interface between a microscopic thin film and a thick substrate, a good prediction of the initiation of unstable growth of separation bubbles, the size of spallation and final kink-off angle are obtained; however, more evidence and details from experimental work are requied to verify the hypothesis completely. A clear direct extension is to study the well known telephone cord buckling phenomenon frequently occurred in thin films. A preliminary study in another PhD project has shown excellent predictions by the PEC model. This may extend the PEC model from idealised straight edged and circular plate to complicated geometry applications. Also, it is one of the main activity for the future work to apply the PEC model to study the thermal barrier coating delamination and spallation.

In the present work, the material elastic mismatch between top layer and substrate is neglected in the developed analytical models. In spite of the good correlation between the analytical models and the test data, it might be still useful to quantify the sensitivity of the analytical models to the material elastic mismatch.

References

1. B. Cotterell, J.R. Rice. Slightly curved or kinked cracks. International Journal of Fracture. Vol. 16, No. 2, April 1980.
2. R.V. Gold'stein, R.L. Salganik. Brittle fracture of solids with arbitrary cracks. International Journal of Fracture 10(4), December 1974.
3. A.G. Evans, J.W. Hutchinson. The thermomechanical integrity of thin films and multilayers. Acta Metall. Mater. 1995; 43:2507–2530.
4. J.W. Hutchinson. Stress and failure modes in thin films and multilayers. Notes for a DCAMM Course, Technical University of Denmark, October 1996.
5. H.H. Yu, M.Y. He, J.W. Hutchinson. Edge effects in thin film delamination. Acta. Mater. 2001; 49:93–107.
6. D.S. Baliant, J.W. Hutchinson. Mode II edge delamination of compressed thin films. Journal of Applied Mechanics 2001; 68:725–730.
7. H.H. Yu, J.W. Hutchinson. Delamination of thin film strips. The Solid Films 2003; 423:54–63.
8. M.Y. He, J.W. Hutchinson, A.G. Evans. A stretch/bend method for in situ measurement of the delamination toughness of coatings and films attached to substrates. Journal of Applied Mechanics 2011; 78:1–5.
9. S.R. Choi, J.W. Hutchinson, A.G. Evans. Delamination of multilayer thermal barrier coatings. Mechanics of Materials 1999; 31:431–447.
10. H.H. Yu, J.W. Hutchinson. Influence of substrate compliance on buckling delamination of thin films. International Journal of Fracture 2002; 113:39–55.
11. M.W. Moon, K.R. Le, K.H. Oh, J.W. Hutchinson. Buckle delamination on patterned substrates. Acta Materialia 2004; 52:3151–3159.
12. Z. Jia, C. Peng, J. Lou, T. Li. A map of competing buckling-driven failure modes of substrate-supported thin brittle films. Thin Solid Films 2012; 520:6576–6580.
13. W. Zhu, Y.C. Zhou, J.W. Guo, L. Yang, C. Lu. Quantitative characterization of the interfacial adhesion of Ni thin film on steel substrate: A compression-induced buckling delamination test. Journal of the Mechanics and Physics of Solids 2015; 74:19–37.
14. J.W. Hutchinson, Z. Suo. Mixed mode cracking in layered materials [J]. Advances in Applied Mechanics, 1992, 29: 63–191.

15. S. Hashemi, A.J. Kinloch, J.G. Williams. The analysis of interlaminar fracture in uniaxial fibre-polymer composites. Proceeding of the Royal Society A, 1990; A427:173–199.
16. A.J. Kinloch, Y. Wang, J.G. Williams, P. Yayla. The mixed-mode delamination of fibre composite materials. Composites Science and Technology 1993; 47:225–237.
17. M. Charalambides, A.J. Kinloch, Y. Wang, J.G. Williams. On the analysis of mixed-mode failure. International Journal of Fracture 1992; 54: 269–291.
18. S. Hashemi, A.J. Kinloch, G. Williams. Mixed-mode fracture in fiber-polymer composite laminates. In: O'Brien TK, editor. Composite materials: fatigue and fracture (third volume), ASTM STP 1110. Philadelphia, PA: American Society for Testing and Materials, 1991. pp. 143–168.
19. B.D. Davidson, P.L. Fariello, R.C. Hudson, V. Sundararaman. Accuracy assessment of the singular-field-based mode-mix decomposition procedure for the prediction of delamination. In: Hooper SJ, editor. Composite materials: testing and design (thirteenth volume), ASTM STP 1242. American Society for Testing and Materials, 1997, pp. 109–128.
20. B.D. Davidson, S.J. Gharibian, L.J. Yu. Evaluation of energy release rate-based approaches for predicting delamination growth in laminated composites. International Journal of Fracture 2000; 105:343–365.
21. B.D. Davidson, R.D. Bialaszewski, S.S. Sainath. A non-classical, energy release rate based approach for predicting delamination growth in graphite reinforced laminated polymeric composites. Composites Science and Technology 2006; 66:1479–1496.
22. C.M. Harvey, S. Wang. Experimental assessment of mixed-mode partition theories. Composite Structures 2012; 94:2057–2067.
23. C.M. Harvey, M.R. Eplett, S. Wang. Experimental assessment of mixed-mode partition theories for generally laminated composite beams. Composite Structures 2015; 124:10–18.
24. S. Wang, C.M. Harvey. Mixed mode partition in one dimensional fracture. Journal of Key Engineering Materials 2011; 462-63:616–621.
25. C.M. Harvey. Mixed-mode partition theories for one-dimensional fracture. PhD Thesis. March 2012, Loughborough University, UK.
26. S. Wang, L. Guan. On fracture mode partition theories. Computational Material Sciences 2012; 52:240–245.

27. S. Wang, C.M. Harvey. A theory of one-dimensional fracture. Composite Structures 2012; 94:758–767.
28. S. Wang, C.M. Harvey. Mixed mode partition theories for one dimensional fracture. Engineering Fracture Mechanics 2012; 79:329–352.
29. C.M. Harvey, S. Wang. Mixed-mode partition theories for one-dimensional delamination in laminated composite beams. Engineering Fracture Mechanics 2012; 96:737–759.
30. M, Conroy, B.F. Sørensen, A. Ivankovic. Combined numerical and experimental investigation of mode-mixity in beam like geometries. In: Proceedings of the 37th Annual Meeting of the Adhesion Society, Feburary 2014, San Diego, California, USA.
31. S. Dai, C.M. Harvey, S. Wang. Digital image correlation of mixed-mode delaminations. The 19th International Conference on Composite Structures (ICCS19) 5th –9th September 2016, Porto, Portugal.
32. Z. Kutlu, F. K. Chang. Composite panels containing multiple through-the-width delaminations and subjected to compression: Part II: experiments and verification. Composite Structures 1995; 31:297–314.
33. A.A. Griffith. The phenomena of rupture and flow in solids. Philosophical Transactions of the Royal Society of London, 1921, A 221, 163–98.
34. G. R. Irwin. Analysis of stresses and strain near the end of a crack traversing a plate. Journal of Applied Mechanics 24(3), 1957, 361–4.
35. G.R. Irwin. Fracture. Handbuch der Physik, 1958, 6, 551–90.
36. J.R. Rice. A path independent integral and the approximate analysis of strain concentration by notches and cracks. Journal of Applied Mechanics, 1968, 35, 379–86.
37. C.E. Inglis. Stresses in a plate due to the presence of cracks and sharp corners. The Institute of Naval Architects, 1913, 55, 219–41.
38. M.L. Williams. On the stress distribution at the base of a stationary crack. Journal of Applied Mechanics, 1957, 24, 109–15.
39. J.G. Williams. On the calculation of energy release rates for cracked laminates. Int J Fract. Mech. 1988; 36:101–19.
40. R.A. Schapery, B.D. Davidson. Prediction of energy release rate for mixed-mode delamination using classical plate theory. Appl Mech Rev 1990; 43: S281–7.

41. Z. Suo, J.W. Hutchinson. Interface crack between two elastic layers. Int J Fract Mech 1990; 43:1–18.
42. M.D. Thouless, A.G. Evans, M.F. Ashby, J.W. Hutchinson. The edge cracking and spalling of brittle plates. Acta Metall 1987; 35:1333–41.
43. M.D.Thouless. Fracture of a model interface under mixed mode loading. Acta Metall Matter 1990; 35:1135–40.
44. J. Wang, P. Qiao. Interface crack between two shear deformable elastic layers. J Mech Phys Solids 2004; 52:891–905.
45. C. Nguyen, A.J. Levy. An exact theory of interfacial debonding in layered elastic composites. Int J Solids Struct 2009; 46:2712–23.
46. Y. Yan, F. Shang. Cohesive zone modelling of interfacial delamination in PZT thin films. Int J Solids Struct 2009; 46:2739–49.
47. Z. Ouyang, G. Li. Nonlinear interface shear fracture of end notched flexure specimens. Int J Solids Struct 2009; 46:2659–68.
48. Z. Zou, S.R. Reid, S. Li, P.D. Soden. General expressions for energy release rates for delamination in composite laminates. Proc R Soc Lond A 2002; 458:645–67.
49. S. Li, S.R. Reid, Z. Zou. Modelling damage of multiple delaminations and transverse matrix cracking in laminated composites due to low velocity lateral impact. Compos Sci Technol 2005; 66:827–36.
50. Z. Suo. Delamination specimens for orthotropic materials. J Appl Mech 1990; 56:627–34.
51. M.L. Williams. The stresses around a fault or crack in dissimilar media. Bull. seism. Sot. Am. 49, W-204 (1959).
52. A.H. England. A crack between dissimilar media. Transactions of the ASME, June 1965.
53. B.M. Malyshev, R.L. Salganik. The strength of adhesive joints using the theory of cracks. ht. J. Fracture 1, 114-128 (1965).
54. J.R. Rice. Elastic fracture mechanics concepts for interfacial cracks. J. appl. Mech. 55, 98-103 (1988).
55. J.R. Rice, G.C. Sib. Plane problems of cracks in dissimilar media. J. appl. Mech. 32, 418-423 (1965).
56. J.W. Hutchinson, M.E. Mear, J.R. Rice. Crack paralleling an interface between dissimilar materials. J. appl. Mech. 54, 828-832 (1987).
57. M. Comninou. The interface crack. J. appl. Mech. 44, 631-636 (1977).

58. C.T. Sun, C.T. Jih. On strain energy release rates for interfacial cracks in bimaterial media. Engng Fracture Mech. 28, 13-20 (1987).
59. C.T. Sun, M.G. Manoharan. Strain energy release rates of an interfacial crack between two orthotropic media. J. compos. Mater. 23, 460478 (1989).
60. G. Manoharan, C.T. Sun. Strain energy release rates of an interfacial crack between two anisotropic solids under uniform axial strain. Compos. Sci. Technol. 39, 99-l 16 (1990).
61. I.S. Raju, J.H. Jr. Crews, M. A. Aminpour. Convergence of strain energy release rate components for edge-delaminated composite laminates. Engineering Fracture Mechanics Vol. 30, No. 3, pp. 383-396, 1988.
62. R. Krueger, D. Goetze. Influence of Finite Element software on energy release rates computed using the virtual crack closure technique. NIA Report No. 2006-06, NASA/CR-2006-214523, 2006.
63. R. Krueger. An approach to assess delamination propagation simulation capabilities in commercial finite element codes. NASA/TM-2008-215123, National Aeronautics and Space Administration, Hampton, VA, USA; 2008.
64. A.C. Orifici, R. Krueger. Assessment of static delamination propagation capabilities in commercial finite element codes using benchmark analysis. NASA/CR-2010-216709, National Aeronautics and Space Administration, Hampton, VA, USA; 2010.
65. A.C. Orifici, R. Krueger. Benchmark assessment of automated delamination propagation capabilities in finite element codes for static loading. Finite Elements in Analysis and Design 54, 2012, (28-36).
66. E.F. Rybicki, M.F. Kanninen. A finite element calculation of stress intensity factors by a modified crack closure integral. Engineering Fracture Mechanics, 1977, vol9, p931-938.
67. B. Dattaguru, K.S. Venkatesha, T.S. Ramamurthy, F.G. Buchholzj. Finite Element estimates of strain energy release rate components at the tip of an interface crack under mode I loading. Engineering Fracture Mechanics Vol. 49, No. 3, pp. 451-463, 1994.
68. J.R. Reeder. An evaluation of mixed-mode delamination failure criteria. NASA technical memorandum 104210. Hampton (VA): Langley Research Center; 1992.

69. M.L. Benzeggagh, M. Kenane. Measurement of mixed-mode delamination fracture toughness of unidirectional glass/epoxy composites with mixed-mode bending apparatus. Composites Science and Technology 56 (1996) 439-449.

70. H. Chai. Three-dimensional fracture analysis of thin film debonding. International Journal of Fracture 1990;46:237–256.

71. Y. Zhang, S. Wang. Buckling, post-buckling and delamination propagation in debonded composite laminates: Part 1 Theoretical development. Composite Structures 2009;88:121–30.

72. S. Wang, Y. Zhang. Buckling, post-buckling and delamination propagation in debonded composite laminates: Part 2 Numerical applications. Composite Structures 2009;88:131–46.

73. T.K. Hosseini, S. Hosseini, B. Mohammadi. Delamination buckling growth in laminated composites using layerwise-interface element. Composite Structures 2010; 92:1846–1856.

74. R.C. Batra, J. Xiao. Analysis of post-buckling and delamination in laminated composite St. Venant–Kirchhoff beams using CZM and layer-wise TSNDT. Composite Structures 2013;105:369–384.

75. Z. Kutlu, F.K. Chang. Composite panels containing multiple through-the-width delaminations and subjected to compression. Part I: analysis. Composite Structures 1995;31:273–296.

76. P.F. Liu, S.J. Hou, J.K. Chu, X.Y. Hu, C.L. Zhou, Y.L. Liu, J.Y. Zheng, A. Zhao, L. Yan. Finite element analysis of postbuckling and delamination of composite laminates using virtual crack closure technique. Composite Structures 2011; 93:1549–1560.

77. S. Wang, C.M. Harvey, L. Guan. Partition of mixed modes in layered isotropic double cantilever beams with non-rigid cohesive interfaces. Engineering Fracture Mechanics 2013;111:1–25.

78. C.M. Harvey, J.D. Wood, S. Wang, A. Watson. A novel method for the partition of mixed-mode fractures in 2D elastic laminated unidirectional composite beams. Composite Structures 2014;116:589–594.

79. A.G. Evans, J. W. Hutchinson. On the mechanics of delamination and spalling in compressed film, Int. J. Solids Structure, Vol.20, No.5, PP 455-466, 1984.

80. J.D. Whitcomb. Parametric analytical study of instability-related delamination growth. Composites Science and Technology 25 (1986) 19-48.
81. B. Storåkers. Nonlinear aspects of delamination in structural members. In “Proc. XVIIth Int. Cobg. Theor. Appl. Mech.” (1988).
82. R.J. Rothschilds, J.W. Gillespie, L.A. Carlsson. Instability-related delamination growth in thermoset and thermos-plastic composites. In “Composite Materials: Testing and Design,” ASTM STP 972 (J.D. Whitcomb, ed.), (1998), pp. 161-179.
83. J.W. Hutchinson, M.D. Thouless, E.G. Liniger. Growth and configurational stability of circular, buckling-driven film delaminations. Acta Metall. Mater. 1992;40:295–308.
84. H.M. Jensen, I. Sheinman. Straight-sided, buckling-driven delamination of thin films at high stress level. International Journal of Fracture 2001;110:371–385.
85. M.W. Moon, H.M. Jensen, J.W. Hutchinson, K.H. Oh, A.G. Evans. The characterization of telephone cord buckling of compressed thin films on substrates. Journal of the Mechanics and Physics of Solids 2002;50:2355–2377.
86. H.M. Jensen, I. Sheinman. Numerical analysis of buckling-driven delamination. International Journal of Solids and Structures 2002;39:3373–3386.
87. H. Chai, C.D. Babcock, W.G. Knauss. One dimensional modelling of failure in laminated plates by delamination buckling. International Journal of Solid and Structures 1981;17:1069–1083.
88. K. Kokini, B.D. Choules, Y.R. Takeuchi. Thermal fracture mechanisms in Ceramic Thermal Barrier Coating. NASA conference publication 3312, 1995.
89. M.D. Thouless et al.. Plain-strain, buckling-driven delamination of thin films: model experiments and mode II fracture. Acta mater, Vol 40, No 10 pp 2639-2649, 1992.
90. M. Gella, E. Jordanb, K. Vaidyanathana, K. McCarrona, B. Barberb, Y.H. Sohna, V.K. Tolpygo. Bond strength, bond stress and spallation mechanisms of thermal barrier coatings. Surface and Coatings Technology 120–121 (1999) 53–60.
91. D. R. Mumm, A.G. Evans, I.T. Spitsberg. Characterization of a cyclic displacement instability for a thermally grown oxide in a thermal barrier system. Acta mater. 49 (2001) 2329–2340.
92. P.K. Wright, A.G. Evans. Mechanisms governing the performance of thermal barrier coatings. Curr. Op. Solid State Mater. Sci., 1999, 4, 255.

93. V. Sergo, D.R. Clarke. Observation of subcritical spall propagation of a thermal barrier coating. J. Am. Ceram. Soc., 1998, 81, 3237.
94. V.K. Tolpygo, D.R. Clarke. Surface rumpling of a (Ni, Pt) Al bond coat induced by cyclic oxidation. Acta mater., 2000, 48, 3283.
95. M.Y. He, A.G. Evans, J.W. Hutchinson. Effect of morphology on the decohesion of compressed thin films. Mater. Sci. Eng., 1998, A245, 168.
96. A.G. Evans, J.W. Hutchinson, M.Y. He. Micromechanics model for the detachment of residually compressed brittle films and coatings. Acta mater. 1999, 47, 1513.
97. P. Deb, D.H. Boone, T.F. Manley II. Surface instability of platinum modified aluminide coatings during 1100 °C cyclic testing. J. Vac. Sci. Tech. A, 1987, 5(6), 3366.
98. J.W. Holmes, F.A. McClintock. The chemical and mechanical processes of thermal fatigue degradation of an aluminide coating. Metall. Trans. A, 1990, 21, 1209.
99. R.C. Pennefather and D.H. Boone. Mechanical degradation of coating system in hightemperature cyclic oxidation. Surf. Coat. Tech., 1994, 76–77, 47.
100. M.Y. He, A.G. Evans, J.W. Hutchinson. The ratcheting of compressed thermally grown thin films on ductile substrates. Acta mater., 2000, 48(10), 2593.
101. A.G. Evens, D.R. Mumm, J.W. Hutchinson, G.H. Meier, F.S. Pettit. Mechanisms controlling the durability of thermal barrier coatings. Material Science 46, (2001) 503-553.
102. C. Mennicke, E. Schulmann, C. Ulrich, M. Ruehle. The effects of reactive element additions, sulfur removal, and specimen thickness on the oxidation behaviour of alumina-forming Ni-and Fe-base alloys. Mater Science forum 1997; 389:251-4.
103. M. Gell, K. Vaidyanathan, B. Barber, J. Cheng, E.H. Jordan. Mechanism of spallation in platinum aluminide/electron beam physical vapor-deposited thermal barrier coatings, Metallurgical and Materials Transactions A. February 1999, Volume 30, Issue 2, pp 427–435.
104. R.J. Christensen, V.K. Tolpygo VK, D.R. Clarke. The influence of the reactive element yttrium on the stresses in alumina scales formed by oxidation. Acta Mater 1997; 45:1761-6.

105. P.-Y. Thery, M. Poulain, M. Dupeux, M. Braccini. Spallation of two thermal barrier coating systems: experimental Spallation of two thermal barrier coating systems: experimental oxidation. J Mater Sci (2009) 44:1726–1733.
106. D.S. Balint, J. W. Hutchinson. An analytical model of rumpling in thermal barrier coatings. Mechanics and Physic of Solids, 53 (2005) 947-973.
107. H. H. Yu, J. W. Hutchinson. Influence of substrate compliance on buckling delamination of thin films. International Journal of Fracture 113: 39–55, 2002.
108. T. Q. Lu, T. J. Wang. Asymptotic solutions for buckling delamination induced crack propagation in the thin film- compliant substrate system. 13th International Conference on Fracture, June 16–21, 2013.
109. B. Cotterell, Z. Chen. Buckling and cracking of thin film on compliant substrates under compression. International Journal of Fracture 104, 169–179, July 2000.
110. S.S. Kim, Y.F. Liu, Y. Kagawa. Evaluation of interfacial mechanical properties under shear loading in EB-PVD TBCs by the pushout method. Acta materialia 55 (2007) 3771-3781.
111. R. Vaßen, Y. Kagawa, R. Subramanian, P. Zombo, D.M. Zhu. Testing and evaluation of thermal-barrier coatings. MRS Bulletin, Volume 37, OCTOBER 2012.
112. R.G. Hutchinson. Lifetime assessment for thermal barrier coatings: Tests for Measuring Mixed Mode Delamination Toughness. J. Am. Ceram. Soc., 94 [S1] S85–S95 (2011).
113. I. Hofinger, M. Oechsner, H.-A. Bahr, M.V. Swain. Modified four-point bending specimen for determining the interface fracture energy for thin, brittle layers. International Journal of Fracture (1998) 92: 213.
114. M. J. Stiger, L. A. Ortman, F. S. Pettit, G. H. Meier. Measurement of interfacial toughness in thermal barrier coating systems by indentation. Poster Paper presented at ATS Annual Program Review November 8-10, 1999.
115. B.D. Davidson, H. Hu, R.A. Schapery. An analytical crack tip element for layered elastic structures. J Appl Mech Trans ASME 1995; 62: 294-305.
116. Y.F. Liu, Y. Kagawa, A. G. Evans. Analysis of a “barb test” for measuring the mixed-mode delamination toughness of coatings. Acta Mat. 56, 43-49, 2008.

117. R.V.Hillery, B.H. Pilsner, R.L. McKnight, T.S. Cook, M.S. Hartle. Thermal barrier coating life prediction model development. Final Report," NASA CR-180807, National Aeronautics and Space Administration, 1988.
118. J. Cheng, E.H. Jordan, B. Barber, M. Gell. Thermal/residual stress in an electron beam physical vapour deposited thermal barrier coating system. Acta mater. Vol. 46, No. 16, pp. 5839-5850, 1998.
119. A.M. Freborg, B.L. Ferguson, W.J. Brindley, G.J. Petrus. Modelling oxidation induced stresses in thermal barrier coatings. Materials Science and Engineering A245 (1998) 182–190.
120. A.M. Karlsson, A.G. Evans. A numerical model for the cyclic instability of thermally grown oxides in thermal barrier systems. Acta Materialia, 49(10) pp. 1793-1804, 2001.
121. U. Hermosilla, I.A. Jones, T.H. Hyde, R.C. Thomson, M.S.A. Karunaratne. Finite element modelling of development of stresses in thermal barrier coatings. Material Science and Engineering A513-514, 2009.
122. U. Hermosilla, M.S.A. Karunartne, I.A. Jones, T.H. Hyde, R.C. Thomson. Modelling the high temperature behaviour of TBCs using sequentially coupled microstructural-mechanical FE analysis; 2013.
123. V.K. Tolpygo, D.R. Clarke. Spalling failure of α-alumina films grown by oxidation: I. Dependence on cooling rate and metal thickness [J]. Materials Science and Engineering: A, 2000, 278(1): 142-150.
124. V.K. Tolpygo, D.R. Clarke. Spalling failure of α-alumina films grown by oxidation. II. Decohesion nucleation and growth [J]. Materials Science and Engineering: A, 2000, 278(1): 151-161.
125. K. Ogawa, T. Okhoshi, T. Takeuchi, T. Mizoguchi, T. Masumoto. Nucleation and growth of stress relief patterns in sputtered molybdenum films, Japanese Journal of Applied Physics 25, 695-700Thin layer del paper Journal of Applied Mechanics, (1986).
126. J.D. Wood, C.M. Harvey, S. Wang. Partition of mixed-mode fractures in 2D elastic orthotropic laminated beams under general loading. Composite Structures. 149, 239 (2016).

127. J.W. Hutchinson, M.Y. He, A.G. Evans. The influence of imperfection on the nucleation and propagation of buckling driven delamintaions. Journal of the Mechanics and Physics of Solids 2000;48:709–734.

128. M.Y. He, A.G. Evans, J.W. Hutchinson. Effects of morphology on the decohesion of compressed thin films. Material Science and Engineering 1998;A245:168–181.

129. F. Gaudette, S. Suresh, A.G. Evans, G. Dehm, M. Rühle. The influence of chromimum addition on the toughness of $\gamma - Ni\alpha - Al_2O_3$ interfaces. Acta Mater. 1997;45:3503–3515.

130. C. Zhu, X.F. Zhao, I.S. Molchan, G.E. Thomson, G.Y. Liang, P. Xiao. Effect of colling rate and substrate thickness on spallation of alumina scale on Fecralloy. Material Science and Engineering 2011; A528: 8687–8693.

131. L.B. Freund, S. Suresh. Thin Film Materials. (January 12, 2003).

132. N.P. Padture, M. Gell, E.H. Jordan. Thermal barrier coatings for gas-turbine engine applications. Science vol. 296 12 April 2002.

133. D.R. Clarke, M. Oechsner, N.P. Padture and Guest Editors. Thermal-barrier coatings for more efficient gas-turbine engines. Clarke, October 2012 Vol. 37, No. 10.

134. R.A. Miller, S.R. Levine, P.E. Hodge. Thermal barrier coating for superalloys. Superalloys 1980; 474.

135. R.A. Miller, C.E. Lowell. Failure mechanisms of thermal barrier coatings exposed to elevated temperatures. 1982, NASA report number TM-82905.

136. R.A. Miller. Oxidation-based model for thermal barrier coating Life. Journal of the American Ceramic Society. Volume 67, No. 8 August 1984.

137. A.S. Argon, V. Gupta, H.S. Landis, J.A. Cornie. Intrinsic toughness of interfaces between Sic coatings and substrates of Si or C libre. J. Mater. Sci. 24, 1207-l 218 (1989).

138. M.J. Stiger, N.M. Yanar, M.G. Topping, F.S. Petti, G.H. Meier. Thermal barrier coatings for the 21st century. Z. Metallk 1999; 90:1069-78.

139. M. Tanaka, Y.F. Liu, S.S. Kim, Y. Kagawa. Delamination toughness of electron beam physical vapor deposition (EB-PVD) Y2O3–ZrO2 thermal barrier coatings by the pushout method: Effect of thermal cycling temperature. J. Mater. Res., Vol. 23, No. 9, Sep 2008.

140. J.M. McKinney. Mixed-mode fracture of unidirectional graphite/epoxy composites. J Compos Mater 1972;6:164–6.

141. S.H. Yoon, C.S. Hong. Interlaminar fracture toughness of graphite/epoxy composite under mixed-mode deformations. Exp Mech 1990;30:234–9.

142. A. Zhuk, A.G. Evans, G, Whitesides, J.W. Hutchsinson, J. Mater. The adhesion energy between polymer thin films and self-assembled monolayers. 1998, 13, 3555.

143. M.Y. He, A.G. Evans, J.W. Hutchinson. Convergent debonding of films and fibers. Acta Mater., 1997, 45, 3481.

144. P.G. Charalambides, J. Lund, A.G. Evans, R.M. McMeeking. A test specimen for determining the fracture resistance of bimaterial interfaces. J. Appl. Mech., 56, 77–82 (1989).

145. J.T. DeMasi. Thermal barrier coating life prediction model development. NASA report number CR-179508, April 1986.

146. T.A. Cruse, S.E. Stewart, M. Ortiz. Thermal barrier coating life prediction model development. Journal of Engineering for Gas Turbines and Power; Vol. 110/611, OCTOBER 1988.

147. T.A. Cruse, S.E. Stewart, M. Ortiz. Thermal barrier coating life prediction model development. ASME, 1991.

148. S.M. Meier, D.M. Nissley, K. D. Sheffler, T. A. Cruse. Thermal barrier coating life prediction model development. ASME, 258/Vol. 114, 1992.

149. D.M. Nissley. Thermal barrier coating life modeling in aircraft gas turbine engines. NASA conference publication 3312, 1995.

150. C.M. Harvey, J.D. Wood, S. Wang. Brittle interfacial cracking between two dissimilar elastic layers: Part 1 – Analytical development. Composite Structures 2015;134:1076–1086.

151. C.M. Harvey, J.D. Wood, S. Wang. Brittle interfacial cracking between two dissimilar elastic layers: Part 2 – Numerical verification. Composite Structures 2015;134:1087–1094.

152. S. Wang, C.M. Harvey, B. Wang, A. Watson. Post-local buckling-driven delamination in bilayer composite beams. Composite Structures 2015;133:1058–66.

153. J. Xu, Q. Zhao, P. Qiao. A critical review on buckling and postbuckling analysis of composite structures. Frontiers in Aerospace Engineering 2013;2:157–168.

154. Z. Kutlu, F.K. Chang. Composite panels containing through-the-width delaminations and subjected to compression. Part II: Experiments and verification. Compos Struct 1995;31:297–314.

155. R.A. Jurf, R.B. Pipes. Interlaminar fracture of composite materials. J Compos Mater 1982;16:386–94.

156. R.J. Sanford, F.R. Stonesifer. Fracture toughness of filament-wound composites. Part 1: Effect of material variables. NRL report 7112, Naval Research Laboratory; 1970.

157. S.L. Donaldson. Fracture toughness testing ofgraphite/epoxy and graphite/PEEK composites. Composites 1985;16:103–12.

158. E.M. Wu. Application of fracture mechanics to anisotropic plates. J Appl Mech 1967;34:967–74.

159. S.P. Koenig et al.. Ultrastrong adhesion of graphene membranes. Nature Nanotechnology. 6, 543–546 (2011).

160. Z. Zong et al.. Direct measurement of graphene adhesion on silicon surface by intercalation of nanoparticles. Journal of Applied Physics. 107, 026104 (2010).

161. Z. Cao et al.. A blister test for interfacial adhesion of large-scale transferred graphene. CARBON. 69, 390–400 (2014).

162. T. Yoon et al.. Direct measurement of adhesion energy of monolayer graphene as-grown on copper and its application to renewable transfer process. NANO Letters. 12, 1448–1452 (2012).

163. K. Yue et al.. Analytical methods for the mechanics of graphene bubbles. Journal of Applied Physics. 112, 083512 (2012).

164. P. Wang et al.. Numerical Analysis of Circular Graphene Bubbles. Journal of Applied Mechanics. 80, 040905 (2013).

165. T. Georgiou et al.. Graphene bubbles with controllable curvature. Applied Physics Letters. 99, 093103 (2011).

166. J.M. Jensen. The blister test for interface toughness measurement. Engineering Fracture Mechanics. 40, 475–486 (1991).

167. J.M. Jensen. Analysis of mode mixity in blister tests. Journal of Fracture. 94,79–88 (1998).

168. L. Tong, Y. Wang. Closed form formulas for adhesion energy of blister tests under pressure and point load. Journal of Adhesion. 92,171–193 (2016).

169. B. Storåkers. Variation principles and bounds for the approximate analysis of plane membranes under lateral pressure. Journal of Applied Mechanics. 50**,**743–749 (1983).

170. Q. Ma, D.R. Clarke. Stress measurement in single-crystal and polycrystalline ceramics using their optical fluorescence. Journal of the American Ceramic Society. 76, 1433-1440 (1993).

171. D.M. Lipkin, D.R. Clarke. Measurement of the stress in oxide scales formed by oxidation of alumina-forming alloys. Oxidation of Metals. 45, 267-280 (1996).